www.mtri.org

Integration of Unmanned Aerial Systems Data Collection into Day-to-Day Usage for Transportation Infrastructure – A Phase III Project

Final Report, No. SPR-1713

Prepared by:
C. Brooks[1], C.Cook[1], R. Dobson[1], T. Oommen[2], K. Zhang[2], A. Mukherjee[2], R.Samsami[2], A.Semenchuk[3], B.Lovelace[4], V.Hung[2], Y.Yang[2], Y.Tan[2], A.Jenkins[1], J.Graham[1], V.C. Lekha[2], M.Billmire[1], V.Barber[1].

[1]Michigan Tech Research Institute (MTRI), Michigan Technological University, 3600 Green Ct., Ste. 100, Ann Arbor, Michigan 48105
[2] Michigan Technological University (MTU), 1400 Townsend Drive, Houghton, Michigan, 49931
[3] Surveying Solutions Inc. (SSI), Standish, MI
[4] Collins Engineers Inc., St. Paul, MN

Project Manager:
Steven J. Cook, P.E.
Michigan Department of Transportation
6333 Lansing Road
Lansing, MI 48917

Research Manager:
André Clover, P.E.
Michigan Department of Transportation
8885 Ricks Road
Lansing, MI 48917

1. Report No. 1713	**2. Government Accession No.** N/A	**3. MDOT Project Manager** Steven J. Cook, P.E	
4. Title and Subtitle Integration of Unmanned Aerial Systems Data Collection into Day-to-Day Usage for Transportation Infrastructure - A Phase III Project		**5. Report Date** March 11, 2022 **6. Performing Organization Code** N/A	
7. Author(s) C. Brooks, C.Cook, R. Dobson, T. Oommen, K. Zhang, A. Mukherjee, R.Samsami, A.Semenchuk, B.Lovelace, V.Hung, Y.Yang, Y.Tan, A.Jenkins, J.Graham, V.C. Lekha, M.Billmire, V.Barber.		**8. Performing Org. Report No.** N/A	
9. Performing Organization Name and Address Michigan Technological University 1400 Townsend Drive Houghton, MI 49931		**10. Work Unit No.** N/A **11. Contract or Grant No.** 2019-0311 Z1	
12. Sponsoring Agency Name and Address Michigan Department of Transportation Research Administration 8885 Ricks Road P.O. Box 33049 Lansing, Michigan 48909		**13. Type of Report & Period Covered** Final Report, 06/12/2019 to 06/11/2022 **14. Sponsoring Agency Code** N/A	
15. Supplementary Notes Conducted in cooperation with the U.S. Department of Transportation, Federal Highway Administration. MDOT research reports are available at www.michigan.gov/mdotresearch.			
16. Abstract The capabilities of unmanned / uncrewed aerial system (UAS) continue to advance, with a wide variety of applications useful for the condition assessment and monitoring of transportation infrastructure. This Phase 3 project focused on four UAS uses cases and how to integrate their results into MDOT databases and workflows. The four use cases were for traffic operations, bridge inspection assessment, construction inspection, and lidar UAS for design survey. Extensive field data collections at multiple sites in Michigan helped to develop and demonstrate how UAS-enabled methods can create high-resolution geospatial outputs useful for MDOT operations and maintenance. Traffic data created included origin-destination results and traffic counts. Bridge inspection data created included automated detection of spalls and delaminations, and 3D models of bridges. Construction inspection data created included rates of production for concrete removal and asphalt paving, and building information model (BIM) data. Lidar UAS data created included high-resolution 3D models useful for surveying. Two additional project tasks documented the data results and methods, and how these could be integrated into appropriate MDOT workflows.			
17. Key Words Unmanned / uncrewed aerial system, UAS, bridges, traffic, lidar, construction, information models, operations, BIM		**18. Distribution Statement** No restrictions. This document is available to the public through the Michigan Department of Transportation.	
19. Security Classification - report Unclassified	**20. Security Classification - page** Unclassified	**21. No. of Pages** 153 155?	**22. Price** N/A

Acknowledgments

The Michigan Tech project team would like to thank the MDOT program manager, Steve Cook, P.E. and the research manager, André Clover, P.E. for their input and advice during this project and the previous two phases that they have guided us through. The advice of the project's MDOT subject matter experts and other MDOT staff was also critical to the success of the project. The Principal Investigator (PI) would like to thank his dedicated project team for their commitment to safely collecting high quality, useful data ready for use by MDOT in its operations.

Research Report Disclaimer

Contents

List of Figures v
Milestone 6: Implement DUAP/TfM Viable Integrations for Each Use Case viii
List of Tables x
1. Executive Summary 1
2. Background 2
2.1 Objectives 2
2.2 Tasks 3
3. Use Case/Milestone Descriptions and Results 4
3.1 Use Case/Milestone 1: Traffic Operations 4
3.1.1 Methodology 4
3.1.2 Findings 19
3.1.3 Discussion 24
3.2 Use Case/Milestone 2: Bridge Inspection Assessment 25
3.2.1 Methodology 25
3.2.2 Findings 27
3.2.3 Discussion 57
3.3 Use Case/Milestone 3: Construction Inspection 58
3.3.1 Methodology 58
3.3.2 Findings 60
3.3.3 Results 72
3.3.4 Discussion 74
3.3.5 Related Training 75
3.4 Use Case/Milestone 4: Lidar UAS for Design Survey 76
3.4.1 Methodology 76
3.4.2 Findings 80
3.4.3 Discussion 91
3.5 Milestone 5: Assess DUAP/TFM Integration With Each Use Case 91
3.5.1 Use Case 1 - Traffic Operations data sets: 92
3.5.2 Use Case 2 - Bridge Inspection Assessment data sets: 92
3.5.3 Use Case 3 - Construction Inspection data sets: 92

3.5.4 Use Case 4 - LiDAR UAS for Design Survey data sets 93
3.6 Milestone 6: Implement DUAP/TFM Viable Integrations for Each Use Case 94
Workflow Diagrams 94
4. Conclusions 97
5. Bibliography 99
6. Appendices 1
6.1 List of Acronyms, Abbreviations and Symbols 1
6.2 Installation of the ArcPro Bridge Inspection Toolset 1
6.3 “Spallgorithm” Manual 3
6.4 Thermal Anomaly and Delamination Detection Algorithm Manual 10
6.5 Lidar Ground Control Target Document 13
6.6 UAS-enabled Bridge Inspection Demonstration Day 32
6.7 ThermoConverter Tool by Aetha Global 32
6.8 TADDA and Spallgorithm Results (Quantitative Delamination and Spall Data) 35

List of Figures

Use Case 1 - Traffic Operations

Figure 3.1.1: Screenshots of drone videos collected at I-96 on August 5, 2019. ……..…5

Figure 3.1.2: Screenshots of drone videos collected at several sites on August 13, 2019. ….….6

Figure 3.1.3: US-23/M-14 Weaving Area Overview. ……..…...7

Figure 3.1.4: Screenshot of drone video collected at the US-23 SB/Plymouth Rd exit for the weaving area on March 3, 2020. …….…….8

Figure 3.1.5: Screenshots of drone video collected for the US23/M14/Plymouth Rd weaving area on July 9, 2020. …….……...9

Figure 3.1.6: Screenshots of drone video collected for the US23/M14 weaving area on July 15, 2020. …….……9

Figure 3.1.7: Screenshots of drone videos collected for the US23/M14 weaving area on July 31, 2020…….…..10

Figure 3.1.8: Screenshots of videos collected for the US23/M14 weaving area on July 27th, 2020. ……..…11

Figure 3.1.9: Screenshots of videos collected for the US23/M14 weaving area on September 17th, 2021. ……....12

Figure 3.1.10: Screenshots of videos collected for the US23/M14 weaving area on October 26th, 2021. ……..…12

Figure 3.1.11: Williamston Road (I-96) Traffic Corridor. ……....13

Figure 3.1.12: Screenshot of videos collected for Williamston Road on October 7, 2020. …….14

Figure 3.1.13: Screenshot of videos collected for Williamston Road on November 13, 2020. ...14

Figure 3.1.14: Screenshot of videos collected for Williamston Road on December 10, 2021. …15

Figure 3.1.15: US23/M14 weaving area traffic monitoring process. ……...16

Figure 3.1.16: Automatic vehicle detection and tracking at US23/M14 weaving area. ……..17

Figure 3.1.17: Probe vehicle trajectory for the US23/M14 weaving area. ……..17

Figure 3.1.18: Probe vehicle appears in upstream and downstream video of the weaving area. .18

Figure 3.1.19: Real-time demonstration of fixed location traffic monitoring at Williamston Rd (Application 2). …….18

Figure 3.1.20: A screenshot of processed streaming video from WIlliamston Rd. on December 10, 2021. ……19

Use Case/Milestone 2: Bridge Inspection Assessment

Figure 3.2.1: Beyer Road bridge, near Saginaw, MI, showing thermal data and optical data from the August 17, 2021 data collection. ……26

Figure 3.2.2: Brian Zakrzweski providing input during UAV-assisted bridge inspection testing and demonstrations in August and September, 2019. ……..……..27

Figure 3.2.3: Relative temperature thermal mosaic and visual orthophoto of Uncle Henry Rd. Bridge. ……..……28

Figure 3.2.4: Relative temperature thermal mosaic from 2016 and 2021 for Uncle Henry Rd. Bridge. ……..29

Figure 3.2.5: Comparison of the 2016 vs 2021 Uncle Henry Rd. delamination results show the growth and newly developed areas of delamination. ……30

Figure 3.2.6: 2021 relative thermal and RGB orthoimages for Beyer Rd. Bridge. ……..31

Figure 3.2.7: Beyer Rd. Bridge relative thermal orthoimages from 2016 and 2021 and output TADDA delamination detections compared. ……32

Figure 3.2.8: Beyer Rd. Bridge RGB orthoimages from 2016 and 2021, with TADDA delamination detection results, compared. ……..…….33

Figure 3.2.9: Result of TADDA analysis of the M99 / I96 bridge. ……..34

Figure 3.2.10: Detected thermal delaminations on the M99 / I96 bridge. ……...35

Figure 3.2.11: Billwood highway bridge divided into 3 sections, A, B, and C. ……..36

Figure 3.2.12: Section A of Billwood highway and detected delaminations. …….37

Figure 3.2.13: Section B of Billwood highway and detected delaminations. …….38

Figure 3.2.14: Section C of Billwood highway and detected delaminations. …….39

Figure 3.2.15: Result of TADDA analysis for the Laplaisance Creek exit ramp. ….……..……40

Figure 3.2.16: Section-wise depiction of delaminations in the Laplaisance Creek exit ramp. …41

Figure 3.2.17: Section-wise depiction of delaminations in the Laplaisance Creek exit ramp, .compared with the bridge inspection report. ……42

Figure 3.2.18: Location of the Houghton-Hancock Bridge / Portage Lake Lift Bridge. ……..43

Figure 3.2.19: Optical and hyperspectral images of the underside of the lift bridge. ……...43

Figure 3.2.20: Averaged spectral curves of rust and non-rust areas of the Houghton - Hancock Bridge. ……...44

Figure 3.2.21: Unsupervised classification of hyperspectral imagery of Houghton - Hancock Bridge beam 1. ……..45

Figure 3.2.22: Unsupervised classification of hyperspectral imagery of Houghton - Hancock Bridge beam 2. ……..45

Figure 3.2.23: Comparison of 2016 and 2021orthomosaic and spallgorithm detection outputs for Uncle Henry Rd. bridge. ……...47

Figure 3.2.24: Uncle Henry orthophoto, hillshaded DEM with 2021 spall detection outputs displayed. ……..48

Figure 3.2.25: Comparison of Beyer Rd. bridge 2016 orthoimage & spallgorithm output and 2021 orthoimage with apparent patched spalls. ……49

Figure 3.2.26: Optical orthophoto and DEM of the M-99/I-96 bridge with spallgorithm results shown in table. ……50

Figure 3.2.27: Laplaisance Creek/I-75 Exit Ramp orthophoto, hillshaded DEM, and spallgorithm detection outputs displayed. ……51

Figure 3.2.28: Example situations highlighting the utility of drones in surveying locations that are otherwise difficult to assess. ……..53

Figure 3.2.29: 3D model of LaPlaisance Creek Exit Ramp bridge and Beyer Rd bridge. …..…54

Figure 3.2.30: Skydio 3D Scan screenshot captured during autonomous scan of the Breyer Road Bridge. ……..…55

Figure 3.2.31: ContextCapture Postprocessing Software showing aero-triangulation of the Breyer Road Bridge. ……56

Figure 3.2.32: Final Beyer Road Bridge Model. ……56

Figure 3.2.33: Cloud-based model of the Beyer Road Bridge showing an example of the photo navigation tool. ……57

Use Case/Milestone 3: Construction Inspection

Figure 3.3.1: Examples of different data types collected as part of the Construction Inspection Use Case/Milestone. ……59

Figure 3.3.2: UAV geometry factors for concrete pavement activity inspection or survey (Samsami et al., 2021). ……60

Figure 3.3.3: Image processing example – MDOT I-496 Project. ……..61

Figure 3.3.4: Image processing example two – MDOT I-496 Project. ……...62

Figure 3.3.5: Image labeling example – MDOT I-496 Project. ……..63

Figure 3.3.6: Example highway corridor geometric parameters. ……63

Figure 3.3.7: Example highway corridor section view and modeling parameters. …….64

Figure 3.3.8: DEM derived from UAS imagery and Civil 3D surface for an example stretch of I-496. ……67

Figure 3.3.9: DEM derived from UAS imagery and Civil 3D surface for an example stretch of I-496. ……68

Figure 3.3.10: UAS-derived hillshade, example polyline transect extracted from the hillshade, and polyline overlain on Civil 3D layer for an example stretch of I-496. ……68

Figure 3.3.11: UAS-derived hillshade (left), example polyline transect extracted from the hillshade (middle), and polyline overlain on Civil 3D layer (bottom) for an example stretch of I-496. ……69

Figure 3.3.12: Thermal and RGB Images collected during the MDOT I-69 HMA pavement project. ……70

Figure 3.3.13: Sample processed thermal images of I-69 asphalt paving. ……..71

Figure 3.3.14: UAV-based inspection workflow for Construction Inspection related tasks. …..75

Figure 3.3.15: Figure 3.3.15: Example images from md4-1000+ training session held in June, 2020 for MDOT and Michigan Tech participants, including the UAS (top left), Michael Soper receiving training from the mdMapper trainer (top right), and a sample image taken during the training held at the MTRI office……76

Use Case/Milestone 4: Lidar UAS for Design Survey

Figure 3.4.1: MLS and UAS-based Lidar data acquisitions performed in Standish, MI, at US-23 junction. ……..……..……77

Figure 3.4.2: SSI's MLS and UAS- based Lidar systems, and example DGN file containing traditional survey data for soft surfaces. ……78

Figure 3.4.3: Three UAS-based Lidar data collection sites along US-127 near Rives Junction, MI. Data were collected Sept 16th, 2020. ……..79

Figure 3.4.4: Visual comparison of UAS and MLS data for one example ground control chevron 4" wide and 2' long on each side. ……..80

Figure 3.4.5: A 1 ft wide transect drawn across both MLS and UAS - derived Lidar data for the Standish, MI, site. ……...83

Figure 3.4.6: Areas of greatest difference between UAS and traditional survey elevation data for the Standish Lidar survey. ……..84

Figure 3.4.7: Analysis of drone-based Lidar accuracy for dense grasses, compared with traditional survey data. ……...85

Figure 3.4.8: Cross-hatched UAS-based Lidar scan intensity data collected at 'Site A', the bridge over Grand River, along US-127 near Rives Junction, MI. ……...86

Figure 3.4.9: Lidar scan intensity point cloud and drone RGB image of the same location at 'Site A'. ……...87

Figure 3.4.10: Example analysis of ground control target intensities at a surveyed site along US-127. ……..88

Figure 3.4.11: A vector-type file (e.g., a shapefile) can be used to recreate a ground control point of known proportions for accurate post-processing of the point cloud. ……89

Milestone 6: Implement DUAP/TfM Viable Integrations for Each Use Case

Figure 3.6.1: Traffic Operations workflow diagram. ……94

Figure 3.6.2: Bridge Inspection workflow diagram. ……94

Figure 3.6.3: Construction Inspection workflow diagram. ……95

Figure 3.6.4: LiDAR UAS for Design Survey workflow diagram. ……..95

Appendices

Figure 6.2.1: Adding a toolbox to ArcGIS Pro project document. ……A-1

Figure 6.2.2: Update the script file location on the local computer. ……...…….…..…..A-2

Figure 6.2.3: Adding the Ribbon Customization. ……..…….A-2

Figure 6.3.1: Identifying the Coordinate System of a DEM in ArcGIS Pro. …….…...…….A-5

Figure 6.3.2: Creating a new shapefile with a specific Coordinate System. ……..A-6

Figure 6.3.3: Drawing a polygon in ArcGIS Pro to set the analysis inclusion zone. …… A-7

Figure 6.3.4: Saving edits made to the new shapefile. ……...A-8

Figure 6.3.5: Selecting the input parameters/layers for use in the Spallgorithm. ……...A-8

Figure 6.3.6: Inspecting the spallgorithm processing while in progress. ……. .A-9

Figure 6.3.7: False positive for Beyer Rd bridge location used as the example. ……. .A-9

Figure 6.4.1: Loading of the TADDA toolbox and selection of input parameters. ……..A-10

Figure 6.4.2: Final processed delamination result exported as a shapefile in the user defined output folder. …….A-11

Figure 6.4.3: The result of the TADDA analysis as delamination polygons overlaid over the corresponding thermal raster. ……A-12

Figure 6.4.4: TADDA processing results saved in the working directory. ……. .A-12

Figure 6.5.1: Example UAS and MLS scan intensity point clouds of hard surfaces from the Standish, MI US-23 survey. ……..A-21

Figure 6.5.2: Example UAS ground-only point cloud of return intensity data of a common 2x2 ft white and black cloth field photogrammetry ground control target. ……A-22

Figure 6.5.3: Comparison of drone orthophoto, UAS LiDAR, and MLS LiDAR data collected in Standish, MI. …….A-23

Figure 6.5.4: LiDAR data collected for ‘Site A’ at the US-127 site over Grand River outside Rives Junction, MI (October 2020). …….A-24

Figure 6.5.5: Test ground control targets at the US-127 over Grand River site outside of Rives Junction, MI (October, 2020). …….……A-25

Figure 6.5.6: Ground control targets seen in RGB imagery and LiDAR point scan intensity of return data collected at US-127 outside of Rives Junction, MI (October, 2020). ……A-26

Figure 6.5.7: RGB image, LiDAR scan intensity data, and three foot wide cross-section of LiDAR scan intensity data that crosses several example ground control targets. ……A-27

Figure 6.5.8: RGB image, LiDAR scan intensity data, and three foot wide cross-section of LiDAR scan intensity data that crosses several example ground control targets. …….. .A-28
Figure 6.5.9: Diagram of incident LiDAR lasers scanned vertically along a flat wall. ……A-29
Figure 6.5.10: Nikon imagery, LiDAR scan intensity data, and 1 foot-wide cross-section, showing scan intensity and elevation data for the transect across test ground control. ……A-30
Figure 6.5.11: A vector-type file (e.g., shapefile) can be used to recreate a ground control point of known proportions and accurately locate ground control in a point cloud. …….A-31
Figure 6.7.1: DJI RGB thermal image and visual image (right) collected simultaneously by the Mavic 2 Enterprise Advanced during asphalt paving. ……..A-32
Figure 6.7.2: ThermoConverter tool interface. ……..…A-33
Figure 6.7.3: Example thermal orthoimage created in Pix4D. ….…….…….…..…A-34

List of Tables

Use Case 1 - Traffic Operations

Table 3.1.1: Comparison of MDOT calculated OD flow and semi-automatically detected OD flow. ……..20
Table 3.1.2: Comparison between the ground truth and automatically detected OD flow results for the US23/M14 weaving area on October 26, 2021. ……21
Table 3.1.3: Comparison of MDOT calculated OD flow and automatically detected OD flow. for the US23/M14 weaving area on October 26, 2021. ……..21
Table 3.1.4: Comparison between the ground truth and automatically detected vehicle counts at Williamston Rd on Dec. 10, 2021. ……22
Table 3.1.5: Comparison of MDOT VDS data and automatically detected analytics - vehicle counts - from December 10, 2021, data collection at WIlliamston Rd. ……23
Table 3.1.6: Comparison of MDOT VDS data and automatically detected analytics - density (veh/mile) - from December 10, 2021, data collection at Williamston Rd. ……..24

Use Case/Milestone 2: Bridge Inspection Assessment

Table 3.2.1: List of data collected and results generated by TADDA and Spallgorithm processing. Full detailed tables for each bridge are found in Appendix 6.8. ……...…..……52

Use Case/Milestone 3: Construction Inspection

Table 3.3.1: Drone platforms and sensors used for surveys for the Construction Inspection use case. ……...59
Table 3.3.2: BIM parameters extracted from UAV images of MDOT I-496 Project. …..…..…...65
Table 3.3.3: BIM parameters extracted from UAV images of MDOT I-69 Project. ……66
Table 3.3.4: Geometric parameters for pavement removal for I-496. ……..69

Table 3.3.5: Production rate comparison for I-496. …….73

Table 3.3.6: Thermal parameters estimated for MDOT I-69 project. ……..74

Use Case/Milestone 4: Lidar UAS for Design Survey

Table 3.4.1: Results of point cloud density, and accuracy, from analysis of ground control targets visible in both the MLS and UAS point clouds for the Standish, MI, survey. …….80

Table 3.4.2: NCHRP Report 748 (2013) - accuracy & resolution levels Guidelines for the Use of Mobile LiDAR in Transportation Applications. ……..……..……81

Appendices

Table 6.8.1: Laplaisance Creek/ I-75 Exit Ramp spallgorithm spall results. ……...……A-35

Table 6.8.2: Laplaisance Creek/ I-75 Exit Ramp delamination TADDA results. ……A-35

Table 6.8.3: M-99/I-96 bridge spallgorithm spall results. ……A-37

Table 6.8.4: M-99/I-96 bridge delamination TADDA results. ……..……A-37

Table 6.8.5: Uncle Henry Rd. bridge spallgorithm spall results. ……A-38

Table 6.8.6: Uncle Henry Rd. bridge delamination TADDA results. ……..……...…A-39

Table 6.8.7: Beyer Rd. bridge delamination TADDA results. ……...…..A-39

Table 6.8.8: Billwood Rd./ I-96 bridge delamination TADDA results. ……...……A-40

1. Executive Summary

This report, SPR-1713, describes the accomplishments of the "Integration of Unmanned Aerial Systems Data Collection into Day-to-Day Usage for Transportation Infrastructure" research project, contract number 2019-0311, authorization number Z1, as funded by the US DOT Federal Highway Administration (FHWA) and Michigan Department of Transportation (MDOT). Senior Research Scientist Colin Brooks of the Michigan Tech Research Institute (MTRI), a research center of Michigan Technological University (Michigan Tech), served as the Principal Investigator on the project, with a period of performance from June 12th, 2019 to June 11th, 2022. Co-Investigators were: Dr. Thomas Oommen of the Michigan Tech Department of Geological and Mining Engineering and Sciences (GMES), Dr. Amlan Mukherjee of the Michigan Tech Department of Civil, Environmental, and Geospatial Engineering (CEGE), and Dr. Kuilin Zhang (CEGE), and Research Scientist Richard Dobson of MTRI. A research project team of numerous Michigan Tech researchers and students provided critical support to performing and documenting the project's milestone research tasks. The project builds directly from MDOT's Phase II project, called "Implementation of Unmanned Aerial Vehicles (UAVs) for Assessment of Transportation Infrastructure", as captured in the Phase II final report (Brooks et al. 2018), the Phase I project, called "Evaluating the Use of Unmanned Aerial Vehicles for Transportation Purposes" (Brooks et al. 2015), and the "Successful Approaches for the Use of Unmanned Aerial System by Surface Transportation Agencies" National Cooperative Highway Research Program (NCHRP) Domestic Scan 17-01 (Banks et al. 2018).

This work has been shared regularly with the project's research advisory panel, composed of the project manager, the research manager, and MDOT subject matter experts. Results and insights were shared at a It has also been presented twice to the Transportation Research Board (TRB) community at the Annual Meeting and through two TRB webinars.

This report describes and summarizes the utility of unmanned aerial systems (UAS, uncrewed aerial systems, UAVs, or "drones") for four primary use cases: the utility of UAS for traffic monitoring, bridge inspection, construction inspection, and drone-based lidar collections for design survey. These were selected by MDOT staff as the most promising areas for likely implementation into day-to-day usage by MDOT staff for collection critical data useful for MDOT operations and maintenance activities, informed by the previous research phases and other technological advances since MDOT's UAS research efforts started in 2013.

For the Traffic Operations use case, data created included origin-destination results and traffic counts. A series of 12 data collections helped establish methods including optimal flying height, how and where to fly UAS to monitor traffic corridors and weaving areas, and how to automatically analyze live video made available to MDOT Traffic Operations Center staff. For the Bridge Inspection Assessment use case, data created through 10 ten data collections included automated detection of spalls and delaminations with completed tools that work in an ESRI ArcGIS Pro environment, plus creation of 3D models of bridges using new UAS with artificial intelligence (AI) enabled collision avoidance. Two bridges first assessed using UAS sensing in

2016 during Phase II were revised in 2021 to demonstrate how optical and thermal data collected via UAS can detect changes in spall and delaminations that occurred in the intervening five years. A demonstration of hyperspectral sensing for detecting rusted areas was completed at the Portage Lift Bridge. For the Construction Inspection use case, data created included detection of geometry parameters for Building Information Models (BIM), identification of thermal anomalies such as cool areas after asphalt paving, and calculation of rates of production for concrete removal and asphalt paving. For the Lidar UAS for Design Survey use case, a review of effective lidar UAS data collection patterns, accuracy comparisons of data created using UAS and mobile lidar systems for hard and soft targets, and recommendations for effective lidar UAS ground control targets.

Two additional project tasks documented how the data results and methods should be integrated into MDOT databases and workflows. The Milestone 5 task focused on documentation of all project results that are ready to be used by MDOT. The Milestone 6 task focused on how UAS data, methods, and analysis results can be integrated into appropriate MDOT workflows and databases. An Implementation Plan plots routes for further adoption of UAS data collection and analysis methods into MDOT's operations.

2. Background

2.1 Objectives

The objectives of this research project, as described in the project Statement of Work, were to:

A. Enable everyday use of unmanned aerial systems (UAS, unmanned aerial vehicles - UAVs, or commonly "drones") by MDOT to meet critical systems operations and maintenance data needs.
B. Work closely with MDOT Sections to implement UAS capabilities into their hands through efficient access to UAS collected data, platforms, sensors, and software tools through integration with MDOT's Data Use Analysis and Processing (DUAP, now known as Terraform Manager / TFM) project, design, construction, operations, corridor asset management, bridge inspection, and other MDOT programs.
C. Develop and deploy four use cases from MDOT Sections, specifically including Bridge Inspections, Design Surveys, Traffic Operations Surveillance Monitoring, and Construction Inspection by working closely with Subject Matter Expert (SME) are members of the Research Advisory Panel (RAP).
D. Deploy and integrate the use of UAS capabilities and data usage as part of day-to-day operations, including implementation-focused cases studies and technology transfer training sessions.

E. Recommend how to effectively work with the private sector to take advantage of rapidly developing sensors and platforms to provide data, applications, and tools for operations and maintenance.

The tasks of this research project needed to complete these objectives are described in the following section. An administrative project task (1A) also enabled set up of the project's administration, including identification of SMEs for each use case.

2.2 Tasks

Task 1 Use Case - Traffic Operations: This use case was focused on investigating the use of UAS for traffic data collection, development of video processing algorithms, and live traffic streaming with real-time traffic analytics.
Task 2 Use Case - Bridge Inspection Assessment: Use case 2 was focused on demonstrating and implementing UAS for bridge inspection into day-to-day use where cost-efficient value could be demonstrated that met the needs of MDOT Bridge Operations.
Task 3 Use Case - Construction Inspection: Use case 3 was focused on evaluating of the use of UAS at active construction sites to assist field inspectors with timely identification of quantities such as pavement placement data, and before-and- after data for analysis of volumetric needs and production rates.
Task 4 Use Case - Lidar UAS for Design Survey: Use case 4 was focused on evaluation of UAS-based Lidar to meet MDOT Design Survey three-dimensional (3D) data needs.

These four use cases provided the data and results the project docuomented on how they can be integrated into MDOT workflows and databases, including ~~Data Use Analysis and Processing (DUAP), now known as~~ Terraform Manager (TFM) (you already qualified this above as the database – don't need DUAP stated again). Documentation of data results was the focus of Milestone Task 5. Meeting regularly with the project's MDOT subject matter experts was an important component of Task 5. Providing MDOT with workflows on how to integrate the results and methods into MDOT's workflows was the focus of Milestone Task 6. Holding final technical demonstrations for the Traffic Operations and Bridge Inspection Assessment use cases in in progress for spring, 2022. Also being held in spring, 2022 is a meeting with the TFM program manager at Mixon-Hill, Chris Poe, which is being used to share final data for all four uses cases so that these results are integrated into TFM.

3. Use Case/Milestone Descriptions and Results

3.1 Use Case/Milestone 1: Traffic Operations

3.1.1 Methodology

This section describes the methodology to use UAS, or other video camera sensors, to monitor traffic for daily traffic operations. This proposed methodology can be applied for two selected daily traffic operations including corridor traffic monitoring (e.g., traffic flow dynamics in a weaving area by monitoring traffic at multiple locations) and fixed location traffic monitoring (e.g, real-time traffic video streaming at a freeway). For each daily traffic operation, we recommend the careful selection of drone flight parameters to meet the specific needs of each traffic monitoring during data collection. These parameters include the choice of drone location, height, camera angle, and effective camera field of view. Using collected UAV videos as the input, ~~wet use~~ (remove all third person references i.e., "we" in the report) machine learning algorithms were used to automatically process videos to detect each vehicle within the camera field of view. Using drone-based videos and machine learning algorithms, ~~we conduct~~ traffic analytics and output results in CSV or video files were created.

Data Collection

This section introduces a summary of data collection activities in Milestone 1 and provides detailed information for data collection series in two selected applications for daily traffic operations using drones: weaving area OD (Origin-Destination) flow monitoring along a freeway corridor and real-time traffic streaming at a fixed location.

Data Collection Summary

A series of UAS data collections were completed from 2019 to 2021 to collect the data necessary to provide representative examples of how UAS could assess traffic flow situations of interest to MDOT. These data collections were:

- I-96 Traffic Monitoring data collection at US-23 Exit 41 area (8/5/2019)
    - Determine optimal height for drone traffic monitoring, established at 200 feet
- I-96 near Grand River / Billwood Highway (8/13/2019)
    - Test the potential use cases for an example intersection and freeway
- US23/M14 Weaving Area Data Collection Series (3/3/2020, 7/15/2020, 7/31/2020, 7/27/2021, 9/17/2021, 10/26/2021)
    - Can compare with calculated results provided by MDOT
- Williamston Road (I-96) Data Collection Streaming Series (7/9/2020, 10/7/2020, 11/13/2020, 12/10/2021)
    - Can compare with data provided by MDOT

Our team met with one or both of the project's Subject Matter Experts (SME), Hilary Owen and Stephanie Palmer, at a series of meetings (3/17/2020, 9/1/2020, 10/28/2020, 4/27/2021) to ensure their priorities were reflected in our data collection objectives and results.

They provided two traffic applications for daily traffic operations using drones to cover: Application 1 - a weaving area traffic monitoring in the US-23/M-14 corridor, and Application 2 - a fixed location at the Williamston Road in the I-96 corridor.

Pre-collected Dataset

I-96 Traffic Monitoring Data of Collection on August 5, 2019

The first planned data collection tested the optimal flying height for drone traffic monitoring. The example screenshots of collected data with different heights including 100, 150, 200, 250, 300, 350, and 400 feet are shown in Figure 3.1.1. Although flying on the height level of 300, 350, and 400 feet could have a larger field of view, the size of vehicles is obviously small. When the vehicles become too small (too few pixels) it makes them more difficult for the algorithm to detect. Compared with the remaining options, 200 feet (61 m) is the ideal height to observe traffic with a drone for our purposes. It captures a great deal of roadway for the classification, and the drone is small and far enough that it does not distract drivers.

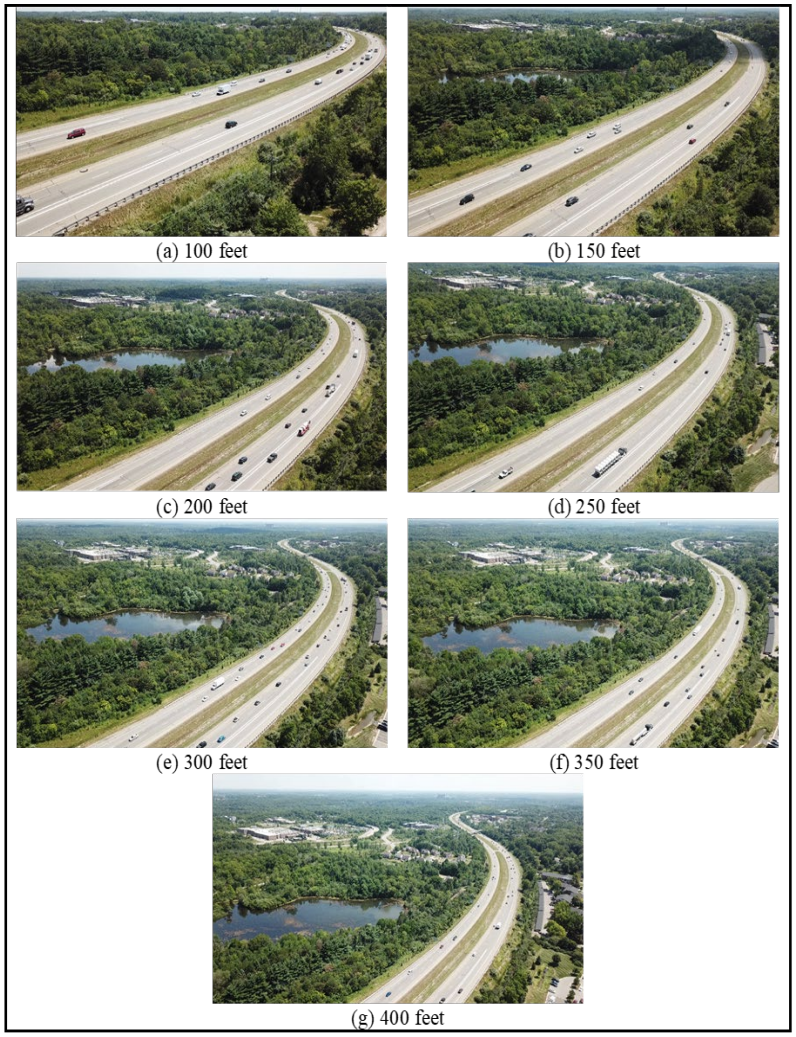

Figure 3.1.1: Screenshots of videos collected at I-96 on August 5, 2019 to test optimal data collection heights for traffic monitoring. 200 ft was found to be optimal.

I-96 near Grand River / Billwood Highway Data of Collection on August 12-16, 2019

A series of field data collection was designed and implemented in August 2019. This pre-collected dataset contained different traffic locations, including freeways and intersections. Collected over the course of 5 days, the total length of videos is about 110 minutes. This dataset provided reference examples of traffic patterns and improved our understanding of the potential of drone applications.

(a) Freeway – Waverly Road

(b) Freeway – Creyts Road

(c) Freeway – Lansing Road

(d) Freeway – Billwood Highway

(e) Freeway – I96-GrandRiver

(f) Freeway – Lansing Road and Clover Drive

(g) Intersection – MDOT Building

(h) Intersection – M99 Highway

Figure 3.1.2: Screenshots of video samples collected on August 13, 2019.

Application 1 - US-23/M-14 Weaving Area

The US-23/M-14 weaving area is about 0.72 miles long, coming from US-23 SB mainline and M-14 SB on-ramp and leaving to US-23 mainline and Plymouth Road off-ramp, on the NE side of Ann Arbor, Michigan. This site is a well-known, local to MTRI, problem traffic area marked by sudden increases in traffic and increases of lane changes as drivers attempt to exit to Plymouth Rd. Collecting UAS traffic data in this area, including in-flow and out-flow information, will help to improve the efficiency and safety of traffic monitors and operations relative to existing methods.

To efficiently collect and utilize UAV videos, there are some field tests and adjustments for experimental design before the long-period data collections in this use case. Considering the collaboration of multiple drones on the long corridor, the view angle and collection location of each drone impact the performance of videos. In addition, video resolution (eg., 4K, 1080p, 720p) plays an important role in determining the effective distance at which one can successfully identify vehicles. Then, with these drone-based videos, the project team develops a fully automatic traffic video processing algorithm to detect and track vehicles and the origin-destination (OD) flow matrix is also automatically generated.

Figure 3.1.3: US-23/M-14 Weaving Area Overview.

Data Collection Series

Date of Collection - March 3, 2020

The first traffic collection in the US-23/M-14 weaving area collected the recorded and streamed datasets at the US-23 exit. To figure out the use capacity of UAVs and test the streaming server, the DJI Mavic 2 Pro was used to record onboard videos with 4K resolution and

streamed on a server with 720p (1280 x 720) resolution. Based on the results of this 30-minute data collection, we decided to increase the streaming resolution from 720p to 1080p.

Figure 3.1.4: Screenshot of drone video collected at the US-23 SB/Plymouth Rd exit for the weaving area on March 3, 2020.

Date of Collection - July 9, 2020

With MDOT's interest in estimating the number of vehicles from M-14 westbound to US-23 southbound Exit 41 (Plymouth Road), a new data collection for traffic monitoring was designed to cover the upstream and downstream in the US23/M14 weaving area. Two options, using a single drone or two drones, were discussed under the consideration of traffic volume movement from the US23/M14 on-ramp to the Plymouth Road (spell-out "road") off-ramp. As for the single drone case, it would need to cover the entire stretch with three possible locations, the north endpoint of the upstream, the south endpoint of the downstream, and the middle points (i.e. the south endpoint of the upstream and the north endpoint of the downstream). ~~We also~~ had the capability of simultaneously flying two drones, where both drones were at the midpoint or each drone surveyed from the northern and southern points. After discussion and coordination between MTRI and MTU, ~~we decided~~ that using two drones at the endpoints of the road of interest was the best path forward at this time.

This was the preliminary 20-minute testing as a preparation for the later long-period of data collection on July 15, 2020. Using the Mavic 2 Pro for both streaming and recording videos, MTRI flew at the recommended height of 200 feet which had been tested in the previous optimal height testing on August 5, 2019. Since at least 32x32 pixels were needed for each vehicle to ensure the quality of detection, 1080p resolution was assumed for streamed data. In addition, onboard videos were recorded as 2K resolution.

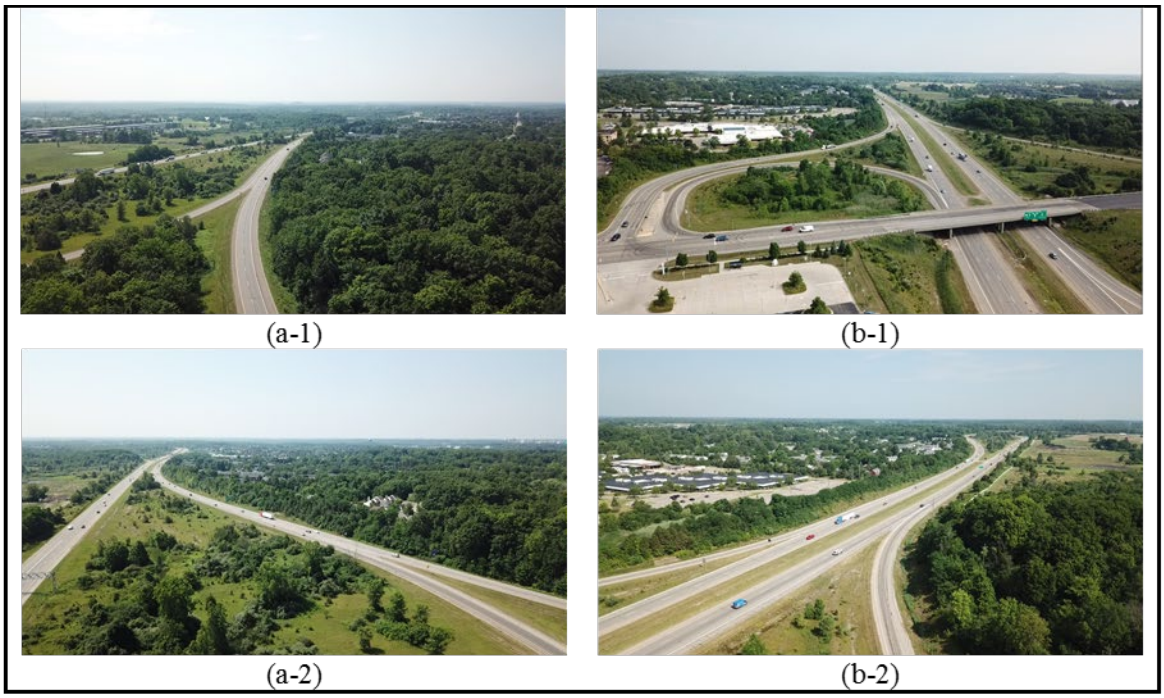

Figure 3.1.5: Screenshots of videos collected for the weaving area on July 9, 2020. (a-1) and (a-2) capture upstream. (b-1) and (b-2) capture downstream.

Date of Collection - July 15, 2020

Based on the previous testing result on July 9, 2020, about one-hour-long UAV videos were collected under similar traffic conditions and drone flight parameters. Collecting from 07:57 to 09:18 AM, two drones collected video simultaneously in the upstream and downstream positions, respectively. The upstream drone facing due south flew at the beginning point (i.e. the north point), while the downstream drone facing to the north flew at the ending point (the southern point). Two pilots collaborated to ensure that the drones were flying and recording video simultaneously. However, there existed a problem in this data collection. Although two drones were used to collect data on this long corridor, there was still a missing distance gap where the vehicles were too small to identify and track between the video of the two drones. This led to some errors for the following traffic analysis that used these videos.

Figure 3.1.6: Screenshots of videos collected for the weaving area on July 15, 2020. (a) captures upstream. (b) captures downstream.

Date of Collection - July 31, 2020

To resolve the distance gap problem between the upstream and downstream videos, a new data collection point was proposed for the downstream drone. Changing the facing direction from the north to the south, both drones recorded data on the beginning side of the responsible area, that is, they were all faced to the south. As of July 15, 2020, this data collection also focused on the long-period continuous traffic flow with some adjustments. A higher resolution of onboard videos was expected, so all data were 4K (3840 x 2160 resolution) and collected from 07:45 to 09:05 AM. With the consideration of the need for real-world geographical coordinates to map to ground truth in the analysis, the probe vehicle with a Trimble GeoExplorer GPS unit looped through the study area about 14 times, recording vehicle GPS location every 0.2 seconds. Analyzing the collected dataset at this time, most vehicles can be clearly identified and used to be annotated for the machine learning algorithm purpose. Although there was still a small gap between upstream and downstream videos considering the limitation of manual annotation, it was obviously improved and better than the previous dataset on July 9, 2020.

Figure 3.1.7: Screenshots of videos collected for the weaving area on July 31, 2020. (a) captures upstream. (b) captures downstream.

Date of Collection - July 27, 2021

According to the previous traffic analysis on the dataset collected July 31, 2020, the next enhanced data collection was planned to solve some existing problems and further examine the developed algorithms. Focusing on the continuous traffic flow information, both the time continuity and distance continuity had significant impacts. The previous dataset was composed of several 5-minute videos and there were several breaks among them because of the limitations of the drone platform. This increased the difficulty to merge them or generate the time-continuous data flow. In addition, we determined that the two pilots should collaborate closely to reach the time synchronization so that the upstream and downstream data could have at least 15 minutes of continuous overlapping time. As for distance continuity, considering the limitation of effective vehicle size, vehicles that were too far from the camera could not be used and were not well-identified for the algorithm because of their small number of pixels. This situation shortened the effective detected area for both upstream and downstream cameras, so the length

of the overlapping area became too short relative to the minimum video overlap determined to be about 328 feet (100 meters).

This data collection was the preliminary testing for three proposed possible scenarios reaching the above requirements. Drone flying positions, camera angle, height, facing direction, and effective field of view were considered. The 5-minute data were collected for each scenario design. Standing side by side one another and launching drones from the same location, the two pilots successfully started work at the same time.

Figure 3.1.8: Screenshots of videos collected for the weaving area on July 27, 2020. (a-1), (a-2), and (a-3) capture upstream. (b-1), (b-2), and (b-3) capture downstream.

Date of Collection - September 17, 2021

Based on the result of testing on July 27, 2021, the second testing before the long-period data collection was designed based upon multiple considerations. Because of time setting errors on one drone due to internet accessibility issues, there was the wrong time information for

recording data. To revise the error and guarantee accuracy in future data collection, this test collected another test of 5-minute data for the chosen scenario with the new adjustments.

Figure 3.1.9: Screenshots of videos collected for the weaving area on September 17, 2021. (a) captures upstream. (b) captures downstream.

Date of Collection - October 26, 2021

Combining with the previous preliminary testing results, a one-hour-long data collection was scheduled. The team noticed and ensured both time and distance continuity between the upstream and downstream drone video locations. They cooperated to maintain the consistency of drone takeoff and landing time, as well as video start and end times, with at least 15-minute-long recording data. Also, the pilots ensured that there were no trees blocking the view of the roadway in the video of either drone. From this collected dataset, the size of vehicles was greatly improved with the longer length of the overlapping area.

Figure 3.1.10: Screenshots of videos collected for the weaving area on October 26, 2021. (a) captures upstream. (b) captures downstream.

Application 2 - Williamston Road (I-96) Traffic Corridor

The segment of interest in this application measures 0.54 miles long and is due west from I-96/Williamston Road on-ramp to I-96, just west of the Williamston Rd bridge over I-96. This application explores the potential of UAS real-time streaming capabilities to monitor traffic flow dynamics on rural corridors and stream this data back to a Traffic Operations Center. Applying the fully automatic traffic video processing algorithm, the real-time traffic analysis can be

rebroadcast to the web server and automatically output the traffic analytics. In addition, the lane detection algorithm will be adopted to detect and calculate vehicle counts by lane.

Figure 3.1.11: Williamston Road (I-96) Traffic Corridor

Data Collection Series

Date of Collection - October 7, 2020

To compare our drone capabilities to the MDOT camera installation at Williamston Rd., and demonstrate real-time traffic monitoring, preliminary testing was planned to check and simulate the situation. We determined that a single drone was sufficient for this application to collect traffic flow and density data on Williamston Road.

Figure 3.1.12: A screenshot of videos collected for Williamston Road on October 7, 2020.

Date of Collection - November 13, 2020

A long-period data collection was set to collect both onboard and streamed drone video data at the same time. Beginning from 11:33 AM to 02:19 PM, MTRI collected 15 videos with a total duration of 110 minutes after considering the breaks between each drone flight and battery changes. As for streaming video, the resolution was 720p and we determined this would need to be improved to 1080p in the future so that vehicles could have larger pixels to improve detection. Also, with the current limit of the network bandwidth in the area at Williamston Rd, jumping frames happened intermittently on streaming videos. Because of these issues, vehicle counts became more practical than the trajectory in this specific data collection and real-time application.

Figure 3.1.13: A screenshot of videos collected for Williamston Road on November 13, 2020.

Date of Collection - December 10, 2021

This was the first real-time demonstration with fully automatic online traffic analytics. The resolution of streaming videos improved from 720p to 1080p (1920 x 1088) and videos

saved onboard the drone remained in 4K resolution. Three project teams collaborated at three completely separate sites to work for this live demonstration, including the on-site team (MTRI, streaming from Williamston Rd.), the broadcasting team (MDOT STOC, Lansing), and the traffic analytics team (MTU, Houghton). The fact that a drone in Lansing can stream to an Ann Arbor server, analytics be performed and monitored in real-time by a group in Houghton, and then these analytics restreamed in near real-time to individuals anywhere is a demonstration of the great utility of this technology. To continuously stream on the web server, two drones (flown by two pilots) used the same stream key in succession so that the quality and smoothness of streaming data were more stable than the previous data collection. For this data collection, the MTRI team used a dedicated 4G Verizon Jetpack dedicated hotspot, which likely improved stream stability relative to the use of a mobile phone hotspot. This may also be improved upon further in the future as 5G communications become more widely available.

Figure 3.1.14: A screenshot of videos collected for Williamston Road on December 10, 2021.

Automatic Video Processing and Traffic Analytics

To provide automatic traffic analytics for the two selected daily traffic operation applications, we use machine learning algorithms to automatically process the videos from drones, detect vehicles, and generate traffic analytics. Specifically, we use a real-time object detection algorithm - You Only Look Once (YOLOv4, Bochkovskiy et al. 2020) to automatically detect vehicles. The following sections indicate the step-by-step details for the algorithm focusing on two focused applications.

Application 1 - US-23/M-14 Weaving Area

Due to the long length of the roadway, two drones are used to collaboratively collect data simultaneously in this application. To observe the continuous flow and obtain the origin-destination (OD) matrix among the mainline (US-23), on-ramp (M-14), and off-ramp (Exit 41 to Plymouth Road), Figure 3.1.15 introduces the flow chart of the algorithm in the weaving area case.

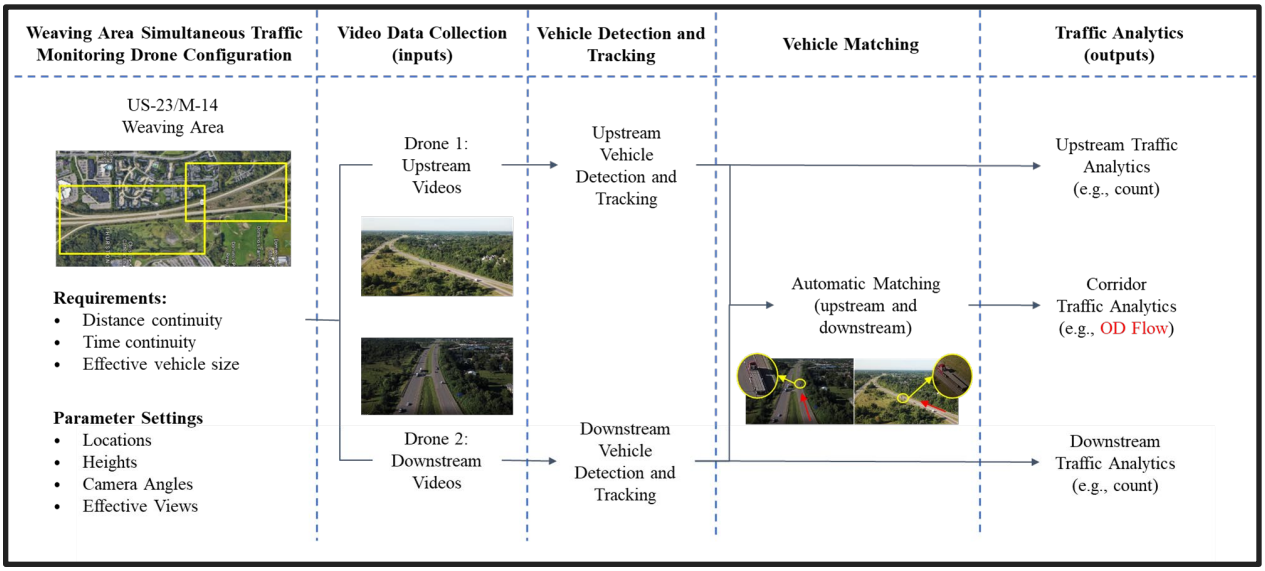

Figure 3.1.15: US23/M14 weaving area traffic monitoring process (Application 1).

Input

The inputs of the algorithm are UAV collected videos with an MP4 format. In this application, we required two videos collected by two drones: one drone at the upstream location and one drone at the downstream location, respectively.

Vehicle Detection and Tracking

To obtain the traffic pattern, the algorithm applies the YOLOv4 algorithm and Simple Online and Realtime Tracking with a Deep Association Metric (DeepSORT, Wojke et al. 2017) algorithm to automatically detect and track vehicles. With the YOLOv4 network weights being trained by the collected video data, the bounding boxes of vehicles can be detected and serve to catch vehicles' movements so that the trajectory of every detected vehicle is derived and recorded. Figure 3.1.16 shows an example of the process of automatic detection and tracking. Moreover, according to the interest of origin and destination, Hough transform is also used for automatic lane detection to determine the origin and destination locations in this step.

Figure 3.1.16: Automatic vehicle detection and tracking at US23/M14 weaving area.

Vehicle Matching

With detected vehicle trajectories information for both upstream and downstream segments, the automatic matching algorithm is applied to match vehicles between the two distinct drone videos. Provided with a sufficiently long overlapping area, vehicles should be detected at the same location at the same time in both the upstream and downstream videos. Based on this data characteristic, the algorithm automatically identifies and matches vehicles from different videos to connect their traffic information.

In the progress of algorithm development, the probe vehicle (a Ford Fiesta ST driven by MTRI) was used for matching result validation. Figure 3.1.17 shows an example of collected probe vehicle trajectory data. Depending on the probe vehicle information, the trajectory is used as ground truth to validate the matching result. The result shows that the automatic matching algorithm correctly matches the probe vehicle from the upstream video and downstream video to find out its actual OD flow as shown in Figure 3.1.18.

TetracamGPSLogger_chris

FID	Shape *	GPS_Date	Time_UTC_	Fix_Q_	Lat_Deg_	Lon_Deg_	Speed_kno	Heading_D	Altitude_	Sats_	Battery_V	LAT	LONG
0	Point ZM	7/31/2020	11:43:36	2	423057133	836884050	0.02	98.38	282.7	9	4.16	42.305713	-83.688405
1	Point ZM	7/31/2020	11:43:37	2	423057133	836884050	0.03	63.43	282.7	9	4.17	42.305713	-83.688405
2	Point ZM	7/31/2020	11:43:37	2	423057133	836884050	0.02	12.06	282.7	9	4.17	42.305713	-83.688405
3	Point ZM	7/31/2020	11:43:37	2	423057133	836884050	0.03	343.84	282.7	9	4.16	42.305713	-83.688405
4	Point ZM	7/31/2020	11:43:37	2	423057133	836884050	0	341.19	282.7	9	4.17	42.305713	-83.688405
5	Point ZM	7/31/2020	11:43:37	2	423057133	836884050	0.02	72.05	282.7	9	4.17	42.305713	-83.688405
6	Point ZM	7/31/2020	11:43:38	2	423057133	836884050	0.03	287.83	282.7	9	4.16	42.305713	-83.688405
7	Point ZM	7/31/2020	11:43:38	2	423057133	836884050	0.04	326.07	282.7	9	4.16	42.305713	-83.688405
8	Point ZM	7/31/2020	11:43:38	2	423057133	836884050	0.11	321.23	282.7	9	4.16	42.305713	-83.688405
9	Point ZM	7/31/2020	11:43:38	2	423057133	836884050	0.27	345.93	282.7	9	4.17	42.305713	-83.688405
10	Point ZM	7/31/2020	11:43:38	2	423057133	836884050	0.32	347.8	282.7	9	4.16	42.305713	-83.688405

24793 (0 out of 25580 Selected)

Figure 3.1.17: Probe vehicle trajectory for the US23/M14 weaving area.

Figure 3.1.18: The probe vehicle appears in the upstream and downstream videos.

Output

After automatic detection and tracking, the segment traffic analytics including vehicle trajectory can be generated. To analyze the whole corridor traffic pattern including OD flow, the analytics also can be output after the automatic matching step. Both output analytics formats are CSV files.

Application 2 - Williamston Rd (I-96) Traffic Corridor

In this application, the live video will stream to the web server simultaneously so that the algorithm can continue to access the streaming video and work on the real-time traffic analytics to stream back to the same web server in the near real-time. Figure 3.1.19 introduces the flow chart of the algorithm for fixed location real-time demonstration.

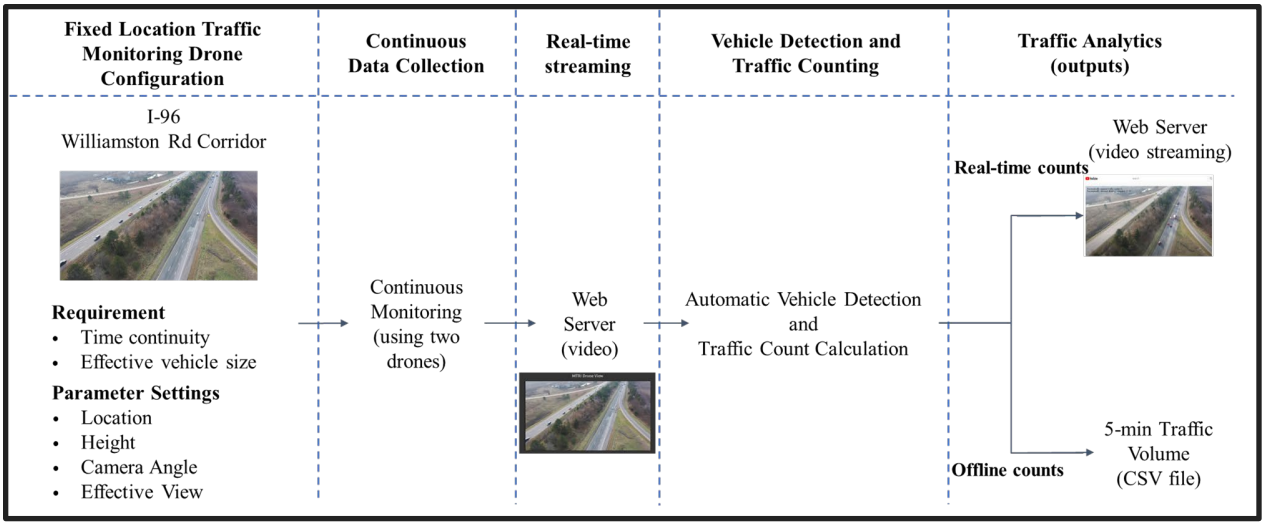

Figure 3.1.19: Real-time demonstration of fixed location traffic monitoring at Williamston Rd (Application 2).

Input

The input of the algorithm is UAV streaming videos. The live video streamed to the web server can be accessed and processed using the algorithm in near real-time.

Vehicle Detection and Traffic Counting

Similar to Application 1, the algorithm needs to automatically detect vehicles in the video using the YOLOv4 algorithm. Also, the automatic lane detection algorithm adopting Hough transform is used to distinguish lanes. Then, a virtual line is drawn using these lane distinctions to determine if there is a vehicle entering the roadway along the line. Following the above steps, the algorithm can obtain the result of cumulative vehicle counts and density calculation for each lane. The algorithm then streams back the processed video showing analytical results to the web server in near real-time. Figure 3.1.20 shows an example of the re-streamed video on the web server now with processed traffic analytics in our first real-time demonstration.

Figure 3.1.20: A screenshot of processed streaming video from Williamston Rd. on December 10, 2021. Vehicle counts and detected density are in the top left corner of the image.

Output

In addition to the streaming video with traffic analytics re-streamed to the web server, the real-time traffic analytical result is also recorded and can be output as a CSV file when the live video stream ends. Moreover, without the constraint of real-time conditions, the offline analysis can generate the result aggregated to calculate the cumulative vehicle counts and the corresponding density information for every 5-minute period for the duration of the live stream.

3.1.2 Findings

After obtaining the traffic analytics in the fully automatic traffic video processing algorithm, some analytical results are disclosed for our two applications. This section focuses on the findings based on the algorithm's generated output and then compares them with the traffic data provided by MDOT.

Application 1 - US-23/M-14 Weaving Area

The target of this application is to obtain the OD flow information in the weaving area for US23/M14. With two origins (i.e. US-23 SB mainline and M-14 on-ramp to US-23 SB) and two destinations (i.e. US-23 SB mainline and Exit 41 to Plymouth Road off-ramp), the flow during the data collection period is investigated. Following the progress of data collection and the algorithm development, two OD flow results are generated, which use the long-period datasets collected on July 31, 2020 and October 26, 2021, respectively. Then, provided by MDOT, the manually calculated OD flow result collected from 07:30 to 08:30 AM is compared with MTU's algorithm outputs.

Semi-automatically detected OD flow based on data collected on July 31, 2020

With the consideration of the distance gap in this dataset, semi-automatically detected OD flow uses manual annotations to match vehicles, which is shown in Table 3.1.1. The dataset was collected from 07:46 to 09:05 AM and the usable video time period (after removing drone battery changes) is about one hour.

Although the traffic pattern changes every day, there are still obvious findings in the comparison in Table 3.1.1. In the similar collected duration of 60 minutes, there were fewer total vehicles in the weaving area on the collection date relative to the MDOT data collection. Coming from the US-23 SB mainline and also leaving to the US-23 SB mainline, both results indicate the same trend with the highest percentage of this origin-destination pair. In contrast, there is no obvious difference in the percentage between US-23 SB mainline to Plymouth Road off-ramp pair and M-14 on-ramp to US-23 SB mainline pair in MDOT data, while the latter is higher than the former in the detected result. But, undoubtedly, M-14 on-ramp to Plymouth Road off-ramp has the lowest percentage in both results.

Table 3.1.1: Comparison of MDOT calculated OD flow and semi-automatically detected OD flow. (should these table descriptions be below the table throughout the report like the Figures above?)**

	US23 (D)	Plymouth Rd (D)	Total
M14 (O)	1096	213	**1309**
US23 (O)	1328	1120	**2448**
Total	**2424**	**1333**	**3759**

MDOT counting result
(07:30 to 08:30 AM)

	US23 (D)	Plymouth Rd (D)	Total
M14 (O)	749	286	**1035**
US23 (O)	1182	408	**1590**
Total	**1931**	**694**	**2625**

Semi-automatically detected result
(07:46 to 09:05 AM, usable 60 minutes)

Percentage share	US23 (D)	Plymouth Rd (D)	Total
M14 (O)	29.2%	5.7%	**34.8%**
US23 (O)	35.3%	29.8%	**65.1%**
Total	**64.5%**	**35.5%**	**100%**

MDOT counting result

Percentage share	US23 (D)	Plymouth Rd (D)	Total
M14 (O)	28.5%	10.9%	**39.4%**
US23 (O)	45.0%	15.5%	**60.6%**
Total	**73.6%**	**26.4%**	**100%**

Semi-automatically detected result

OD percentage (07:30 to 08:30 AM)	OD percentage (07:46 to 09:05 AM, usable 60 minutes)

Automatically detected OD flow based on data collected on October 26, 2021

After improving the length of overlapping area between the upstream and downstream drone video field of view, the new dataset collected on October 26, 2021 is used for the implementation of fully automatic detection. As shown in Table 3.1.2, the automatically detected OD flow result is compared with the manually counted ground truth result. The result clearly reveals that most vehicles can be automatically detected with 99% detection accuracy. Although there exist detection errors for the algorithm, most OD pairs are correctly matched and identified. Moreover, focusing on the OD pair from M-14 on-ramp to Plymouth Road (Exit 41) off-ramp, vehicles can be precisely identified with higher than 95% accuracy. These results strongly suggest that UAVs have the capability of traffic monitoring with the algorithm implementation in this case.

Table 3.1.2: Comparison between the ground truth and automatically detected OD flow results for the US23/M14 weaving area on October 26, 2021.

	Time	US23-US23	US23-PlymouthRd	M14-US23	M14-PlymouthRd	Total
Ground Truth	10:20 – 10:36 AM	340	61	189	49	**639**
	10:40 – 10:58 AM	364	76	226	52	**718**
	11:02 – 11:18 AM	251	68	145	41	**505**
	11:23 – 11:38 AM	262	62	148	55	**527**
Automatically Detected Result	10:20 – 10:36 AM	340	59	192	48	**639**
	10:40 – 10:58 AM	358	80	226	35	**699**
	11:02 – 11:18 AM	221	82	160	42	**505**
	11:23 – 11:38 AM	258	58	166	41	**523**

Comparing the MDOT OD flow counting result with the drone video and algorithm result, Table 3.1.3 indicates that the two results detected similar traffic patterns, despite being collected on different days and times. The OD pair, US-23 SB mainline to US-23 SB mainline, has the highest percentage in both results, while the M-14 on-ramp to Plymouth Road off-ramp pair has the lowest percentage. However, in contrast to the similar 29.2 and 29.8 percentages of the other two OD pairs in MDOT data, the automatically detected result indicates that M-14 on-ramp to US-23 SB mainline pair has an obviously higher percentage than US-23 SB mainline to Plymouth Road off-ramp pair on October 26, 2021. This result implies that unique traffic flow conditions do happen for a segment of the highway, which may be caused by the different time periods and dates of data collection.

Percentage share	US23 (D)	Plymouth Rd (D)	Total
M14 (O)	29.2%	5.7%	**34.8%**
US23 (O)	35.3%	29.8%	**65.1%**
Total	**64.5%**	**35.5%**	**100%**

MDOT counting result
OD percentage
(07:30 to 08:30 AM)

Percentage share	US23 (D)	Plymouth Rd (D)	Total
M14 (O)	31.4%	7.0%	**38.5%**
US23 (O)	49.7%	11.8%	**61.5%**
Total	**81.2%**	**18.8%**	**100.0%**

Automatically detected result
OD percentage
(10:20 to 11:38 AM, usable 65 minutes)

Table 3.1.3: Comparison of MDOT calculated OD flow and automatically detected OD flow for the US23/M14 weaving area on October 26, 2021.

Application 2 - Williamston Road Traffic Corridor

As part of Task 1, the demonstration of real-time traffic monitoring displays the potential of UAVs and shows the competitive capability to compare with permanently installed roadside cameras. In this application, the real-time vehicle counts and density analysis for each lane is the focused issue of our traffic analytics. Implementing the algorithm, the traffic counts are automatically detected and calculated in real-time. Considering the validation of algorithm results, Table 3.1.4 shows the comparison between the ground truth determined by manual counting and fully automatically detected results on the dataset collected on December 10, 2021. Although the algorithm result does not have the completely same value as the manual counting due to some interference errors, it reaches a minimum 82 percent and an average 95 percent of accuracy for all results. That is, most vehicles are detected and counted well by the video processing algorithm for this site and traffic conditions.

Time	Ground truth			Automatically detected			
	Lane 1	Lane 2	Total	Lane 1	Lane 2	Total	Accuracy
02:45 – 02:50 PM	88	74	162	85	77	162	100.0%
02:50 – 02:55 PM	101	78	179	96	80	176	98.3%
02:55 – 03:00 PM	91	66	157	86	69	155	98.7%
03:01 – 03:05 PM	71	45	116	68	47	115	99.1%
03:05 – 03:10 PM	89	69	158	79	72	151	95.6%
03:10 – 03:15 PM	82	66	148	86	64	150	98.6%
03:17 – 03:20 PM	55	42	96	45	43	88	91.7%

Time	Ground truth			Automatically detected			
	Lane 1	Lane 2	Total	Lane 1	Lane 2	Total	Accuracy
03:20 – 03:25 PM	98	75	173	87	75	162	93.6%
03:25 – 03:30 PM	90	63	153	86	61	147	96.1%

Table 3.1.4: Comparison between the ground truth and automatically detected vehicle counts at Williamston Rd on Dec. 10, 2021.

Also, the vehicle detection sensor (VDS) data provided by MDOT, near to the installed traffic camera, is compared with the algorithm-detected traffic analytics. The VDS and drone are similarly located in position; however, lane 3 is not recorded in the drone detecting area (the lane three on-ramp ends underneath the bridge) and they have different lengths of the detected area on this corridor so it may lead to several seconds delay between the two data. Thus, lane three VDS traffic counts are likely included in lane 2 of the drone-based algorithm detections. Table 3.1.5 and Table 3.1.6 show the vehicle counts and density analysis for both data. It is clear that the two data have similar analytical values considering some detecting errors. Hence, it proves that UAS also works well on real-time traffic monitoring.

Time	MDOT VDS data				Automatically detected			
	Lane 1	Lane 2	Lane 3	Total	Lane 1	Lane 2	Total	Difference
02:45 – 02:50 PM	85	72	2	159	85	77	162	1.9%
02:50 – 02:55 PM	96	78	2	176	96	80	176	0.0%
02:55 – 03:00 PM	87	63	0	150	86	69	155	3.3%
03:05 – 03:10 PM	85	67	5	157	79	72	151	3.8%
03:10 – 03:15 PM	76	65	6	147	86	64	150	2.0%
03:20 – 03:25 PM	87	72	2	161	87	75	162	0.6%
03:25 – 03:30 PM	91	59	1	151	86	61	147	2.6%

Table 3.1.5: Comparison of MDOT VDS data and automatically detected analytics - vehicle counts - from December 10, 2021, data collection at Williamston Rd.

Time	MDOT VDS data				Automatically detected			
	Lane 1	Lane 2	Lane 3	Total	Lane 1	Lane 2	Total	Difference
02:45 – 02:50 PM	13	12	1	26	14	12	26	0.0%
02:50 – 02:55 PM	15	13	1	29	15	13	28	3.4%
02:55 – 03:00 PM	13	10	0	23	14	11	25	8.7%
03:05 – 03:10 PM	13	11	2	26	13	12	25	3.8%
03:10 – 03:15 PM	11	10	2	23	14	10	24	4.3%
03:20 – 03:25 PM	14	12	1	27	14	12	26	3.7%
03:25 – 03:30 PM	14	10	0	24	14	10	24	0.0%

Table 3.1.6: Comparison of MDOT VDS data and automatically detected analytics - density (veh/mile) - from December 10, 2021, data collection at Williamston Rd.

3.1.3 Field Demonstration of Live Streamed Drone Video & Traffic Analytics

On the morning of May 24th, 2022, the project team performed a field demonstration of live streamed drone video and traffic analytics at the North Williamston Road exit along I-96 near Williamston, Michigan. This is the same site that was chosen for previous demonstrations of live streamed traffic analytics (in previous sections of this report, "Application 2"). At this site there is a traffic camera and traffic monitoring tool affixed to a pole near the overpass that reports video and traffic numbers in near real time.

The field team used two DJI Mavic 2 Pro drones to collect the required video. Two pilots flew two separate drones (one drone flying and streaming video while the other operator was changing batteries) in order to ensure continuous video collection and streaming. The drones were flown at approximately 200 feet altitude and directly over top of the permanent traffic camera at the site. Video was live streamed over the local 4G wireless network (using a dedicated 4G Verizon Jetpack Hotspot with an unlimited data plan) to a secure server that was located at MTRI. The MTU team had access to this stream and performed real-time traffic analytics on the live-streamed video, and then re-streamed these traffic analytics in near real time (Figure 3.1.21).

3.2 Use Case/Milestone 2: Bridge Inspection Assessment

A series of UAS data collections were completed from 2019 to 2021 to provide the data and examples necessary to show how UAS could perform or supplement MDOT bridge, and other structures of interest, inspections. These data collections were performed at a variety of sites to capture a wide sampling of conditions that MDOT bridge inspectors encounter on a daily basis.

3.2.1 Methodology

- Uncle Henry and Beyer Rd 2021 thermal data collections and comparison with 2016 data collected in Phase 2 (8/17/2021, December 2016)
    - TADDA analysis
- Laplaisance Creek hyperspectral and thermal data collections (10/14/2020, 11/9/2020, and 8/31/2021)
    - Description of platforms, sensors, analysis of data (hyperspectral and TADDA)
- Peacock Rd (9/25/2019), Laplaisance Creek (10/14/2021) and Beyer Rd over Cheboyganing Creek (8/17/2021) 3D models from imagery using various drone platforms
- August 12-16, 2019 bridges:
    - Waverly Road
    - Creyts Road
    - M-99
    - I-96 over Grand River / Billwood Highway
- September 4, 2019 training session to MDOT Aeronautics staff on use of the Bergen Hexacopter system transferred to MDOT for their use.
    - Usable for more than just bridge inspections.
- Upcoming UAV-assisted bridge inspection demonstration to MDOT staff, to be held in April or May of 2022 once the weather enables a higher likelihood of having a successful field session.
    - The concept of a UAV-assisted bridge inspection day was reviewed with Brian Zakrzweski during the 2/16/2022 Milestone 2 update and data sharing meeting. ~~and~~ This was endorsed as an interesting and useful step for this project that will help with integration of methods and results.
    - The spring demonstration outline we agreed on includes:
        - Including as many Region Bridge Engineers to the demonstration day as can make it.
        - Holding a live demonstration of the data collection methods developed through this project, at a site with existing UAS data collected previously

for this project, such as the Beyer Road bridge (STR 9293, see Figure 3.2-1) near Saginaw visited in 2016 in Phase II and 2021 in Phase III.

- Showing the results of the previous data collections made possible through these previous visits.
- Discuss paths to day-to-day use by the MDOT Bridge Inspection Program, in coordination with MDOT Aeronautics.

Figure 3.2.1: Beyer Road bridge, near Saginaw, MI, showing thermal data (left) and optical data (right) from the August 17, 2021 data collection. ~~We are~~ Recommending this low-traffic bridge with known defects and two years of UAS data as an excellent location for the planned spring 2022 UAS-assisted bridge inspection demonstration day to be held with MDOT bridge inspection staff. **(move this to body of report, shouldn't be under figure title)**

Our team held dedicated meetings with MDOT's SME, Brian Zakrzewski, on the following dates to help ensure that his priorities were reflected in our work: 8/6/2020, 5/17/2021, and 2/16/2022. Brian also joined the Michigan Tech team during field data collections in August and September of 2019 (see Figure 3.2.2) to provide feedback on collection methods and outputs. Brian's priorities can be summarized as **(need to check on first person referring in research reports with Andre Clover):**

- Providing quantitative results that can be integrated into element-level reporting requirements.
- Being able to detect delaminations as early action on these sub-surface distresses can help reduce maintenance costs.
- Developing methods that can be used on a practical basis by MDOT's bridge inspection program.

Figure 3.2.2: Brian Zakrzweski, MDOT Bridge Inspection Program Manager, providing input during UAV-assisted bridge inspection testing and demonstrations in August and September, 2019.

3.2.2 Findings

Our results from the above data collections can be summarized into delamination detection, spall detection, imaging of difficult to reach locations, and the generation of 3D models of bridges from drone-based imagery. Results of these analyses are summarized below by site.

Uncle Henry Road Bridge

Uncle Henry Road Bridge is 60 feet long, 26 feet wide, and has a concrete deck. A 2015 MDOT bridge inspection states that there were several spalls (12 sq. ft. in five locations) and delaminations (15 sq. ft in five locations) present on the bridge deck, which was assigned a surface rating of '5' ('Fair' condition) at that time. On 12/30/2016, drone-based Nikon D810 and Phantom 3A imagery were collected at this site and processed to create an orthophoto, digital elevation model (DEM), and hillshade model of the bridge. Thermal imagery was collected using a FLIR Vue Pro thermal camera flying aboard a Bergen Hexacopter. The bridge had little maintenance done after the 2016 data collection and thus a second drone-based survey of the site was performed on 08/17/2021 to assess for changes in delamination or bridge condition. The 2021 survey made use of the DJI Mavic 2 Enterprise Advanced (M2EA) drone platform, which has an integrated thermal and optical camera. Figure 3.2.3(a) shows the 2021 thermal mosaic of the bridge while 3.2.3(b) shows the 2021 Mavic Pro visual orthophoto.

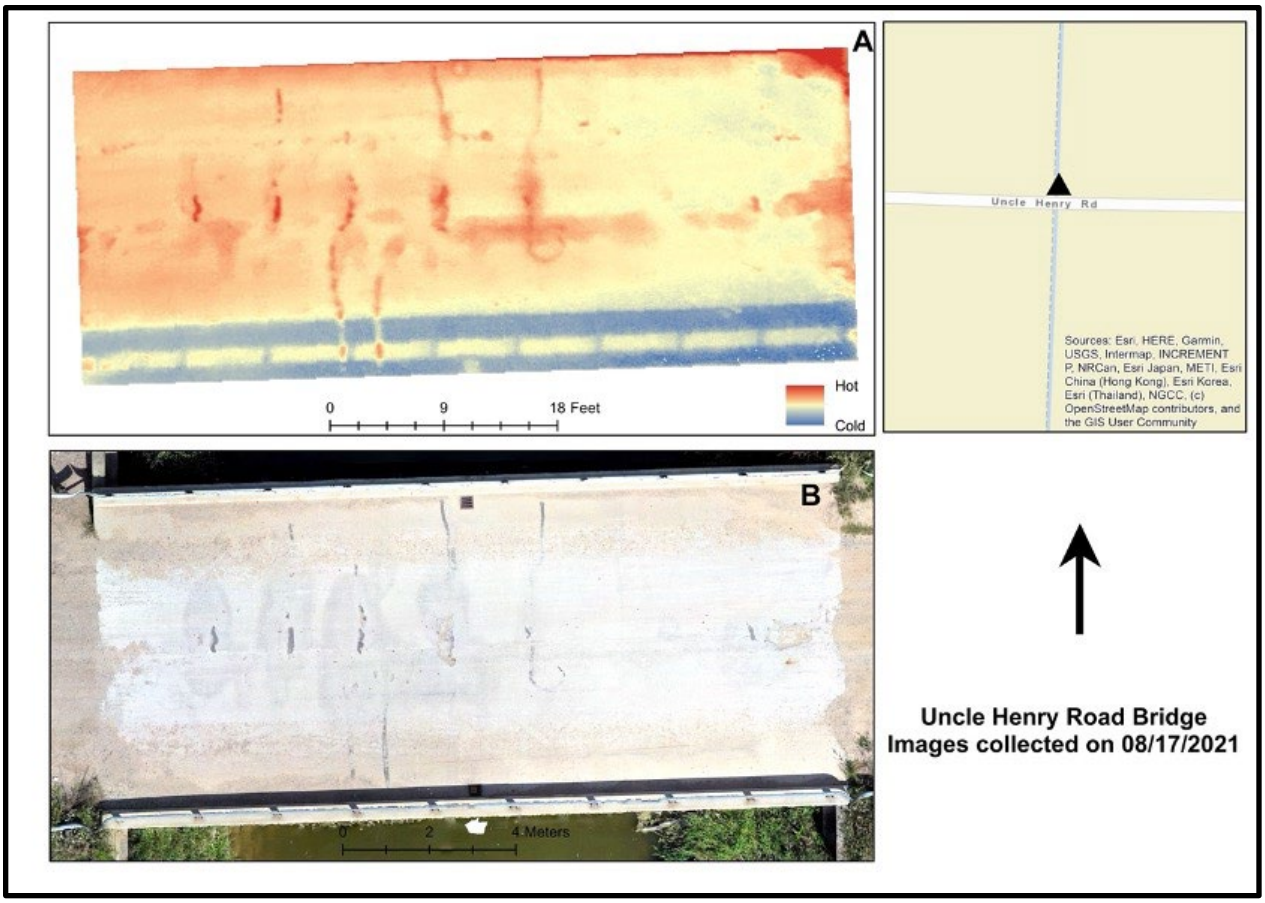

Figure 3.2.3: (a) Shows the thermal mosaic of relative temperature; (b) shows the visual orthophoto of the Uncle Henry Road Bridge (August, 2021).

Delamination analysis on the newly acquired 2021 data for the Uncle Henry Road bridge was performed using the Thermal Anomaly and Delamination Detection (TADDA) algorithm. The results of delamination from 2016 and 2021 data were then compared. Figure 3.2.4 shows a side-by-side comparison of the 2016 and 2021 results for the bridge.

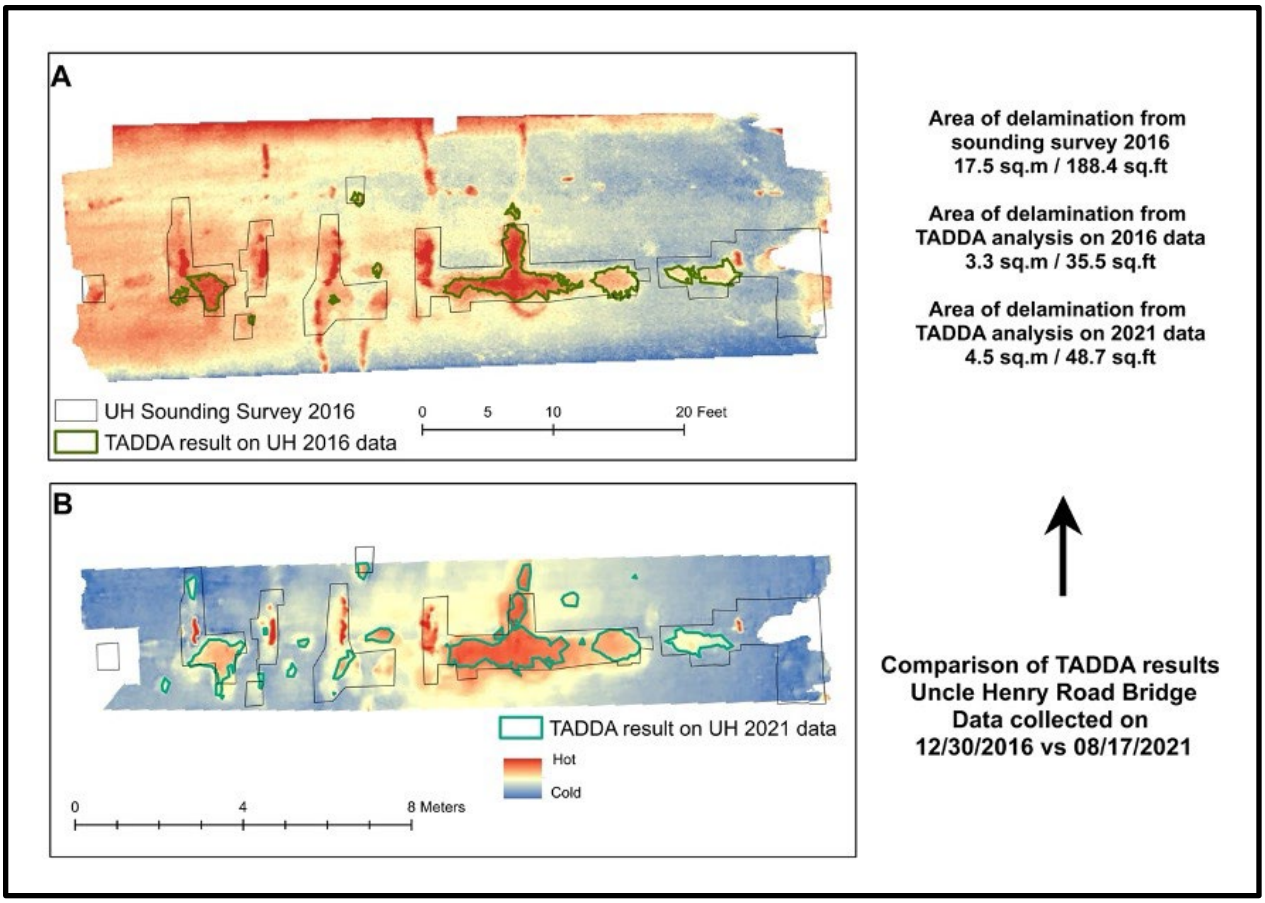

Figure 3.2.4: (a) Shows the thermal mosaic and TADDA outputs from 2016 and (b) shows the thermal mosaic and TADDA outputs from 2021. An increase in total area of delamination was observed from 2016 to 2021. The extent of the thermal mosaics corresponds to the extent used for the analysis (areas with shadow, foreign materials, construction equipment, moving bodies etc. are removed from the analysis). The bridge had considerable dirt on the edges of the bridge in 2021 which obscured the sensor view and thermal data, so analysis extent was more limited in 2021 relative to 2016. **(move this to body of report, shouldn't be under figure title)**

A growth in the total area of delamination is observed from 2016 to 2021; 1.2 sq. m (13.2 sq. ft) more of delamination is observed in 2021 relative to 2016. Areas which had no apparent delamination in 2016 appeared delaminated in the 2021 thermal data. While 0.3 sq. m or 3.2 sq. ft of previously unaffected areas developed newly detected delamination, 0.9 sq. m or 9.7 sq. ft of newer delaminations were a result of growth in previously affected areas. In total, a 40.5% increase in area of delamination was observed over this five year interval. Figure 3.2.5 shows the areas of growth in delamination, and the newly affected areas, from 2016 to 2021.

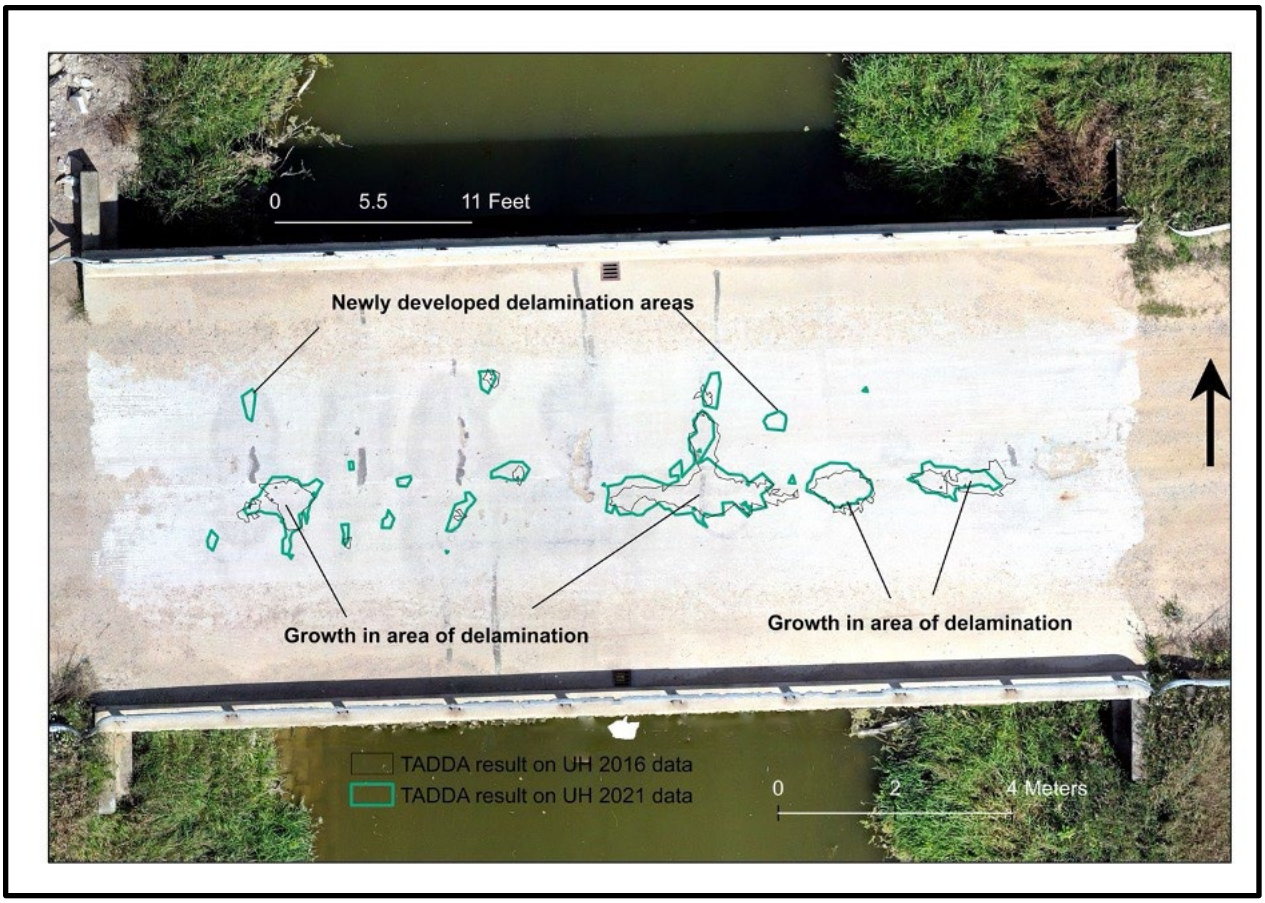

Figure 3.2.5: Comparison of the 2016 vs 2021 Uncle Henry Rd. delamination results show the growth of, and newly developed, areas of delamination. (in the figure, can "TDDA result on UH 2016 data" font be white so I can be seen better? – also is "UH" defined somewhere?)

Beyer Road Bridge

The bridge on Beyer Road over Cheboyganing Creek is 67 feet long, 26 feet wide and has a concrete deck surface (Figures 3.2.6 - 3.2.8). A 2016 MDOT bridge report indicated that there were four significant spalls and one delaminated region on the bridge deck at the time, which was assigned a surface rating of '5' ('Fair' condition). At this site, RGB imagery using the Nikon D810 and DJI Phantom 3A, and thermal imagery using the Flir Vue Pro, were collected on 12/30/2016. GIS-based layers created include an orthophoto, DEM, hillshade and thermal layer of the site and SSI provided survey-ground GPS ground control points for georeferencing outputs.

The bridge had little maintenance done since the data 2016 collection and thus a revisit of the site was made on 08/17/2021 to assess the change in delamination, if any. The DJI M2EA was used in 2021 to obtain thermal and optical images for Beyer Road bridge. Figure 3.2.6 (a) shows the thermal mosaic of the bridge while 1 (b) shows the Mavic Pro visual orthophoto.

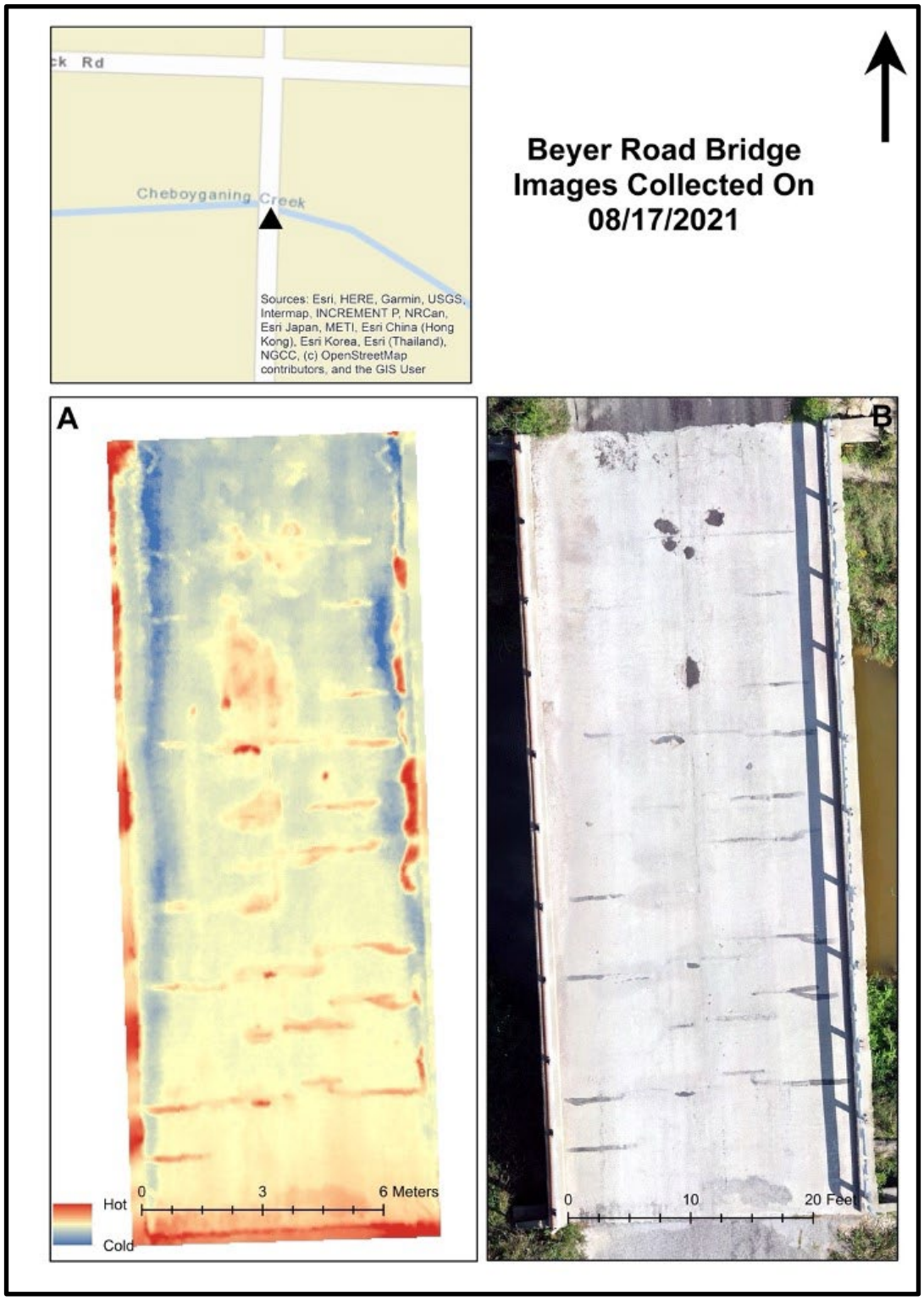

Figure 3.2.6: (a) shows the thermal mosaic of relative temperature; (b) shows the visual orthophoto of the Beyer Road Bridge.

Delamination analysis on the newly acquired 2021 data for Uncle Henry Road bridge was performed using the Thermal Anomaly and Delamination Detection (TADDA) algorithm. The results of delamination detected using 2016 and 2021 data were then compared. Figure 3.2.7 shows the comparison of these results.

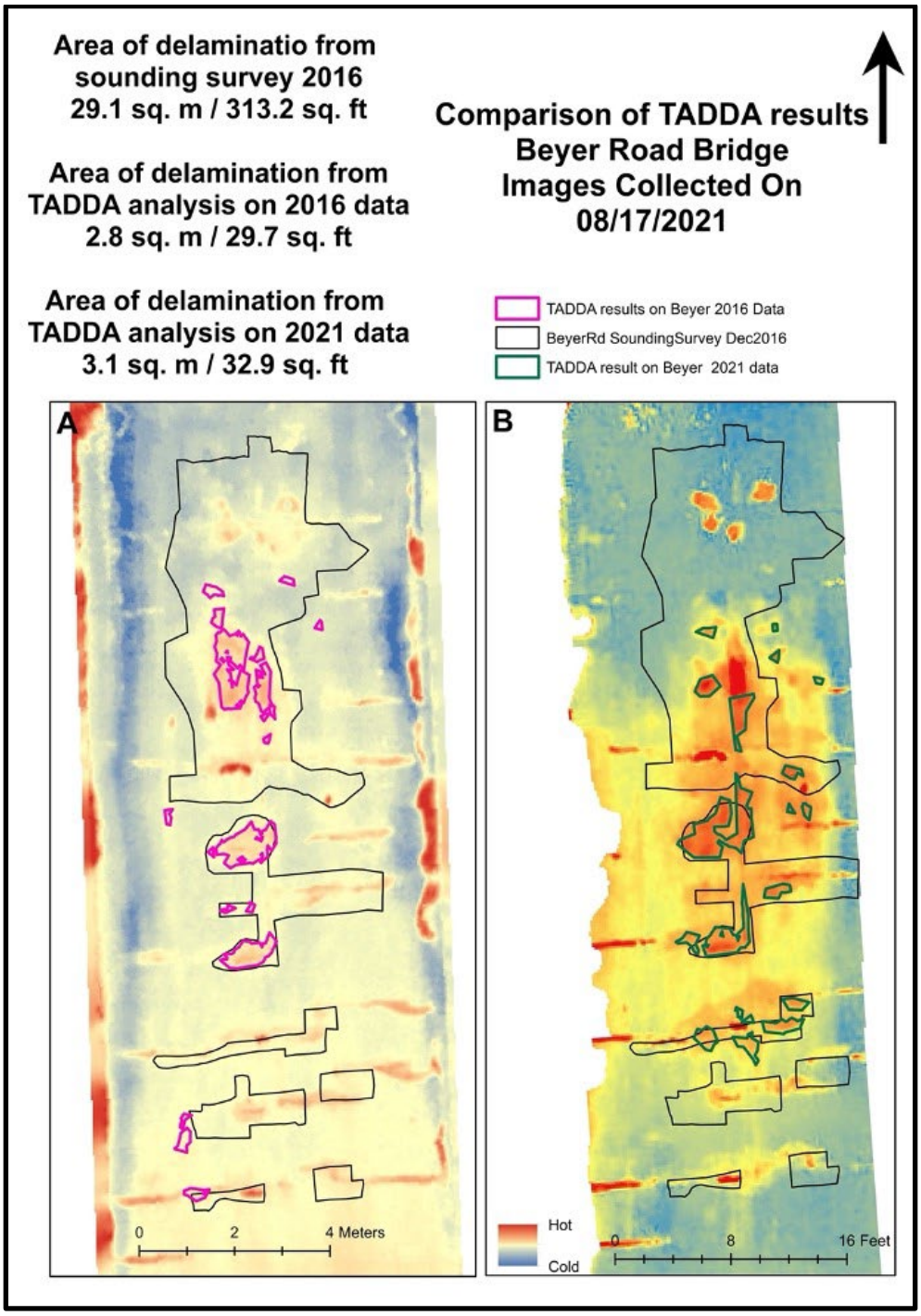

Figure 3.2.7: (a) shows the thermal mosaic from 2016 and (b) shows the thermal mosaic from 2021. An increase in area of delamination was observed from 2016 to 2021. The extent of the

thermal mosaics corresponds to the extent used for the analysis. **(move this to body of report, shouldn't be under figure title)**

A slight growth in the total area of delamination is observed from 2016 to 202;. 0.3 sq. m or 3.2 sq. ft more of delamination is observed over the five-year interval. This growth appears to be less when compared to that in Uncle Henry Road Bridge. However, the Beyer Road Bridge seems to have some patched spalls shown in Figure 3.2.8. Some areas that were detected delaminations in 2016 had surface patches in 2021 and this contributed to the shrinkage of delamination polygons in certain areas. However, new delaminations developed in previously unaffected areas and this contributed to a significant increase of 0.9 sq. m or 9.7 sq. ft.

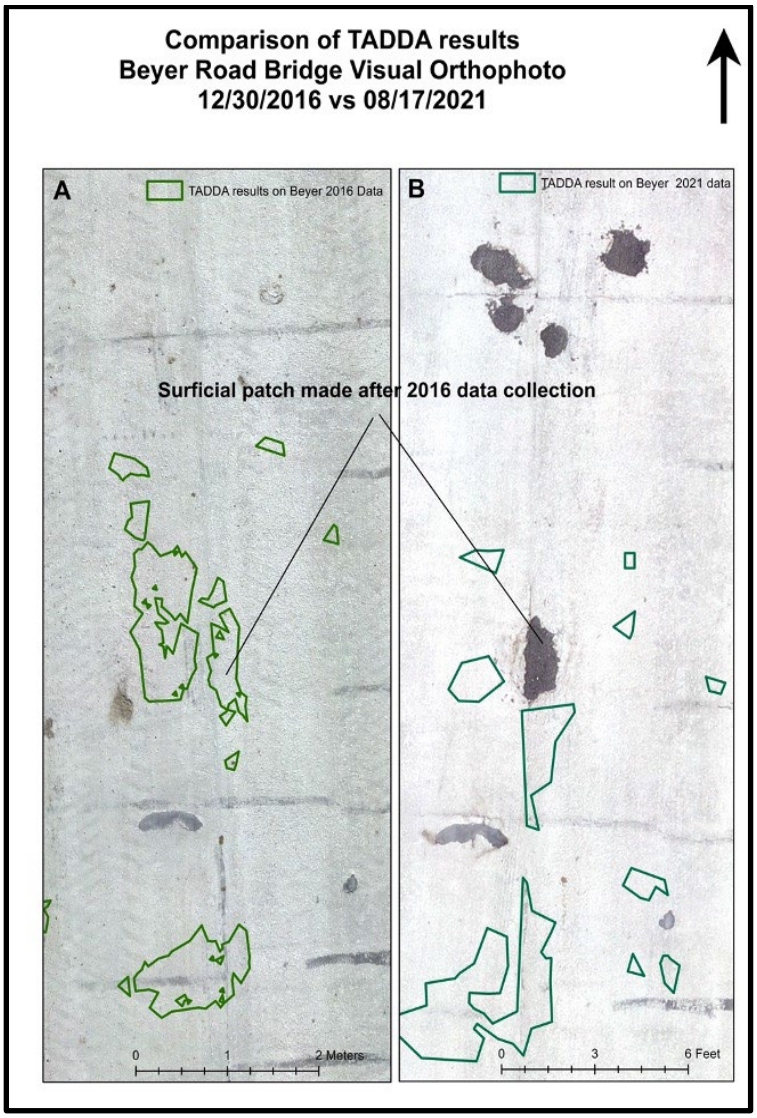

Figure 3.2.8: A surface patch is seen in the 2021 visual orthophoto of Beyer Road Bridge (b) which was not seen in the 2016 (a) visual orthophoto. This is likely a patch made to repair a spall that had formed in the bridge deck between 2016 and 2021. Maintenance like this could be a

possible reason for the shrinkage in the delamination area seen in certain portions of the Beyer Road Bridge. **(move this to body of report, shouldn't be under figure title)**

M-99/I-96

The M99 / I96 bridge near Eaton Rapids had visual and thermal data collected on 08/16/2019 (believe in reports, this is spelled out "August 8, 2019"). The DJI Mavic 2 Pro was used to collect RGB imagery and the FLIR Vue Pro flown on the Bergen Hexacopter was used for thermal imagery collection. Visual orthophoto, thermal mosaic, DEM, hillshade, spall, and delamination layers were generated from this RGB and thermal imagery. Figure 3.2.9 shows the result of TADDA analysis on the M-99/I-96 eastbound bridge.

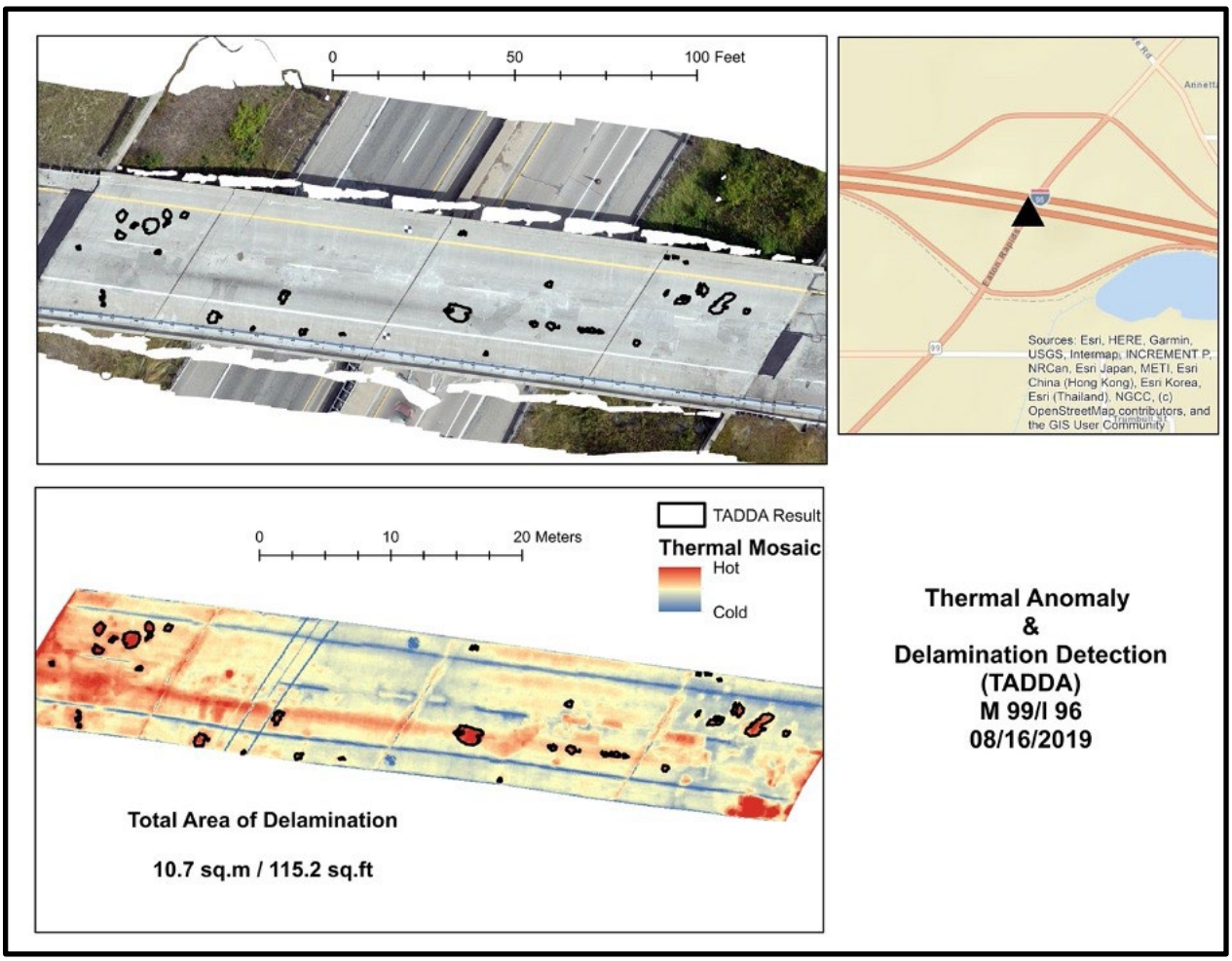

Figure 3.2.9: Result of TADDA analysis on the M99 / I96 EB Bridge. A total area of delamination of 10.7 sq. m / 115.2 sq. ft was detected.

A total delamination area of 10.7 sq. m / 115.2 sq. ft was observed through the UAS data collection. The eastern and western ends of the bridge showed the most significant grouping of likely delaminated areas. Figure 3.2.10 shows a section wise breakup of the delamination areas

that highlight the larger delamination polygons detected by the TADDA algorithm. The largest delamination polygon is observed in the eastern section close to the center of the bridge. This polygon has an area of 1.96 sq. m or 21.1 sq. ft. Towards the western end of the bridge there is another polygon that has an area of 1.2 sq. m or 12.9 sq. ft.

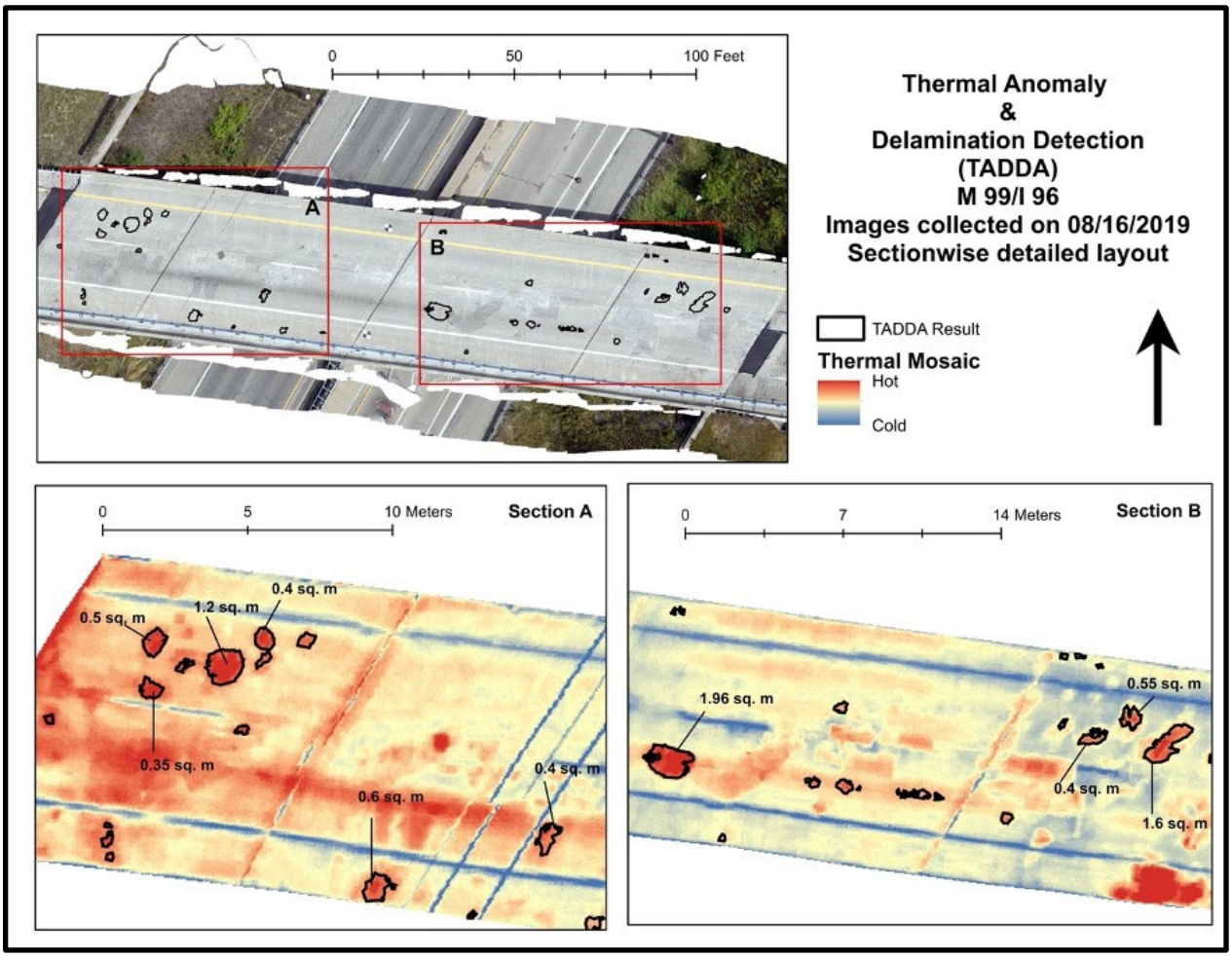

Figure 3.2.10: Section-wise depiction of delaminations in the M99 Road Bridge. Section A represents the western half and Section B represents the eastern half of the bridge. The delamination areas are shown here in square meters.

I-96 over Grand River / Billwood Highway

The Billwood Highway, or I-96 over Grand River, bridge had visual and thermal data collected on 08/15/2019. The DJI Mavic 2 Pro was used to collect RGB imagery and the FLIR Vue Pro flown on the Bergen Hexacopter was used for thermal imagery collection. A visual orthophoto, thermal mosaic, DEM, hillshade, spall, and delamination layer was generated from this RGB and thermal imagery. Figure 3.2.11 shows the full expanse of the bridge. The detailed TADDA analysis results of each of the three sections depicted in figure 3.2.11 is shown in detail in figures 3.2.12 - 3.2.14. Though the largest area of delamination was observed in Section A, the pattern of delamination was largely evenly spread through the bridge. The delamination of this

bridge was observed such that there were many small delamination polygons spread through the length of the bridge. It should also be noted that a considerable area in Section A had construction materials and shadow which caused the exclusion of a large portion of the area from the delamination analysis.

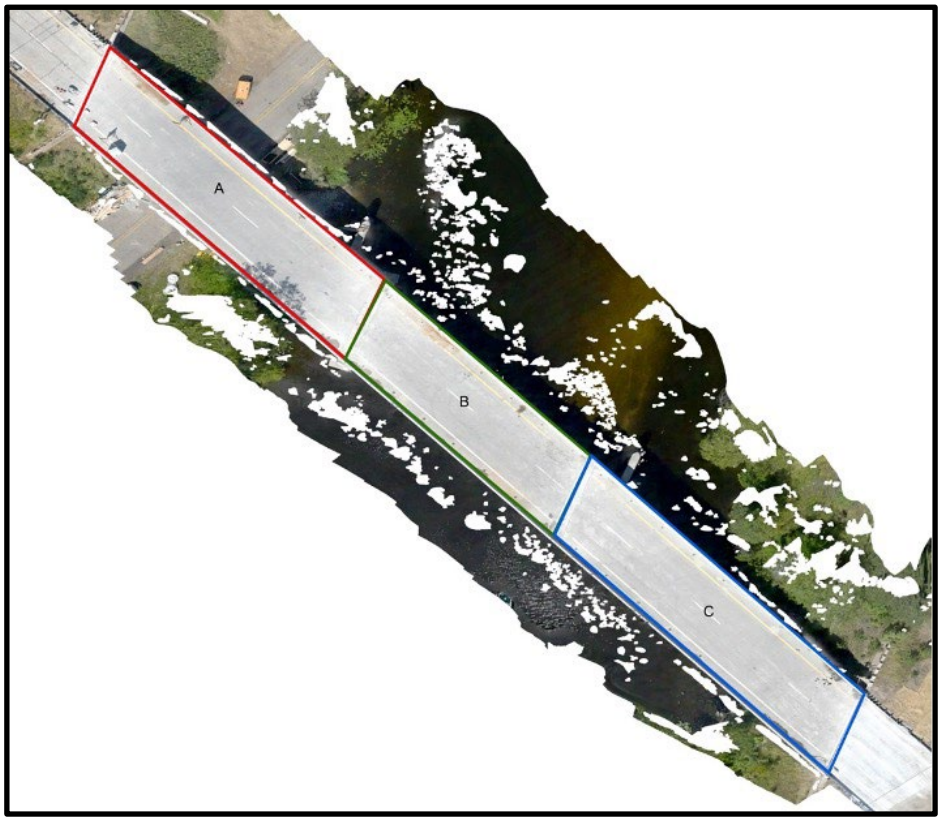

Figure 3.2.11: Billwood highway bridge divided into 3 sections, A, B, and C. Enhanced views of each section are displayed in subsequent figures.

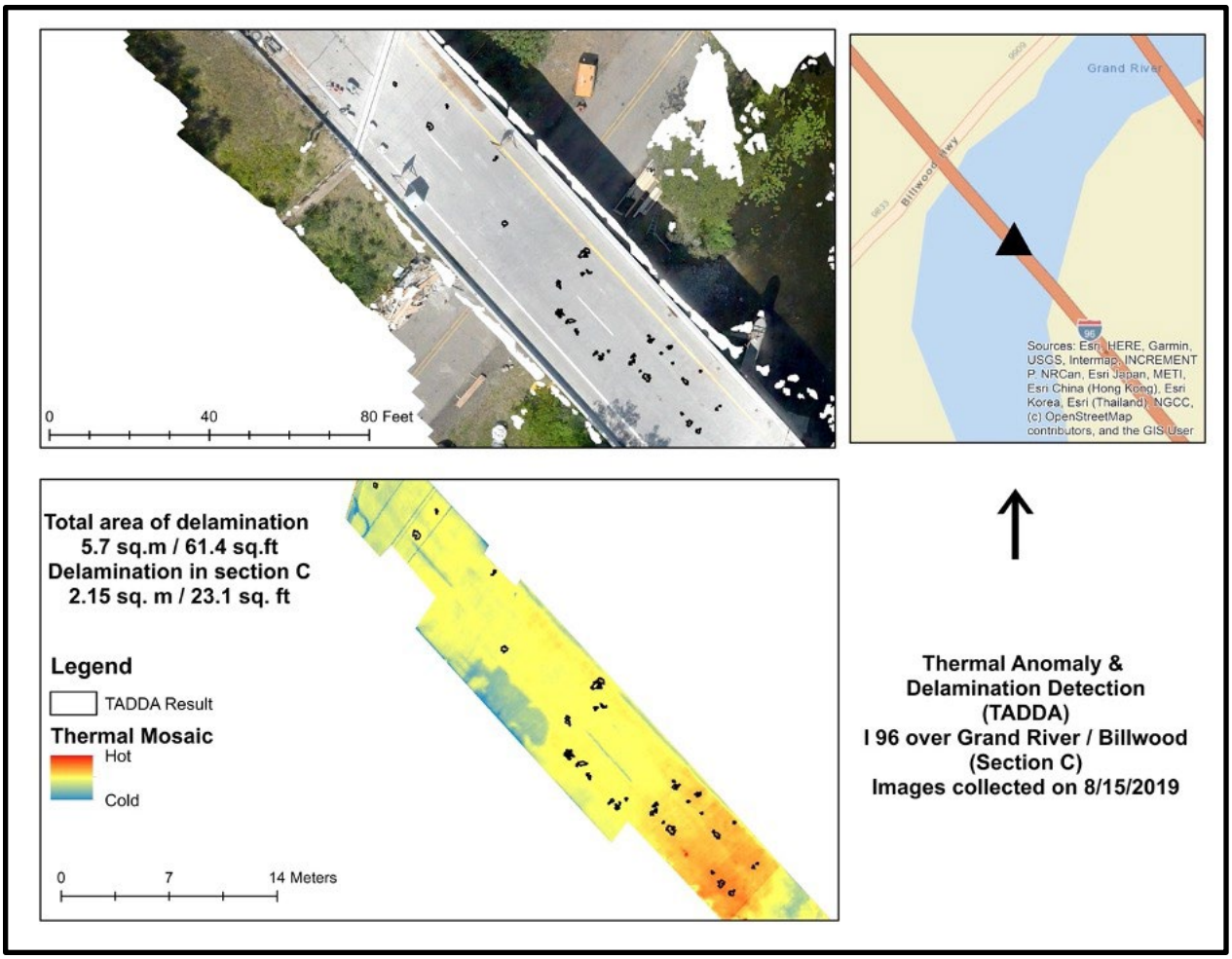

Figure 3.2.12: Section A of Billwood highway. This is the western section of the bridge and reported 2.15 sq. m or 23.1 sq. ft of delamination from the TADDA analysis.

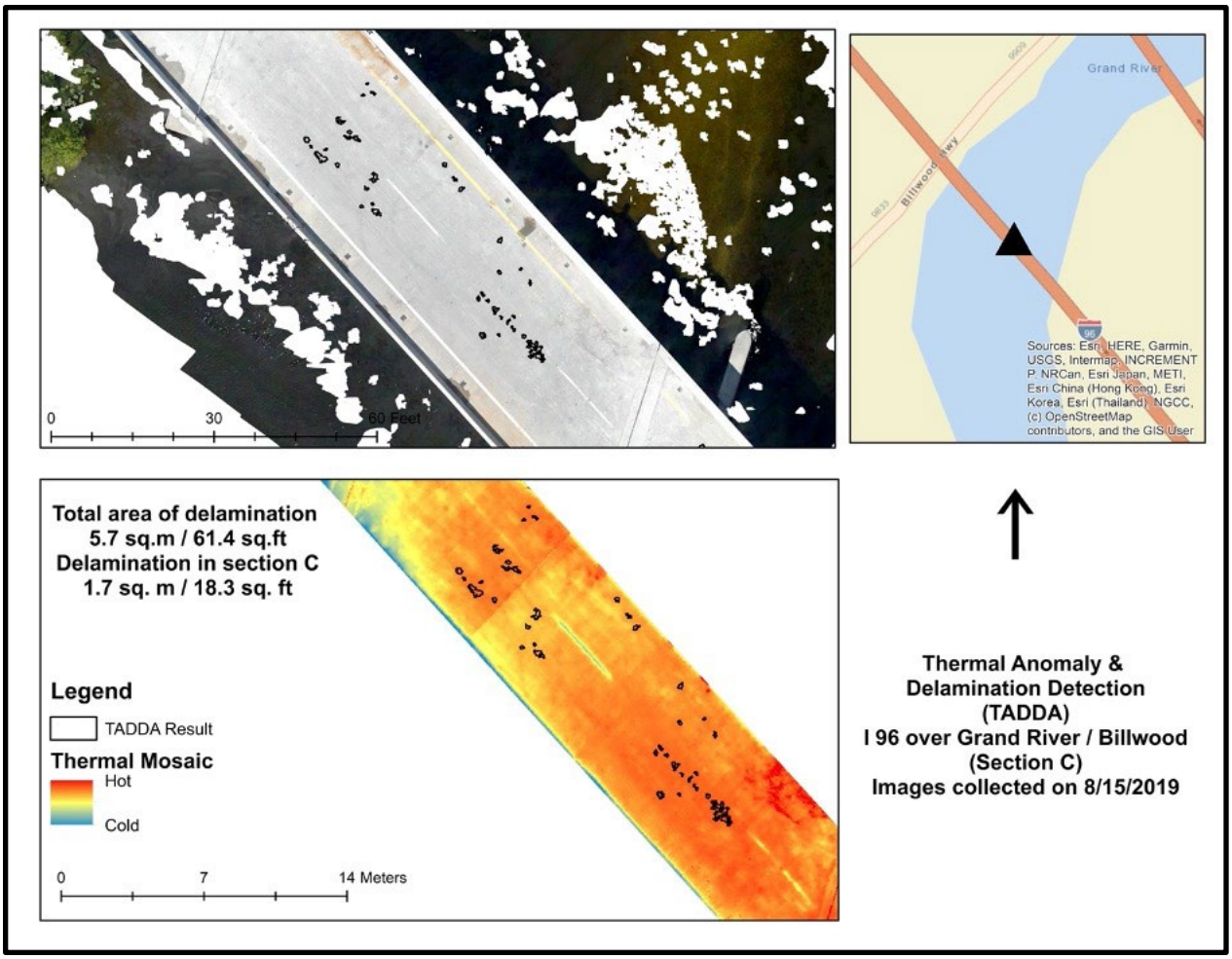

Figure 3.2.13: Section B of Billwood highway. This is the middle section of the bridge and reported 1.7 sq. m or 18.3 sq. ft of delamination from the TADDA analysis.

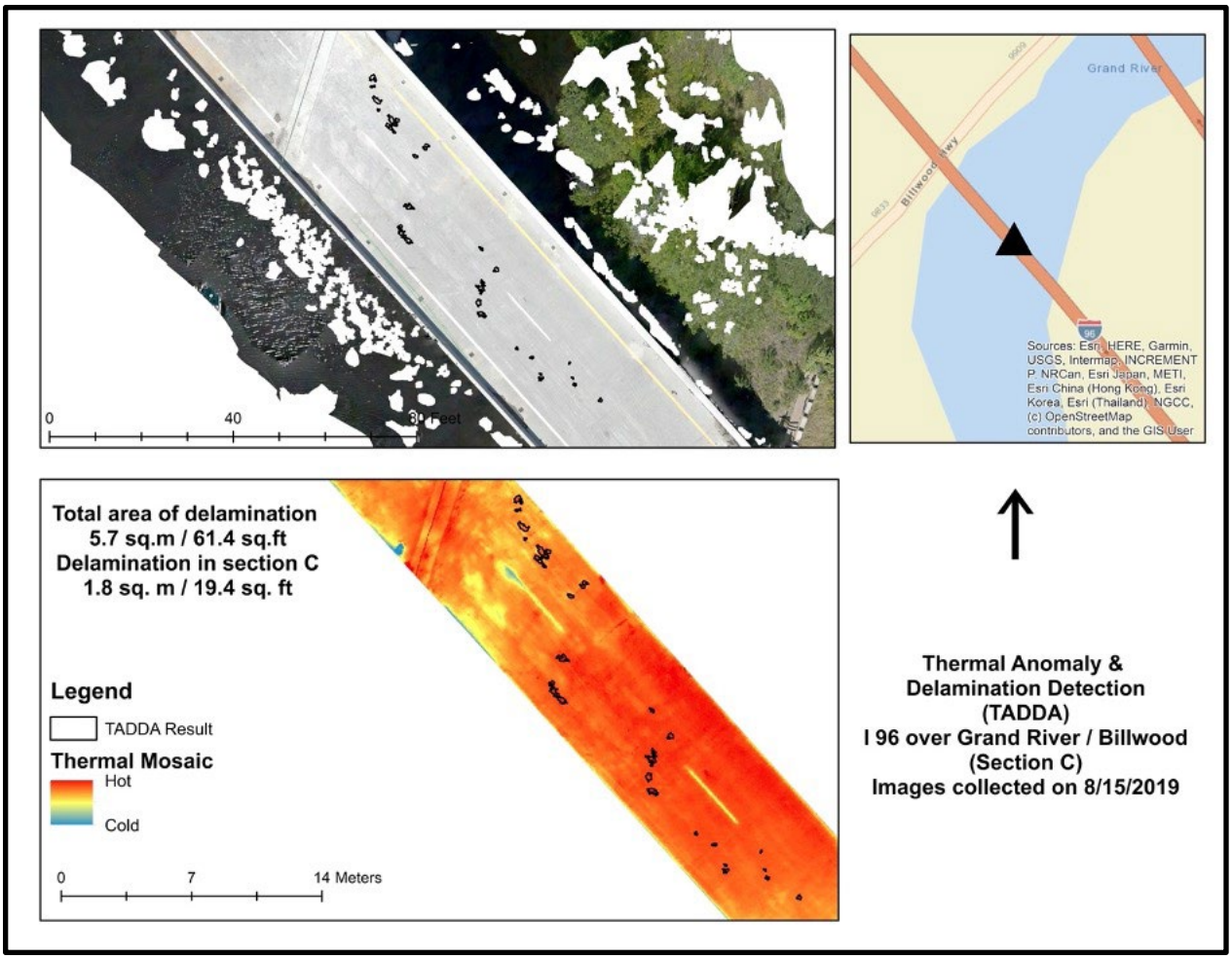

Figure 3.2.14: Section C of Billwood highway. This is the eastern section of the bridge and reported 1.8 sq. m or 19.4 sq. ft of delamination from the TADDA analysis.

Laplaisance Creek Exit Ramp

The Laplaisance Creek northbound exit ramp near Monroe, MI had visual and thermal data collected on 08/31/2021. This was part of a revisit to the site as the initial data collection on 11/09/2020 failed to capture sufficient imagery due to unfavorable weather and ambient temperatures. The Mavic 2 Enterprise advanced was used for this data collection to capture both optical and thermal data for the bridge. A visual orthophoto, thermal mosaic, DEM, hillshade, spall, and delamination layer was generated from this RGB and thermal imagery.

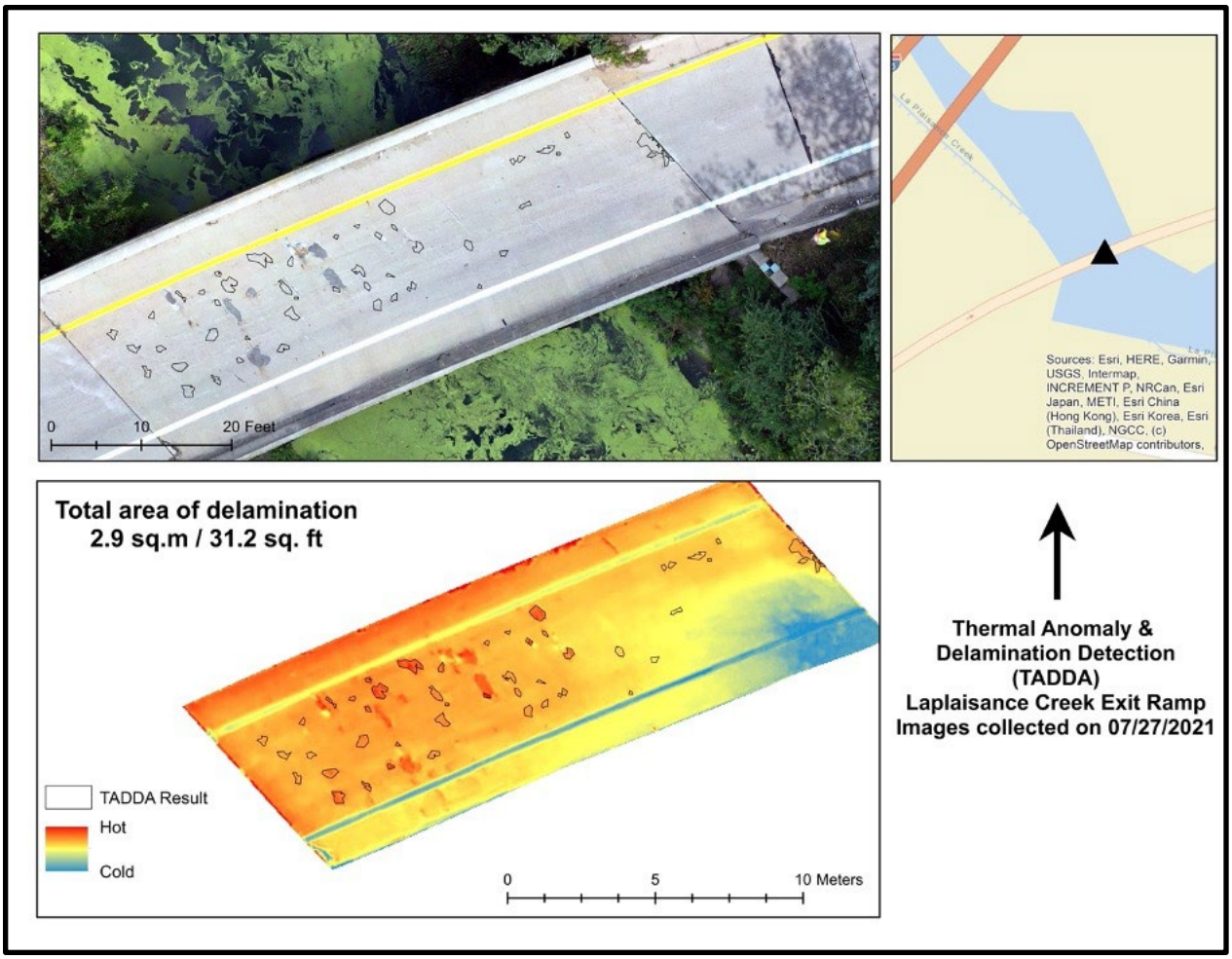

Figure 3.2.15: Result of TADDA analysis for the Laplaisance Creek exit ramp. A total area of delamination of 2.9 sq. m / 31.2 sq. ft was observed.

After analyzing the thermal data for the Laplaisance Creek exit ramp, it is apparent that there are several likely delaminations and spalling in the bridge deck. Spalls and patches are seen primarily in the western half of the bridge; this area also has most of the total delamination polygons, suggesting issues may be focused in the western half of the bridge. It is possible that the presence of tree shadows influenced the quality of thermal imagery collected over the eastern half of the bridge (see large relatively cold area on the east side of the bridge). However, the largest delamination polygon is observed towards the eastern end of the bridge reporting an area of 0.3 m^2 or 3.2 ft^2. Figure 3.2.16 shows a section-wise breakup of the significant detected bridge delaminations. A comparison of the TADDA results with the MDOT reported delaminations is shown in Figures 3.2.16 and 3.2.17.

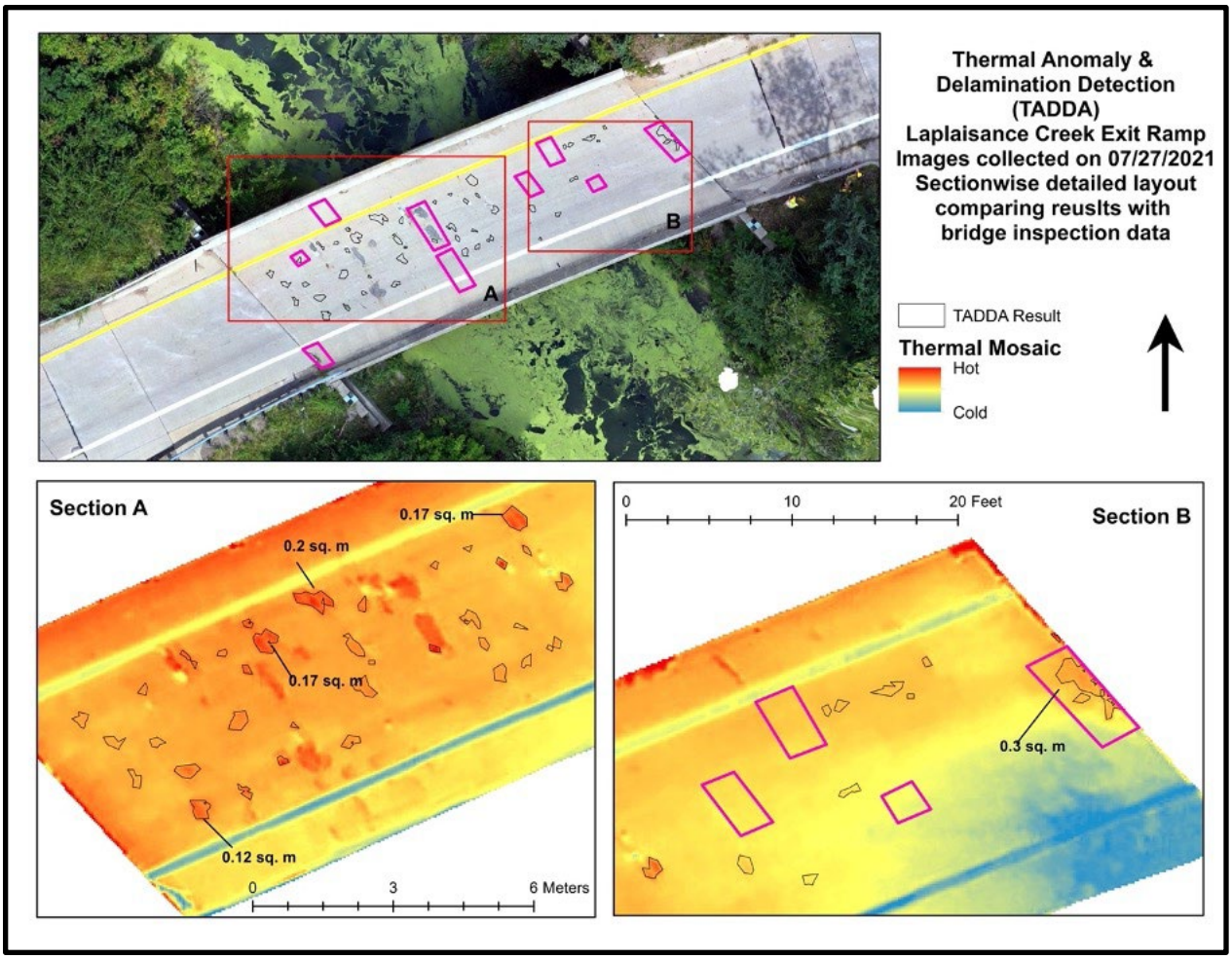

Figure 3.2.16: Section-wise depiction of delaminations in the Laplaisance Creek exit ramp. Section A represents the western half and Section B represents the eastern half. More delaminations are seen in the western half while the single largest delamination polygon is seen towards the eastern end of the bridge.

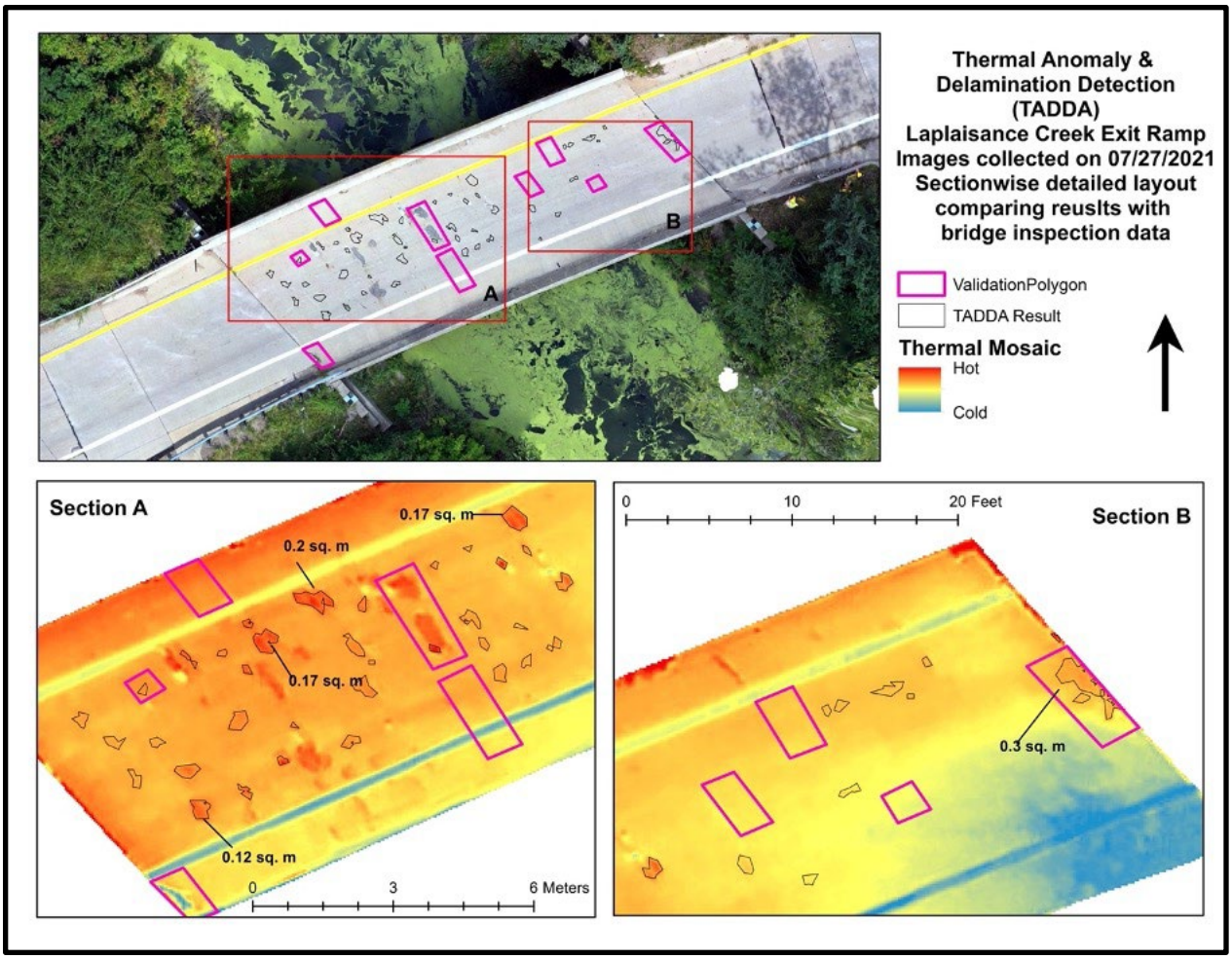

Figure 3.2.17: Section-wise depiction of delaminations in the Laplaisance Creek exit ramp, compared with the bridge inspection report. The layer validation polygon represents the delaminations as identified by the bridge inspection report. Section A represents the western half and Section B represents the eastern half.

Hyperspectral survey of Portage Lake Lift Bridge / Houghton – Hancock Bridge

The Portage Lake Lift Bridge / Houghton–Hancock Bridge connects the cities of Hancock and Houghton, in Michigan's upper peninsula. It crosses Portage Lake which cuts across the Keweenaw Peninsula with a canal linking the final several miles from Keweenaw Bay to western Lake Superior. US Highway 41 and M-26 are both routed across the bridge, and as a result sees significant amounts of traffic on a daily basis. The bridge has a length of approximately 500 feet (150m) and height 180 feet (55m). Figure 3.2.18 shows the location of the bridge.

Figure 3.2.18: Location of the Houghton-Hancock Bridge / Portage Lake Lift Bridge

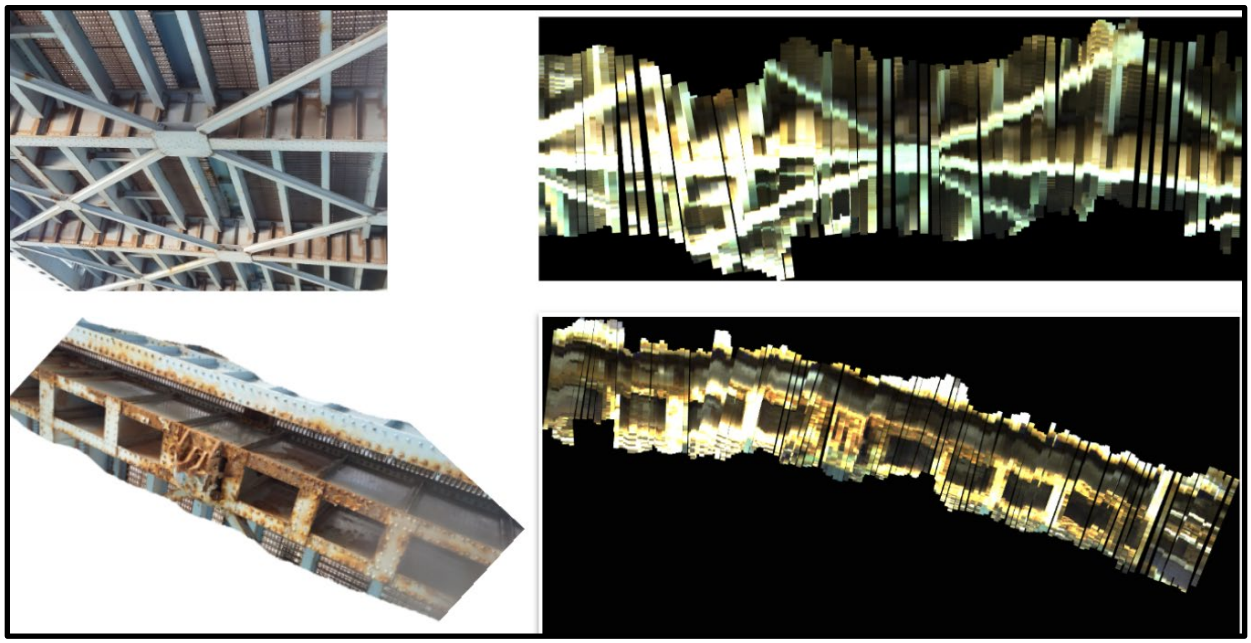

Figure 3.2.19: Optical images of the underside of the lift bridge bridge (left). Hyperspectral image of the underside of the bridge (right). Hyperspectral imaging for two beams was performed. The beam on the top left had limited rusting while the beam on bottom left had more extensive rusting.

The Bayspec OCI-F series push broom sensor, which covers the visible to infrared spectrum of 400 to 1000 nm with 75 distinct bands, was used for hyperspectral image capture. The spectral signatures of rusted and non-rusted areas measured with the hyperspectral sensor showed distinct spectral properties (figure 3.2.20).

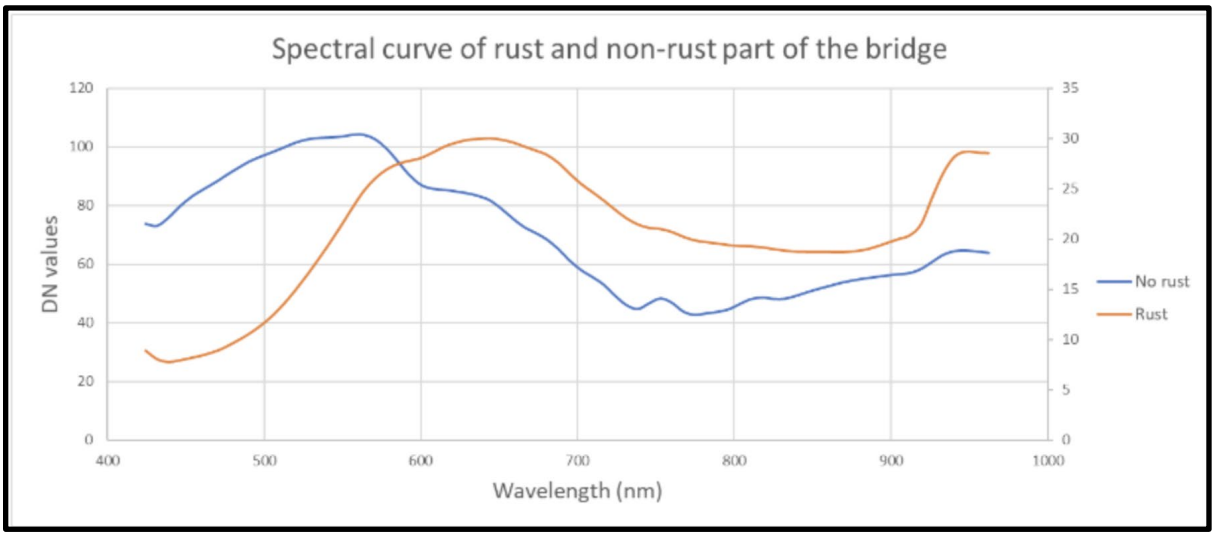

Figure 3.2.20: Averaged spectral curves of rust and non-rust areas of the Houghton - Hancock Bridge.

The hyperspectral images were then classified using a K-means unsupervised classification algorithm. The first three Principal Component (PC) bands were extracted and 5 distinct classes were generated using the K-means algorithm with the PC images as input. Two classes were removed as they represented primarily shadow and background values. Out of the three remaining classes, two classes were merged which represented non-rusted pixels and one class represented rusted pixels. Figures 3.2.21 and 3.2.22 show the classification results of the two beams respectively. This preliminary investigation demonstrates the applicability of hyperspectral sensor for characterizing the condition of steel bridges. The areas with significant rust have a very different spectral signature compared to areas that have no rust, allowing the classification of these two unique classes.

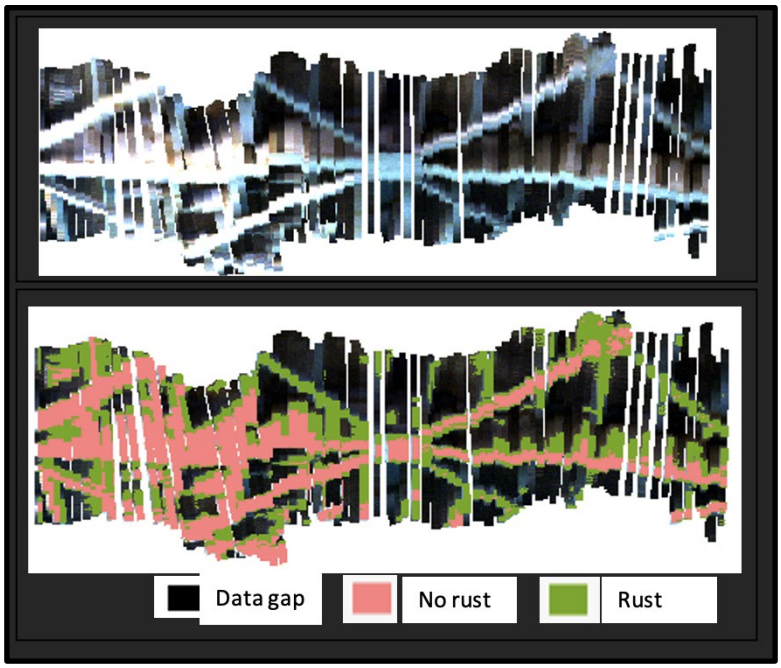

Figure 3.2.21: Unsupervised classification of hyperspectral imagery of Houghton - Hancock Bridge beam 1.

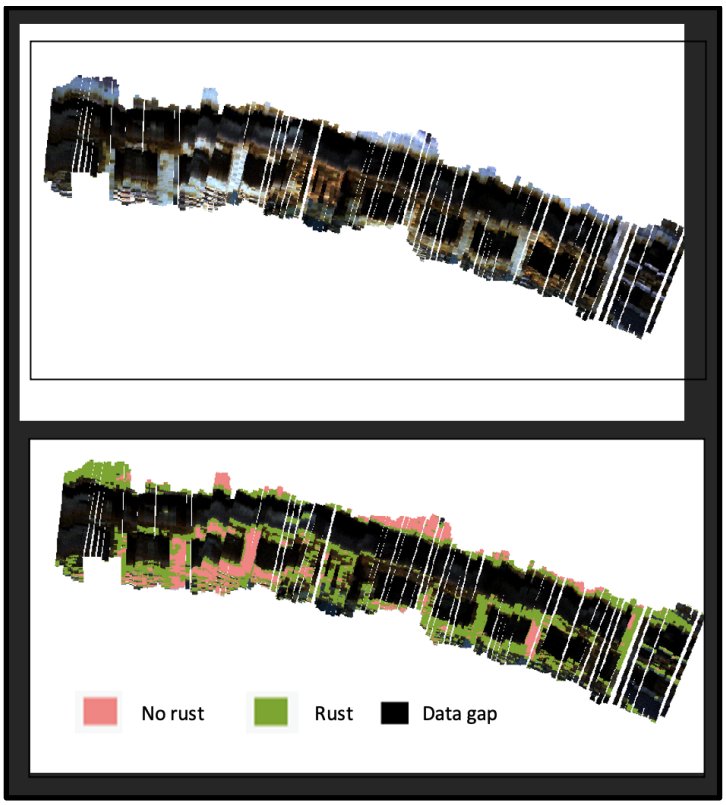

Figure 3.2.22: Unsupervised classification of hyperspectral imagery of Houghton - Hancock Bridge beam 2.

Spallgorithm Updates

In Phase III of this project the spallgorithm was significantly upgraded from the version 4.2 described in Phase II. The new version, 5.1, has been developed for use in ArcPro 2.X and is considered a more robust version in that it requires less user input and generally produces fewer false positives. Additionally, it uses python 3.6 which is upgraded from python 2.7 used in ArcGIS Desktop. Several of the input parameters that were required in version 4.2 have been removed and the algorithm automatically determines ideal values for these parameters. The newest version only requires the following inputs: 1) A directory where temporary products can be stored, 2) A digital elevation model (geotiff file format), 3) an inclusion zone (shapefile format), 4) a sensitivity value (0-10, decided by the user), 5) Output directory and filename. There is an optional checkbox to have the output added to the map in the running instance of ArcGIS Pro. The major modifications to the spallgorithm involve how it handles different projections of data, the way in which the DEM is processed to detect spalls, and false positive filtering, making it overall more user friendly and intuitive.

In contrast to the previous version where input data was required to be in a state plane coordinate system, the new version will work with data of any projected coordinate system input by the user. The units of the input coordinate system are used to create the appropriate parameters for the detection algorithm. Rather than attempting to detect elevation deviations on the input DEM directly by using a convolutional kernel that returns the range, the input DEM is first filtered iteratively over using a growing kernel. This creates a localized flat plane across the DEM, from which the input is subtracted from. Negative values are areas where the actual elevation values are below an idealized flat surface, which serves as our technical definition of a detected spall. An additional filtering process utilized the range kernel to only keep depressions that have a steep dropoff in elevation values, rather than a smooth depression.

Overall the new version is more mature and requires fewer inputs, fewer lines of code, is more flexible, and produces better and more intuitive results than previous versions.

Uncle Henry Road Bridge Spallgorithm Results

The Uncle Henry Road bridge had visual and thermal data collected on 08/17/2021, with initial data collected on 12/30/2016. This analysis uses the same visual data described in the previous TADDA section of this report. A visual orthophoto, thermal mosaic, DEM, hillshade, spall, and delamination layer was generated from this RGB and thermal imagery. The spallgorithm detected 6 spalls in the August 2021 imagery as opposed to 3 spalls found in December of 2016. New spalls detected in 2021, spall numbers 3-5, are seen in Figures 3.2.23 and 3.3.24 below. The total area of spalling in 2016 was 1.78 square feet which increased to 3.15 square feet in 2021.

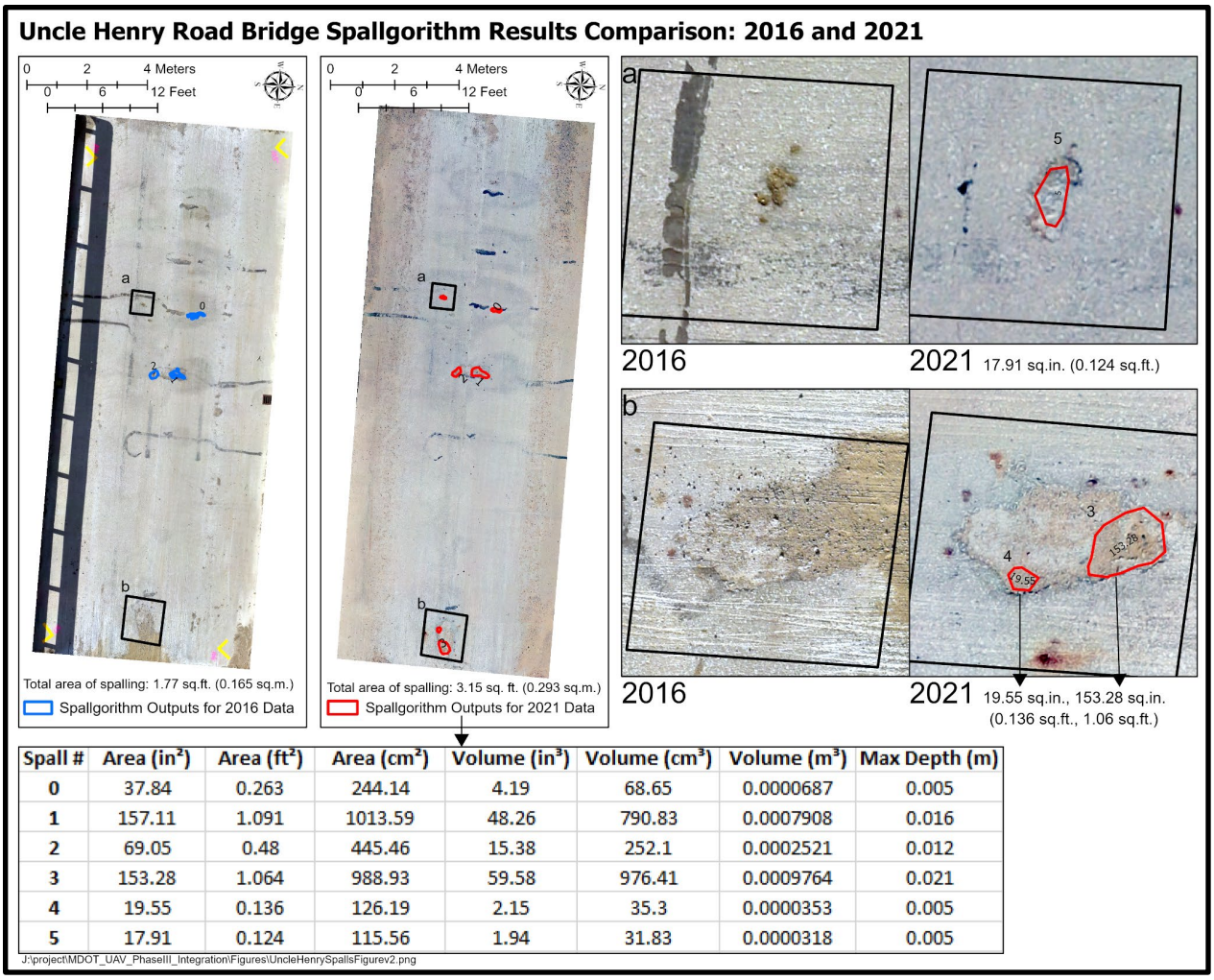

Spall #	Area (in²)	Area (ft²)	Area (cm²)	Volume (in³)	Volume (cm³)	Volume (m³)	Max Depth (m)
0	37.84	0.263	244.14	4.19	68.65	0.0000687	0.005
1	157.11	1.091	1013.59	48.26	790.83	0.0007908	0.016
2	69.05	0.48	445.46	15.38	252.1	0.0002521	0.012
3	153.28	1.064	988.93	59.58	976.41	0.0009764	0.021
4	19.55	0.136	126.19	2.15	35.3	0.0000353	0.005
5	17.91	0.124	115.56	1.94	31.83	0.0000318	0.005

J:\project\MDOT_UAV_PhaseIII_Integration\Figures\UncleHenrySpallsFigurev2.png

Figure 3.2.23: Comparison of 2016 and 2021orthomosaic and spallgorithm detection outputs for Uncle Henry Rd bridge.

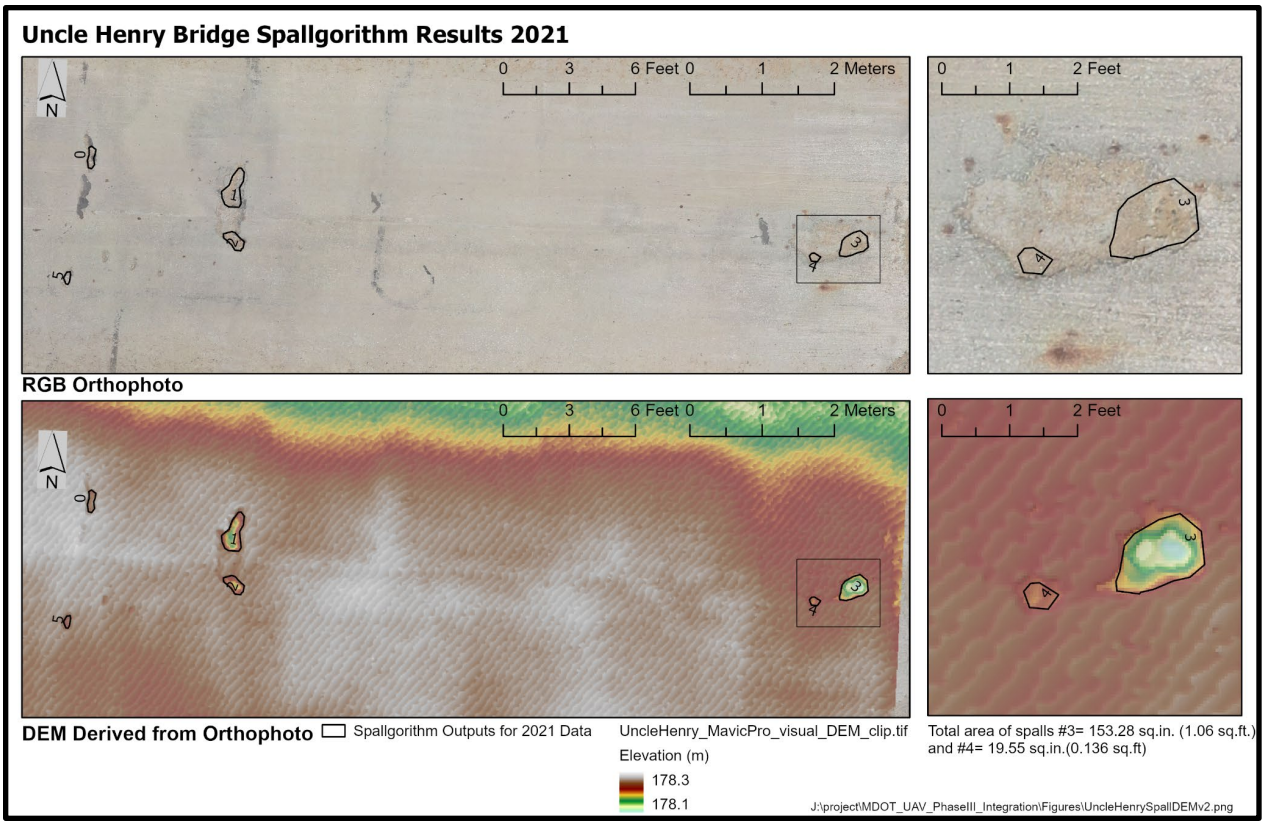

Figure 3.2.24: Uncle Henry orthophoto, and hillshaded DEM, with 2021 spall detection outputs displayed.

Beyer Road Bridge Spallgorithm Results

The Beyer Road bridge had visual and thermal data collected on 08/17/2021, with initial data collected on 12/30/2016. This analysis uses the same visual data described in the previous TADDA section of this report. A visual orthophoto, thermal mosaic, DEM, hillshade, spall, and delamination layer was generated from this RGB and thermal imagery. The spallgorithm detected zero spalls in 2021 with evidence that a previously detected spall was patched since 2016. The total area of spalling in 2016 was 1.22 square feet, which decreased to 0 square feet in 2021 due to spall patching as seen in Figure 3.2.25. In Figure 3.2.25 it is visually apparent that 4 or 5 spalls formed and were patched between the 2016 and 2021 drone-based surveys that were performed by MTRI/MTU.

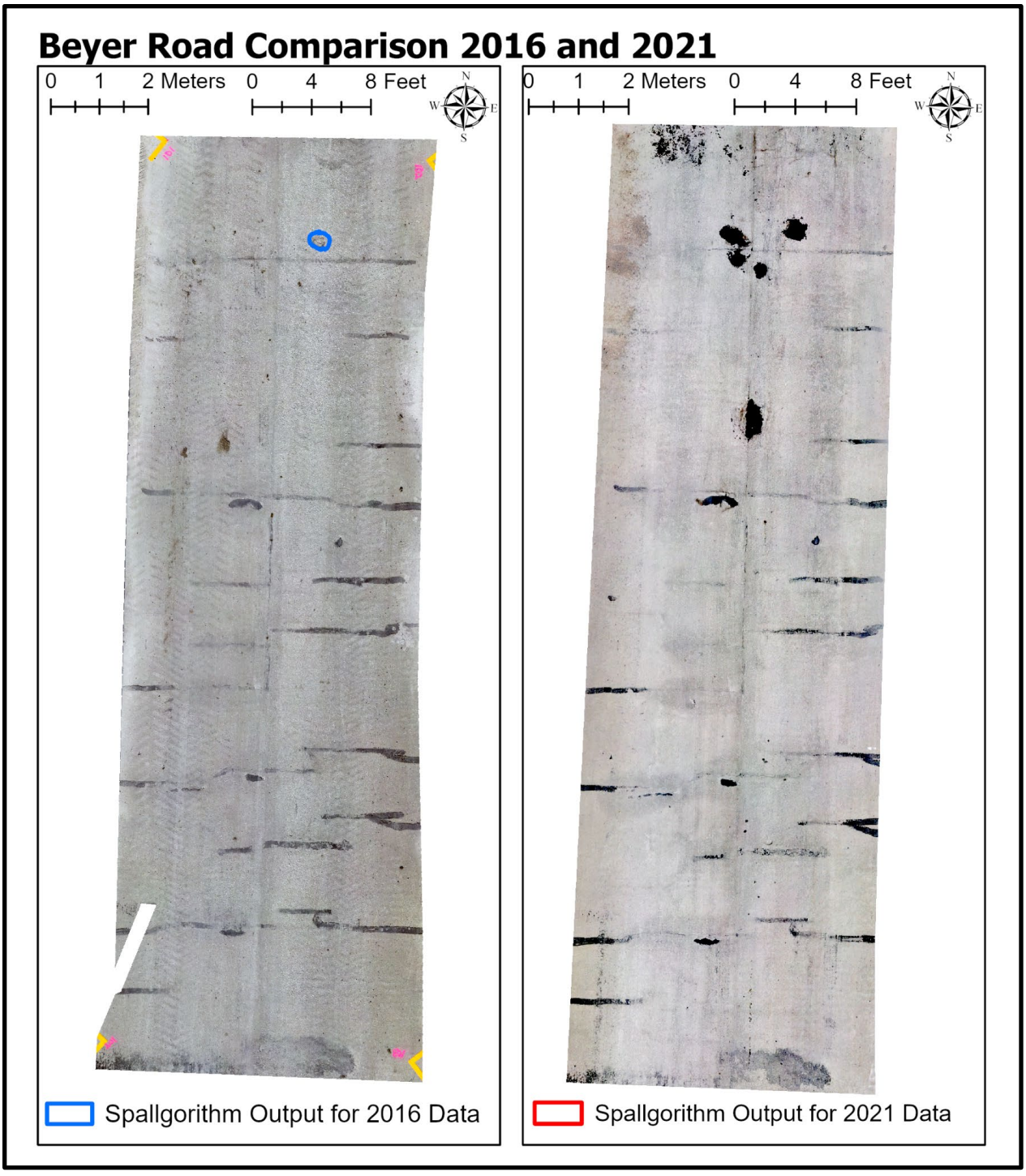

Figure 3.2.25: Comparison of Beyer Rd. bridge 2016 orthoimage & spallgorithm output and 2021 orthoimage with apparent patched spalls.

M-99/I-96 Bridge Spallgorithm Results

The M-99/I-96 bridge had visual and thermal data collected on 08/16/2021. This analysis uses the same visual data described in the previous TADDA section. A visual orthophoto, thermal mosaic, DEM, hillshade, spall, and delamination layer was generated from this RGB and thermal imagery. The spallgorithm detected 4 spalls in the imagery and orthophoto from August of 2019. The total area of spalling was 3.09 square feet or 0.287 square meters (Figure 3.2.26).

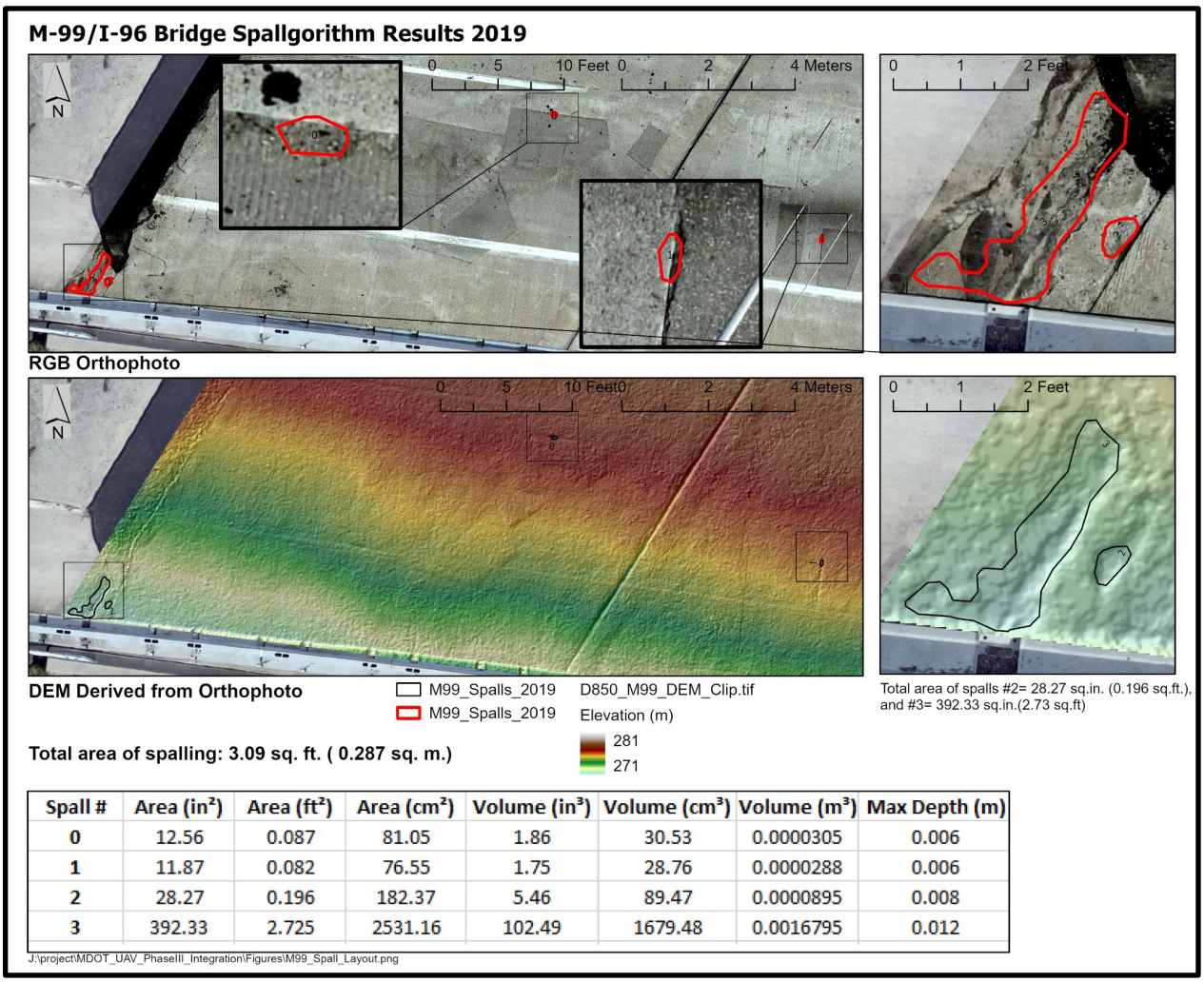

Spall #	Area (in²)	Area (ft²)	Area (cm²)	Volume (in³)	Volume (cm³)	Volume (m³)	Max Depth (m)
0	12.56	0.087	81.05	1.86	30.53	0.0000305	0.006
1	11.87	0.082	76.55	1.75	28.76	0.0000288	0.006
2	28.27	0.196	182.37	5.46	89.47	0.0000895	0.008
3	392.33	2.725	2531.16	102.49	1679.48	0.0016795	0.012

J:\project\MDOT_UAV_PhaseIII_Integration\Figures\M99_Spall_Layout.png

Figure 3.2.26: Top optical orthophoto of the M-99/I-96 bridge with spall outputs and the digital elevation model below. There were four spalls detected for this site.

I-96 over Grand River / Billwood Highway

The Billwood Highway or I-96 over Grand River had visual and thermal data collected on 08/15/2021. This analysis uses the same visual data described in the previous TADDA section of this report. A visual orthophoto, thermal mosaic, DEM, hillshade, spall, and delamination layer was generated from this RGB and thermal imagery. Due to the considerable area of Section A that had construction materials and shadow present in UAV images, the spallgorithm results were

deemed insufficient with many false positive spalls. Surveying with less material on the bridge deck would be desired for future analyses. No significant spalls were detected for Section B or C of the Billwood Highway bridge (see Figures 3.2.12-3.2.14 for visual reference).

Laplaisance Creek/ I-75 Exit Spallgorithm Results

The Laplaisance Creek/ I-75 Offramp Bridge had visual and thermal data collected on 08/31/2021. This analysis uses the same visual data described in the previous TADDA section of this report. A visual orthophoto, thermal mosaic, DEM, hillshade, spall, and delamination layer was generated from this RGB and thermal imagery. The spallgorithm detected 4 spalls in August of 2021. The total area of spalling was 3.44 square feet or 0.320 square meters (Figure 3.2.27).

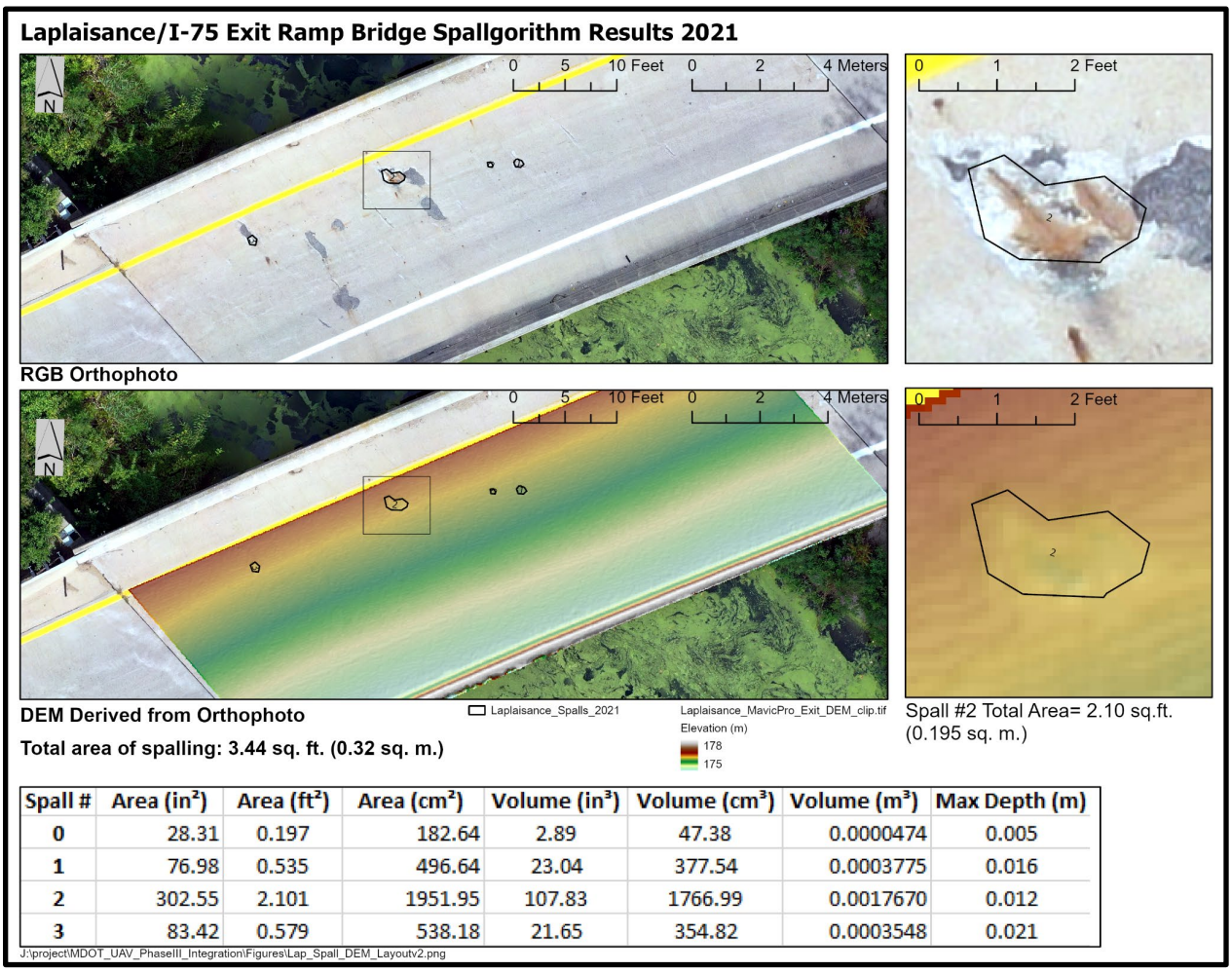

Spall #	Area (in²)	Area (ft²)	Area (cm²)	Volume (in³)	Volume (cm³)	Volume (m³)	Max Depth (m)
0	28.31	0.197	182.64	2.89	47.38	0.0000474	0.005
1	76.98	0.535	496.64	23.04	377.54	0.0003775	0.016
2	302.55	2.101	1951.95	107.83	1766.99	0.0017670	0.012
3	83.42	0.579	538.18	21.65	354.82	0.0003548	0.021

J:\project\MDOT_UAV_PhaseIII_Integration\Figures\Lap_Spall_DEM_Layoutv2.png

Figure 3.2.27: Laplaisance Creek/I-75 Exit Ramp orthophoto, hillshaded DEM, and spallgorithm detection outputs displayed.

Table 3.2.1 below lists the total area of delaminations and spalls detected by the TADDA algorithm or Spallgorithm for each surveyed bridge. More detailed spall and delamination data for each bridge can be found in Appendix 6.8

.

Table 3.2.1: List of data collected and results generated by TADDA and Spallgorithm processing. *Full detailed tables for each bridge are found in Appendix 6.8.*

Location	Date of Collection	Type of Data	Type of File	File Name	Count	Total Area (m^2)	Total Area (ft^2)
Beyer	8/17/2021	Delaminations	Shapefile (.shp)	Beyer_Delaminations_2021.shp	19	3.06	32.94
Billwood/ I-96	8/15/2019	Delaminations	Shapefile (.shp)	Billwood_Delaminations_2021.shp	113	5.70	61.35
Laplaisance/ I-75 Exit	8/31/2021	Delaminations	Shapefile (.shp)	Laplaisance_Delaminations_2021.shp	52	2.95	31.75
		Spalls	Shapefile (.shp)	Laplaisance_Spalls_2021.shp	4	0.32	3.41
M-99/I-96	8/16/2019	Delaminations	Shapefile (.shp)	M99_Delaminations_2021.shp	42	10.70	115.17
		Spalls	Shapefile (.shp)	M99_Spalls_2021.shp	4	0.29	3.09
Uncle Henry	8/17/2021	Delaminations	Shapefile (.shp)	UncleHenry_Delaminations_2021.shp	20	4.50	48.44
		Spalls	Shapefile (.shp)	UncleHenry_Spalls_2021.shp	6	0.29	3.16

Imaging of Difficult to Reach Locations

In this Phase 3 project, we explored the utility of UAS for imaging bridges or bridge structures that are particularly difficult to access without closing a bridge or using specialized equipment such as reach-alls. We (remove third person in report) found that UAS can be a suitable alternative to expensive equipment for documenting potential problem areas, frequently without having the need to close a lane or the entire bridge (Figure 3.2.28). The reduced need for reach-alls is also likely to increase safety of bridge inspections.

Figure 3.2.28: Example situations highlighting the utility of drones in surveying locations that are otherwise difficult to assess. A drone pilot captures imagery of bridge beams under I-96 at Grand River (top-left), a caged drone system is able to get very close to difficult to see areas (top-right), imagery of bridge substructure at Beyer Rd (bottom-left and bottom-right).

3D Modeling of Bridges

Digital Twins are digital representations of physical assets. These digital twins are in the form of a 3D model that closely represents the asset both from a visual standpoint but also in location and dimension. These models can be created from images along with GPS and ground control information, as was demonstrated for this project. The images are post-processed on computers using specialized software programs, including Bentley's ContextCapture or Pix4D, that are able to build 3D models using the imagery and GPS information (Figure 3.2.29).

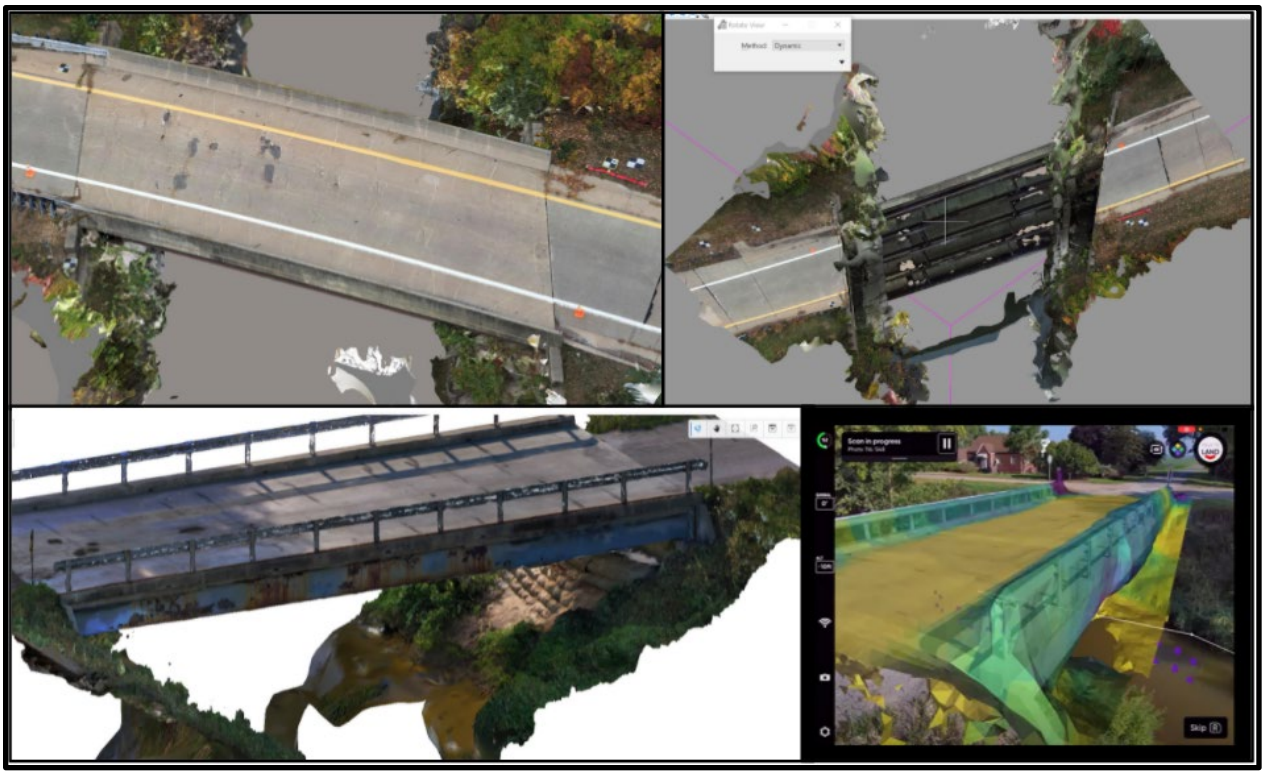

Figure 3.2.29: 3D model of LaPlaisance Creek Exit Ramp bridge deck (top-left) and underside (top-right) generated using UAS-collected imagery and built within Bentley ContextCapture. Beyer Rd bridge 3D model (bottom-left) and example Skydio 2 3D scan software collecting data for Beyer Rd bridge in an automated flight mode.

Data required for building 3D models can be collected in a few different ways. The first includes flying the UAS manually with the drone pilot triggering images as they fly. The second method includes the pilot preprogramming missions for the UAS to take images autonomously along pre-planned flight lines. The third method includes using the 3D scan application from Skydio where the Skydio 2 UAS explores the 3D space autonomously and determines the extents of the 3D object that needs to be modeled then calculates the flight lines and flying, completely autonomously, to collect the data (Figure 3.2.30). This last method is an example of utilizing artificial intelligence (AI) to perform work normally performed manually by the pilot. The Skydio 2 UAS has advanced on-board AI image-based capabilities to provide collision avoidance capabilities. Care should still be taken to ensure that the AI-enabled flight patterns are progressing properly, including setting a data collection floor if flying over water.

Figure 3.2.30: Skydio 3D Scan Screenshot during autonomous scan of the Beyer Road Bridge.

Once data is collected the images and any ground control information is input into the post processing software. The software processes the images into a 3D model that is dimensionally correct by finding common points and using trigonometry to create a 3D model (Figure 3.2.31).

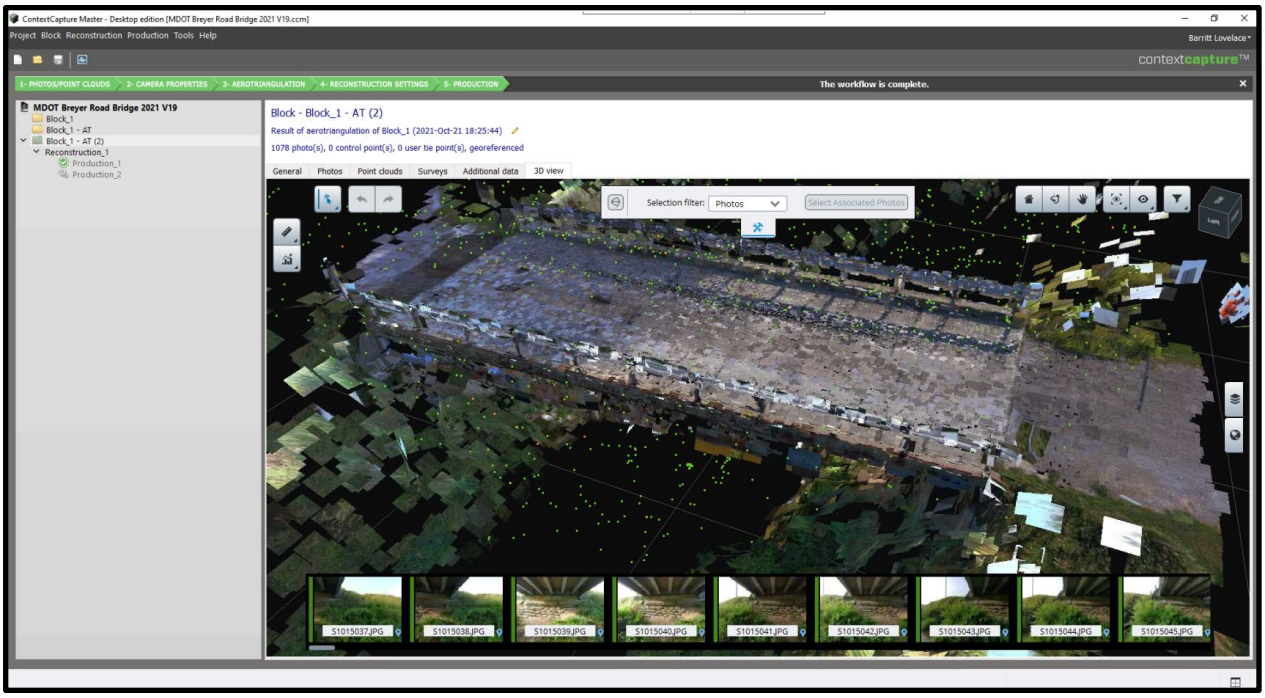

Figure 3.2.31: ContextCapture Postprocessing Software showing aero-triangulation of the Beyer Road Bridge.

The bridge models or digital twins can be viewed locally or uploaded to the cloud to share among team members (Figure 3.2.32). The models can also be opened directly in CAD applications if maintenance or repair drawings need to be generated.

Figure 3.2.32: Final Beyer Road Bridge Model.

Since the digital twins are created from images and the image GPS information, the original photos can easily be viewed through a photo navigation system giving the user the ability to view multiple images of any single point on the bridge (Figure 3.2.33).

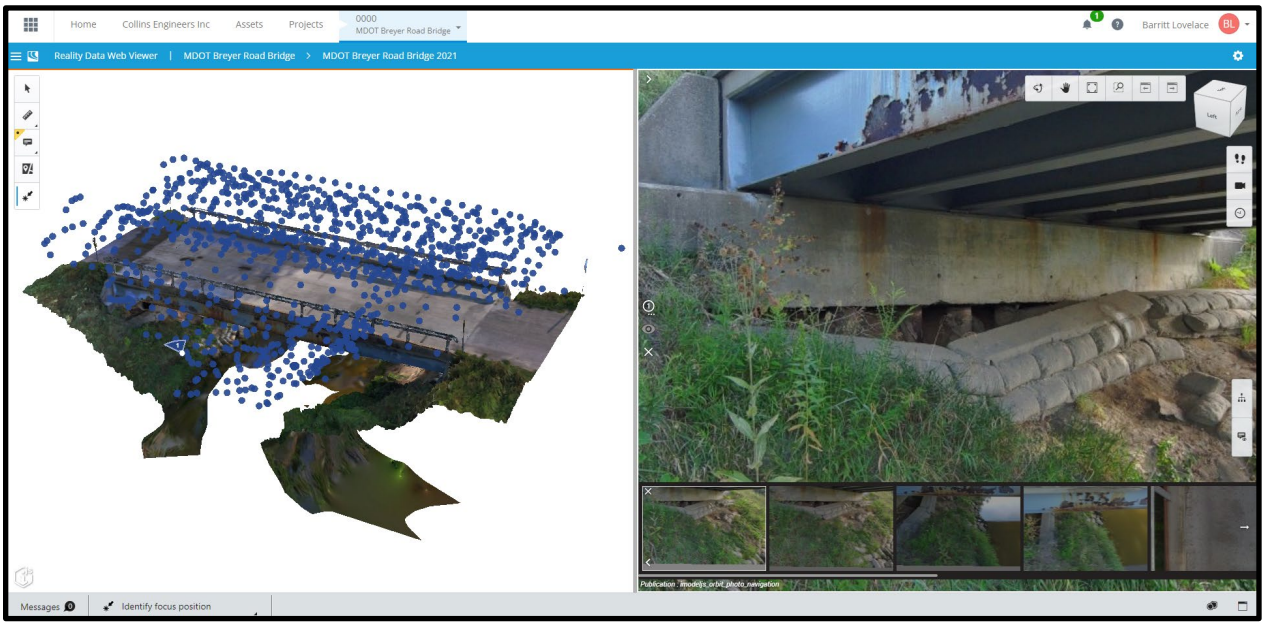

Figure 3.2.33: Cloud based model of the Beyer Road Bridge showing the photo navigation tool.

3.2.3 Discussion

Comparison of Uncle Henry Road Bridge delamination from 2016 and 2021 data showed detectable growth in delamination areas. This growth was observed in two different manners: (a) an outward growth in prominent delamination areas previously detected in 2016; (b) the formation of new delaminations identified in the 2021 data but not present in the 2016 data. The newer delamination areas identified in the 2021 data were smaller in size, and their potential for significant contribution towards bridge deterioration could be a subject of further monitoring. The Beyer Road Bridge also showed the presence of newer, smaller delamination polygons not originally detected in the 2016 data. However, due to extensive surface patching, some of the delamination areas identified in 2016 were repaired and showed no patterns of a delamination in the 2021 data.

The total area of delamination identified in both the Uncle Henry Road and Beyer Road bridges are significantly less than the area identified by the sounding method used by MDOT to identify delamination. However, there is significant spatial overlap between the TADDA-identified delaminations and the MDOT sounding polygons. The finer resolution of analysis of the TADDA algorithm relative to the MDOT sounding polygons may help better identify the extent of delaminations in bridge decks, potentially reducing the need to remove larger chunks of concrete material for smaller areas of bridge deterioration. The use of thermal data in identifying thermal

delaminations may be especially useful in surveying large or long bridge decks that might require a large amount of time (and traffic closures) to survey using the sounding method.

The M99 and Laplaisance Creek Exit Ramp bridges also showed significant areas of TADDA-detected delamination. A lack of MDOT sounding survey for these locations hampered the validation of the TADDA-generated delamination areas in both these bridges.

The hyperspectral data collection and analysis of the Houghton - Hancock bridge showcased the ability of hyperspectral images to accurately identify corrosion in bridges. Distinct spectral signatures were obtained for rusted and non-rusted areas and an unsupervised classification was able to classify rust and non-rust classes accurately.

3.3 Use Case/Milestone 3: Construction Inspection

The primary motivation of the Construction Inspection milestone is to illustrate a framework that uses UAV-based inspection to support a DOT project manager in monitoring project progress and quality during the construction phase. As a secondary outcome, our developed framework also allows for creating as-built Building Information Models (BIM) post construction. This milestone is explained in 3 stages of (1) data collection, (2) data analysis, and (3) results. To verify the methodology developed for this milestone, two major MDOT projects were visited in several efforts as case studies for the integration of UAS into construction inspection activities. These cases are summarized in the following, and will be elaborated in the next sections:

- Pave the Way: I-496 WB (8/7/2020 - removal , 9/2/2020 - paving, 9/11/2020 - paving) - Concrete removal and paving (mainline, ramp) inspection
- I-69 Lansing (6/22/2021) asphalt paving
- I-69 Charlotte asphalt paving (10/5/2021) and Revisit (11/24/2021)

3.3.1 Methodology

Three drone platforms were used for the construction inspection use case to monitor pavement removal, concrete paving, and asphalt paving. These platforms included the DJI Mavic 2 Pro and md4-1000 for the collection of optical imagery and the DJI Mavic 2 Enterprise Advanced for optical and thermal imagery. The md4-1000 is a quadcopter produced by the German company 'Microdrones' and was specifically purchased for Use Case 3. This drone comes with an integrated Sony RX1R II 42.4-megapixel camera for capturing RGB imagery. A DJI Mavic 2 Pro with a 20-megapixel camera was used to collect optical imagery for the generation of base maps and to monitor pavement removal and concrete paving.

For asphalt paving monitoring, a DJI Mavic 2 Enterprise Advanced (M2EA) was used as it has both optical and thermal cameras. The optical camera is a quad bayer 48-megapixel camera while the thermal camera has a 640x512 pixel sensor. The thermal sensor was important for asphalt paving as this enabled the team to map temperature variations in the asphalt as it is being

paved and monitor the cooling rates for any anomalies. Table 3.3.1 shows the drones and sensors flown for construction inspection as well as altitudes flown with orthoimage and DEM resolutions.

Table 3.3.1: Drone platforms and sensors used for surveys for the Construction Inspection use case.

Date	Purpose	Platform	Altitude (ft)	Sensor	Res - Ortho (cm)	Res - DEM (cm)
08/07/2020	Monitoring Pavement Removal	Mavic 2 Pro	200	20 MP	1.5	2.9
		md4-1000	300	42.2 MP	1.2	2.4
09/02/2020	Monitoring Concrete Paving	Mavic 2 Pro	200	20 MP	1.5	2.9
09/11/2020	Monitoring Concrete Paving	Mavic 2 Pro	400	20 MP	2.8	11.3
		Mavic 2 Pro	200	20 MP	1.5	2.9
		md4-1000	300	42.2 MP	1.2	2.4
11/05/2021	Monitoring Asphalt Paving	Mavic 2 Pro	200	20 MP	1.5	2.9
		M2EA - Optical	100	48 MP	0.8	3.2
		M2EA - Thermal	100	0.3 MP	4.2	NA
11/24/2021	Monitoring Asphalt Paving	Mavic 2 Pro	200	20 MP	1.5	2.9
		M2EA - Optical	100	48 MP	0.8	3.2
		M2EA - Thermal	100	0.3 MP	4.2	NA

The drones are used to collect imagery and construction data by flying over the target locations of the project site. Multiple flights were performed during each site visit to monitor the progress over time. The UAS-collected images are processed through Structure from Motion (SfM) photogrammetric software packages such as Agisoft Metashape to create Digital Elevation Models (DEMs), Hillshade imagery, GeoTIFFs, and R-JPG formats of data. Figure 3.3.1 is an example of data collected from MDOT I-496 (A, B, C) and I-69 (D) in formats of DEM, Hillshade, GeoTIFF, and R-JPG Thermal Image (consecutively).

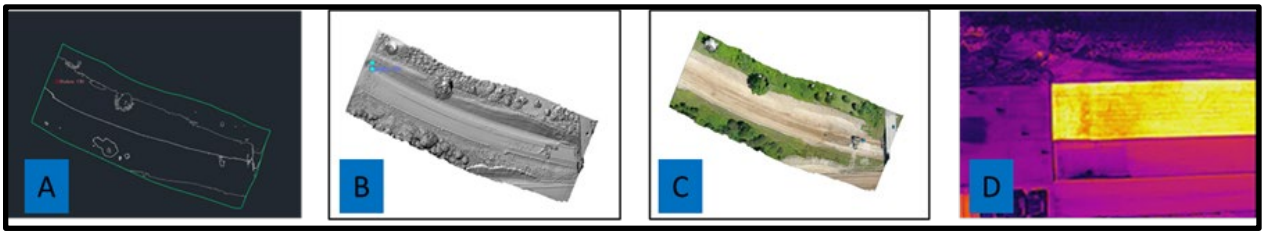

Figure 3.3.1: Examples of different data types collected as part of the Construction Inspection Use Case/Milestone (A: DEM, B:Hillshade. C: Geo-TIFF, and D: RJPG).

3.3.2 Findings

The collected data items are used as input for image processing processes to produce geometry and thermal parameters. To better describe the data analysis process, it is divided into progress monitoring and thermal profiling.

Progress Monitoring

The main question we seek to answer in this section is: what are the features that need to be extracted from the UAV data to estimate work progress quantities? To answer this question, consider Figure 3.3.2. The quantity of concrete pavement (in cubic yards) laid by a construction crew can be estimated by having the length, width, and thickness parameters of the pavement placed. These parameters can be extracted from UAV collected images using Image Processing tools and algorithms.

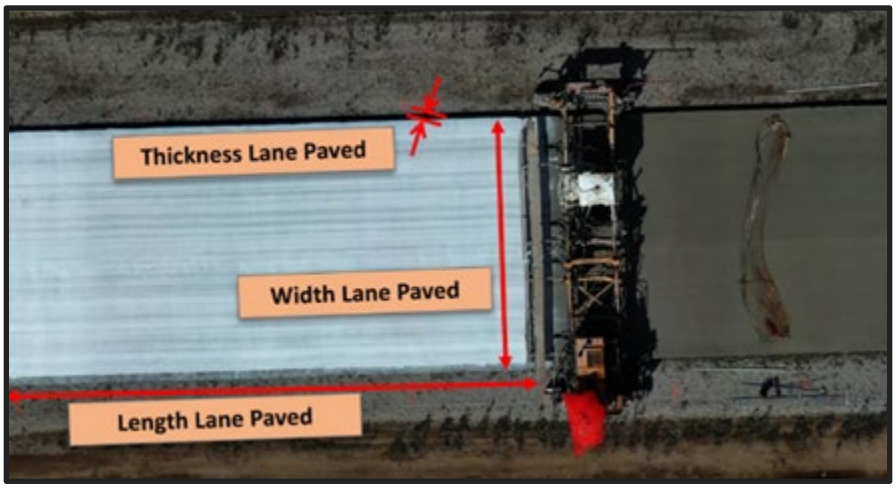

Figure 3.3.2: UAV geometry factors for concrete pavement activity inspection or survey (Samsami et al., 2021).

Image Processing is a computer vision tool that assists in analyzing an image based on its color, texture, or other property of interest. To make these tools easily understandable, consider Figure 3.3.3. In this picture, a concrete removal activity underway by MDOT on a section of I-496 is captured at two different times by a UAV. As shown in Figure 3.3.3, the color differences of the dirt at the (former) road surface can assist in differentiating between a recently removed pavement ("Just Removed") and a pavement that has not been removed yet ("Not Touched"). A recently removed pavement appears darker in color than an untouched stretch of pavement in the imagery due to the nature of the operation. A well-developed programming code can use existing Image Processing techniques to identify the recently removed pavement, allowing an inspector to understand the ongoing "Pavement Removal" on the jobsite.

Figure 3.3.3: Image processing example one – MDOT I-496 Project (Samsami et al., 2021). Example image parameters used to identify disturbed vs. undisturbed areas during pavement removal.

In Figure 3.3.4, the two captured and time-stamped images shown in Figure 3.3.3 are merged together. This visualization is done by using the "mapshow" code in MATLAB, where the geo-reference information of the images are extracted to place the images in the correct location on map and ultimately merge them together. Using the color differences on the merged image, it is possible to locate where the pavement removal activity has started and where it has ended for the time interval of the imagery collection. This area is automatically detected and shown by a polyline visible on Figure 3.3.4. This process is automated using an Image Processing tool available and programmed within MATLAB.

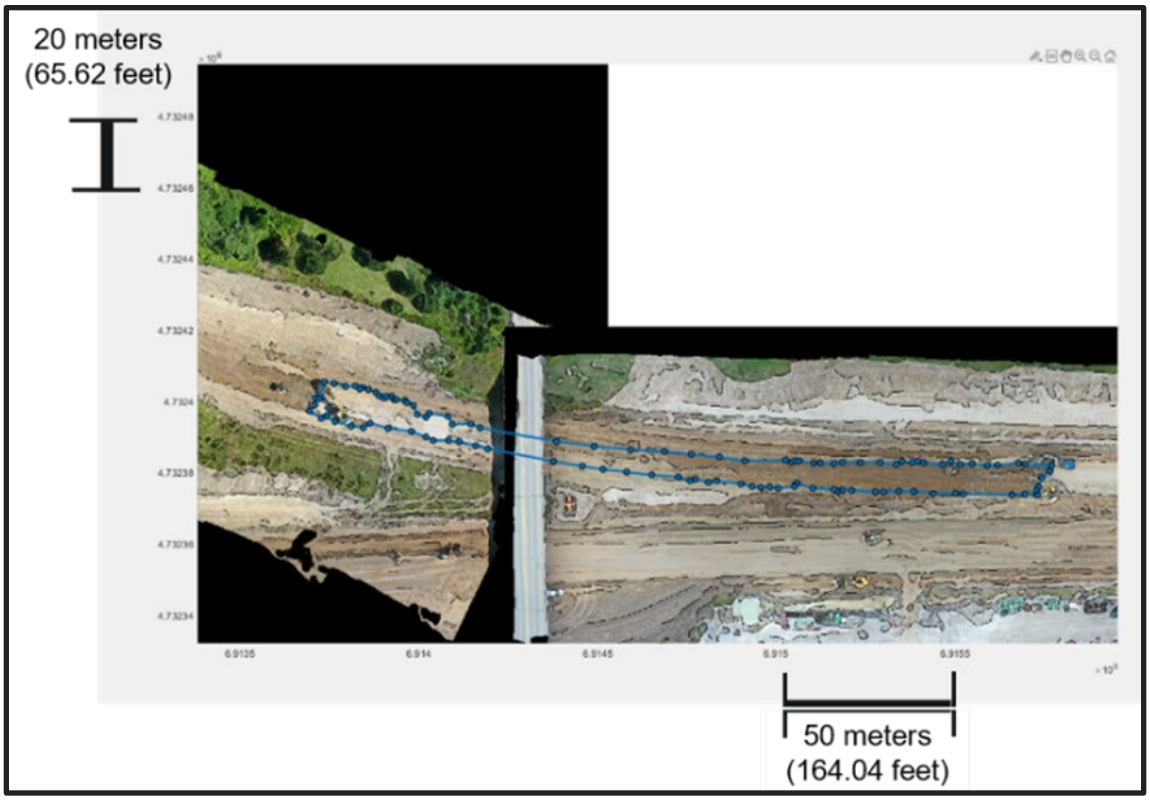

Figure 3.3.4: Image processing example two – MDOT I-496 Project (Samsami et al., 2021). Result of automated processing identifying where pavement removal activity has started and ended.

Another computer vision tool that can be used to assist in automating the image analysis process is Image Labeling. Image labeling is used to recognize and locate distinct target objects in an image. For example, consider Figure 3.3.5. There are several pieces of pavement equipment shown in this image. Two pieces of ~~these~~ equipment are shown in red and green rectangles on this image. A computer algorithm can be taught to recognize ~~these~~ equipment and then assign a label to it. By tracking the target equipment from image to image, it is possible to monitor the progress of an ongoing construction operation. For example, by using an algorithm to locate equipment '1' in Figure 3.3.5 in multiple time-stamped images, it is possible to determine the start and end points of the pavement placing activity over the time interval surveyed by the drone.

Figure 3.3.5: Image labeling example – MDOT I-496 Project (Samsami et al., 2021). Equipment can be identified in drone imagery/orthoimages using automated image processing packages available in MATLAB.

After images are collected, computer vision tools described here are used to analyze the images. An expected outcome is a set of geometric parameters such as length and area that can be used to assist in estimating the quantity of work performed over a time interval. For example, consider Figure 3.3.6 which captures an example concrete paving crew. By knowing the Length/Width/Thickness of the pavement placed, the quantity of work can be estimated (by multiplying Lane*Width*Thickness). This same equation can be applied to any similar construction activity, such as HMA Pavement laying, Concrete Pavement Removal, etc.

Figure 3.3.6: Example highway corridor geometric parameters (Photo from: https://www.bridgemi.com Photo Courtesy: MDOT).

Having extracted geometry parameters from UAV images, they can then be mapped to BIM parameters for creating a 3D Model of the project. Figure 3.3.7 is an example of a highway corridor and its related parameters. As illustrated, the corridor is divided into a westbound and eastbound surface and divided by a median. Each direction consists of two lanes, a median, and a shoulder. Different parameters such as Width and Slope are needed to model this cross section.

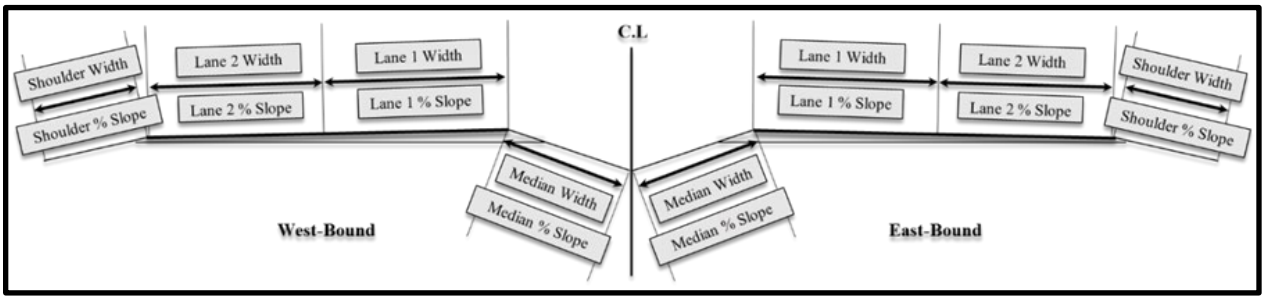

Figure 3.3.7: Example highway corridor section view and modeling parameters (Samsami et al., 2021).

The BIM parameters can be mapped to UAV geometric parameters, and extracted from images collected, using computer vision tools. To demonstrate an example, the feature extraction code is used on MDOT I-496 and MDOT I-69 project data, and all the necessary parameters are extracted from these data. Tables 3.3.2 and 3.3.3 summarize these parameters for these two case studies. As shown, the cross section captures the daylighting, shoulder, and mainline BIM parameters. It must be noted that the subsurface parameters are extracted manually from project documents and reports provided by the SME.

Table 3.3.2: BIM parameters extracted from UAV images of MDOT I-496 Project.

BIM PARAMETERS (MDOT I-496)	Surface	South-Bound	Lane 1	Width	4.26 m
				Length	482 m
				% Slope	2%
			Lane 2	Width	3.69 m
				Length	482 m
				% Slope	2%
			Shoulder 1	Width	2.67 m
				Length	482 m
				% Slope	4%
			Shoulder 2	Width	3.05 m
				Length	482 m
				% Slope	4%
			Daylight 1	Width	0.85 m
				Length	482 m
				% Slope	1:04
			Daylight 2	Width	1.41 m
				Length	482 m
				% Slope	1:04
	Subsurface	South-Bound	Lane 1	Pavement Thickness	0.25 m
				Base Thickness	0.15 m
				Subbase Thickness	0.25 m
			Lane 2	Pavement Thickness	0.25 m
				Base Thickness	0.15 m
				Subbase Thickness	0.25 m
			Shoulder	Pavement Thickness	0.25 m
				Base Thickness	0.15 m
				Subbase Thickness	0.25 m

Table 3.3.3: BIM parameters extracted from UAV images of MDOT I-69 Project.

BIM PARAMETERS (MDOT I-69)	Surface	South-Bound	Lane 1	Width	3.76 m
				Length	1557 m
				% Slope	2%
			Lane 2	Width	3.55 m
				Length	1557 m
				% Slope	2%
			Shoulder 1	Width	3.16 m
				Length	1557 m
				% Slope	4%
			Shoulder 2	Width	1.42 m
				Length	1557 m
				% Slope	4%
			Daylight 1	Width	0.85 m
				Length	1557 m
				% Slope	1:04
			Daylight 2	Width	1.41 m
				Length	1557 m
				% Slope	1:04
	Subsurface	South-Bound	Lane 1	Pavement Thickness	0.08 m
				Base Thickness	0.15 m
				Subbase Thickness	0.46 m
			Lane 2	Pavement Thickness	0.08 m
				Base Thickness	0.15 m
				Subbase Thickness	0.46 m
			Shoulder	Pavement Thickness	0.08 m
				Base Thickness	0.15 m
				Subbase Thickness	0.46 m

The next step is to create a visual representation of the project. It is done by taking the BIM parameters and creating as-built models of the project. In this project, Civil 3D is selected

as the main BIM platform. The following steps are taken to create as-builts of the two case study projects:

- A DEM surface is defined using the UAS DEM file created for the project.
- An alignment is defined using the UAS Hillshade file created for the project.
- A profile is defined on the defined DEM surface, and along the created alignment, to illustrate the changes in grade.
- An assembly is created using the BIM parameters, discussed in the previous sections. It shows the cross section of road, and different components of mainlines, shoulders, etc.
- The last step is to create a corridor, using these assembly parameters, and along the alignment.

The final BIMs are attached to this report in two formats of Civil3D and Bentley Microstation files. These files are visualized in Figures 3.3.8 - 3.3.11.

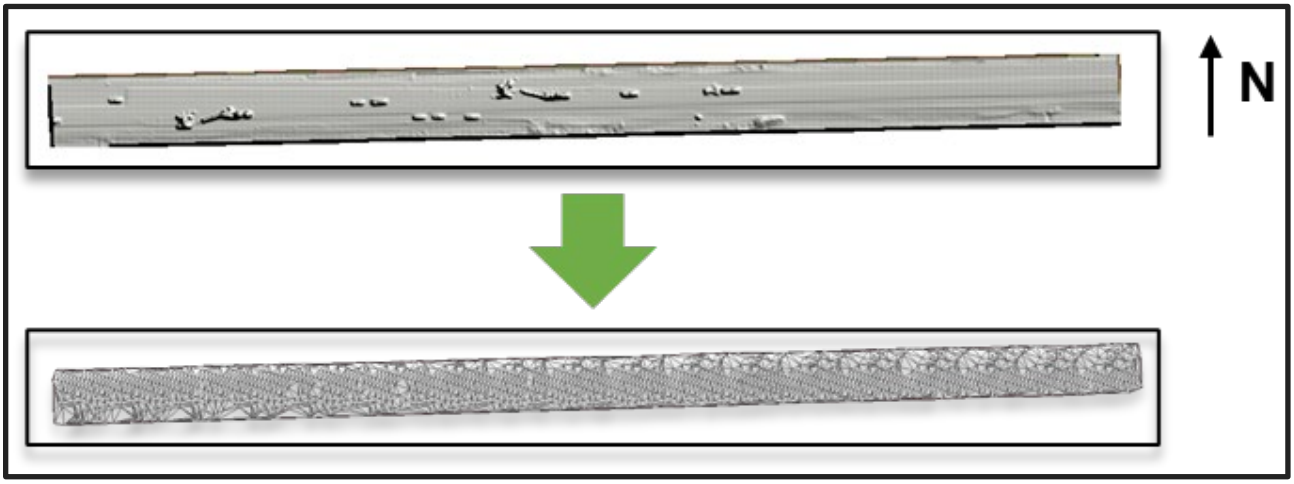

Figure 3.3.8: DEM derived from UAS imagery (top) and Civil 3D surface (bottom) for an example stretch of I-496.

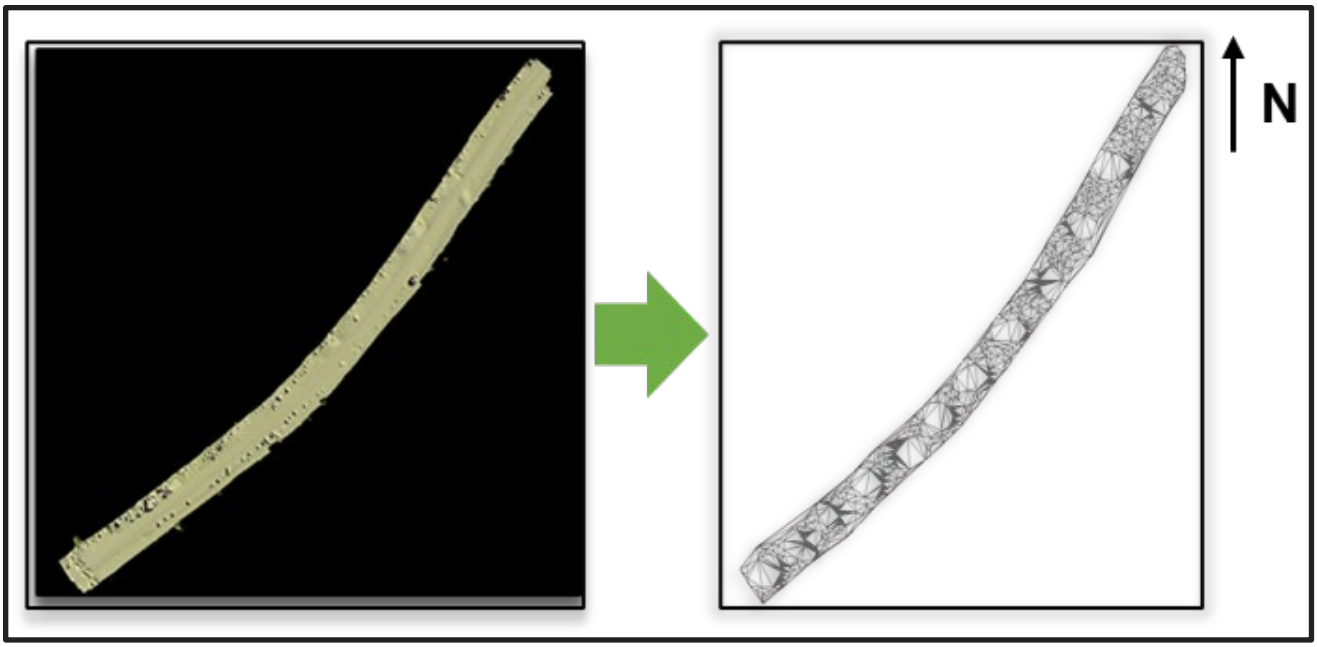

Figure 3.3.9: DEM derived from UAS imagery (left) and Civil 3D surface (right) for an example stretch of I-496.

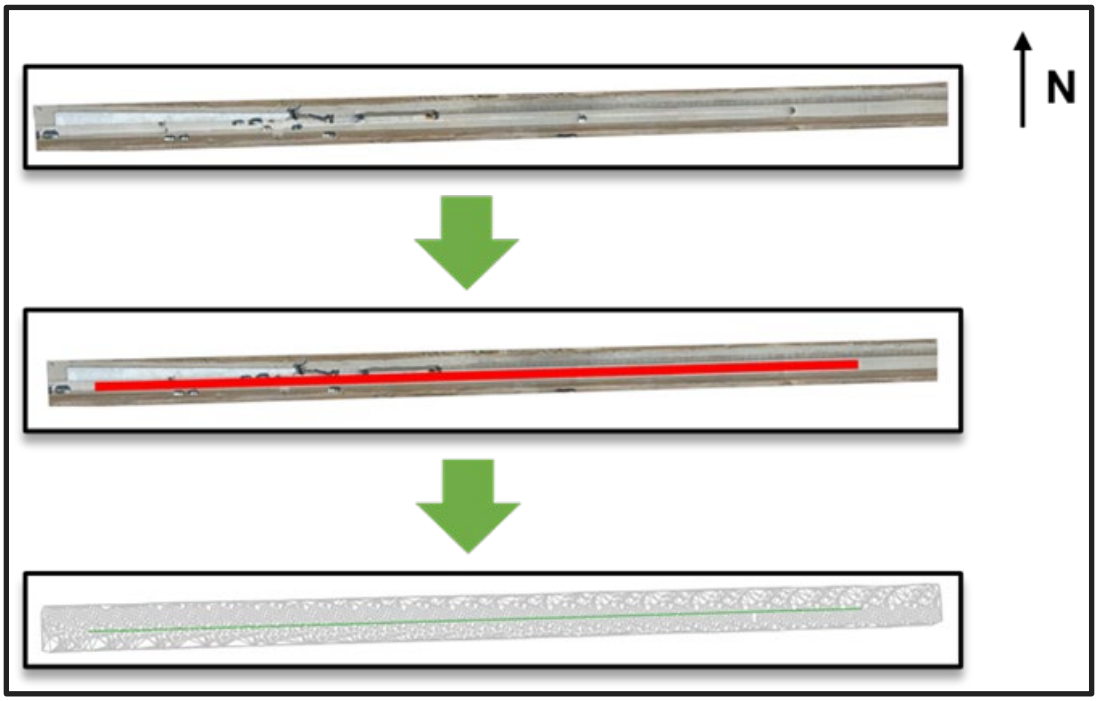

Figure 3.3.10: UAS-derived hillshade (top), example polyline transect extracted from the hillshade (middle), and polyline overlain on Civil 3D layer (bottom) for an example stretch of I-496.

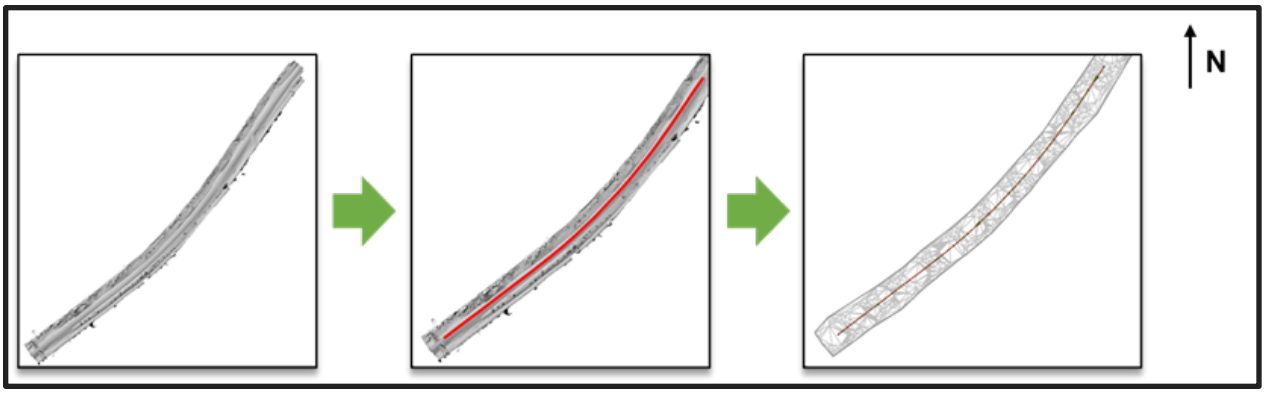

Figure 3.3.11: UAS-derived hillshade (left), example polyline transect extracted from the hillshade (middle), and polyline overlain on Civil 3D layer (right) for an example stretch of I-496.

Another step after extracting the UAV parameters is to estimate the progress metrics. Planned and actual production rates can be calculated using Equations 1 and 2. By comparing these two rates, a project manager can tell whether the monitored activity is on track with anticipated rates or not. These two rates are calculated for MDOT I-496 project and the results are summarized in the results section.

Equation 1: Actual Production Rate

Actual Production Rate = (Quantity of work observed by UAS)/(Duration of observation)

Equation 2: Planned Production Rate

Planned Production Rate = (Quantity of work per project plans)/(Duration of observation)

An example of production rate calculation for Pavement Removal activity data, at T1 = 11:34 and T2 = 15:42, is shown below in Table 3.3.4.

Table 3.3.4: Geometric parameters for pavement removal for I-496.

Reference Section	Activity	Unit	Parameter	Measure	Unit	Parameter	Measure	Unit
259	Pavement Removal	SY (square yards)	Length	690.51	Ft	Width	22.80	Ft

Estimated Production Rate = (Quantity of Work Observed by UAV)/(Duration of Observation)
= (690.51ft*22.80ft)/(4.133 hr) (change font to reflect that of report)
= 428.42 (SY/Hr)

Thermal Profiling

Temperature segregation in HMA pavement can cause several performance issues. Some of the main problems caused by temperature include pavement segregation, reduced fatigue life, reduced stiffness, reduced tensile strength, and increased permeability. Temperature segregation is defined as "non-uniform temperature distribution across the mat of uncompacted asphalt mixtures during paving operation" (Mohammad et al. 2019).

Considering the negative effect of temperature segregation in an HMA pavement operation, thermal images were collected and analyzed using UAV during multiple paving projects. Thermal imaging by drone is based on IR Imaging, where sensors mounted on the UAV captured the differences in road surface temperature.

Figure 3.3.12 provides examples of thermal and visual images collected from MDOT I-69 HMA pavement project. As it is clear on the thermal image, the recently paved surface has much higher temperature relative to the existing old road due to the temperature of the warm asphalt and its albedo.

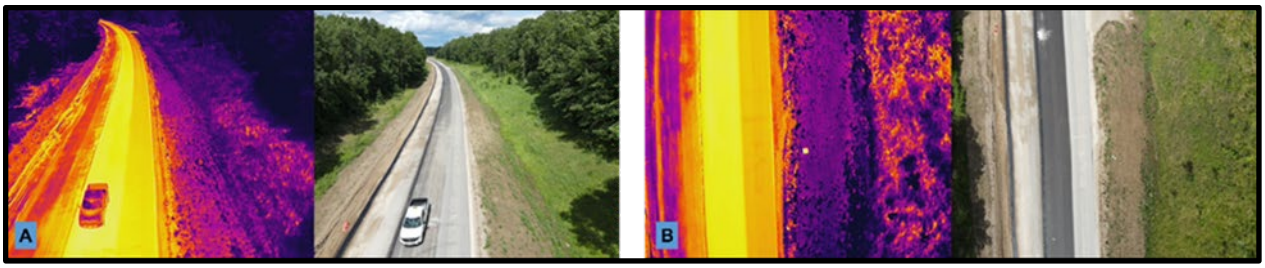

Figure 3.3.12: Thermal and RGB Images collected during MDOT I-69 HMA pavement project.

A critical step in finding temperature anomalies in the asphalt using the UAV data is to find the relationship between a pixel intensity and that pixel's temperature. In other words, the DJI Thermal Analysis app is used to analyze each image, and provide the thermal range within the image (Tmin and Tmax). This tool is currently unable to provide the relationship between image intensity (I) and image temperature (T) such that one can extract a point ~~point's~~ temperature by knowing its location (XYZ) on the image. To solve this problem, an image processing code was developed to estimate each pixel's temperature (T) using two parameters of Tmin (the minimum temperature observed) and m (the scaling factor for the image). Tmin is found for each image by using the DJI App, while m can be calculated using the information given in Equation 3.

Equation 3: Temperature Value of Pixel with Intensity I

$$T = I/m + T_{min} \quad \text{Where } m = (255-0)/(355-0)$$

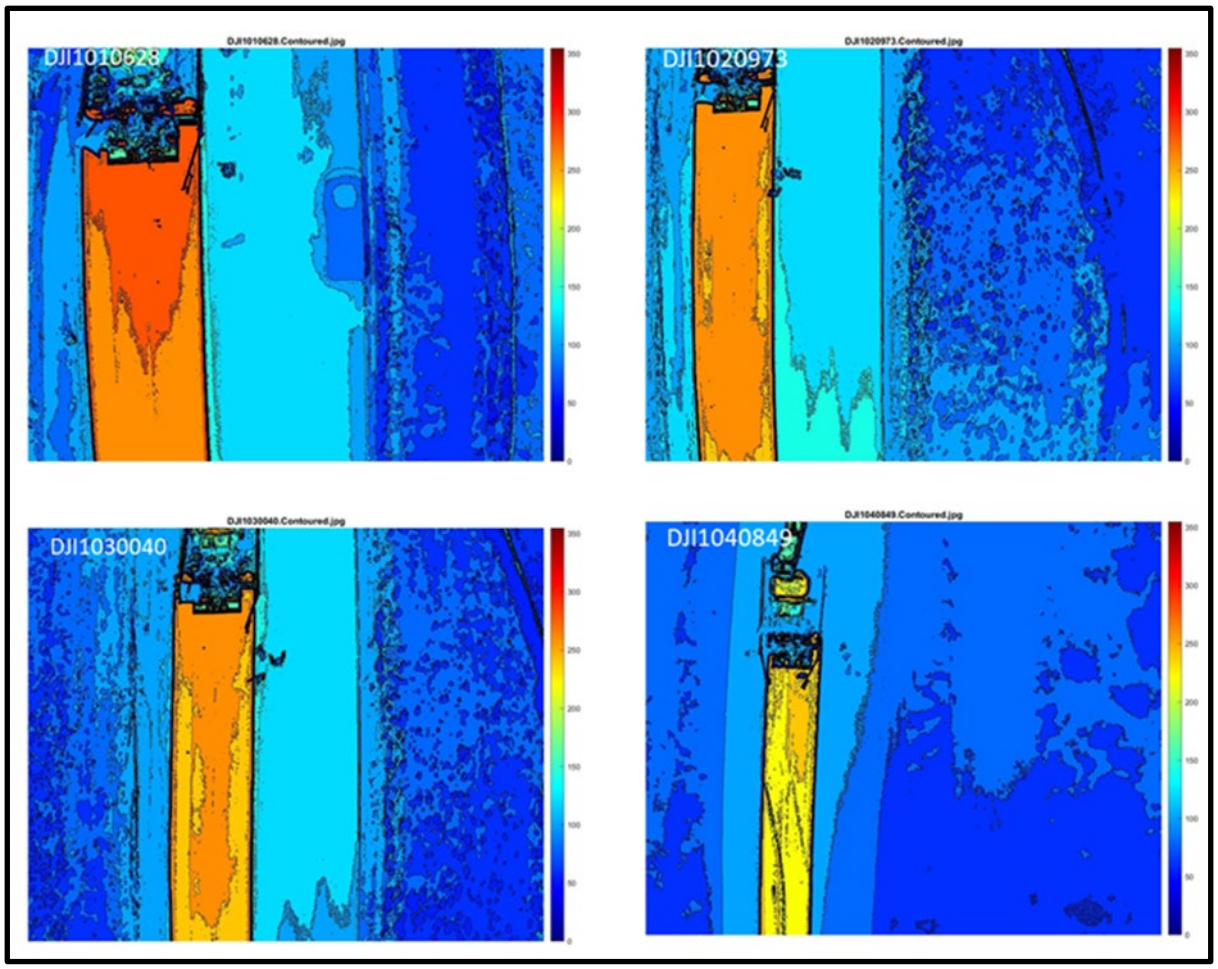

Figure 3.3.13: Sample processed thermal images of I-69 asphalt paving.

Figure 3.3.13 is an example of four thermal images from the same drone flight capturing the surface asphalt mat temperature behind the paver. As shown in the image, areas with red and orange colors have higher temperatures than those of yellow, green, or blue colors. The area surrounding the freshly paved asphalt is much cooler and is therefore shown in blue. As it can be seen on these images, the temperature along the MAT is not completely uniform, with cooler areas, which may be indicators of potential segregation.

Although the visual information given in Figure 3.3.13 can be helpful in understanding the temperature differentials behind the paver, some quantitative parameters must be also defined to provide numeric results. After studying the existing literature and DOT manuals, three parameters are defined to reflect the quality control metrics on HMA pavement.

The first parameter is designed based on the recommended temperature window for HMA pavement. The existing guidelines recommend a range of (185ºF 293ºF) as the most desirable temperatures for freshly laid HMA pavement. Any area with a T value outside this range is defined as a "Cool Area". Equation 4 can be used to find the ratio of 'cool' areas to acceptable areas in an image. It must be noted that the surrounding areas including the old pavement must be extracted from images to make this parameter meaningful.

Potential segregation is studied in the existing guidelines. It is defined as temperature differentials in the range of (19ºF 36ºF). Potentially segregated areas can be also identified on a given image, and quantified using Equation 5.

Any temperature differential greater than 36ºF results in high segregation. This is taken into account in Equation 6, and a ratio is defined for highly segregated areas. These three parameters are estimated for the MDOT I-69 project and summarized in the results section.

Equation 4: Ratio of Cool Areas

Rc =1-(Number of Pixels with Temperatures within (185ºF 293ºF))/(Total Number of HMA Mat Pixels)

Equation 5: Ratio of Potentially Segregated Areas

Rps =(Number of Pixels with Temperatures Differentials within (19ºF 36ºF))/(Total Number of HMA Mat Pixels)

Equation 6: Ratio of Highly Segregated Areas

Rhs =(Number of Pixels with Temperatures Differentials greater than 36ºF)/(Total Number of HMA Mat Pixels)

In addition to the above method used to analyze the temperature of individual images, MTRI and MTU investigated the use of a third-party tool called "ThermoConverter", released in late 2021 by AethaGlobal. This tool was made with the expressed purpose of converting DJI thermal RGB images into more usable thermal data formats like R-JPEG or GeoTIFF. The use of this tool, and products one can produce using this tool, is described in greater detail in Appendix 6.7.

3.3.3 Results

This section is built on the two previous sections, where data collection and analysis is explained.

Progress Monitoring

As-planned production rates for the three activities of (1) Pavement Removal, (2) Mainline Concrete Pavement, and (3) Shoulder Concrete Pavement, are calculated using the project documents and plans. As-built production rates are also reported by the contractor and provided by the SME for two of these activities. UAV-based estimates are also summarized for all three activities. All of this information is summarized in Table 3.3.5.

Table 3.3.5: Production rate comparison for I-496.

No	Activity description	As-Planned Production Rate (SY/hr)	As-Built Production Rate (SY/hr) (Why is data missing in box below?)	Estimated Production Rate (SY/hr)
259	Pavement Removal	321.85		428.42
339	Mainline Concrete Pavement	712.55	592.73	804.68
340	Shoulders Concrete Pavement	230.16	336.84	430

By comparing the three quantities of as-planned vs. as-built vs. estimated production rates, it is clear that the estimates are in the same range, but different from the as-planned. This can be caused by several sampling reasons, such as:

- Data collected on peak hours, where the production rates are higher than average rates
- Nonuniform production rates
- Paving ramps ~~is~~ are different from paving the mainline; more detailed as-planned data must be available to categorize these activities.

Thermal Profiling

A sample of eight images are selected to study behind the paver mat temperatures. The DJI APP and MATLAB-based Image Processing are used to estimate the three parameters of Rc, Rps, and Rhs in these eight images. The results show that the ratio of cool areas (Rc) is in the range of (0.2%, 5.3%) for these samples., which indicates that at least 94.7% of the mat area had acceptable temperatures, and the cool areas were minimized. The ratio of potentially segregated

and highly segregated areas are also negligible, accounting for a maximum 1.8% and 2% of the mat area, respectively. These parameters are summarized in Table 3.3.6.

Table 3.3.6: Thermal parameters estimated for MDOT I-69 project.

Image	%Rc	$\%R_{ps}$	$\%R_{hs}$
DJI1010628	5.3	0.4	0.8
DJI1020973	1.7	0.4	0.8
DJI1030040	0.2	0.2	0.5
DJI1040849	1.4	1.8	2
DJI1050081	1.1	1.5	1.3
DJI1060783	0.7	1.2	1
DJI1070237	0.4	0.7	1.1
DJI1070435	0.7	0.4	1.6

3.3.4 Discussion

To verify this project's results with the manual data collected by MDOT inspector, thermal data is extracted from Inspector's Daily Report (IDR) provided by MDOT SME for the MDOT I-496 project. According to this report "Behind paver mix temperature average between 277-F to 310-F"for the MTRI's data collection day on "10/5/2021". This verifies that the methodology taken in this section conforms to the data provided by MDOT. The ratio of cool and segregated areas are negligible, and the mat is paved within the acceptable temperature range.

Our results imply that implementation of the UAV thermal imaging framework proposed by this project can improve HMA pavement construction QA/QC inspections, by automating the process. Figure 3.3.14 is the workflow diagram designed for this milestone. It integrates different types of data collected from different construction activities, with information products created from them. These products impact different phases of the project, and contribute to different stakeholders, including DOT project managers, contractors, Inspectors, etc. A set of metrics are deducted from these products to assist the decision-making process.

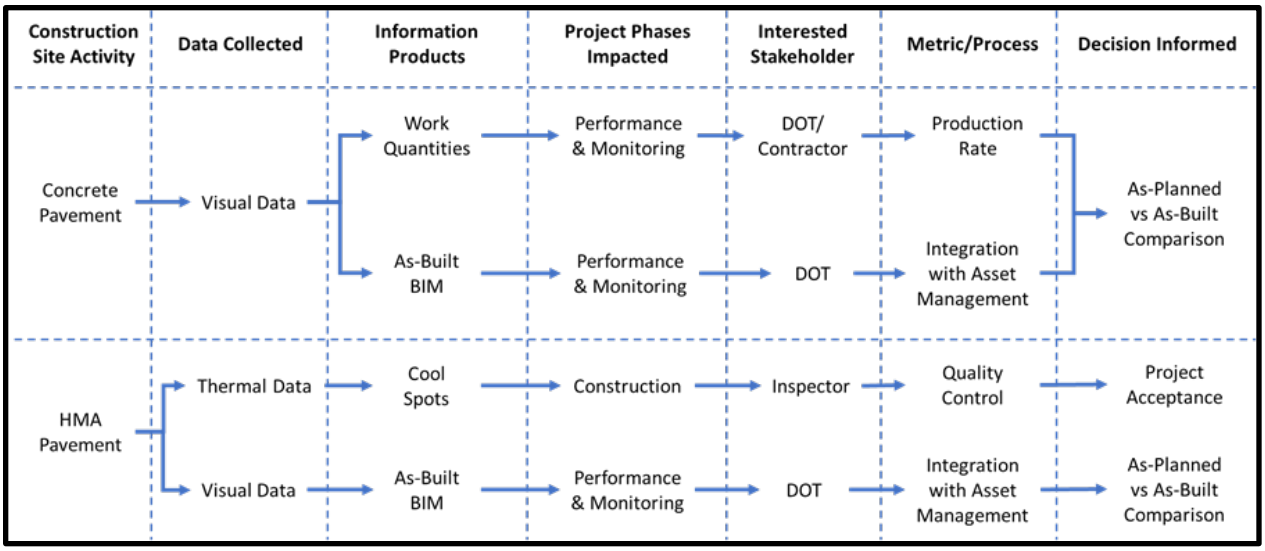

Figure 3.3.14: UAV-based inspection workflow for Construction Inspection related tasks.

3.3.5 Related Training

The highest-resolution system used for documenting construction inspection was the mdMapper md4-1000+, bought for this project to provide close-range photogrammetry capabilities with its Sony RX1R II 42.4 mp camera and up to 40 minutes of flight time. The purchase price included training for two people, which mdMapper expanded to four people so that both MDOT and Michigan Tech staff could learn how to use the system.

Joint training on use of md4-1000+ by an mdMapper employee was held with MDOT and Michigan Tech staff on June 16 to 18, 2020 (Figure 3.3.15). Four Part 107 certified UAS pilots took part in the training (two MDOT employees and two MTRI employees):

- Michael Soper (MDOT)
- Frank Boston (MDOT)
- Colin Brooks (Michigan Tech)
- Richard Dobson (Michigan Tech)

This was a multi-day course to help attendees gain familiarity with operating the large UAS for efficient data collections with safety procedures. Attendees were required to complete a flight test to prove proficiency before completing the course, and all passed.

The md4-1000+ system was demonstrated in 2020 for monitoring concrete removal as part of the construction inspection use case. It will be handed over to MDOT in spring 2022 as part of project completion tasks.

Figure 3.3.15: Example images from md4-1000+ training session held in June, 2020 for MDOT and Michigan Tech participants, including the UAS (top left), Michael Soper receiving training from the mdMapper trainer (top right), and a sample image taken during the training held at the MTRI office.

3.4 Use Case/Milestone 4: Lidar UAS for Design Survey

3.4.1 Methodology

Data Collection at Standish / US-23 Junction

In November of 2019, a UAV-based LiDAR survey was performed in Standish, MI, in an effort to compare drone-based LiDAR to existing Mobile LiDAR (MLS) data (Figure 3.4.1). Also, drone-based LiDAR point cloud accuracy was compared to traditional survey data to

determine the utility and accuracy of drone-based LiDAR for Design Survey relative to existing methods. The drones flown for this survey included the DJI Matrice 600 with the RIEGL MINIVUX-DL LiDAR sensor as well as the DJI Mavic 2 Pro for orthoimage creation (Figure 3.4.2).

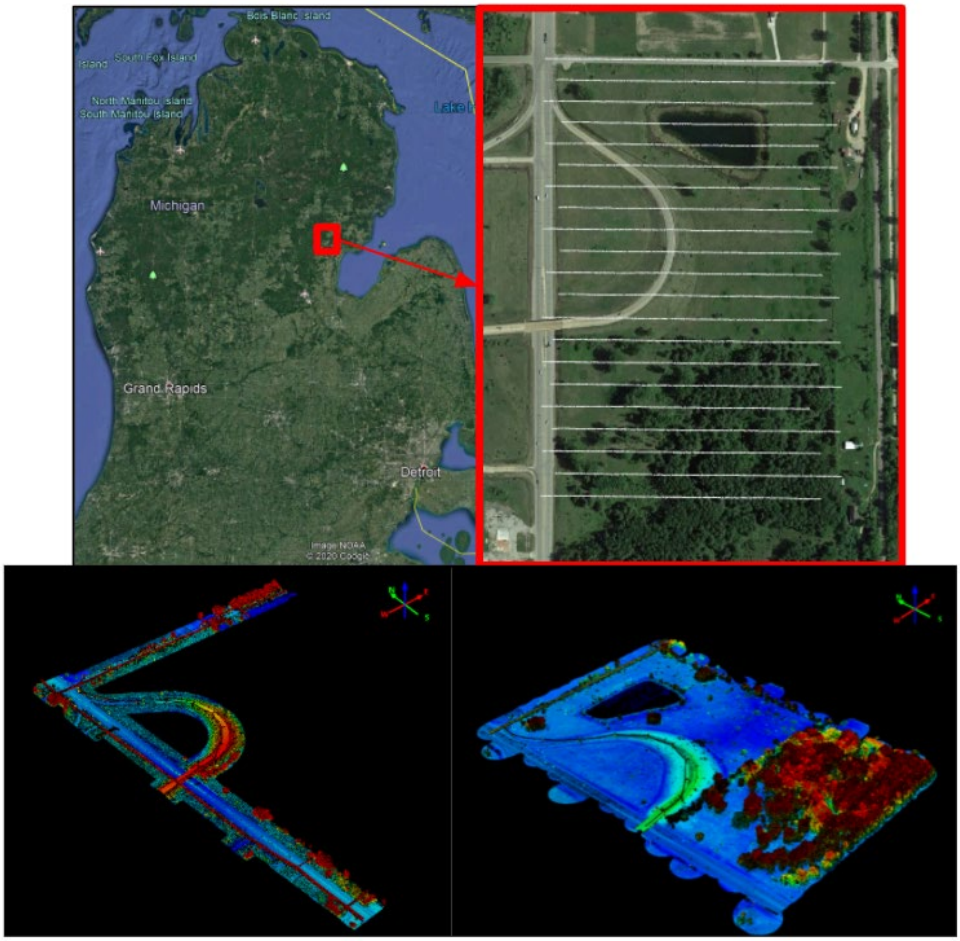

Figure 3.4.1: MLS and UAS-based LiDAR data acquisitions performed in Standish, MI, at US-23 junction. Top-right image shows the data collection area and UAS flightlines used to collect the UAS-based LiDAR data. Bottom-left image shows the collected MLS data, while the bottom-right shows the collected UAS data.

The MLS data were collected using a RIEGL VMX-1HA LiDAR sensor. Surveying Solutions, Inc. (SSI) collected the drone-based Lidar data in November of 2019 as well as the MLS data in summer of 2019. MTRI collected the imagery necessary to create an orthoimage of the surveyed area in November of 2019 on the same day of the drone-based LiDAR flight. Traditional survey data for soft surfaces were collected in the spring of 2019 by SSI.

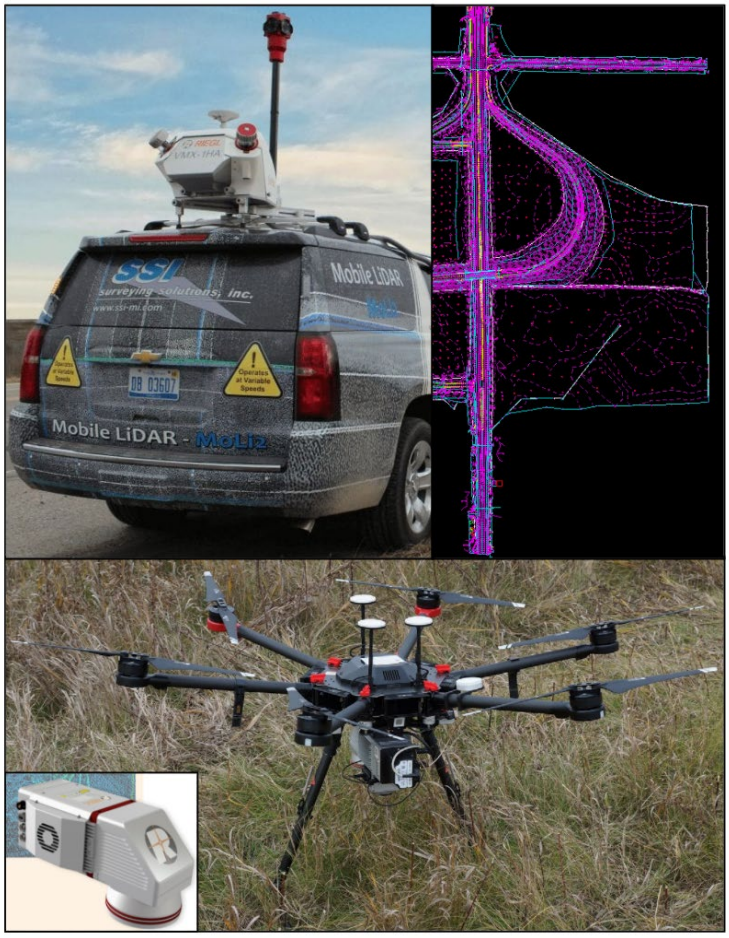

Figure 3.4.2: SSI's MLS and UAS- based LiDAR systems (top left, bottom-right), and example DGN file containing traditional survey data for soft surfaces.

Data collection at Rives Junction / US-127

On September 16th of 2020, a UAV-based LiDAR survey was performed at three sites along a stretch of US-127 near Rives Junction, MI. Because this survey was performed in September, leaves were still present on trees within the surveyed area. LiDAR data collection was performed by SSI using the DJI Matrice 600 platform and RIEGL miniVUX sensor. Orthoimages were produced for the three sites using DJI Mavic 2 Pro imagery collected by MTRI (Figure 3.4.3).

MTRI created several test ground control targets from ½ inch thick plywood to compare visibility to common photogrammetry-type cloth ground control targets. The home-made targets had two orientations, including a 3x3 sqft square field and a 4x1 sqft chevron. These test targets were covered with beaded glass tape and/or matte black spray paint to provide enhanced contrast to improve ground control target center identification in the LiDAR-derived point cloud.

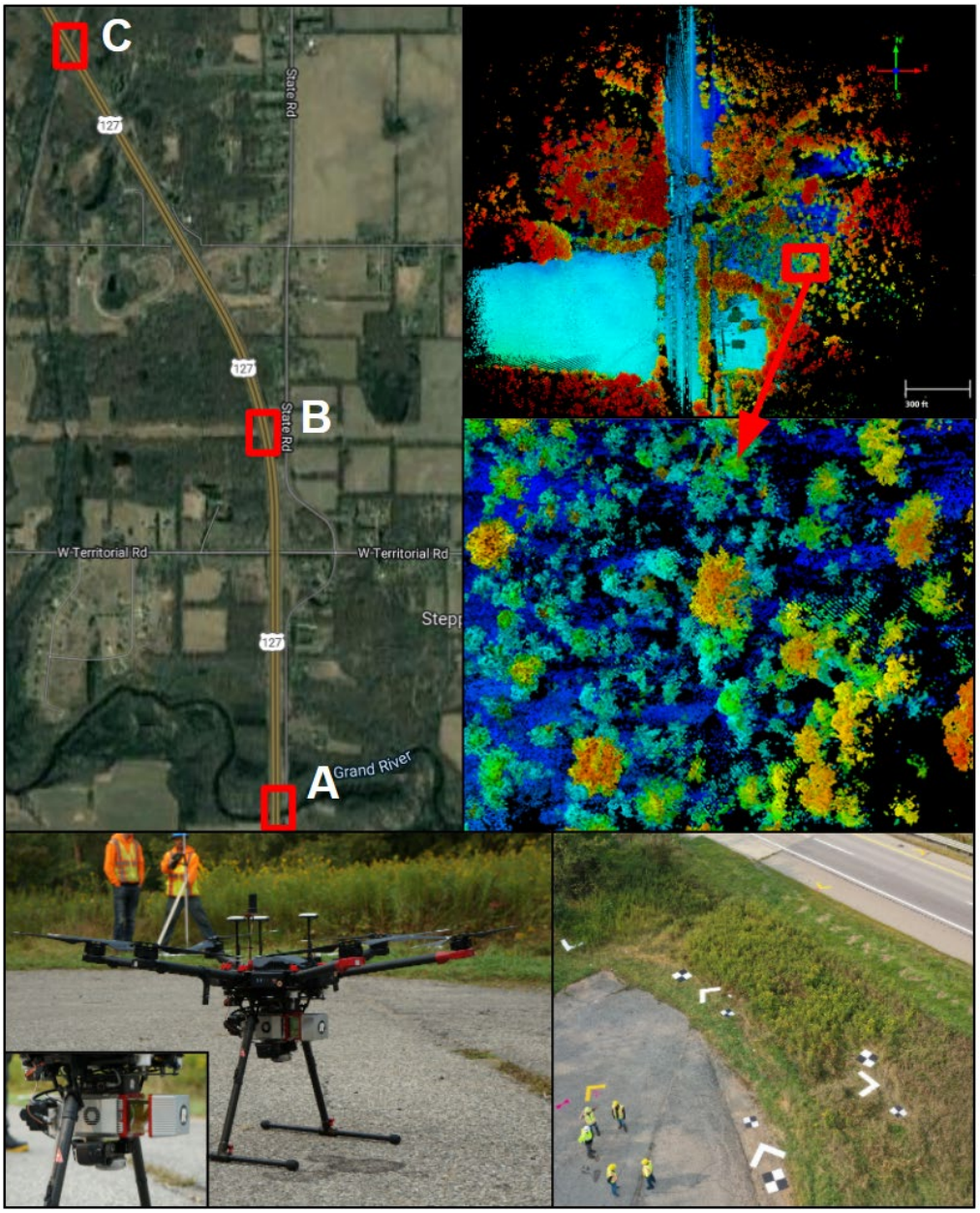

Figure 3.4.3: Three UAS-based LiDAR data collection sites along US-127 near Rives Junction, MI. Data were collected September 16, ~~Sept 16th~~, 2020.

'Site A' was centered on the US-127 bridge over the Grand River, 'Site B' was centered at high power lines over US-127, and 'Site C' was centered at a bridge over train tracks. UAS-based Lidar data for Site A are shown in the top-right and middle-right figures. The middle-right image shows a close up of a canopied area with shadows apparent where the LiDAR was unable to penetrate to the ground surface or the LiDAR only captured at shallow view angles due to the flightpath (or edges of that flightpath). Bottom-left shows the DJI Matrice 600 and attached RIEGL miniVUX, and bottom-right shows tested ground control targets made by MTRI at site 'A'. **(move this to body of report, shouldn't be under figure title)**

3.4.2 Findings

Data Collection at Standish / US-23 Junction

The collection of MLS, UAS, and traditional survey data at the US-23 Standish site allowed for comparisons between these three data types. Analysis of the point clouds (using open-sourced CloudCompare software) showed that the average ground point density for MLS data was much higher for the ground surface at an average 585.9 pts/ft^2, compared to the point density of the UAS ground surface of 29.4 pts/ft^2 (Figure 3.4.4). This is to be expected because UAS-based systems are limited in capability by their payload capacity, while an MLS system can have multiple heavy scanners with a much higher scan rate. Both the UAS and MLS data achieved a 'Fine' point cloud density based upon NCHRP Report 748 *Guidelines for the Use of Mobile LiDAR in Transportation Applications* (Table 3.4.2).

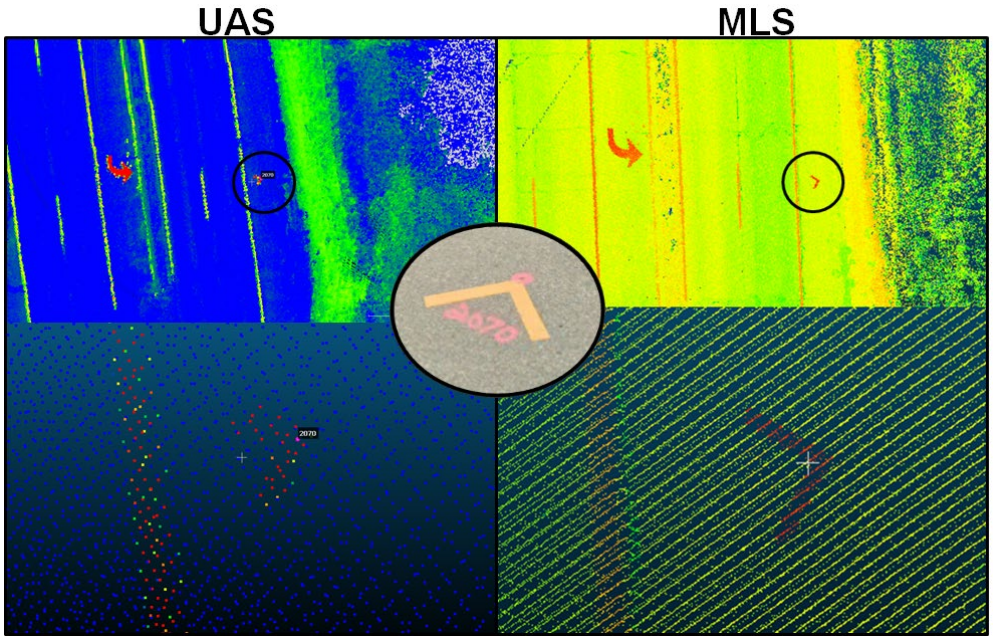

Figure 3.4.4: Visual comparison of UAS and MLS data for one example ground control chevron 4" wide and 2' long on each side. The differences in achieved point cloud density are apparent.

Using common ground control targets within the field of view of both the MLS and UAS-based LiDAR (reflective chevrons placed on the roadway and surveyed with GPS), the vertical and horizontal accuracy for both of these point clouds were determined. SCATs (Scan Acquisition Targets) were used to orient the cloud, while VATs (Validation Acquisition Targets) were used to check the accuracy of the resultant orientation. The results showed that the MLS data achieved a higher vertical and horizontal positional accuracy relative to the UAS data (Table 3.4.1).

Table 3.4.1: Results of point cloud density, and accuracy, from analysis of ground control targets visible in both the MLS and UAS point clouds (analysis limited to the roadway) for the Standish, MI, survey.

Data Source	Point Count	Point Spacing (ft)	Point Density (pts/ft²)	Density Category (NCHRP)
UAS	361964904	0.18	29.54	FINE
MLS	1029598360	0.04	585.89	FINE

	MTRI ACCURACY CALCULATION		SSI ACCURACY CALCULATION	
UAS DATA SUMMARY	**SCATs**	**VATs**	**SCATs**	**VATs**
Radial RMSEr (ft)	0.08	0.17	N/A	N/A
NSSDA HORIZONTAL Accuracy at 95% Accuracy Level (ft)	0.13	0.29	N/A	N/A
NSSDA VERTICAL Accuracy at 95% Accuracy Level (ft)	0.11	0.08	0.03	0.11

	MTRI ACCURACY CALCULATION		SSI ACCURACY CALCULATION	
MLS DATA SUMMARY	**SCATs**	**VATs**	**SCATs**	**VATs**
Radial RMSEr (ft)	0.05	0.07	N/A	N/A
NSSDA HORIZONTAL Accuracy at 95% Accuracy Level (ft)	0.08	0.12	N/A	N/A
NSSDA VERTICAL Accuracy at 95% Accuracy Level (ft)	0.03	0.02	N/A	N/A

Based on NCHRP Report 748 guidelines, MLS VAT accuracy achieved 'HIGH' vertical and horizontal accuracy, while UAS VAT accuracy achieved 'HIGH' vertical accuracy but 'MEDIUM' horizontal accuracy. It should be noted that all ground control used in this comparison of UAS and MLS-based LiDAR were on the roadway on hard surfaces (not within or obscured by vegetation) (Table 3.4.2).

Table 3.4.2: NCHRP Report 748 (2013) - Table 1 - accuracy & resolution levels Guidelines for the Use of Mobile LiDAR in Transportation Applications. This table determines the suitability of LiDAR point clouds for use in Transportation Applications dependent on their achieved point density and positional accuracy.

Accuracy	HIGH < 0.05 m (< 0.16 ft)	MEDIUM 0.05 to 0.20 m (0.16 to 0.66 ft)	LOW > 0.20 m (> 0.66 ft)
Density	1A	2A	3A
FINE >100 pts/m² (>9 pts/ft²)	• Engineering surveys • Digital terrain modeling • Construction automation/ Machine control • ADA compliance • *Clearances** • *Pavement analysis* • Drainage/Flooding analysis • Virtual, 3D design • CAD models/Baseline data • BIM/BRIM** • Post-construction quality control • As-built/As-is/Repair documentation • Structural inspections	• *Forensics/Accident investigation** • *Historical preservation* • Power line clearance	• Roadway condition assessment (general)
	1B	2B	3B
INTERMEDIATE 30 to 100 pts/m² (3 to 9 pts/ft²)	• Unstable slopes • Landslide assessment	• General mapping • *General measurements* • Driver assistance • Autonomous navigation • Automated/Semi-automatic extraction of signs and other features • Coastal change • *Safety* • Environmental studies	• Asset management • Inventory mapping (e.g., GIS) • Virtual tourism
	1C	2C	3C
COARSE <30 pts/m² (<3 pts/ft²)	• *Quantities (e.g., earthwork)* • Natural terrain mapping	• *Vegetation management*	• Emergency response • Planning • Land use/Zoning • Urban modeling • Traffic congestion/ Parking utilization • Billboard management

**Network accuracies may be relaxed for applications identified in red italics.*
***BIM/BRIM: BIM = Building Information Modeling; BRIM = Bridge Information Modeling.*
These are only suggestions; requirements may change based on project needs and specific transportation agency requirements.

For a more visual comparison of UAS and MLS data, the two point clouds were overlaid and analyzed using QTModeler software. A transect was drawn over the US-23 exit ramp, which spanned the west to east right-of-way and road surface gradient (Figure 3.4.5). Analysis confirmed the far greater point density and improved vertical accuracy achieved by the MLS system relative to the UAS system. However, the similarity of these two datasets diverged the further one goes from the road surface. This indicates that the accuracy of the MLS data decreases as one moves further from the roadway. This likely occurs because the further one is from the road surface, the shallower the angle the MLS data is collected and the greater the amount of occluding vegetation preventing the MLS sensor from penetrating to the true ground surface. As one moves away from the road surface, the accuracy of the UAS data is likely greater than the accuracy of the MLS data because the nadir-facing UAS-based LiDAR will be less impacted by an oblique-looking system in the presence of dense vegetation. In the presence of

vegetation, the accuracy of the UAS-based LiDAR will be determined by the density and height of the vegetation.

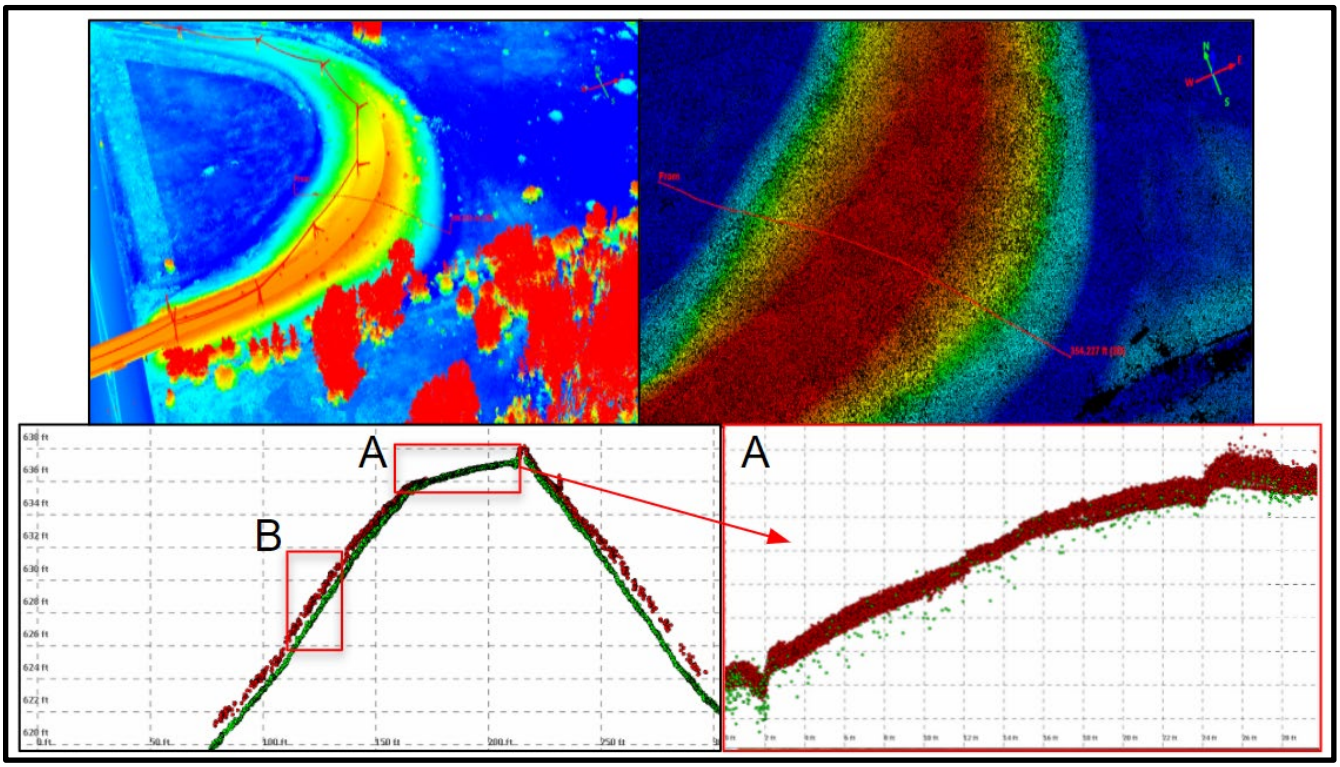

Figure 3.4.5: A 1 ft wide transect drawn across both MLS and UAS - derived LiDAR data (top-left, top-right).

This transect is shown in profile (y-axis = elevation, x-axis = distance along profile) in the bottom-left image with MLS data in red and UAS data in green. In the bottom-right image 'A' one can see the much greater point density achieved using MLS data and improved accuracy for the hard surface (a tighter envelope of data points for the 1ft wide transect). In the window 'B', however, one can see that the MLS data gradually loses accuracy relative to the UAS-based data as one moves further from the road surface (where the MLS sensor focuses its accurate data collection). This is due to the steeper view angle, distance from the sensor, and presence of occluding dense grasses between the MLS sensor and the ground surface. **(move this to body of report, shouldn't be under figure title – use figure number to reference back to it)**

MTRI and SSI solutions then investigated comparing the elevation of the ground surface determined by the UAS point cloud to the elevation estimated using traditional survey data. Traditional survey data were collected on the same date as the UAS Lidar data (November, 2019). This comparison was performed for soft surfaces where vegetation (dense grasses or forest floor) were present. Elevation for the UAS Lidar point cloud was determined by averaging all Lidar ground points within a 0.25 ft radius of the traditional survey locations. MTRI

performed this analysis by visualizing the point cloud in ArcGIS Pro, while SSI used specialized software developed for this analysis.

Using a kriging-based interpolation performed in ArcGIS, MTRI produced a smoothed surface map that represented the difference in point cloud and traditional survey elevation surfaces (Figure 3.4.6). Areas of greatest difference between the UAS Lidar point cloud and the traditional survey elevation data were in the northern areas with dense grasses. Areas of greatest similarity between the Lidar point cloud and traditional survey data were in the southern areas which were forested.

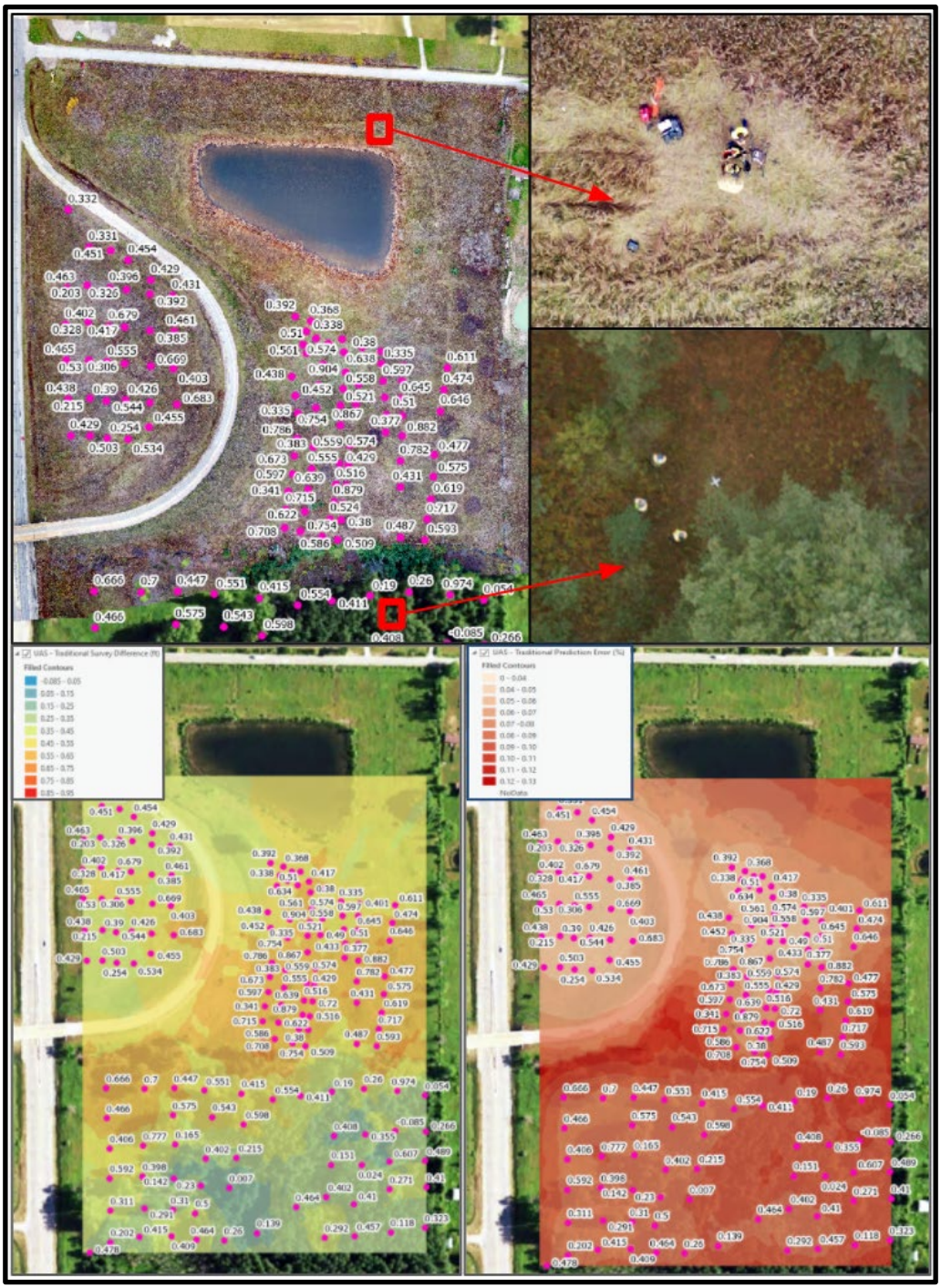

Figure 3.4.6: Areas of greatest difference between UAS and traditional survey elevation data appear to occur in the area made up of dense grasses (bottom-left, orange areas are areas of greatest difference in the interpolation). The bottom-right image shows the estimated percent error for the interpolation in the left figure (affected by data density and variability). Areas of least difference between these elevation sources appear to be predominantly in the southern canopied area where the understory was less densely vegetated ~~thean~~ than the tall grasses in the northern field.

For the comparison between UAS Lidar and traditional survey data, MTRI found that for a subsample of all the surveyed soft surfaces the UAS-based Lidar predicted a 0.48 ft higher ground surface than the traditional survey data (n=31). SSI found that for all traditional points surveyed on soft surfaces at the US-23 Standish site (n=156), the UAS-based Lidar point cloud predicted a ~0.47 ft higher ground surface than the traditional survey data (Figure 3.4.7). In addition, MTRI found that UAS Lidar and traditional survey data were more dissimilar for soft surfaces in dense grasses (n=20, average difference = 0.56 feet) than soft surfaces under leaf-free canopies (n=11, average difference = 0.34 feet). This is likely because the dense standing vegetation occluded the ground surface more than the low leaf-litter present on the forest floor.

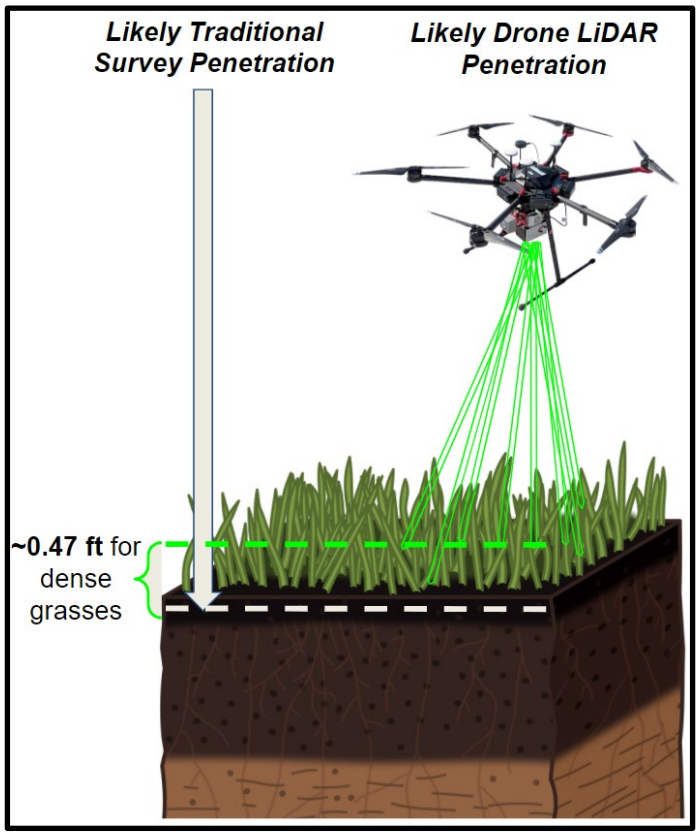

Figure 3.4.7: For the Standish / US-23 data collection, MTRI and SSI separately analyzed the drone-based Lidar data and traditional survey data for the canopied areas and dense grass "soft surfaces" (MTRI n = 31, SSI n = 156). Both groups found that, for areas covered in dense grasses, the drone-based LiDAR predicted an ~0.48 ft higher elevation surface (on average) than the traditional survey elevation data.

Data collection at Rives Junction / US-127

For the Rives Junction Lidar data collection, MTRI performed an extensive analysis of the ground control used in the survey. The information learned from this analysis can be found in Appendix 6.5, the 'Lidar Ground Control Target Document'.

In summary, MTRI found that reflective ground control (using glass-beaded tape) were much more visible in the point cloud scan intensity data (Figure 3.4.8) than cloth targets or bare plywood targets. The use of scan intensity data (and not RGB point cloud data) for accurately locating ground control is important for achieving the most precise selection of ground control point data. While it is possible to locate ground control in an RGB point cloud (made using camera imagery collected at the same time as Lidar imagery), the RGB point cloud is created using algorithms that will not locate features as precisely as the Lidar scan intensity data. These, albeit slight, differences can impact positional accuracy of ground control on the scale of an inch to a foot, which is considerable when one considers the slim margin for 'Fine' accuracy point clouds as determined by the NCHRP (see Table 3.4.2 in the previous section). To achieve such high accuracy, a mentality of "every centimeter (or inch) counts" needs to be present in the minds of surveyors when deploying UAS-based Lidar or evaluating its accuracy.

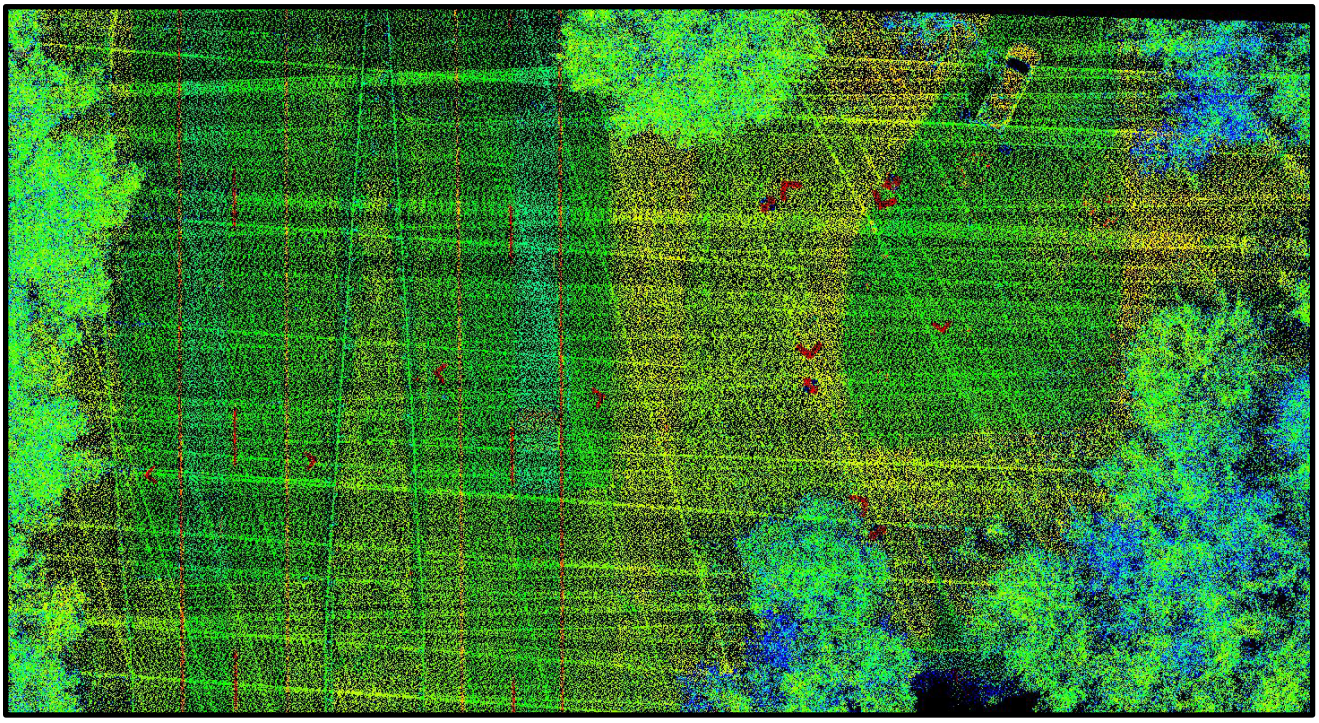

Figure 3.4.8: Cross-hatched UAS-based Lidar scan intensity data collected at 'Site A', the bridge over Grand River, along US-127 near Rives Junction, MI. In this figure, red objects are the most reflective, which are road edge and centerlines, as well as reflective ground control (chevrons, square fields).

Because scan intensity data is the best method for accurately locating ground control, it is important to ensure that ground control stands out relative to the surrounding environment

(Figure 3.4.9). We found that standard 2x2ft cloth photogrammetric targets (Figures 3.4.9 and 3.4.10) were not reflective enough to reliably be visible in scan intensity data. This is because the scan intensity is being symbolized by a color ramp that is scaled to the brightest and least bright objects within the sensor's field of view. This means that any bright or reflective surfaces that happen to be within a surveyed area (e.g., metal signs or structures, road edgelines) will impact the ease of visibility of ground control in the scan intensity data.

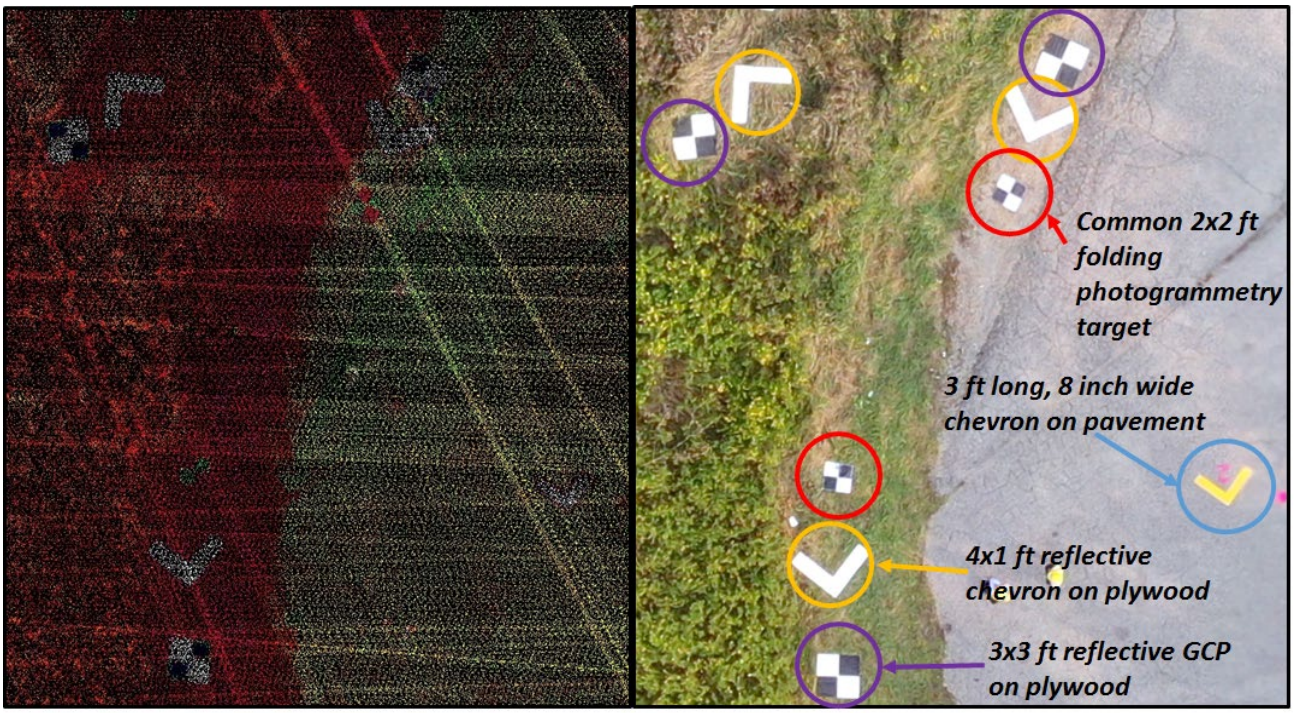

Figure 3.4.9: Lidar scan intensity cloud and drone RGB image of the same location at 'Site A'. Reflective surfaces are much more visible in Lidar scan intensity point clouds.

Ground control point Lidar scan intensity comparisons are explored more quantitatively in Figure 3.4.10. Cloth photogrammetry targets were only slightly brighter in the scan intensity data than the surrounding vegetation, and were not as reflective as bare plywood. Further comparisons of ground control intensities can be found in Appendix 6.5: Lidar Ground Control Target Document.

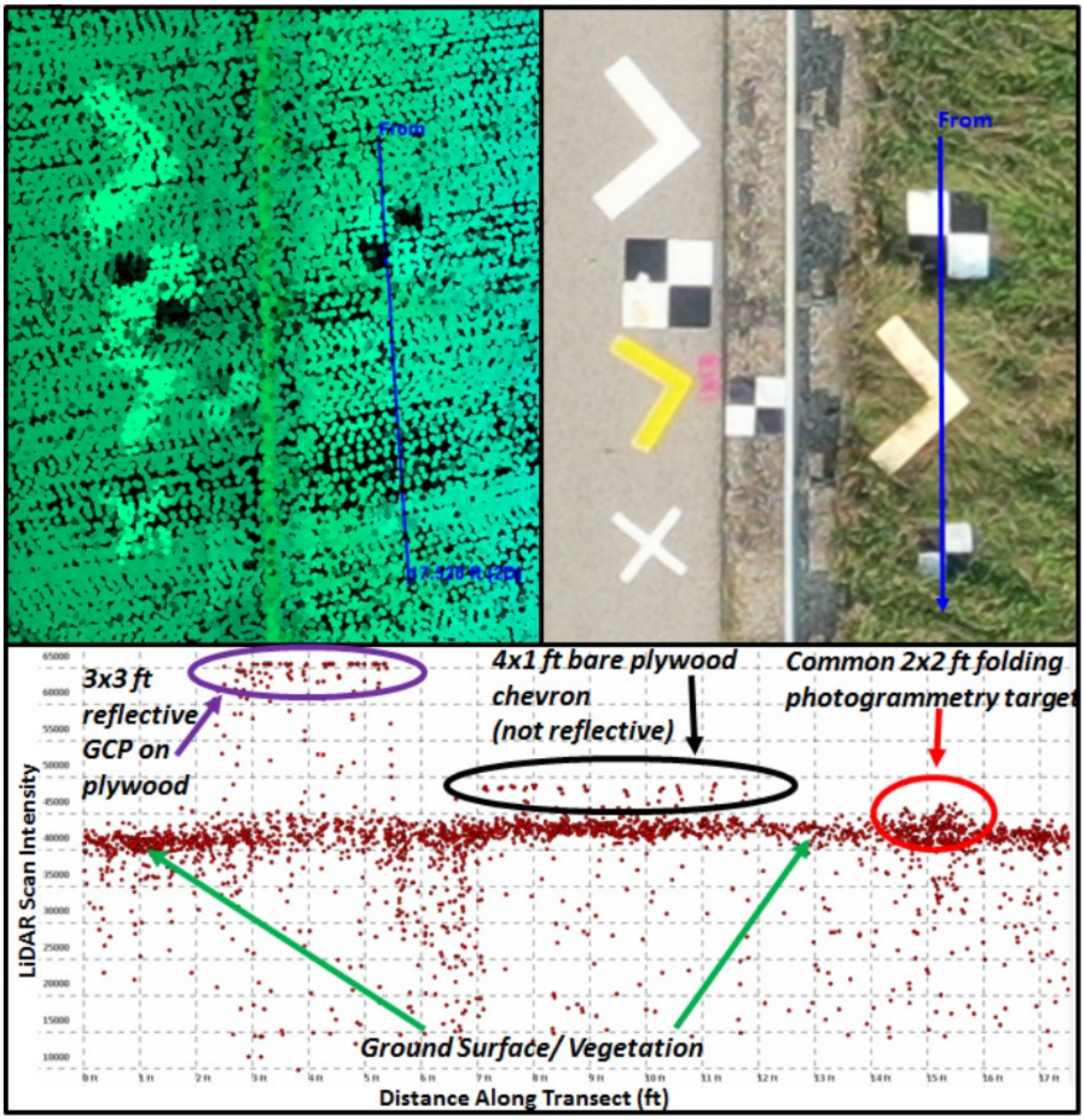

Figure 3.4.10: Example analysis of ground control target intensities (lidar intensity shown in top-left, orthoimage for the same location in top-right) at a UAS Lidar site along US-127.

A transect drawn across these targets shows the achieved lidar scan intensity for each target. The bare wood chevron was more distinct that the cloth target, but the 3x3sqft target with glass bead tape and matte black paint was most dissimilar in scan intensity relative to the ground surface and surrounding objects. More such ground control target comparisons were performed and are found in the 'Lidar Ground Control Target Document' in the Appendix of this Report. (move to body of report)

In addition to the reflectivity of ground control targets, surveyors need to take ground control size into account when planning for a UAS-based Lidar survey. Results of an accuracy assessment of a point cloud will be in part related to the ability of a surveyor to precisely place and orient the ground control in the scan intensity point cloud. The ease with which one can identify the GPS-surveyed tip or center will be influenced by the number of Lidar points that hit the target, which is dependent on the Lidar sensor mirror speed, drone flight speed and height, and the drone flight transect spacing (overlap). Surveyors planning a Lidar survey can determine ahead of time their ground control needs if they have an anticipated point cloud density for the ground surface. Ground control size can be adjusted ahead of time depending on the anticipated ground point cloud density to ensure that a minimum number of points hit the target.

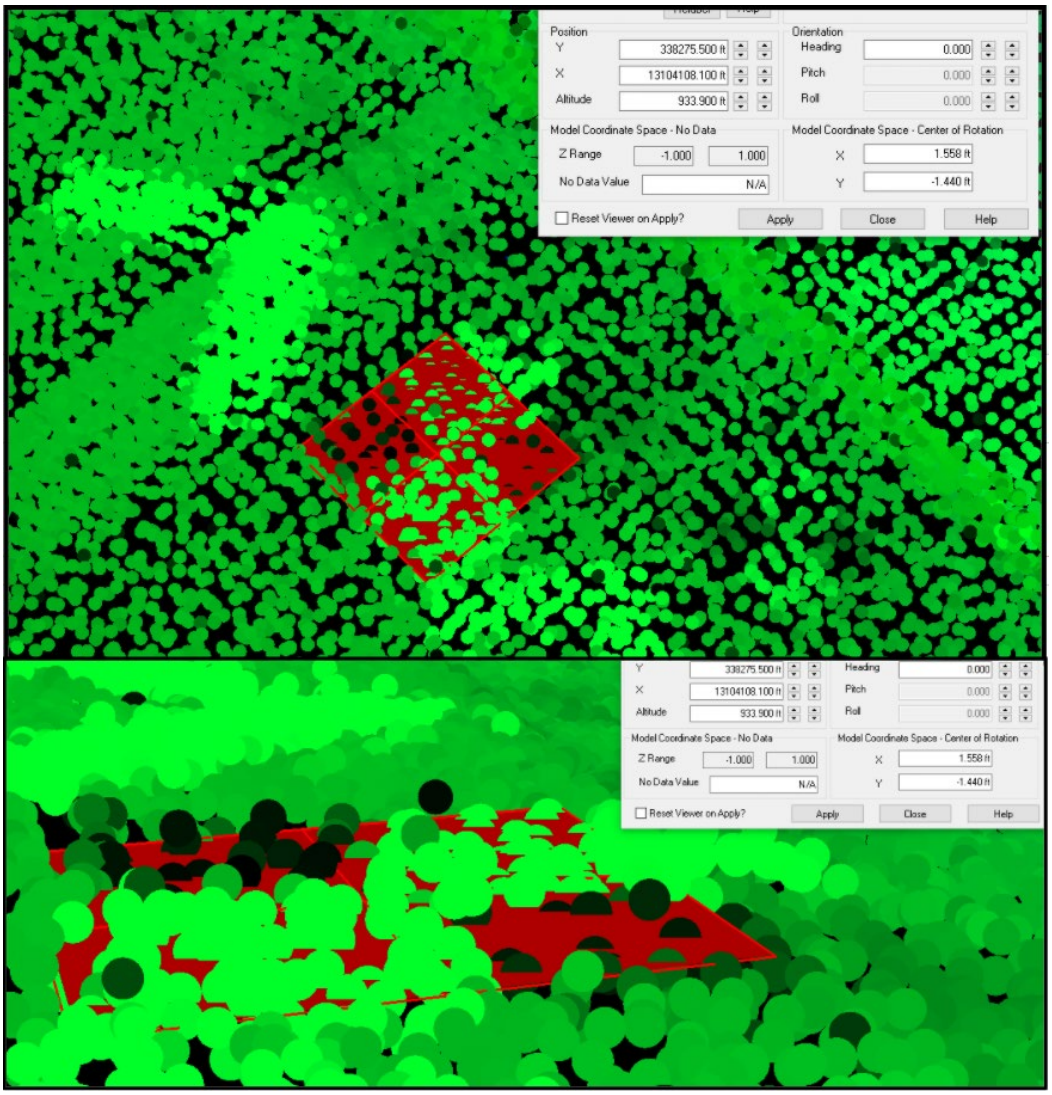

Figure 3.4.11: (figure title?) A vector-type file (e.g., a shapefile) can be used to recreate a ground control point of known proportions (pictured: a 3x3 sq ft vector field with four fields positioned on top of the 3x3 sq ft target in the LiDAR point cloud). Translating, rotating, changing elevation, and changing the roll and pitch of the vector file is possible (using most

LiDAR manipulation softwares) in order to achieve the best possible alignment of the vector file in the point cloud data. This is especially useful when approximating ground control point centers for sparse data clouds. (move to body of report)

3.4.3 Discussion

The differences in soft surface elevation accuracy between UAS-based Lidar, MLS, and traditional survey data seen at the Standish site arise from the limited ability of the Lidar to penetrate through dense vegetation and leaf litter to the true ground surface. This is not an issue for traditional survey GPS because it reports the elevation for the base of the sensor which rests on the ground surface. In addition, the accumulation of errors in the drone and Lidar unit (e.g., drone/Lidar IMU, RTK GPS accuracy, etc.) contribute to the differences seen between the UAS Lidar and traditional survey data. While one may consider these errors for UAS Lidar to be relatively small (on the order of 0.1ft for RTK error, 0.4ft for dense vegetation), they are sizable when one considers that NCHRP guidelines indicate a 'HIGH' point cloud vertical accuracy (necessary for engineering surveys, drainage/flooding analysis, CAD models, unstable slopes assessment) is <0.16ft. The drone-based Lidar also predicted slightly higher elevations than the traditional survey for the canopied area (~0.2 ft). This difference is lower than the difference for the dense grass areas, and this is likely because the vegetation density at the forest floor was less than that of the dense grass areas.

Ground control selection for a UAS-based Lidar survey is dependent upon the limitations of the sensor technology and pre-planned flight characteristics. Ground control characteristics should be based upon pre-calculated point density (ground control size) and the knowledge that ground control should stand out in intensity relative to other objects in the surveyed area (ground control composition). The data collections performed at the sites along US-127 showed that ground control selection can influence accuracy assessment of a Lidar point cloud.

Lidar is a specialized surveying tool, and its use for engineering and high accuracy surveys needs to be evaluated on a case by case basis. For optimal data collection and accuracy site conditions, and specifically surfaces of interest, need to be ideal and relatively unobscured. Surveyors, however, should temper their expectations and recognize that field conditions can influence the accuracy of a survey when using UAS-based Lidar systems. Even though UAS-based LIDAR could (given the right situations) meet NCHRP type 1A surveys, the reality is that the point cloud accuracy and resolution from a UAS survey may not be adequate for detecting and identifying certain features needed for engineering type surveys.

3.5 Milestone 5: Assess MDOT's Data Use Analysis Process (DUAP) program/TerraForm Manager (TFM) Integration With Each Use Case

For milestone 5, our project team built from the Phase II efforts to organize and document data results into formats easily usable by MDOT. These efforts make the data easier to integrate into TFM, as was demonstrated with for a bridge inspection UAS data set with DUAP in Phase

II. These data sets can be integrated into other MDOT databases as well, as has been discussed with the MDOT subject matter experts. The section below describes the main, documented outputs prepared for each of the four uses. These data sets are:

3.5.1 Use Case 1 - Traffic Operations data sets:

1. Application 1 - US-23/M-14 Weaving area
    a. Origin-Destination flow (OD flow) in a CSV format
    b. The OD flow information from two origins (US-23 mainline and M-14 on-ramp) to two destinations (US-23 mainline and Exit 41 Plymouth Road off-ramp)
2. Application 2 - I-96 Williamston Road Traffic Corridor
    a. Real-time traffic analytics
        i. Video streaming using YouTube
        ii. Real-time cumulative calculation of vehicle counts for each lane
    b. Offline traffic analytics
        i. Vehicle counts in a 5-minute interval in a CSV format
        ii. The aggregated calculation of vehicle counts information for each lane
        iii. Density in a 5-minute interval in a CSV format
        iv. Offline calculated density information for each lane

3.5.2 Use Case 2 - Bridge Inspection Assessment data sets:

1. RGB and Thermal Orthophoto (GeoTIFF file), Digital Elevation Model - DEM (GeoTIFF file), Hillshade (GeoTIFF file)
    a. Beyer Road
    b. Uncle Henry Road
    c. Laplaisance Creek/I-75 Exit Ramp
    d. Billwood/I-96
    e. M-99/I-96
2. Spalling - Spallgorithm Outputs (Esri Shapefile - polygons)
    a. Uncle Henry Road
    b. Laplaisance Creek/I-75 Exit Ramp
    c. M-99/I-96
3. Delamination (TADDA) Outputs (Esri Shapefile - polygons)
    a. Beyer Road
    b. Uncle Henry Road
    c. Laplaisance Creek/I-75 Offramp
    d. Billwood/I-96
    e. M-99/I-96

3.5.3 Use Case 3 - Construction Inspection data sets:

1. I-69 Survey Data, 10/5/2021
    a. Orthophoto, DEM, Hillshade (GeoTIFF)

b. Converted UAV images, Temperature Thresholded Images, Contoured Images, Temperature Differential Images (JPEG)
c. Per-Pixel Temperature Orthophoto (GeoTIFF)
d. BIM Parameters (Excel Sheet (CSV))
e. Production Rates (Excel Sheet (CSV))
f. Corridor Solids (Civil 3D and Microstation)
g. BIM models (Civil 3D and Microstation)
h. Behind the Paver Thermal Image Samples (JPEG)

3.5.4 Use Case 4 - LiDAR UAS for Design Survey data sets

1. US-23/Standish Survey - files processed to meet the MDOT Geopak file requirement.
    a. UAS Standish 3D extraction_2021_09. DGN = Open Roads File of the line work and assets that were extracted.
    b. UAS Standish Terrain_2021-09.DGN = This is the Open Roads Terrain (Surface) File .
    c. UAS Standish_DELTA Terrain_2021-09.XML = Land XML File of the Difference between the MLS and UAS Terrain Files
    d. UAS Standish_Terrain_2021_09.XML = This is the same file as the .DGN terrain in Lnd XML format.
    e. UAS-MTL Delta Terrain.2021-09.DGN = This is the difference between the MLS and UAS files in OPEN Roads Format.

A series of review meetings with each of the SMEs were held primarily in January through March of 2022 as part of Milestones 5 and 6. The lidar UAS for design survey Task 5 data sharing meeting was held on June 3, 2021, with input from Frank Boston and Karl Brandys, and all data results were shared with them via a MTRI ftp site. The traffic operations data sharing meeting was held on March 8, 2022, with input from Hilary Owen and Stephanie Palmer. The bridge inspection assessment data sharing meeting was held on February 16, 2022, with input from Brian Zakrzweski. A result of this meeting was the names and regions of all MDOT Part 107 certified staff being shared with Brian Zarkzweski so that he could understand the larger extent of UAS operators now available to meet MDOT data collection needs. As of late February, 2022, MDOT has 22 Part 107 certified Federal Aviation Administration (FAA) unmanned pilots and 21 drones. The construction inspection meeting was on ~~has been scheduled for~~ March 22, 2022, ~~(after this draft was due)~~ with Michael Meyer, who took over from Jason Early in 2021 as the use case's SME. The results of this final SME meeting will be reviewed in the revised version of this project final report. The outputs above were reviewed with the SMEs at these meetings to ensure that they could be integrated with workflows in their subject areas. All meetings so far have resulted in agreement that the data sets are useful for MDOT operations.

To help further promote adoption of project methods with MDOT sections, two final project demonstrations will be held in spring of 2022 when weather is more favorable. A "UAS-assisted bridge inspection demonstration" day for MDOT's region bridge engineers will focus on

the methods developed in this project using example results. Included will be a live demonstration of the spall detection, thermal delamination detection, and AI-enabled 3D model creation methods documented above. We are likely to hold this demonstration at the Beyer Rd bridge near Saginaw, which has been visited in Phases II and III and has complete data sets that can be shared with the region bridge engineers.

A final demonstration of the traffic operations methods is also being scheduled for April or May of 2022 so that PI Brooks can meet with MDOT Traffic Operations Center (TOC) staff during a live demonstration of UAS-enabled methods. The demonstration will include live video streaming from the Williamston Road / I-96 corridor site, with real-time analytics, as was successfully shown during the December 10, 2021, data collection. Input from TOC staff will be documented in the revised final report as part of Task 5 and 6 documentation.

3.6 Milestone 6: Implement DUAP/TFM Viable Integrations for Each Use Case

The interim and final review meetings with the SMEs have prepared the way for Milestone 6. PI Brooks has reached out to Chris Poe from Mixon-Hill to have a meeting in late March or early April of 2022 that will focus on reviewing the data described above in Task 5 and how these can be integrated into TFM. We expect that the traffic operations data may be most similar to the type of data already being stored in TFM and used for MDOT applications. Phase II collaboration with Mixon-Hill did demonstrate that bridge inspection geospatial UAS results could be imported into DUAP. The results of this meeting and any follow-up will be added to this document as part of revising the final report for submittal by the end of the project on June 11, 2022.

Workflow Diagrams

The project's statement of work for Task 6 includes developing workflow diagrams that map the UAS-collected data onto MDOT decision-making processes. The following section is the result of the SME's listening session ~~to the~~ input ~~of the SMEs~~ for the four uses.

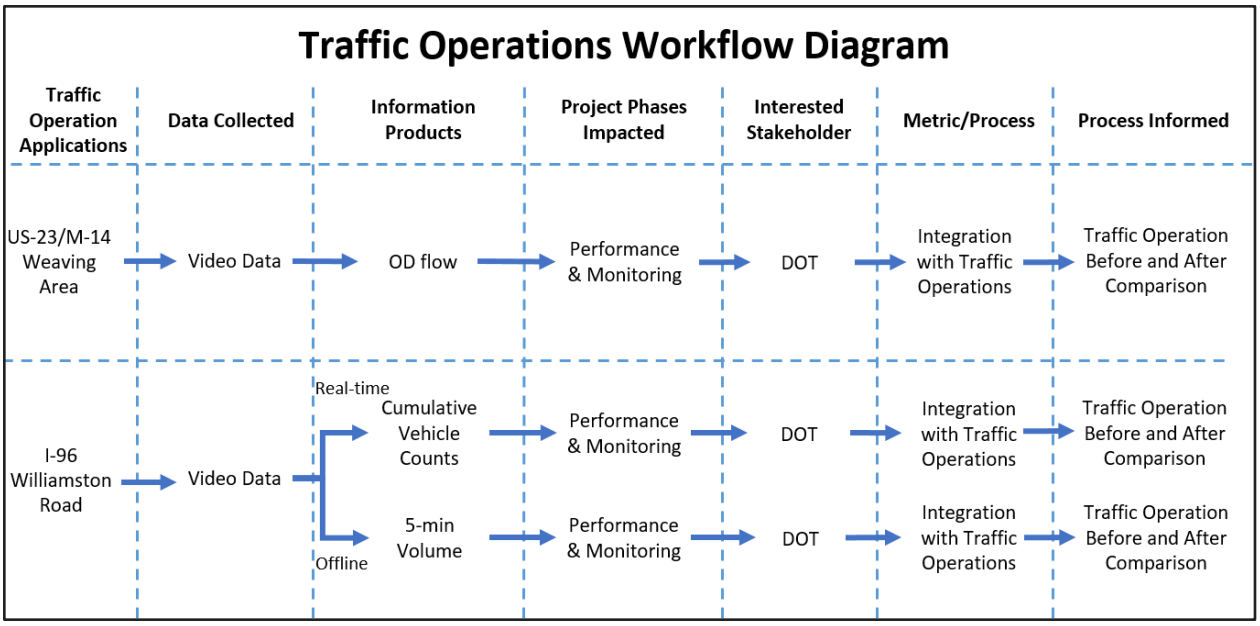

Figure 3.6.1: Traffic Operations workflow diagram.

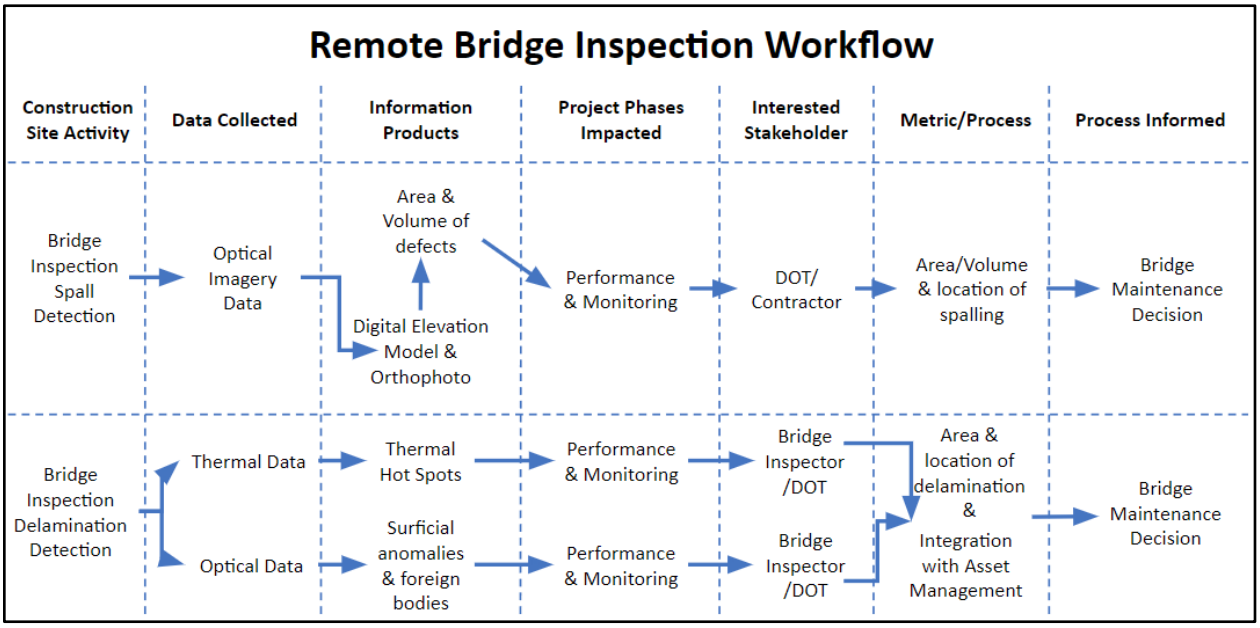

Figure 3.6.2: Bridge Inspection workflow diagram.

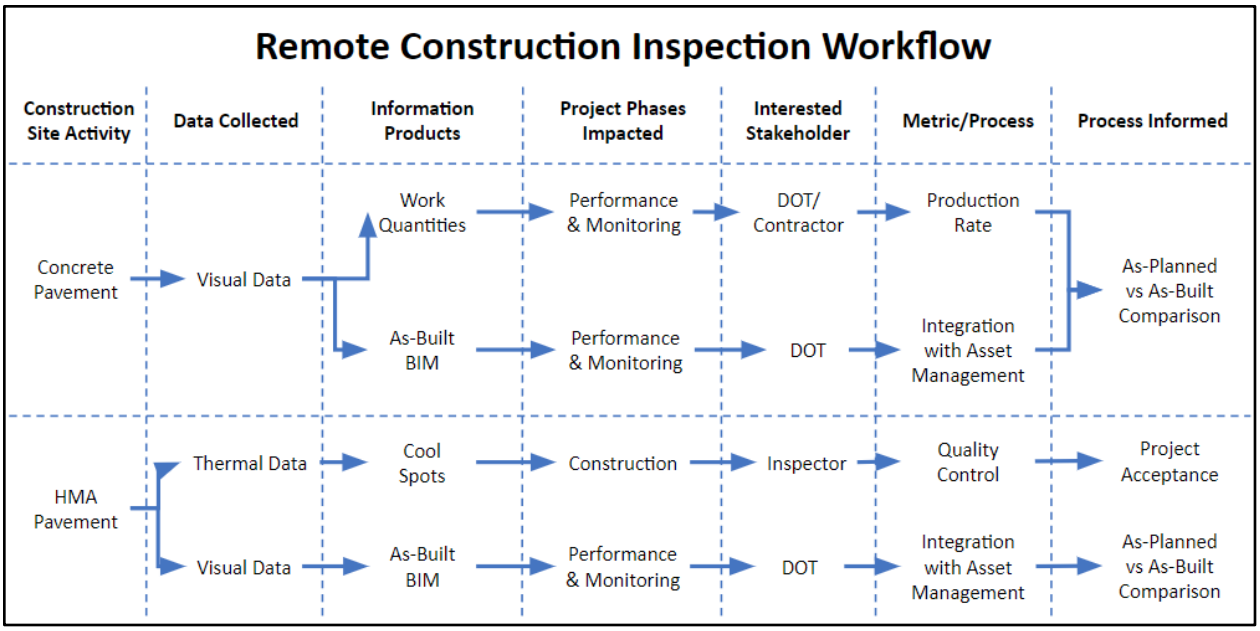

Figure 3.6.3: Construction Inspection workflow diagram.

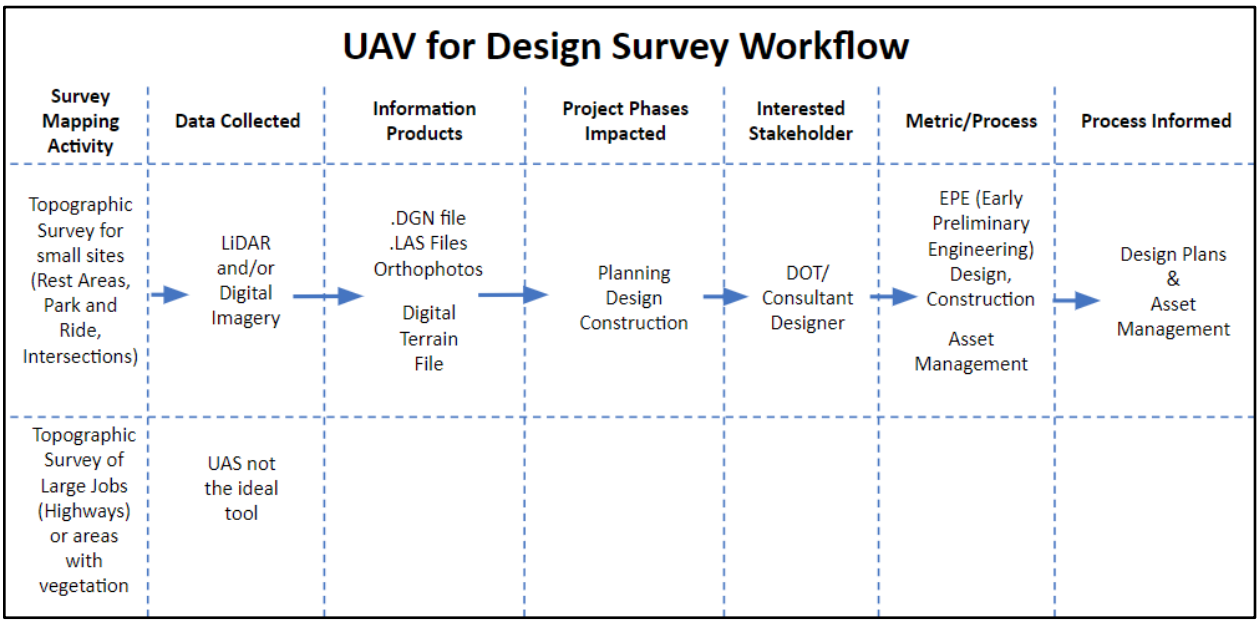

Figure 3.6.4: LiDAR UAS for Design Survey workflow diagram.

These workflow diagrams have been designed to serve as an easy-to-understand documentation of how the data and output products map into MDOT's processes. Challenges and gaps do remain in making these types of UAS data fully integrated into MDOT's day-to-day workflows. In previous phases, MDOT had limited UAS pilot resources and few available UAS, which was changed with the leadership of MDOT's Aeronautics division. Helping disseminate the availability of these resources will help UAS-enabled methods and results to become a more common feature of MDOT operations. Continuing staff training will help, as will dedicating

resources to make sure that UAS hardware, along with data processing software tools, stay up-to-date. New FAA rules on beyond visual line of sight (BVLOS) and operations over people (OOP) will be fully implemented by early 2023, which should enable more practical deployment of UAS. Being able to tangentially cross traffic during flights will make traffic operations data collection easier. Easier BVLOS rules will enable longer data collections and also enable brief out-of-sight operations possible at bridges and other structures.

There is likely to be a need to work closely with MDOT's IT support at the Department of Technology, Management, and Budget (DTMB) to ensure that MDOT's databases can handle the large amounts of data that can be generated by UAS sensors, and in formats that may not be standard for data management platforms such as TFM. This challenge can likely be overcome by close collaboration between MDOT, DTMB, and SMEs to make sure that databases are sufficiently flexible and do not have a gap in data format support.

4. Conclusions

4.1 Conclusions from the Study

This applied research project enabled the testing and demonstration of the utility of UAS for four use cases based upon Phase I and II project findings, guided by input from MDOT and its subject matter experts. Useful, detailed, and documented data were collected and analyzed for all four use cases, and these were shared with MDOT subject matter experts. The closing quarter of the project focused on final technical demonstrations and how the results can be integrated with data handling systems such as TFM.

The data analysis and results of this project's efforts have clearly shown the utility of UAS to assist with day-to-day MDOT operations, and more specifically for traffic operations, bridge inspection, construction inspection, and lidar for design survey. For the traffic operations use case, the project team demonstrated the ability to use single or multiple UAS to calculate, in real time, the total traffic or traffic density along a corridor using livestreamed UAS video and automated traffic parsing algorithms developed by Michigan Tech. Using collected video, the project team demonstrated the ability to use multiple drones to calculate OD flow matrices, which is valuable data that can assist in understand traffic flows for corridor updates. For the bridge inspection use case, the project team demonstrated the use of UAS-derived orthophotos, DEMs, and thermal orthomosaics for detecting spalling and delaminations in roadways or bridge decks.

Michigan Tech and project subcontractor ~~collaborator~~ Collins Engineers demonstrated, for several bridges, the usefulness and relative ease of having 3D digital models of structures constructed from UAS-collected imagery. These results for the bridge inspection use case have implications for improving bridge surveyor's safety by greatly reducing the amount of time spent on a bridge or near traffic, and reducing the need for closing bridges to traffic to perform surveys.

For the construction inspection use case, the project team demonstrated the usefulness of orthoimagery and image processing techniques for identifying pavement removal or asphalt laying rates. In addition, MTU developed novel methods of processing thermal imagery and image processing to calculate imaged asphalt temperatures and identify potential regions where thermal anomalies might be present in recently laid asphalt.

For the lidar for design survey use case, project subcontractor ~~collaborator~~ SSI supported analysis of drone- and vehicle-based lidar that revealed the benefits and limitations of using lidar for design survey applications. While accuracy and density of the point cloud was typically found to meet NCHRP standards, MTRI and SSI both independently found that dense vegetation often present on soft surfaces can negatively influence the accuracy of the point cloud.

4.2 Recommendations for Further Research

This project is the culmination of three phases of research funded by MDOT to evaluate how UAS can help meet the needs of MDOT operations. With these phases completed, the Michigan Tech is recommending that MDOT focus on smaller, more specific use cases for future research. Based on our experience, we are recommending:

- Implementing a tethered UAS for longer duration data collections for ~~for~~ traffic monitoring. This could involve multi-UAS traffic surveys for complex corridors.
- Integration of as-built 3D bridge models from UAS workflows into MDOT bridge management system databases. This would include training for MDOT bridge operations staff to use the types of UAS able to collect complete 3D bridge models.
- Training of MDOT staff on how to deploy UAS for construction monitoring activities, based on the capabilities documented above.
- Demonstration and evaluation of newer UAS lidar systems to help MDOT evaluate this rapidly advancing technology. Rental systems enable short-term testing of new systems that would be part of this future research.

4.3 Recommendations for Implementation (*The Implementation Plan may be part of the final report or a separate document*)

- Describe methods that are ready to implement
- Pg. 57 (3-24) of MDOT Research and Implementation manual:
  - ✓ "The PI writes and submits an Implementation Action Plan Proposal (IAPP), which is a technical report of 10 pages or less that explains how MDOT could best use the result(s) of the study. The report should note the recommended implementation steps, the estimated cost of implementation and the benefits of adopting the implementation plan."

- ✓ "If a project requires outreach to a larger audience than the RAP, a component of the implementation plan should include an outreach plan that at a minimum indicates the message(s), the audience(s) and the medium(s)."

As the third and final phase of MDOT's main wide-ranging UAS research program, the above results have shown that traffic, bridge, construction, and design survey applications are now available for implementation at MDOT. The main steps ~~we are recommending~~ recommended for implementation are:

- Continued investment in training of MDOT staff to ensure that MDOT sections can implement UAS into their operations.
- Continued investment into UAS hardware and data processing software so that MDOT can stay on the forefront of UAS-enabled data collections.
- Single-topic focused research projects to enable implementation in specific areas, with a focus on tethered UAS, 3D bridge model creation, construction monitoring, and latest lidar tools.
- Continued work with the private sector to maintain access to the latest methods of UAS-enabled data collection.
- Working closely with DTMB to make sure that data formats and data amounts can be supported over the long term.

The cost of implementation will vary by step. MDOT has a training budget that could potentially include the staff training costs mentioned above. Hardware and software budgets will vary. With the types of UAS demonstrated here costing from $1,500 to $35,000, these do not need to be overwhelming costs.

Many MDOT staff appear well versed on UAS capabilities. So, the main recommended outreach ~~we are recommending~~ is the type of single-topic research ideas mentioned above. With training, hardware, software, and use case research investments, MDOT can continue to be a leader in applications of UAS.

5. Bibliography

Bailey, Brian, 2012. "Three Acronyms You Should Know in Mobile Mapping". Point Of Beginning. Article published on GeoDataPoint.

Bochkovskiy, A., Wang, C. Y., & Liao, H. Y. M. (2020). Yolov4: Optimal speed and accuracy of object detection. *arXiv preprint arXiv:2004.10934*.

California Department of Transportation (CALTRANS), 2018. Surveys Manual. Chapter 15: Terrestrial Laser Scanning Specifications. Date Page Last Revised: June 2018.

Surveys Manual | Caltrans

Certainty3D. Establishing Requirements, Extracting Metrics, and Evaluating Quality of LiDAR Data. Technote #1021. March 31, 2015. Technote #1021: Requirement Metrics

Kashani AG, Olsen MJ, Parrish CE, Wilson N. A Review of LIDAR Radiometric Processing: From *Ad Hoc* Intensity Correction to Rigorous Radiometric Calibration. *Sensors*. 2015; 15(11):28099-28128. https://doi.org/10.3390/s151128099

Michigan Department of Transportation, 2018. Development Guide. Chapter 9: Remote Sensing. Date Page Last Revised: 16 June 2017. Chapter 9 - Remote Sensing - MediaWiki

Wojke, N., Bewley, A., & Paulus, D. (2017, September). Simple online and realtime tracking with a deep association metric. In *2017 IEEE international conference on image processing (ICIP)* (pp. 3645-3649). IEEE.

6. Appendices

6.1 List of Acronyms, Abbreviations and Symbols

Above Ground Level (AGL)
American Society for Photogrammetry and Remote Sensing (ASPRS)
Bridge Management System (BMS)
Building Information Model (BIM)
Certificate of Authorization (COA)
Chain Dragging (CD)
Content Standard for Digital Geospatial Metadata (CSDGM)
Continuously Operating Reference Station (CORS)
Da-Jiang Innovations (DJI)
Data Use Analysis and Processing (DUAP)
Digital Elevation Model (DEM)
Digital Single-lens Reflex (DSLR)
Federal Aviation Administration (FAA)
Federal Geographic Data Committee (FGDC)
Fourth (or Fifth) Generation Mobile Communications Standards (4G, 5G)
Geographic Information System (GIS)
Global Navigation Satellite System (GNSS)
Global Positioning System (GPS)
Graphical User Interface (GUI)
Ground Sampling Distance (GSD)
Hammer Sounding (HS)
Hot Mix Asphalt (HMA)
Implementation Action Plan (IAP)
Inertial Measurement Unit (IMU)
Integration Pilot Program (IPP)
Intelligent Transportation System (ITS)
Light Detection and Ranging (LiDAR or Lidar)
Michigan Department of Transportation (MDOT)
Michigan Tech Research Institute (MTRI)
Michigan Technological University (MTU)
National Bridge Inventory (NBI)
National Cooperative Highway Research Program (NCHRP)
Net Present Value (NPV)
Non-Destructive Testing (NDE)
Open Computer Vision (OCV)
Origin-Destination Flow (OD Flow)
Pilot in Command (PIC)
Principal Component Analysis (PC or PCA)
Real Time Kinematic (RTK)
Research Advisory Panel (RAP)
Rights-of-Way (ROW)
Root Mean Square Error (RMSE)
Square Yard (SY)
Statewide Transportation Operations Center (STOC)
Structure from Motion (SfM)
Surveying Solutions Inc. (SSI)
Subject Matter Experts (SMEs)
Terraform Manager (TFM)
Thermal Anomaly and Delamination Detection Algorithm (TADDA)
Three Dimensional (3D)
Transportation Research Board (TRB)
Unmanned Aerial System (UAS)
Unmanned Aerial Vehicles (UAVs)
Visual Line Of Sight (VLOS)
Visual Observer (VO)

6.2 Installation of the ArcPro Bridge Inspection Toolset

The bridge inspection tools are a series of python scripts for the processing, an Esri toolbox file, and an ArcPro customization file. The python scripts hold the code that is executed upon

command from the user. The toolbox files holds the definitions of the tool dialogues, and the customization file allows a user to add the tools to a toolbar. Both the spallgorithm and TADDA (Thermal Anomaly and Delamination Detection Algorithm) can be installed together. The files will likely be delivered as a compressed file archive in .zip format.

The first step is to unzip the folder to a directory where the script will run from. This can be a location on either a network or local drive. Right click on the zipped folder and use any decompression tool (e. g. 7-Zip) to decompress the files. It is recommended to use the same name for the folder in which you will decompress the .zip files. To add the toolbox open ArcGIS Pro and choose to create a new project or open an existing one. In the toolbar, there is an option to add toolbox (Figure 6.2.1).

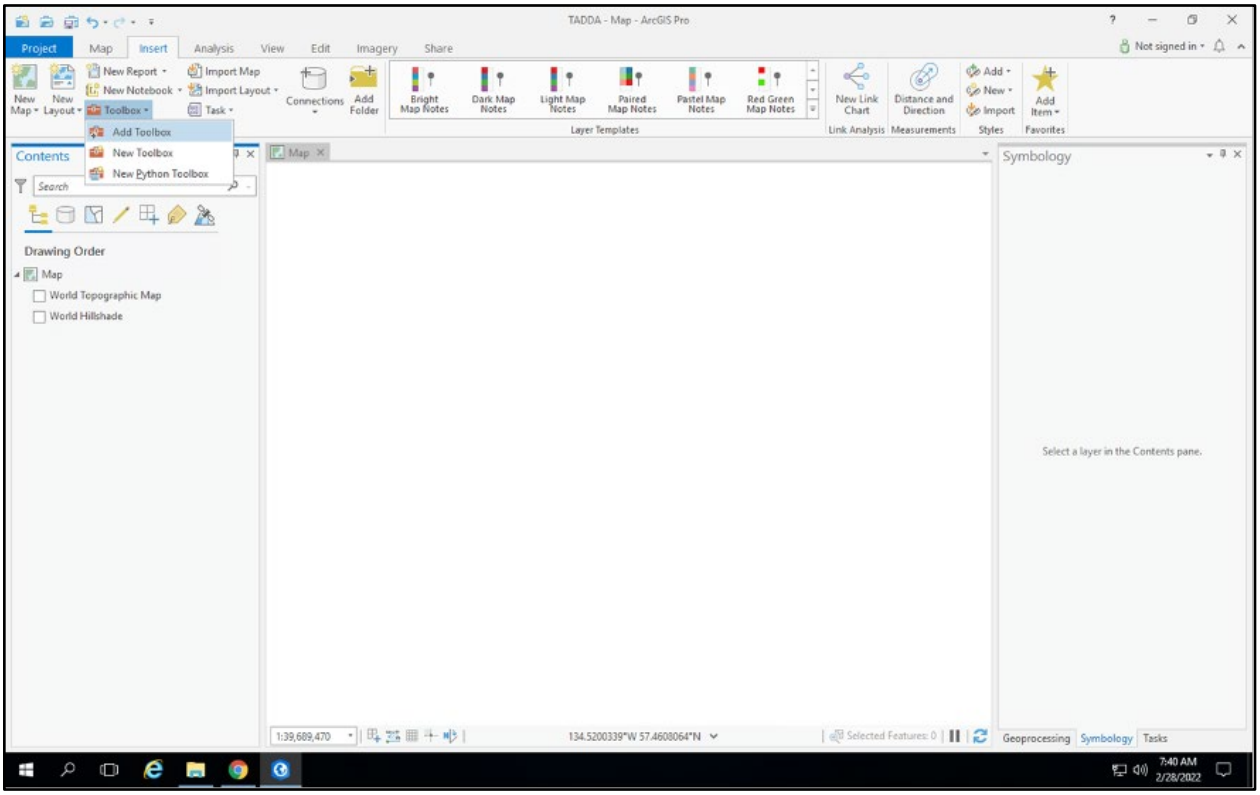

Figure 6.2.1: Adding a toolbox to ArcGIS Pro project document.

The added toolbox can be accessed from the Catalog pane (usually on the right side or can be added from view < Catalog). Once the toolbox is added double click to see the attached scripts. TADDA Merged corresponds to the TADDA tool and spallgorithm 5.1 corresponds to the spallgorithm. At the time of installation the path for the script will have to be changed from default to that of the local computer (Figure 6.6.2). For both spallgorithm and TADDA Merged right click on the file and choose “properties”. On the window that pops up browse for the script in the local computer in the Script File dialogue.

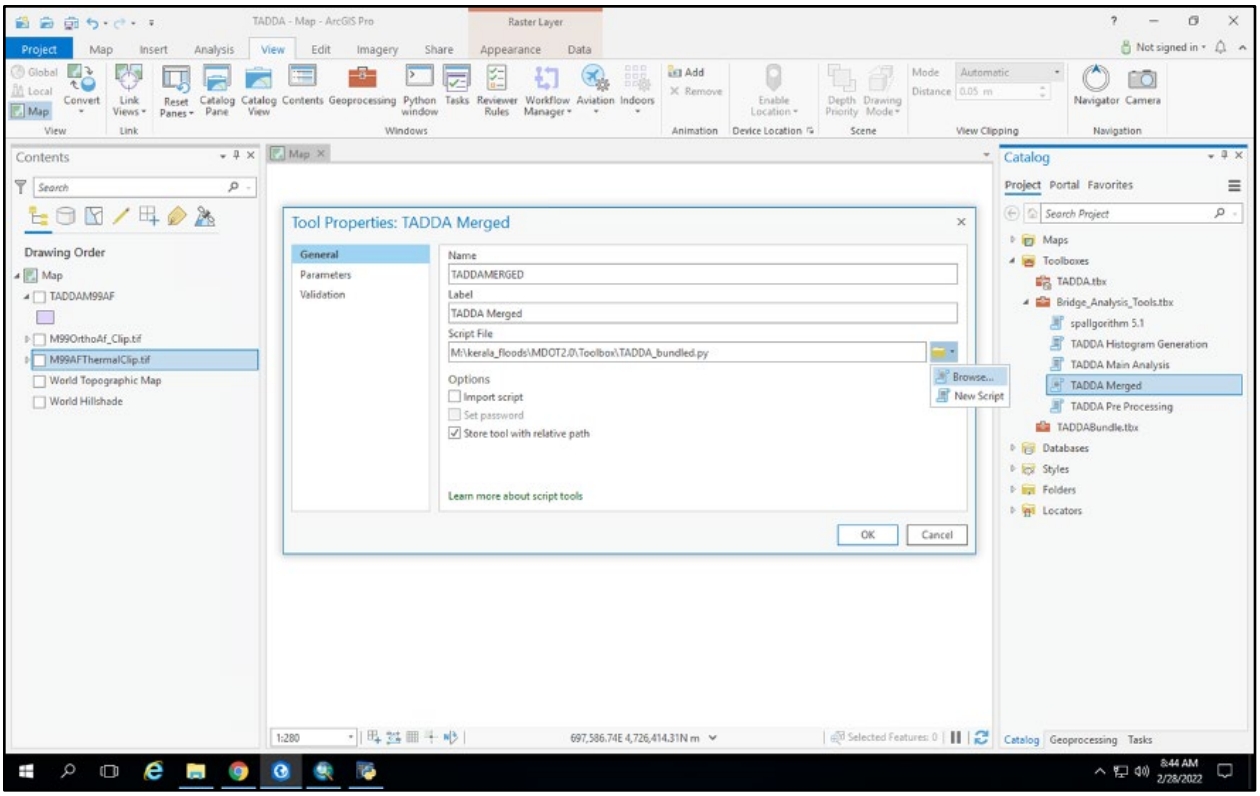

Figure 6.2.2: Update the script file location on the local computer

To have the tools available in a toolbar right click in the toolbar and select "Customize the Ribbon". In the next popup dialogue next to "Customizations" click on "Import/Export", and "Import customization file". Navigate to where the files were extracted and choose the toolbar_customUI.proExportedUI. After a few moments there should be a new ribbon toolbar titled Bridge Inspection Tools (Figure 6.2.3).

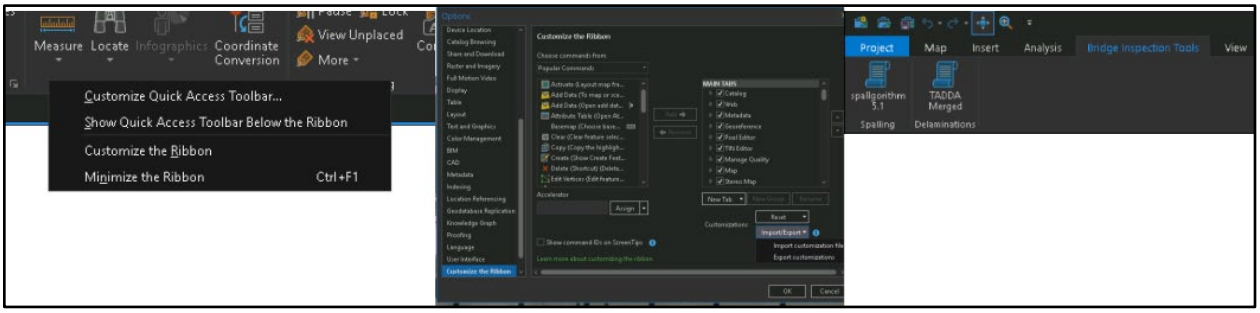

Figure 6.2.3: Adding the Ribbon Customization

6.3 "Spallgorithm" Manual

The spallgorithm takes an input Digital Elevation Model (DEM) and returns a shapefile containing spatial extent of spalls along with attributes including area, depth, and volume. Other inputs include a shapefile limiting the extent of the analysis to the bridge deck only, a directory

for holding temporary files created during the code execution, a sensitivity parameter, an output directory, and an output name.

The input DEM should be a geotiff, however other raster formats should work. The DEM can be in any projected coordinate system, but not a geographic coordinate system. It is required that the linear units of the coordinate system be either: Meter, Foot, Inch, US Feet, or centimeter; which covers most projected coordinate systems. The shapefile defining the exclusion zone should be in the same projection as the DEM.

Because the algorithm creates and stores several temporary files during the analysis a working directory is required. This directory should be somewhere on the local machine of the computer running the tools, so delays with read and write speeds across network spaces do not cause issues. This directory will be treated as the ArcGIS scratch folder. The folder self-cleans after the program closes.

The sensitivity parameter, (default =0), increases with the sensitivity of the detections with increasing values. If spalls are not being detected and a user believes they exist, then re-run the tool with higher sensitivity values. This value gets translated to minimum depth of which an elevation needs to be below an idealized flat surface across the bridge deck to be considered a spall. High sensitivity values result in a lower threshold, possibly finding more spalls, but with more false positives. If no spalls are detected at any point during the analysis the code will exist with no errors. A user can check the messages to see if this is the case.

Figures

1. Finding the coordinate system of the DEM

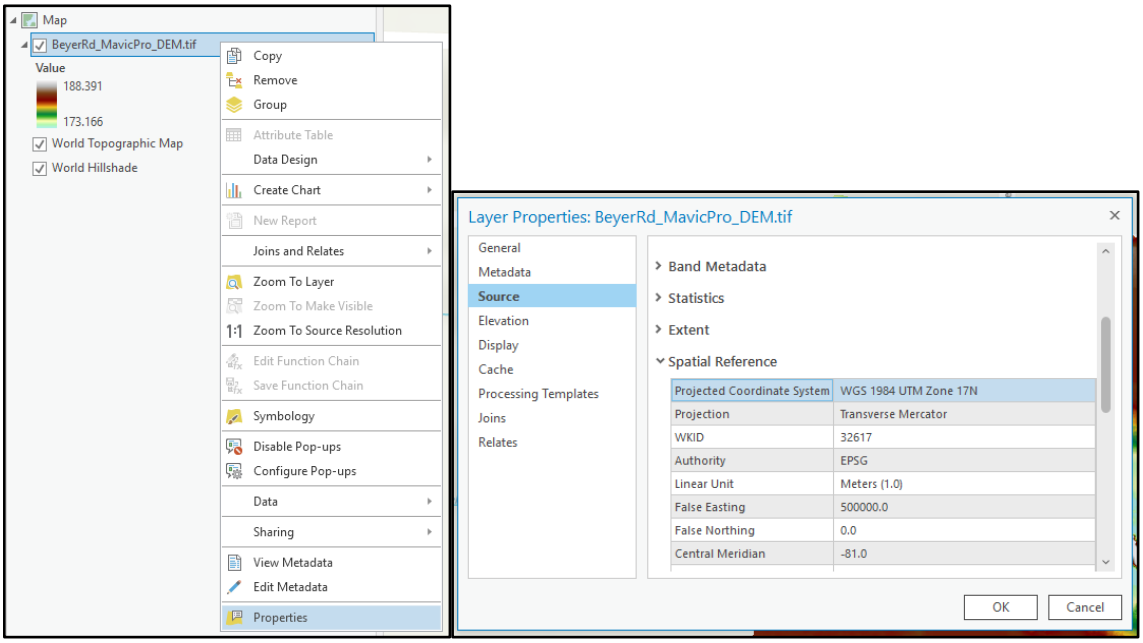

Figure 6.3.1: Identifying the Coordinate System of a DEM in ArcGIS Pro.

2. Creating a blank shapefile with the coordinate system identified in step one above.

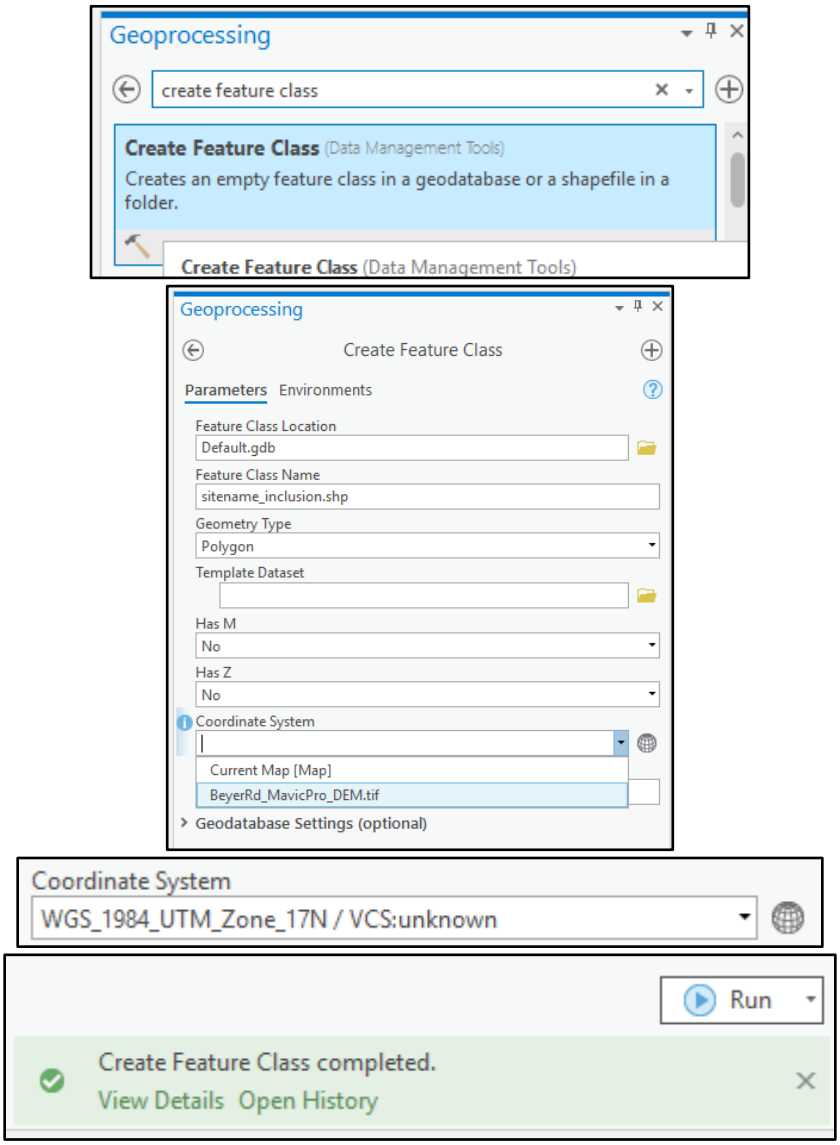

Figure 6.3.2: Creating a new shapefile with a specific Coordinate System.

3. Creating a polygon to be used as the inclusion zone.

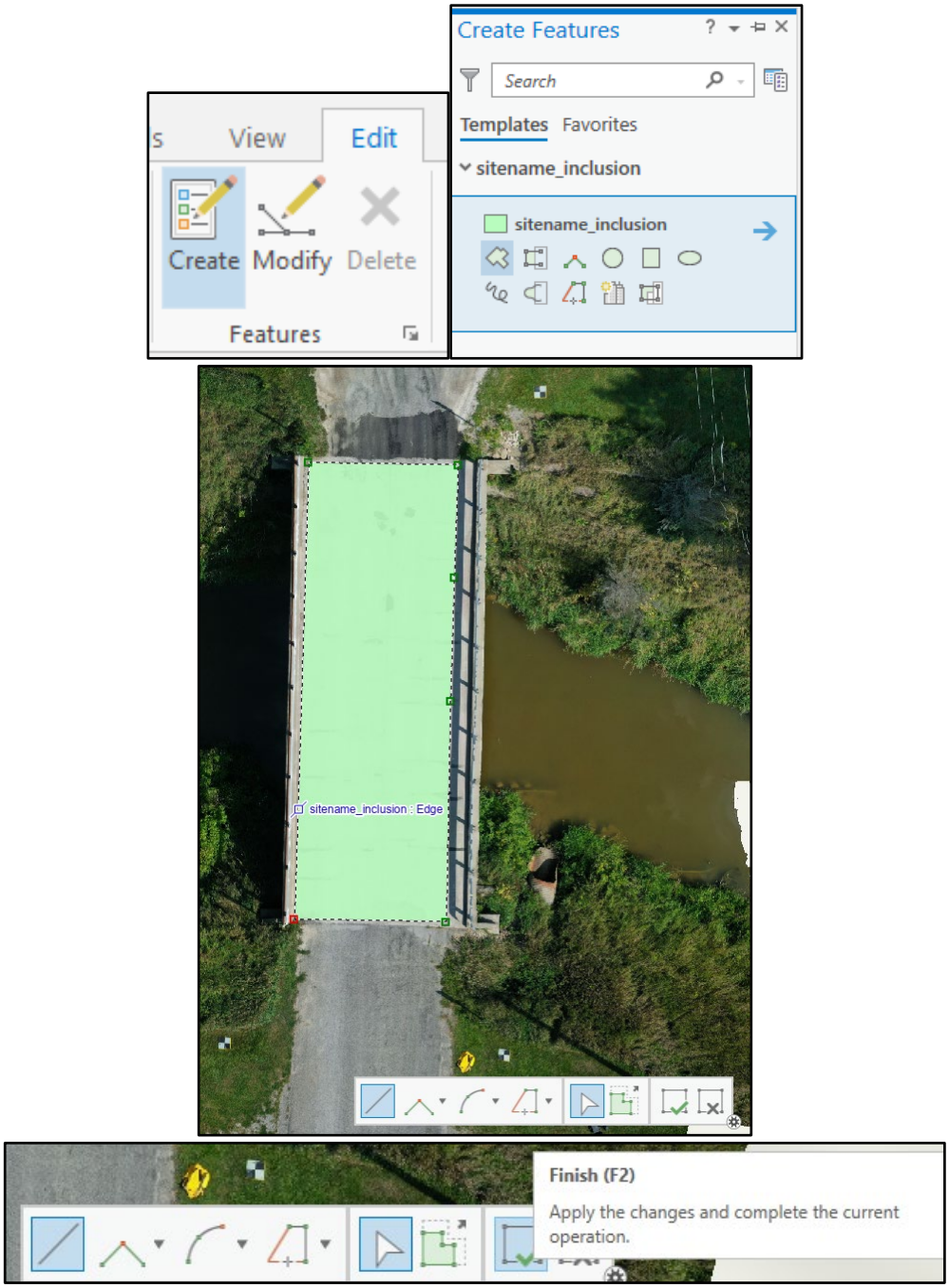

Figure 6.3.3: Drawing a polygon in ArcGIS Pro to set the analysis inclusion zone.

4. Saving the shapefile.

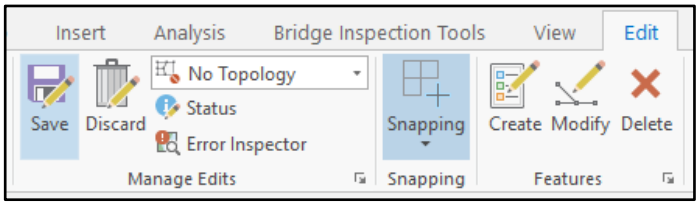

Figure 6.3.4: Saving edits made to the new shapefile.

5. Loading the parameters in the tool dialogue.

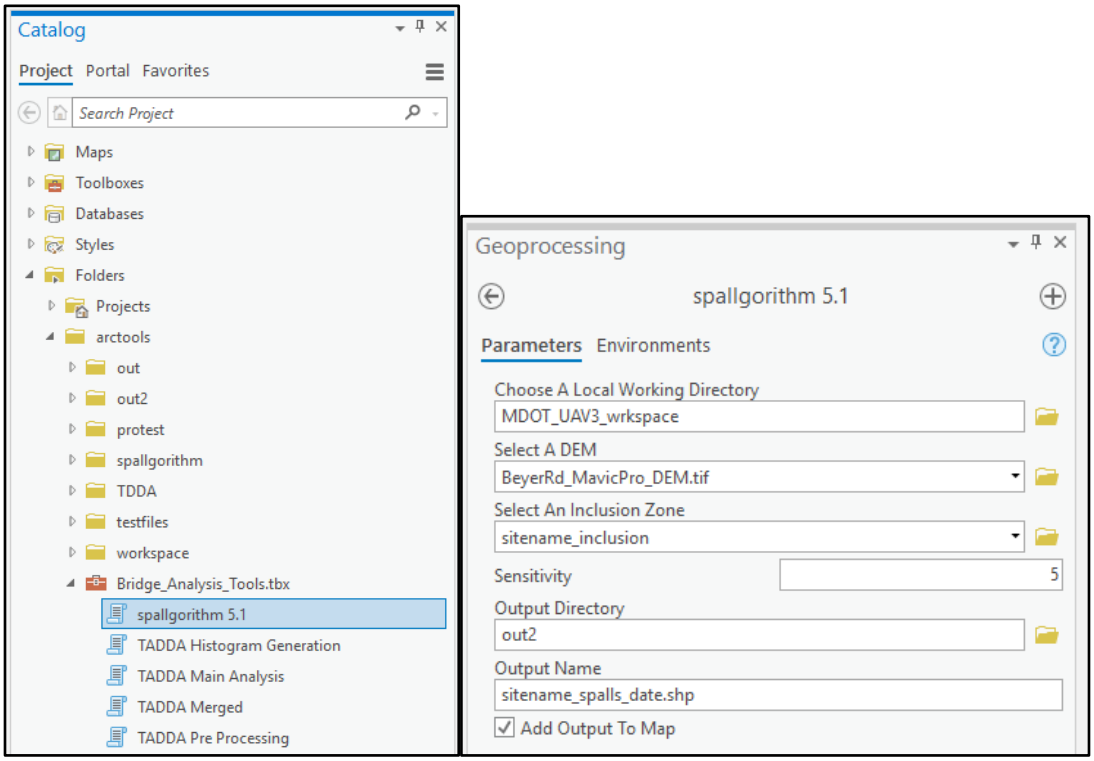

Figure 6.3.5: Selecting the input parameters/layers for use in the Spallgorithm.

6. Looking at the tool messages.

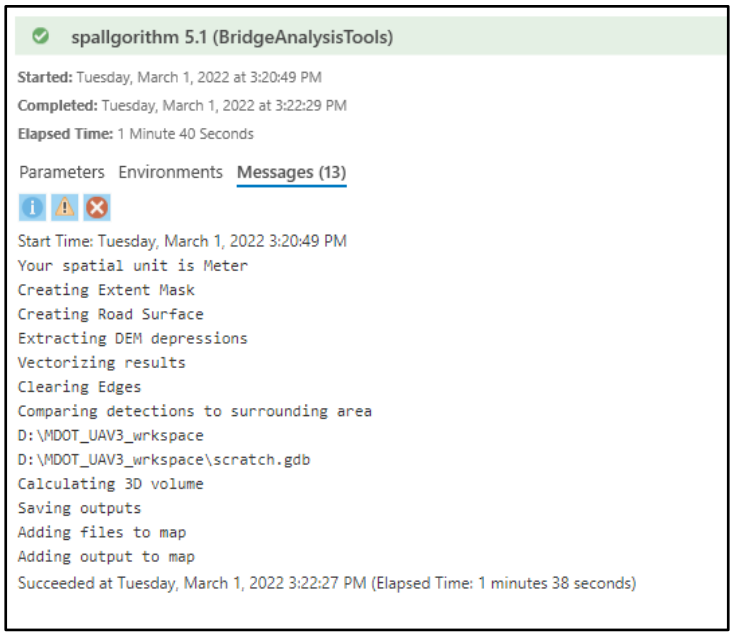

Figure 6.3.6: Inspecting the spallgorithm processing while in progress.

7. Spall output example.

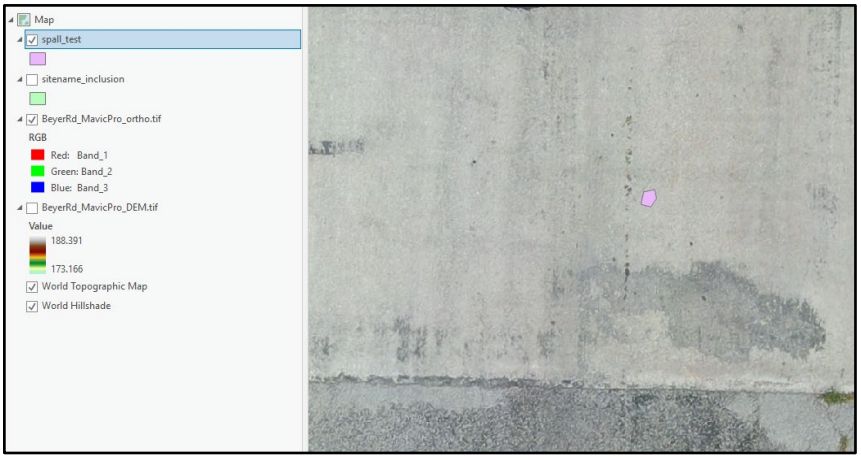

Figure 6.3.7: False positive for Beyer Rd bridge location used as the example. Output is a polygon shapefile with detected spalls. Adjust sensitivity higher to detect more potential spalls, lower to detect less false positives.

6.4 Thermal Anomaly and Delamination Detection Algorithm Manual

1. Overview

The Thermal Anomaly and Delamination Detection Algorithm (TADDA) is an ArcGIS Pro toolbox to detect bridge delaminations. The toolbox is run by a python script that takes in thermal and optical raster for a user defined Region of Interest (ROI) and return delamination polygons.

2. Running the tool

Once the installation is done click on the TADDA Merged script to open the tool execution window (Figure 6.4.1). Add the thermal and optical raster and the area of inclusion (ROI). The optical limit is a user defined entry which can be provided after inspecting the histogram of the optical imagery. This optical imagery should be a one band image which is an average of the three optical bands. A minimum area of threshold and unit of computation should also be entered. The area units can be in square meters or square feet. There is an optional check box that gives the ability to see a histogram of the processed optical data. If checked this will open as a separate window which will remain open even as the other process runs in the background. The working directory, output folder and default output name are the remaining inputs.

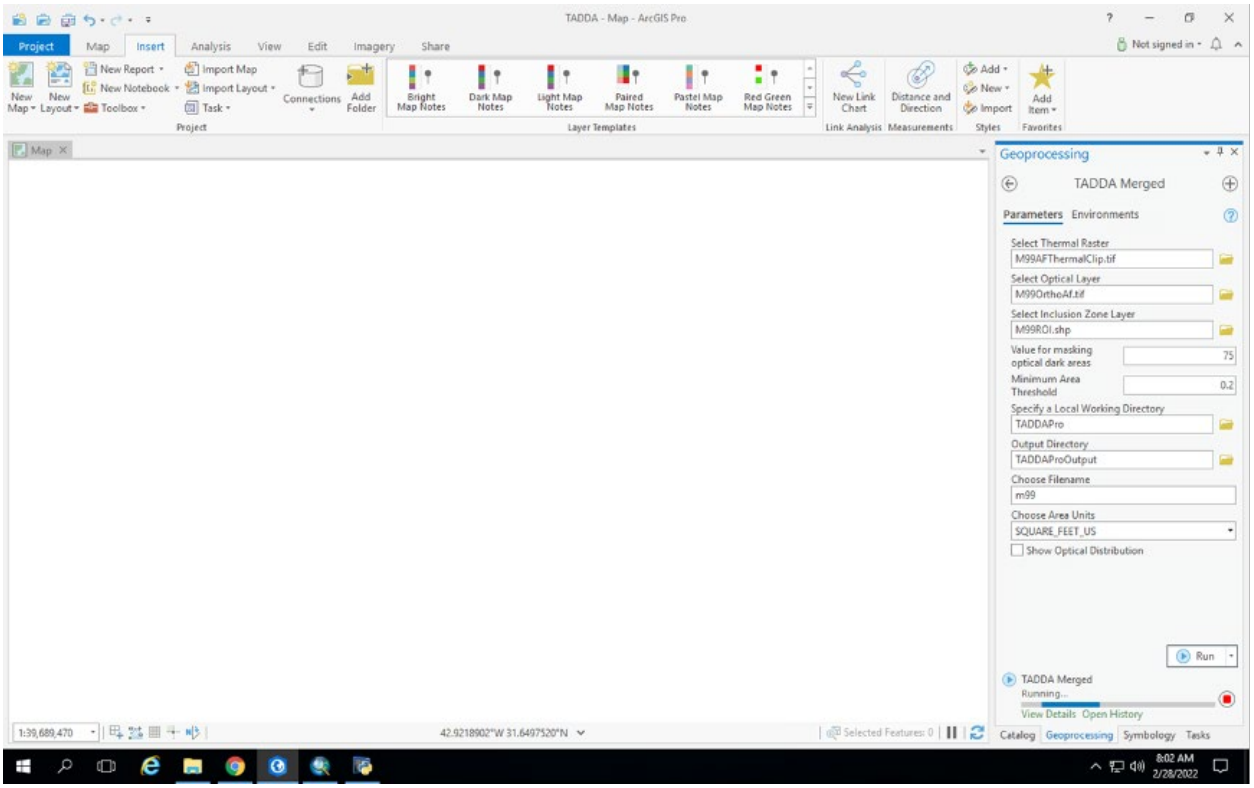

Figure 6.4.1: Loading of the TADDA toolbox and selection of input parameters.

3. Understanding the output

Once the algorithm is run, the final processed delamination result will be stored as a shapefile in the user given folder (Figure 6.4.2) and displayed in the map (Figure 6.4.3). The processing results including the optical and thermal raster clipped to the extent of the ROI and the delamination polygon before eliminating smaller areas will be available in the working directory folder (Figure 6.4.4). It is recommended to have the working directory and output folder as the same path as this would assimilate all the results into one location.

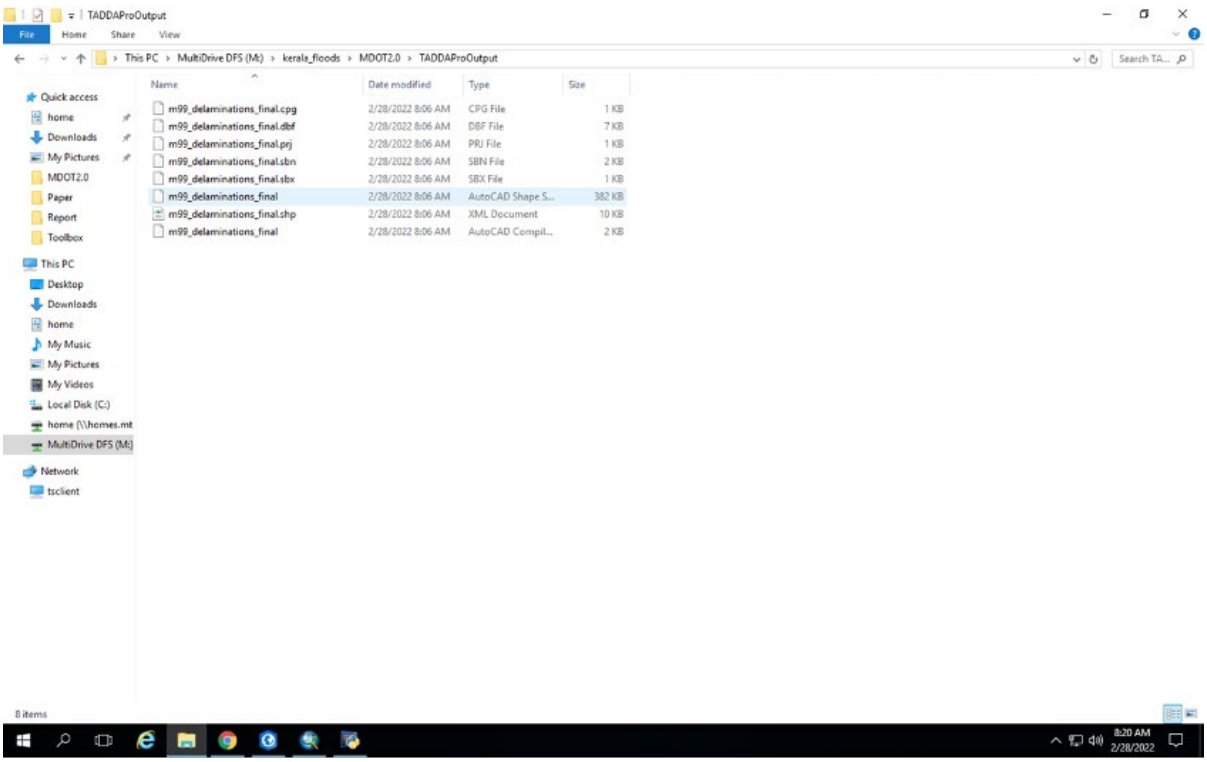

Figure 6.4.2: Final processed delamination result exported as a shapefile in the user defined output folder.

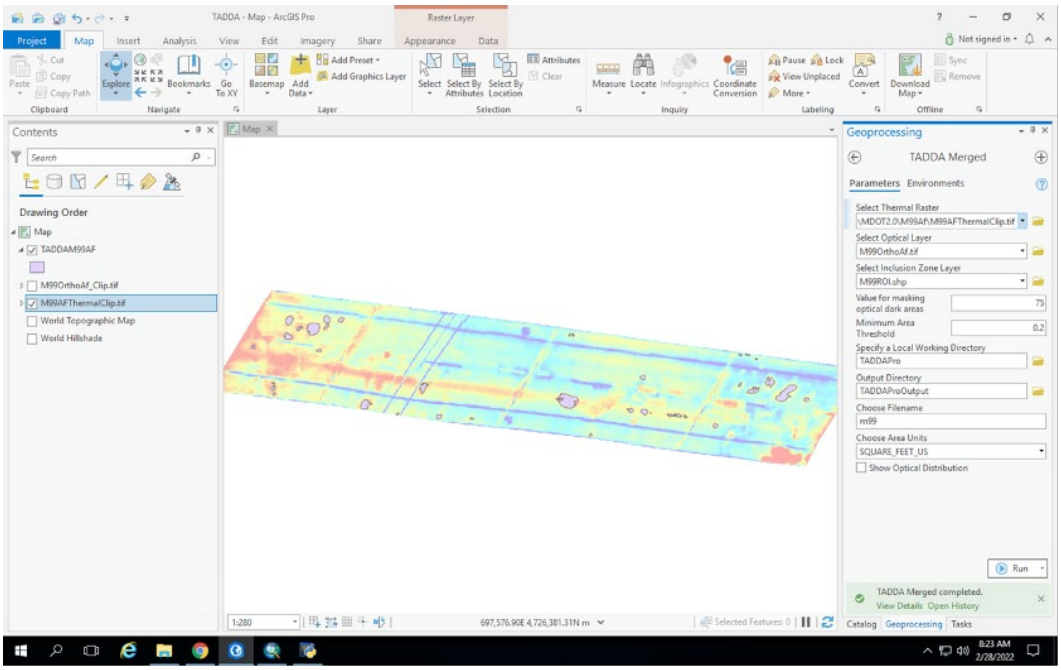

Figure 6.4.3: The result of the TADDA analysis as delamination polygons overlaid over the corresponding thermal raster.

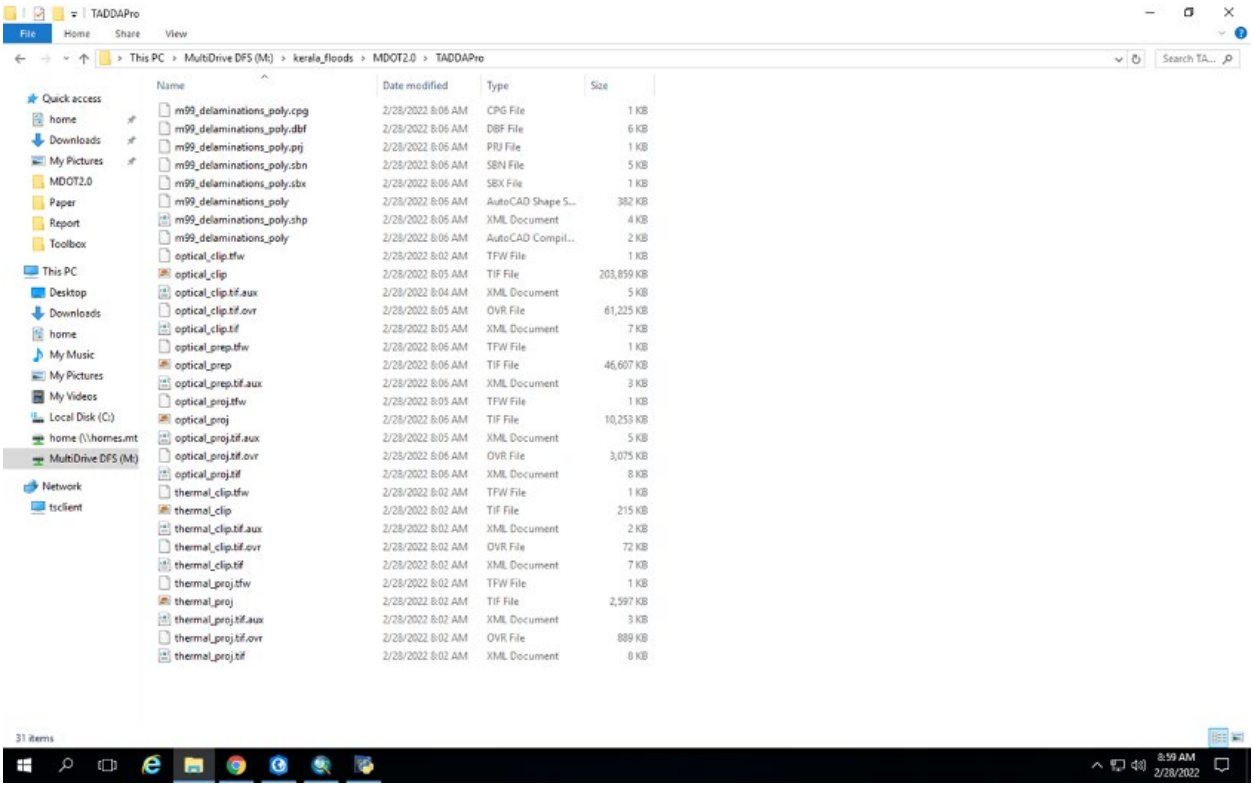

Figure 6.4.4: TADDA processing results saved in the working directory.

6.5 Lidar Ground Control Target Document (FONT SIZE should be consistent throughout report)

LiDAR Ground Control Target Best Practices Write-Up based on US-127 Rives Junction (October 2020) and US-23 Standish (November 2019) UAS LiDAR Data Collections

Chris Cook, Michigan Tech Research Institute (MTRI)
Andy Semenchuk, Surveying Solutions Inc. (SSI)
Colin Brooks, MTRI
February 19, 2021

Completed as part of Use Case Milestone 4: LiDAR UAS for Design Survey, for the Integration of Unmanned Aerial Systems Data Collection into Day-to-Day Usage for Transportation Infrastructure MDOT Research project, Contract No. 2019-0311/Z1

SUMMARY

- Ground control target size and composition should be planned for both hard and soft surfaces prior to the day of a UAS-based LiDAR data collection.
- Ideal ground control target size is dependent upon the point density that one will achieve with the chosen LiDAR sensor and planned flight paths.
  - LiDAR point cloud density is dependent on the speed (mirror speed) of the LiDAR sensor, the drone flight speed, flight altitude, and the amount of drone flight path overlap (minimum 100% overlap is recommended). Software(s) exist that can estimate point cloud density with planned parameters ahead of a survey.
- 3x3 ft plywood (½ inch thick) targets with reflective tape, and 4x1 ft chevron plywood targets also with reflective tape, both made effective ground control targets for standing out in the UAS-based LiDAR scan data. However, they can be unwieldy to deploy. Potential future improvements include changing to lighter materials and making the targets foldable. Additional potential designs and ideas toward target design are included below.
- Simple white and black cloth 2x2 ft photogrammetry-type targets are not large enough or reflective enough for reliably accurate determination of ground control target centers within drone-based LiDAR return intensity data of an average point cloud density.
- Ground Control Targets should be placed at intervals of roughly 500 ft (MDOT and CALTRANS current specification for Mobile and Terrestrial LiDAR), dependent upon necessary data accuracy and the type of surface surveyed, with the survey boxed in by ground control to improve data accuracy at the corners of the surveyed area. Data outside of the area boxed in by ground control should be assumed to be too inaccurate for design survey use.
- LiDAR scan intensity data is scaled for individual tiles; the appearance of the intensity data within a tile will depend on the brightest (and least bright) objects within the tile.

    - If any reflective targets are being used at all as ground control targets in the survey, or if other reflective objects exist within the survey area (e.g., white paint, past survey markers, reflective signage), it then follows that all ground control targets in the survey should be reflective in order to be easily visible within LiDAR scan intensity data (on both hard and soft surfaces).
- It is best to use standardized ground control target types to avoid user confusion and error during point cloud data processing and accuracy assessment. Recording of basic information of each target (e.g., target/point unique number, latitude/longitude/height, photograph taken by the surveyor) should prove to be very useful during data processing, helping to interpret the LiDAR data at each individual ground control target location.
- Due to the potential for conditions to change at a survey site over time (due to seasonal changes or human-induced changes, especially prevalent in “soft” areas), it is best to complete all required portions of a survey (e.g. traditional survey, lidar survey) on the same date or within several days of one another.
- Colorized point cloud data, while useful for LiDAR point cloud visualization, is positionally inaccurate relative to scan intensity data and therefore should not be used for accuracy assessments.
- While using reflective targets will likely appear “fuzzier” than non-reflective targets, the impact of fuzziness on target elevation accuracy can be mitigated by using vector files identical in size and shape to the ground control to identify the true center or surveyed point of the rigid ground control.

Introduction

Selection of adequate ground control targets is an important part of any UAS-enabled LiDAR data survey because the targets must be readily visible within the LiDAR return scan intensity data to be useful in point cloud orientation during processing as well as accuracy assessment . Target visibility within the intensity point cloud will depend on the point cloud density, the design of the ground control target itself, and the reflectiveness of other objects within the surveyed area. The ability of the user to identify the precise x,y, and z location of ground control targets within the LiDAR scan intensity point cloud will in part determine the error of a user’s accuracy assessment of the point cloud.

Effects of Point Cloud Density on Ground Control Target Appearance

As mentioned above, the point cloud density is important in determining the visibility of ground control targets. Density of a point cloud is determined by the mirror speed and pulse repetition rate of the LiDAR sensor being flown, the drone altitude, the drone flight path overlap, as well as the flight speed. Several views of a drone (UAS) point cloud are compared with the point cloud from a mobile (vehicle-based) LiDAR sensor (MLS) below (**Figure 6.5.1**). While MLS data obviously achieves a far greater point density with a much faster sensor that is closer to its ground targets, UAS data are not limited to the extent of smooth drivable surfaces. Drone flight paths can be overlapped and crossed (cross hatching) by the drone operator to increase point cloud density, if desired. Flight speed can also be reduced to increase the density of the point cloud. Mission planning softwares (e.g., Geo-MMS) can provide an estimated point cloud density of a planned survey if one knows the above parameters. Users should note that

increasing the flight path overlap or reducing flight speed will increase the total survey duration and additional flights and batteries may be required to complete the survey.

Knowing the anticipated ground-only point cloud density, one can then estimate the minimum ground control target size required for the survey. Between 50 and 100 points on a ground control target typically provides a usable visualization of a reflective target in the scan intensity point cloud. One can then estimate that using a 3x3 foot square target would be acceptable for a point cloud with a minimum point density of 5.6 points/sqft (50 points/ 9 sqft = 5.6 points/sqft). If one knows the point cloud density ahead of the survey, one can then estimate the minimum ground control target size required for the survey (a point cloud density of 10 points/sqft would suggest a minimum necessary target size of 50 points/ 10 pts per sqft = 5 sqft).

Ground Control Target & Survey Planning

Before getting into ground control target design, it should be noted that ground control targets used in a drone LiDAR survey should be well documented prior to the mission. This is especially important if one is using several different types or designs of ground control targets within a single survey. A situation where this may occur is if one has a large survey and needs to gather together all ground control targets they can find. If one is using several targets with different designs in a single survey (e.g. a white “X” on black field vs. two white and black square fields), the user could find themselves in a “which target was where” scenario and have greater difficulty in identifying the precise center of the ground control point (See **Figure 6.5.2**). This can in part be remedied by achieving a higher point density, or by using standardized ground control targets, but it will be good standard practice to catalog the ground control target type(s) used in each survey.

After reviewing MDOT’s Development Guide, Chapter 9: Remote Sensing Section 9.1.3, it is apparent that careful inventory (via whiteboard and photographs) of ground control targets within the survey area is recommended, but optional, to surveyors (**MDOT, 2018**). We would recommend, at minimum, a GPS-enabled photograph be taken of each ground control point (GCP) along with its name/unique identifier. Surveyors should note for each GCP precisely where on the target its GPS coordinates were collected. This information would provide surveyors with general lat/long and visual ground-truth to return to when processing data and locating GCP centers or edges in LiDAR scan intensity data. Unique identifiers for the GCP can be added to the picture using a whiteboard or similar method. Surveyors should avoid altering the ground control points in ways that might make it more difficult to identify the exact surveyed location in the scan intensity point cloud. For instance, tagging the surveyed corner of the GCP with paint may actually make it more difficult to determine the precise location of the surveyed GCP tip in the scan intensity point cloud during post-processing. If surveyors need to tag ground control to show that it has already been surveyed, or to show where it has been surveyed, tags should be placed a distance from the GCP greater than double the anticipated point cloud spacing (at minimum).

Placement of ground control targets in the survey area should occur at roughly 500 foot intervals to align with MDOT’s current specifications for mobile and terrestrial LiDAR, which are based upon California DOT’s MTLS Local Registration and Validation Requirements (**CALTRANS, 2018**). As specified by CALTRANS’s target recommendations, high-accuracy

surveys of hard surfaces (“Type A” surfaces, as described in CALTRANS, 2018) like roadways should have ground control on both sides of the roadway at a maximum of 500 ft spacing. Soft surfaces or surveys requiring less accuracy (“Type B” surfaces (CALTRANS, 2018)) can have ground control point spacing of up to 1500 ft. If a higher accuracy survey of Type B surfaces is desired, more closely spaced ground control will be needed. The extent of the surveyed area should also be bounded by ground control. This will help to avoid the presence of inaccurate point cloud data at the edges of the point cloud. Any data that extends out beyond the survey area bounded by ground control should be assumed inaccurate. The survey should consist of scan-acquisition targets (SCATs) and validation targets (VATs). SCATs will be used to accurately orient the point cloud during processing, while VATs will be used only for post-processing accuracy assessment of the processed point cloud. SCATs should be placed uniformly as described above, while VATs can be placed semi-randomly but evenly in the surveyed area. VATs should be placed such that they cover all types of ground cover within the survey area (both hard and soft surfaces), and such that they are distributed over the entire survey area (capture roughly the full extent of the surveyed area), to ensure that one’s accuracy assessment from these VATs is representative of the entire survey area (**Bailey, 2012**).

Surveyors planning a UAS-based LiDAR survey should understand that the majority of surveyed areas (especially “soft” areas) are subject to subtle changes in elevation due to environmental factors (i.e. erosion, subsidence, deposition, and decomposition of vegetation) as well as human factors (i.e. mowing, plowing, management, and movement of materials). See **Figure 6.5.3** for an example where gravel piles were present in drone LiDAR data (collected in November 2019) but not the MLS data (collected in Summer 2019) at the Standish, MI, site. Surveyors should note that an area that experiences such considerable change may change rapidly over short time intervals. Because of this, surveyors should try to complete all types of surveys (i.e. traditional surveys, drone LiDAR surveys, MLS surveys) of a single location at the same time or within a few days of one another whenever possible. While the user might not be surveying privately-held areas that may be subject to faster or unpredictable rates of change in elevation (such as vegetation control), it can be assumed that the elevation of soft surfaces along right-of-way corridors and similar areas that are mown will be more subject to changes in elevation over time relative to hard surfaces (e.g., pavement, asphalt, packed dirt). This could confuse surveyors' attempts to compare the accuracy of different LiDAR data collection methods, leading surveyors to misattribute differences between datasets collected at different times as an inaccuracy inherent in a collection method or survey.

In addition to soft Type B surfaces being more susceptible to changes in elevation, surveyed soft surfaces are more likely to be underneath dense vegetation (e.g., trees) that can shadow the ground surface from the drone-based LiDAR (**Figure 6.5.4**). Although LiDAR (like radar) scan patterns create dense enough point clouds for surveying the ground, the presence of vegetation, foliage, and especially woody vegetation effectively filters the number of LiDAR points that are able to reach the ground and be reflected back to the LiDAR scanner. This can create a point “shadow” effect where the LiDAR point cloud is less dense or less evenly distributed underneath trees. While this can be in part remedied by performing LiDAR data collections following leaf-off, this will not be effective for surveys of coniferous areas where point cloud shadows will be unavoidable or when data collection has to be completed during leaf-on seasons. Cross-hatching, or flying the LiDAR sensor over the same area in multiple different

directions, is one effective method of reducing the size of tree-induced shadows and improving distribution uniformity in the point cloud for the ground surface. Surveyors could pre-plan ground control placement in these areas by placing targets on the ground in areas that are beneath larger holes in the canopy (i.e., by checking the area in recent imagery in Google Earth). This will at least improve the point cloud density achieved on the ground control targets in these densely vegetated areas.

Ground Control Target Construction and Design

We have tested ground control targets that varied in construction, materials, and size to determine what composition provides adequate visibility within a LiDAR intensity point cloud. For the survey area flown by project partner Surveying Solutions, Inc. (SSI) at three areas along US-127 near Rives Junction, MI, we constructed and compared several different example ground control targets: 3x3 sq ft matte black paint and reflective white survey tape fields on 15/32 inch plywood, 4x1 ft reflective white survey tape on 15/32 inch plywood in a chevron shape, 4x1 ft 15/32 inch bare plywood (with no tape or finish), and 3 ft x 8 inch reflective tape chevron placed directly on asphalt/concrete (see **Figures 6.5.5 & 6.5.6**). We found that the reflective tape (already commonly used in road surveys) is an effective way to make the ground control targets stand out or “pop” from the background in the scan intensity data. In Figures 6.5.5 & 6.5.6 we are able to see how the 2x2 ft photogrammetry targets (made of semi-porous, foldable cloth) are not as visible as the reflective targets included in the survey. In **Figures 6.5.6 & 6.5.7** we can see that a bare plywood 4x1 ft chevron was not reflective enough to be visible within the scan intensity data, suggesting that painting targets or adding reflective tape to them is a minimum requirement for targets to be visible. The lack of reflectivity of the bare plywood is described further below.

In **Figure 6.5.7**, we can see a plotted cross-section (3 feet wide) of scan intensity points that correspond to several different ground control targets tested during the US-127 survey. Plotted values show the intensity of return points along the 17-foot-long transect. One can see that the highest intensity points correspond to the 3x3 ft reflective square GCP, while the unfinished plywood target and 2x2 ft cloth photogrammetry target both had considerably lower intensity values. The larger and more reflective targets make it easier to discern the exact center or tip of the target where the high-accuracy GPS data were collected.This will in turn make it easier for the user to assess and more precisely estimate the point cloud accuracy.

While using these targets in the field we noted several additional benefits and drawbacks of the larger plywood targets as we had designed them. The 15/32” plywood (for both the 3x3 ft and 4x1 ft targets) was sufficiently heavy that it was able to ‘mat’ down the vegetation underneath the target to allow the target to sit relatively flush with the ground surface. This is an improvement over the cloth-type photogrammetry target which was more difficult to force to stay in contact with the ground in an area densely vegetated with tall grasses and horsetail (a common soft road-side surface). There was little risk of these plywood targets blowing away or shifting due to wind gusts or passing vehicles because of their weight. The 3x3 ft square targets and 4x1 ft chevrons were, however, relatively heavy, and unwieldy, which made it difficult to quickly deploy several targets at one time. It is feasible that one could build folding (hinged) plywood targets that would be easier and faster for surveyors to transport/store (if they fold down) and deploy (carry and place more than one target at a time). Smaller targets may be

possible and still provide sufficient reflective area for target identification (dependent on point cloud density).

An additional and likely improved chevron design option, although not tested in these field surveys, would be a white reflective chevron (similar to as tested) with matte black cloth, tape, or wood underneath the surveyed tip of the chevron. The addition of the matte black material would enhance the contrast of the tip of the chevron with the underlying ground material. Reflective tape on wood designs tested and shown here could be made much lighter and easier to carry by using a thick matte black fabric (could be painted matte black) in place of wood. White or yellow reflective tape could be stapled to the matte black fabric in a square (or chevron) pattern that allows the target to be folded down to a quarter of its size, making it easier for a single surveyor to carry and deploy several GCPs at one time. While this would make the targets lighter, the rigidity of the ground control target can be beneficial to exploit during post-processing (this discussed in more depth later).

Other Factors Controlling Ground Control Target Visibility

Ultimately, the visibility of ground control targets within the LiDAR scan intensity data is going to be determined by the point cloud density and the relative brightness of the target to other objects in the data tile. This is counterintuitive to a typical assumption (e.g., with photogrammetry) that the target must simply stand out relative to the surface onto which it is placed. Visibility of the precise tip (e.g., of a chevron) or center (e.g., of a square field) of a GCP will be determined by the GCPs intensity relative to the ground surface it is sitting on as well as the intensity of all other objects within the data tile.

Also, each tile will be scaled somewhat differently depending on what was visible to the LiDAR sensor in that tile during the survey. If the entire survey area is created as a single tile, then the scan intensity data will be scaled to the most and least reflective objects in the whole survey area. If there are objects that are more reflective than the ground targets in the survey area then these objects will effectively “dim” the appearance of the ground control in the scan intensity data. Figures 6.5.7 and 6.5.8 show an unfinished plywood 4x1 ft chevron (no reflective tape) compared to a 4x1 ft chevron with reflective tape in both an RGB orthophoto and the LiDAR scan intensity data. The plywood is very difficult to see because the LiDAR scan intensity data has been scaled to the brightest and dimmest objects within the tile (the reflective ground control targets and pavement lines, and the matte black of the ground control targets, respectively). **Figure 6.5.8** shows how several ground control targets vary in their scan intensity relative to the road surface and road edge lines (white paint). Because road edge lines are going to usually be present in LiDAR surveys of paved road ways, we recommend the use of reflective tape or other reflective materials in the construction of ground control targets. Unpaved (dirt) roadways or old roads with worn-away lane markings are likely to have fewer painted or reflective surfaces within the surveyed area, but reflective signage, guardrails, or other objects not predicted to be within the survey area may still impact the intensity scaling of LiDAR data.

Colorized (RGB) point clouds also exist to aid in the display of LiDAR data. Colorized point clouds are essentially made by performing both image collection (using RGB camera) and LiDAR data collection (using LiDAR sensor) onboard a drone at the same time. A camera

calibration matrix is created to allow the mapping of the image pixel values onto the LiDAR points. This process involves the user manually selecting points on both the point cloud and the image to calculate this matrix. The RGB color is then estimated for each LiDAR data point in post-processing. While useful for visualization of the point cloud in color familiar to the eye, users should note that these data should NOT be used for assessing the horizontal or vertical accuracy of the point clouds. The algorithms used to tie the RGB color to the LiDAR point clouds are not going to be as accurate as the scan intensity data in determining precise location of ground control because of the inaccuracies caused by the mapping of the image pixels to the LiDAR points.

Potential Adverse Impacts of Reflective Targets on Elevation Determination

It is known that all surfaces surveyed by LiDAR systems develop a “fuzziness” in their distance ranging estimates due to both systematic and random sources of error inherent in the system and other processes that reduce point cloud precision (**Figure 6.5.9, Certainty3D, 2015**). In addition, LiDAR and laser ranging systems scan intensity values are impacted by system transmittal power, range to object, angle of scan incidence, atmospheric transmittance, and a number of other parameters. Highly reflective objects that are close to the LiDAR scanner can exceed the scanner’s detection threshold, resulting in truncating the peak of the return pulse (saturation) and causing an underestimation of the distance to the reflective object. Reflective objects that are far from the sensor can experience a blooming effect that makes the object appear larger in the point cloud than they truly are because of a bleeding effect of the reflective object on adjacent LiDAR pulses (**Kashani, 2015**).

While reflective tape is a useful way to make ground control targets “pop” from the background and improve x&y target localization during post-processing, surface reflectivity will be an additional source of error that impacts the ability of the user to determine the precise elevation of the targets in LiDAR data (**Figure 6.5.10**). Figure 6.5.10 shows an example where the reflective targets have a significant, albeit small, impact on the elevation of the ground surface that cannot be explained by the thickness of the rigid plywood ground control (15/32 inches).

Because of this additional source of elevation error caused by using reflective ground control, point-picking (e.g., pointing and clicking) for identification of ground control centers (or points) is likely going to be less accurate for z-coordinates relative to x/y coordinates.

To ensure the most accurate possible elevation estimate of ground control elevation for GCPs, surveyors conducting LiDAR post-processing should use 3-dimensional vector files that accurately represent the ground control to determine precise GCP point location and elevation (**Figure 6.5.11**). Moving these vector files by altering their position, pitch, roll, and elevation within the point cloud will help accurately estimate the elevation of the center of the ground control points (or edge if using chevrons). Using this more accurate method for identification of ground control centers will help get away from point-picking and produce more accurate estimates of ground control elevation.

The impact of reflective surfaces on fuzziness also suggests the importance of having non-reflective surfaces (e.g., matte black fields) integrated into the ground control target. The reduction in fuzziness for these fields in a ground control target will aid in determining the precise elevation of the target, while the reflective fields will assist in determining the precise x,y

location of the target. Knowing the impact of the reflective and non-reflective portions of the ground control will assist post-processors in fitting the 3D vector file to the LiDAR data to best approximate the ground control center in x,y, and z.

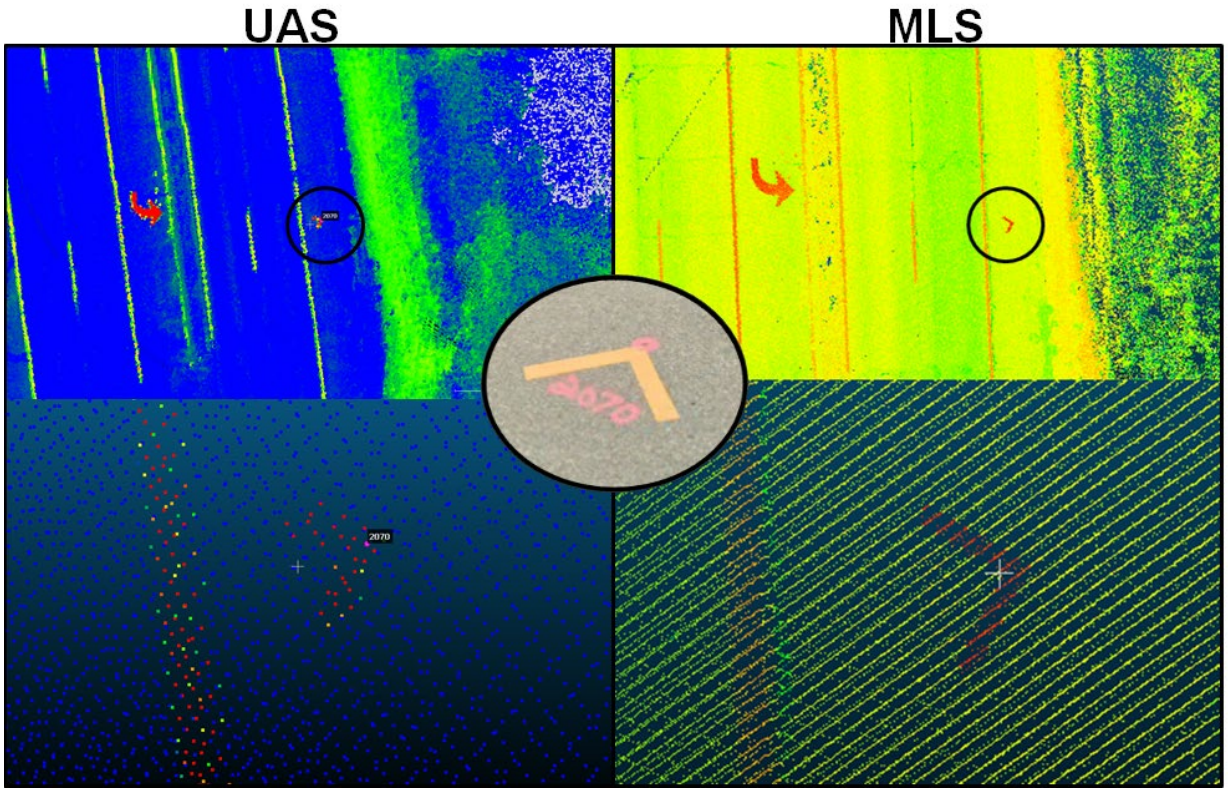

Figure 6.5.1: Example UAS and MLS scan intensity point clouds of hard surfaces from the Standish, MI US-23 survey completed by SSI for MDOT.

~~The~~ This UAS LiDAR data was collected November, 2019, while the MLS data was collected in the summer ~~sumer~~ of 2019. Comparison of UAS (left) and MLS (right) LiDAR point cloud ground-only points as represented by the point return intensity values (blue/green/yellow = relatively low intensity, orange/red = high intensity) of a commonly used surveyor ground control point "chevron". This chevron is made of 4" wide by roughly two-foot-long pieces of glass-beaded reflective tape (e.g., Brite-Line Tape) formed at a roughly right angle. Locations displayed are the same for the UAS and MLS data. Note the increased point cloud density of the MLS data relative to the UAS data. **Accurate MLS data collection is limited to 10-20 feet within the roadway (areas driven by vehicle) while the drone data extends beyond the roadway and its extent is defined by the drone flight path.**

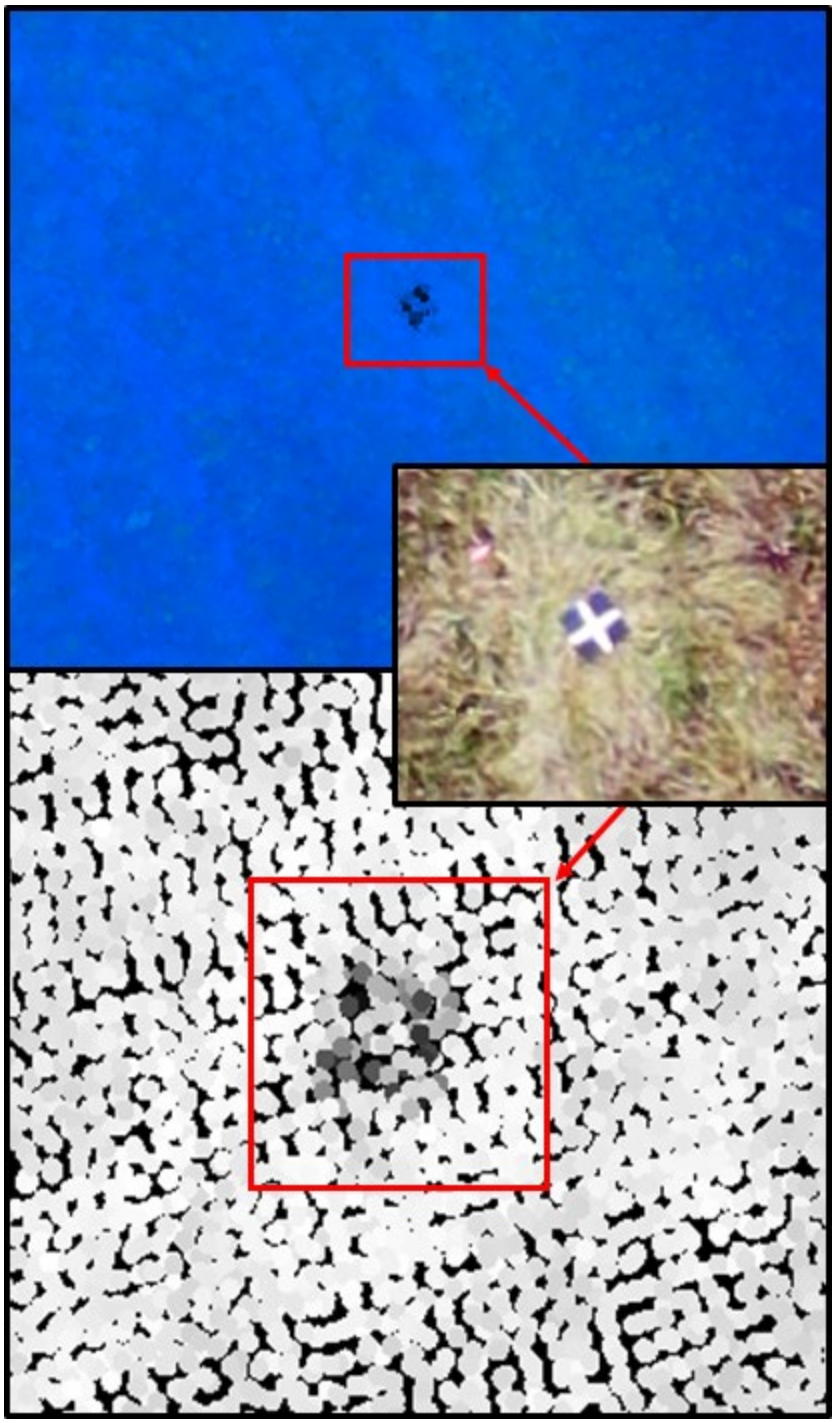

Figure 6.5.2: Example UAS ground-only point cloud of return intensity data of a common 2x2 ft white and black cloth field photogrammetry ground control target on top of soft surfaces (grassy field) (Standish, MI, November 2019).

Figure 6.5.2 is showing the relative low intensity contrast of the cloth material, and the relatively small size of the target (coupled with the low point cloud density) makes it difficult to determine the precise center of the target where it was surveyed for its X,Y, Z position. **It would be difficult to discern the type of**

ground control target this was if the scan intensity data was the sole information a surveyor had to identify the target type.

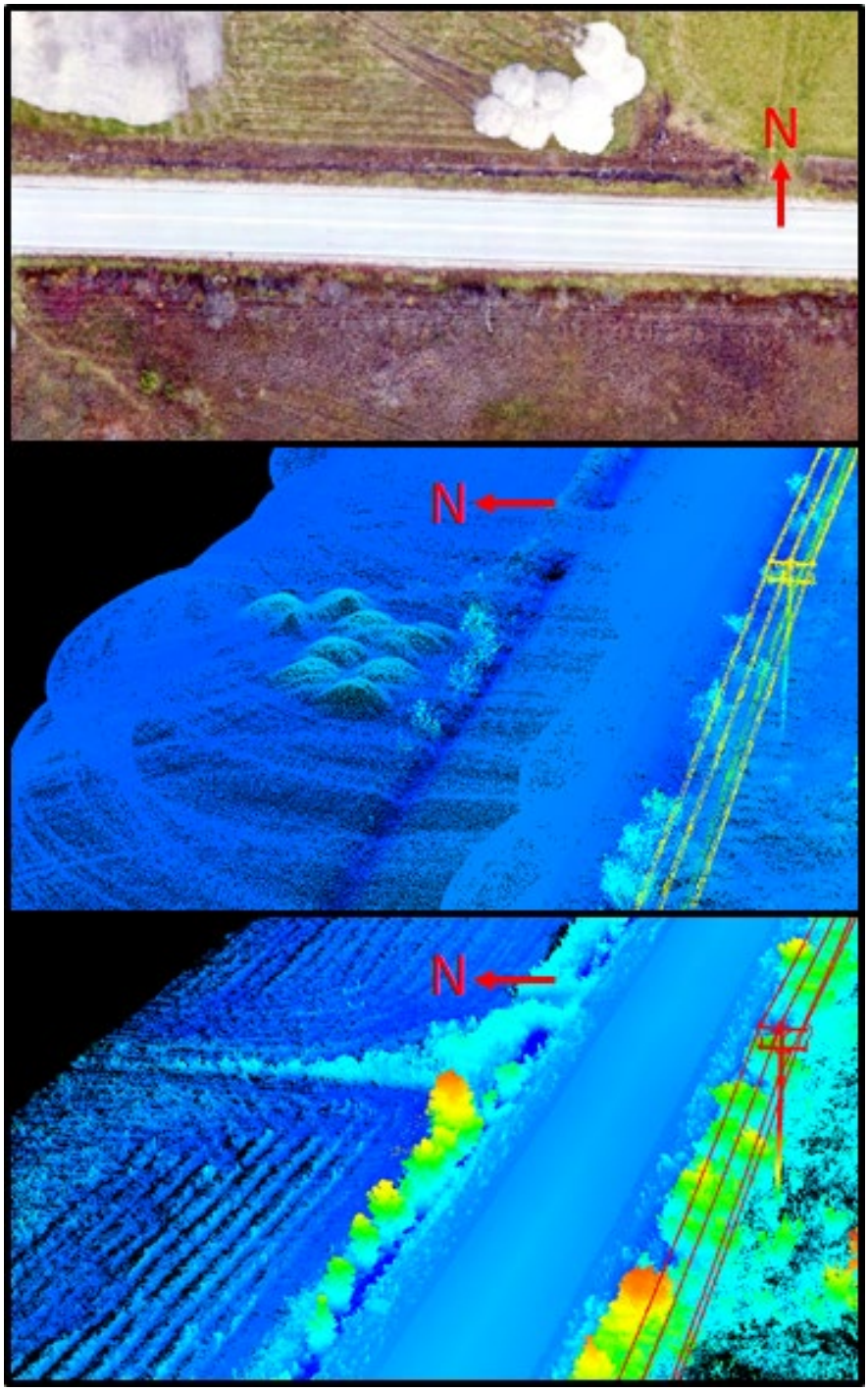

Figure 6.5.3: Comparison of drone orthophoto (top), UAS LiDAR (middle), and MLS (bottom) LiDAR data (color scale indicates elevation) collected in Standish, MI.

The drone orthoimage and LiDAR data were collected in November 2019 while the MLS data was collected in summer of 2019. One can see ephemeral features (white gravel piles, rows of planted crops) that are present in the drone orthophoto and LiDAR data that are not present in the MLS data and vice

versa. **Surveyors and engineers should not assume that soft ground surfaces for private areas, or public areas managed for vegetation, will maintain a consistent elevation (on a centimeter level) over even very short time scales.**

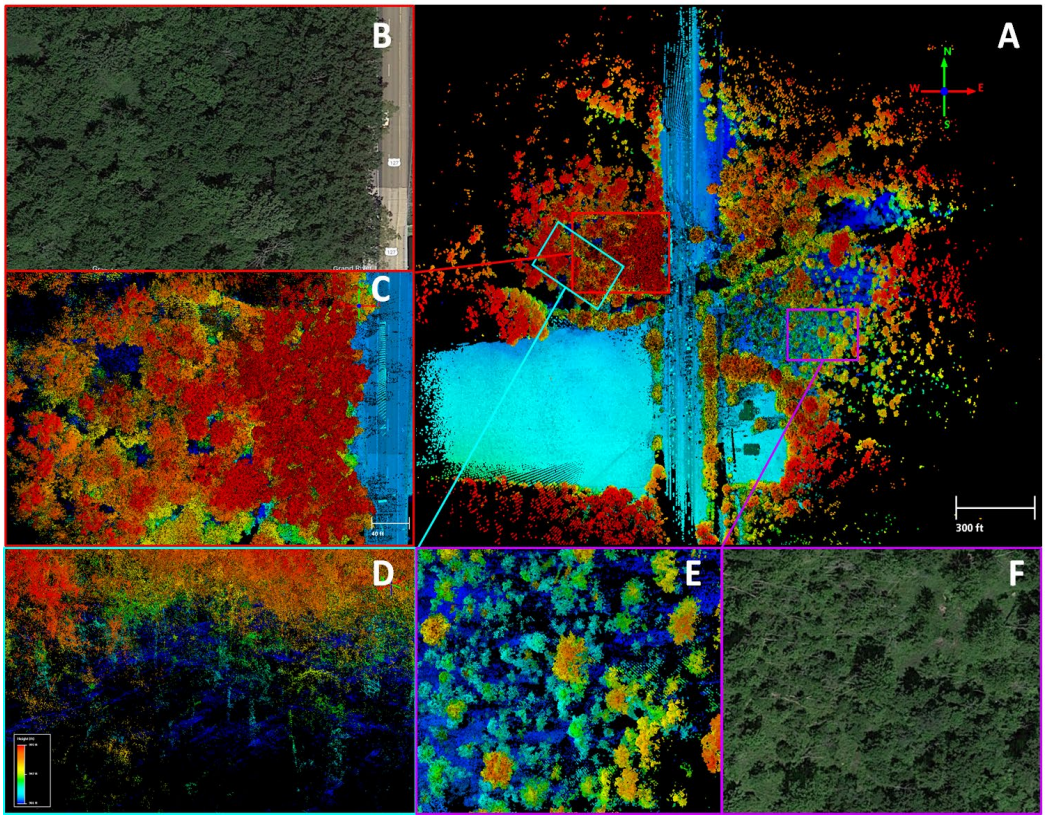

Figure 6.5.4: A: LiDAR data collected for site US-127 site over Grand River outside Rives Junction, MI (October 2020).

In Figure 6.5.4, LiDAR points are symbolized by elevation (blue = low, red = high) and intensity (brighter color = more intense return). In this image the blue areas tend to indicate the ground surface while yellow/orange/red indicates tree canopies. Black areas indicate areas with no data. LiDAR data was collected in September, 2020, when leaves were still present on trees. B: Google Earth imagery of a subset selection of the survey. Canopy is mostly deciduous with some holes present. C: LiDAR data for the same subset as shown in B. D: LiDAR point cloud viewed from the side profile showing shadows/ nonuniform distribution in the ground point data caused by trees. E: Shadows present in a more sparsely vegetated area that did not experience cross hatching, and F: Google Earth imagery of the subset shown in E. The area shown in E and F did not experience the same amount of cross hatching as in areas B through D, so longer single-direction shadows exist in E and F. **While LiDAR can penetrate vegetated tree canopies to the ground surface, some LiDAR scans are intercepted by woody vegetation which reduces achieved ground point cloud density under dense vegetation.**

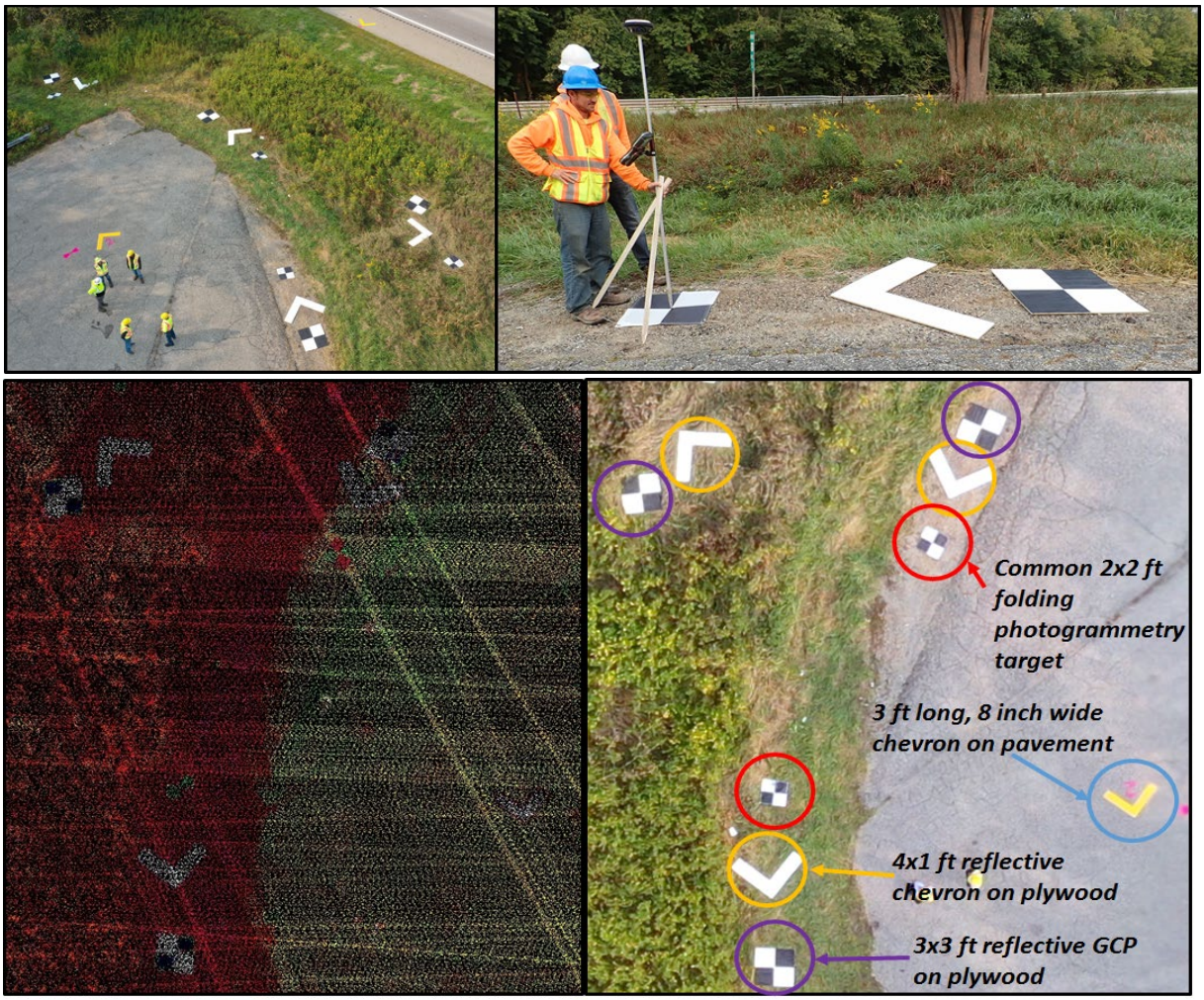

Figure 6.5.5: Top left: Test ground control targets at the US-127 over Grand River site outside of Rives Junction, MI (October, 2020). Top right: 2x2sqft photogrammetry target, 4x1sqft plywood chevron target with reflective tape, and 3x3sqft plywood square target with reflective tape and matte black paint. Bottom right: A selection of different ground control targets as seen in a Mavic 2 drone RGB orthoimage. Bottom left: LiDAR point scan intensity of return data collected at the Grand River site.

Ground control targets constructed for this data collection show how reflective and enlarged 3x3 ft targets "pop" to the viewer's eye more readily than common 2x2 ft photogrammetry ground control targets which had a brightness similar to background vegetation. **Any improvement of visibility of targets in the drone LiDAR scan intensity data will improve the ability of users completing data processing to precisely pick locations surveyed for GPS, ultimately improving the user's ability to determine X and Y accuracy for point clouds.**

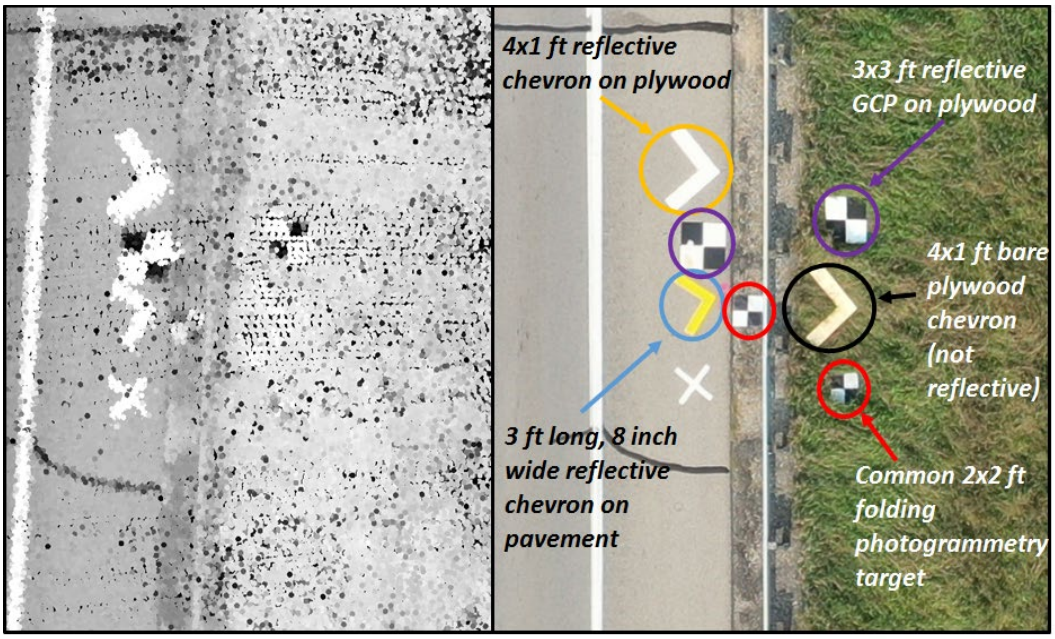

Figure 6.5.6: A selection of different ground control targets as seen in Mavic 2 RGB imagery (at right) and LiDAR point scan intensity of return data (at left) collected at US-127 over railroad site outside of Rives Junction, MI (October, 2020).

This figure shows how reflective ground control targets are more visible than non-reflective targets in LiDAR scan intensity data. Notice how the 4x1 ft bare plywood chevron (not reflective) is relatively bright and easily apparent within the Mavic 2 RGB image, but is almost indistinguishable from the surrounding area within the LiDAR scan intensity data.

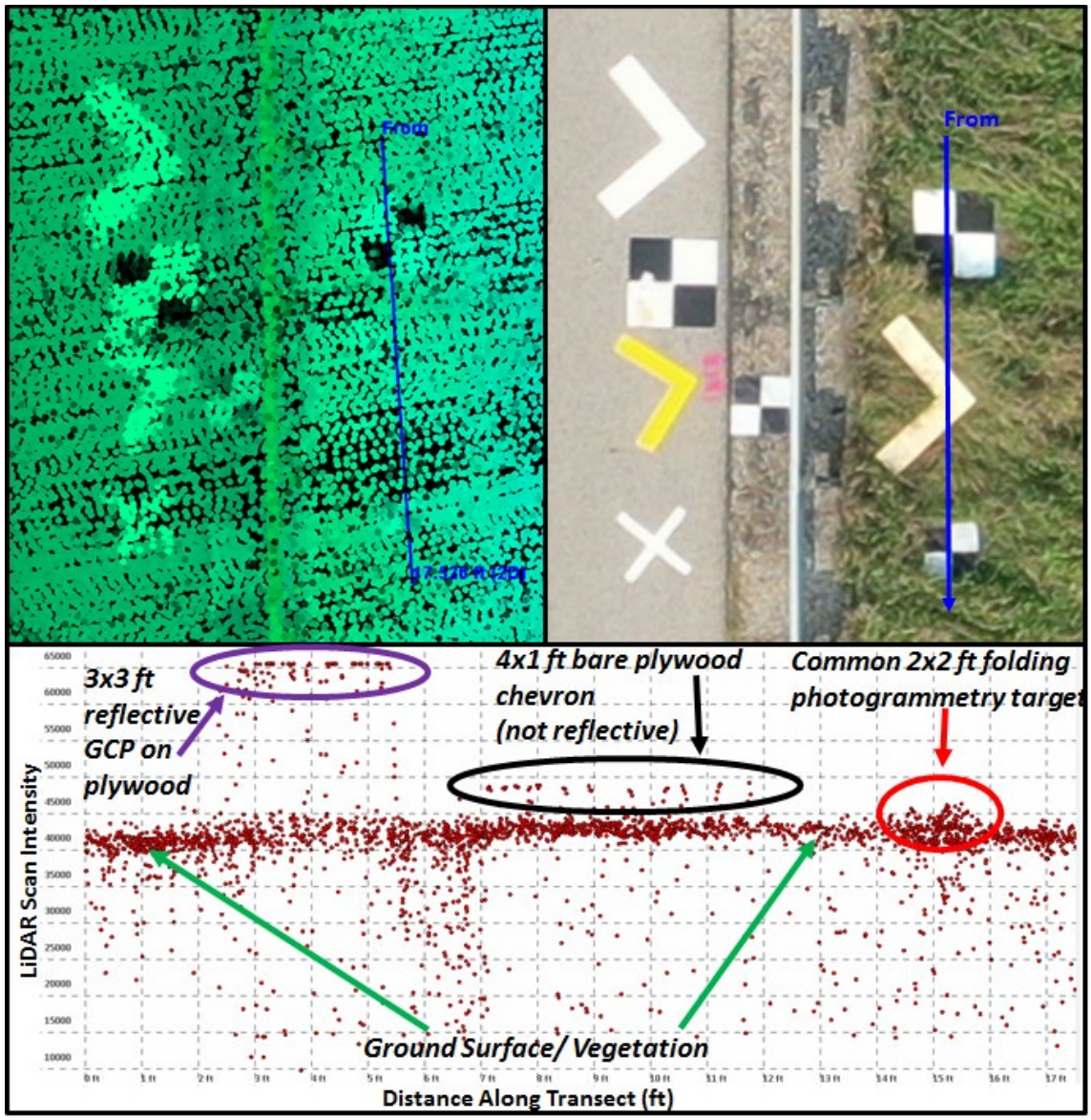

Figure 6.5.7: Mavic 2 RGB image (top right), LiDAR scan intensity data (top left), and three foot wide cross-section of LiDAR scan intensity data that crosses several example ground control targets (bottom). See figure E for a description of each type of target in this image.

This figure quantitatively shows how ground control targets made of different materials appear differently in LiDAR scan intensity data, with more reflective targets being more visible and having a greater scan intensity. The blue line drawn in the top two images is the cross-section shown in the bottom image.

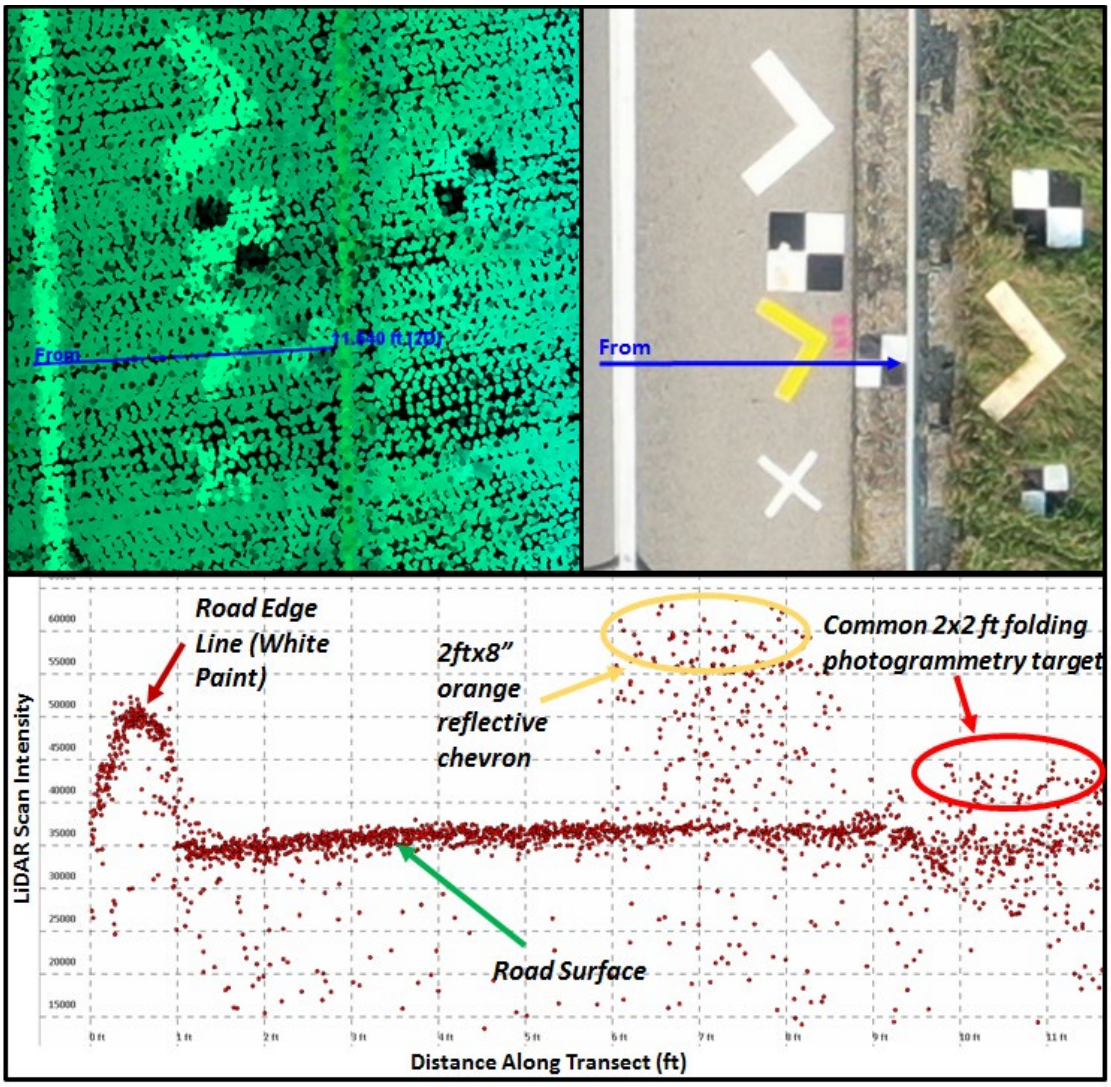

Figure 6.5.8: Mavic 2 RGB image (top right), LiDAR scan intensity data (top left), and three foot wide cross-section of LiDAR scan intensity data that crosses several example ground control targets (bottom).

This figure shows how ground control targets compare in scan intensity relative to painted road edge lines, features that will likely be pervasive in LiDAR surveys of paved road ways. The blue line drawn in the top two images is the transect shown in the bottom image.

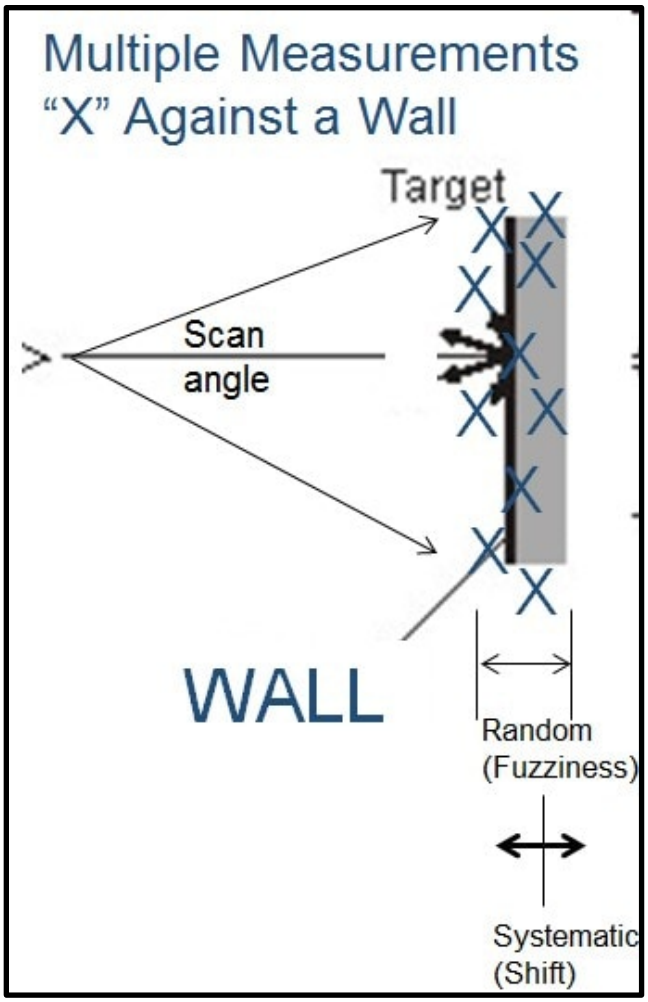

Figure 6.5.9: Diagram of incident theoretical LiDAR lasers scanned vertically along a flat wall. Each measurement is represented by an "X". Long or short measurements (caused by various sources of error) therefore represent the wall with some thickness (fuzziness). Image courtesy of Certainty3D/TopoDOT (Certainty3D, 2015). **Objects of enhanced reflectivity can enhance this "fuzzyness" or surface elevation error.**

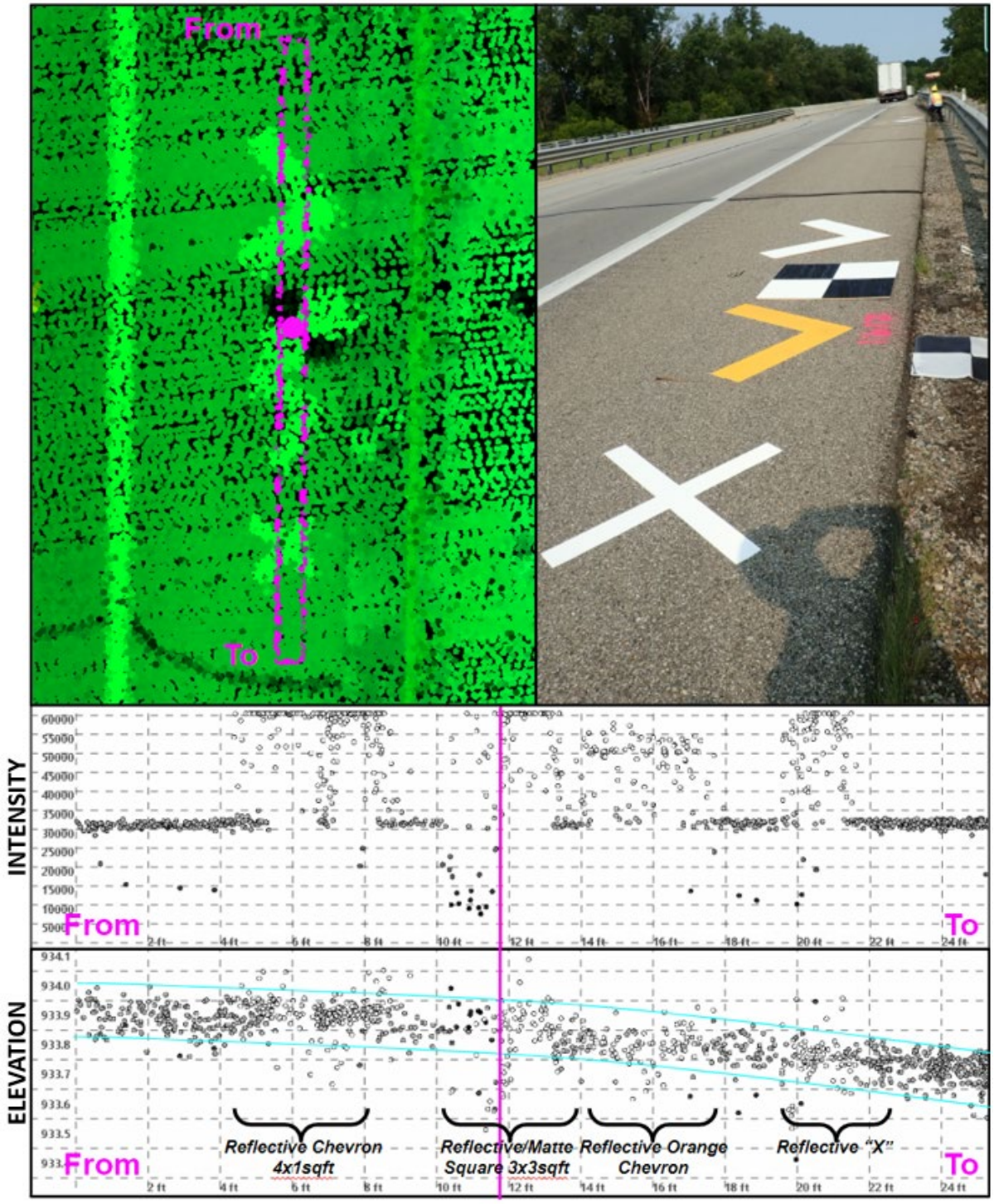

Figure 6.5.10: Top-right: Nikon imagery, Top-left: LiDAR scan intensity data and 1 foot-wide cross-section, Middle: Cross-section showing scan intensity, vertex color indicating intensity, Bottom: Cross-section showing LiDAR elevation, vertex color indicating intensity.

The magenta line in the middle and bottom panels indicates an approximate center for the cross-section and is represented in the top-left panel as a magenta dot. The blue lines in the bottom panel show an approximation of the road shoulder surface visually estimated from the non-target road surface points. **Points outside of this**

envelope are largely represented by reflective ground control, suggesting that reflectivity of the surface does have an impact on the elevation accuracy of the surface.

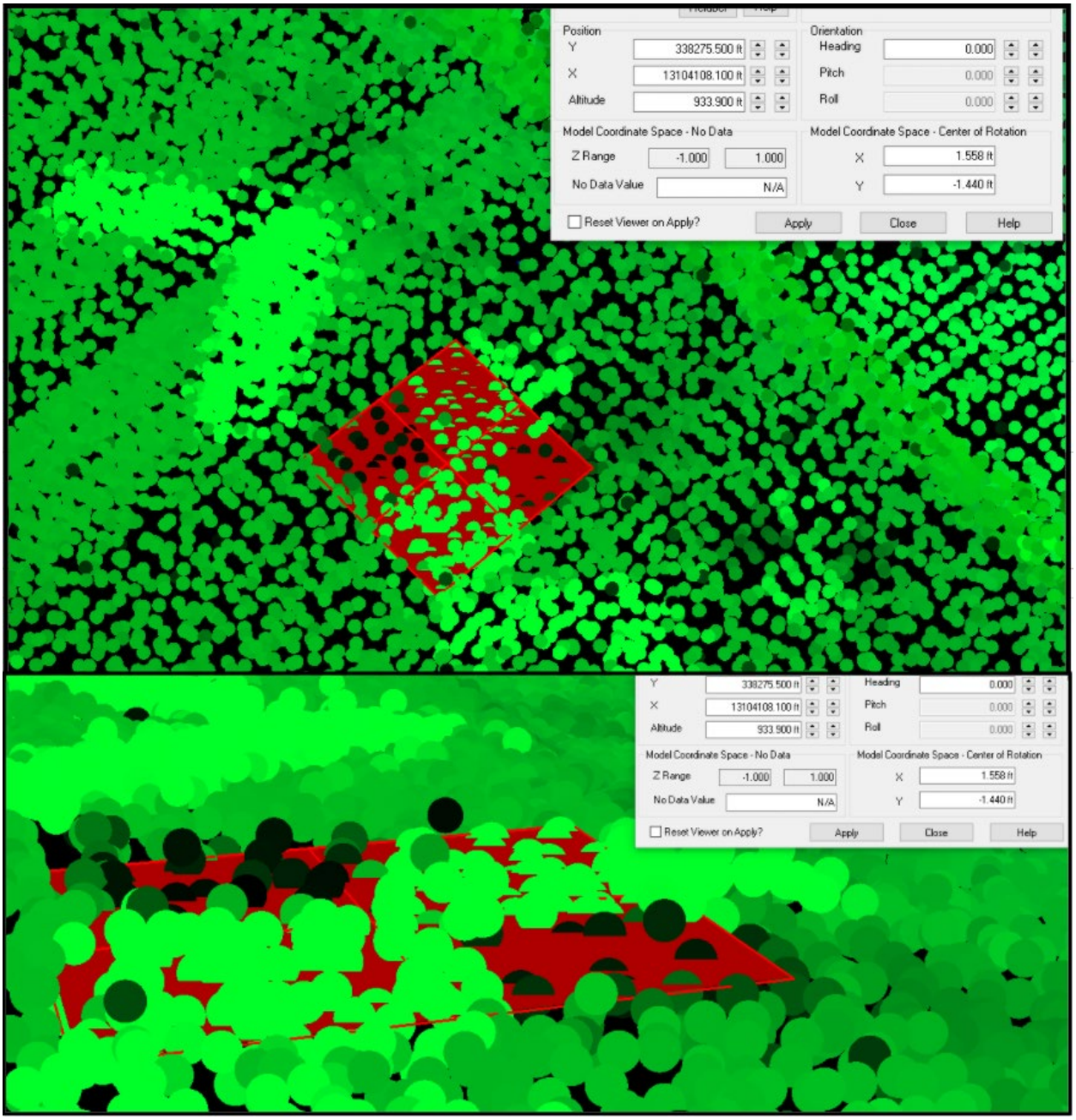

Figure 6.5.11: Vector-type file (e.g., a shapefile)

A vector-type file (e.g., a shapefile) can be used to recreate a ground control point of known proportions (pictured: a 3x3 sq ft vector field with four fields positioned on top of the 3x3 sq ft target in the LiDAR point cloud).Translating, rotating, changing elevation, and changing the roll and pitch of the vector file is possible (using most LiDAR manipulation software ~~softwares~~) in order to achieve the best possible alignment of the vector file in the point cloud data. **Assuming one uses a rigid ground control target, orienting this vector file to the LiDAR point data will provide the best possible estimate of the**

ground control center in the x,y, and z dimensions. This is especially useful when approximating ground control point centers for sparse data clouds.

6.6 UAS-enabled Bridge Inspection Demonstration Day

Appendix 6.6 will review the outcomes of the UAS-enabled bridge inspection demonstration once it has been completed, which will be after this draft Final Report that is due March 11, 2022. This event has been planned for the April/May 2022 time period.

6.7 ThermoConverter Tool by Aetha Global

ThermoConverter is a new tool developed by Aetha Global that converts thermal image formats provided by DJI into more readable image formats like R-JPEG (FLIR format) or TIFF (a standard raster image format). While DJI does have a Thermal Tool in beta release for analyzing temperature data within single images, ThermoConverter allows batch conversion of the DJI Mavic 2 Enterprise Advanced or DJI Zenmuse H20T thermal RGB imagery into single band thermal data (Figure 6.7.1). This is because ThermoConverter, likely through partnership with DJI, is able to read the unique RGB file metadata created by DJI (proprietary to DJI) such that it can convert to these more readable (R-JPEG, TIFF) formats (Figure 6.7.2).

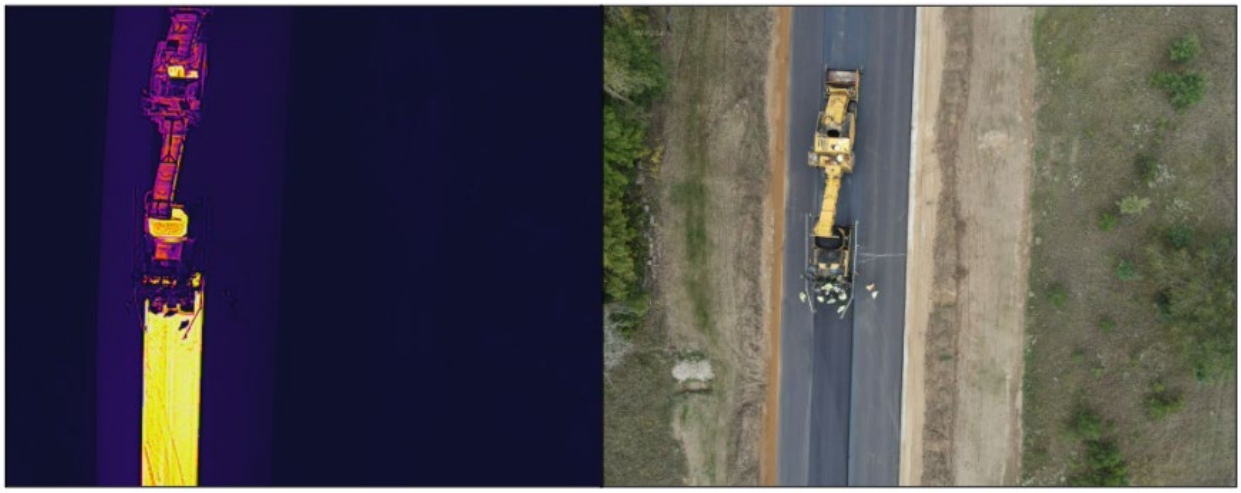

Figure 6.7.1: DJI RGB thermal image (left) and visual image (right) collected simultaneously by the Mavic 2 Enterprise Advanced during asphalt paving. The image on the left is an RGB representation of the thermal data captured by the M2EA's thermal camera and does not contain true-temperature thermal information (made inaccessible by DJI for batch processing).

This file conversion step is necessary for our purposes because the thermal information stored in DJI's images are not able to be batch processed or analyzed in non-DJI software. DJI currently only allows for thermal image export as an RGB representation of thermal data which has no associated thermal data, and the use of this RGB imagery in the production of a true-

temperature thermal orthoimage is not possible because each individual RGB image is scaled uniquely (based on the warmest and coldest objects in the camera field of view).

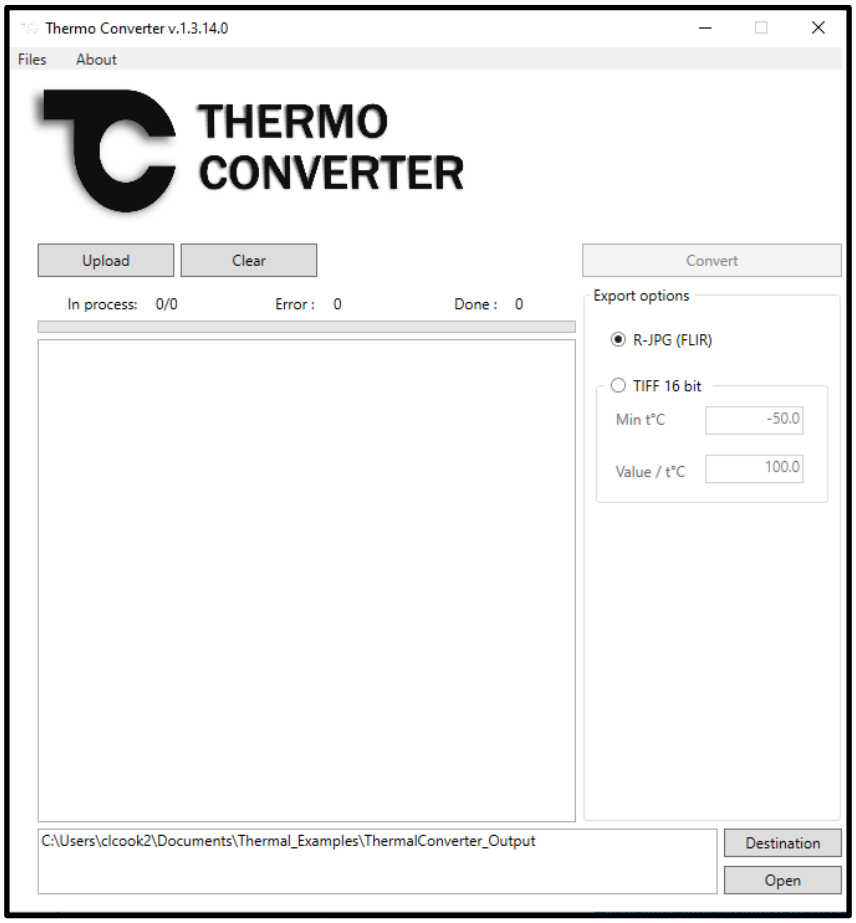

Figure 6.7.2: ThermoConverter tool interface. ThermoCOnverter allows for batch import of DJI thermal RGB images and can batch export them as an R-JPEG or GeoTIFF format. ThermoConverter is currently free for public institutions.

Once DJI RGB thermal images have been batch processed into R-JPEGs, they can be processed into a point cloud and then a thermal orthoimage using Pix4D image processing software (Figure 6.7.3). Images can also then be analyzed individually for true temperature differences using software like ArcGIS Pro, which could prove useful for using single thermal images (after georeferencing) as input to tools like the thermal delamination (TADDA) tool developed by MTU through this project.

Individuals producing thermal orthoimages should note that because a thermal mapping mission requires an interval of time to complete, and because a high amount of forward lap and sidelap is needed to create a thermal orthoimage, the final thermal orthoimage could output average thermal values that integrate changes in temperature that occur over the duration of the mapping mission (5-15 minutes). While this would normally have a very small impact on the output orthoimage, this could have a sizable impact when the thermal camera is capturing a wide

range of temperatures in an image or mission, or temperatures are changing considerably over a short time (e.g., during asphalt laying).

A wide variety of observed temperatures within a mapping mission can also make temperature orthoimage difficult because the thermal images, after being rescaled by ThermoConverter, can be 'washed out' by the presence of abnormally hot or cold objects (e.g. engines or motors, very reflective surfaces) within the mapped area. This 'washing out' of images makes it more difficult for software like Pix4D to find tie points to build a dense cloud and orthoimage. For these reasons, Pix4D and other software ~~softwares~~ (DroneDeploy) recommend achieving a thermal image overlap of 90% (which is much higher than mapping missions for visual imagery) if one plans to make a thermal orthoimage.

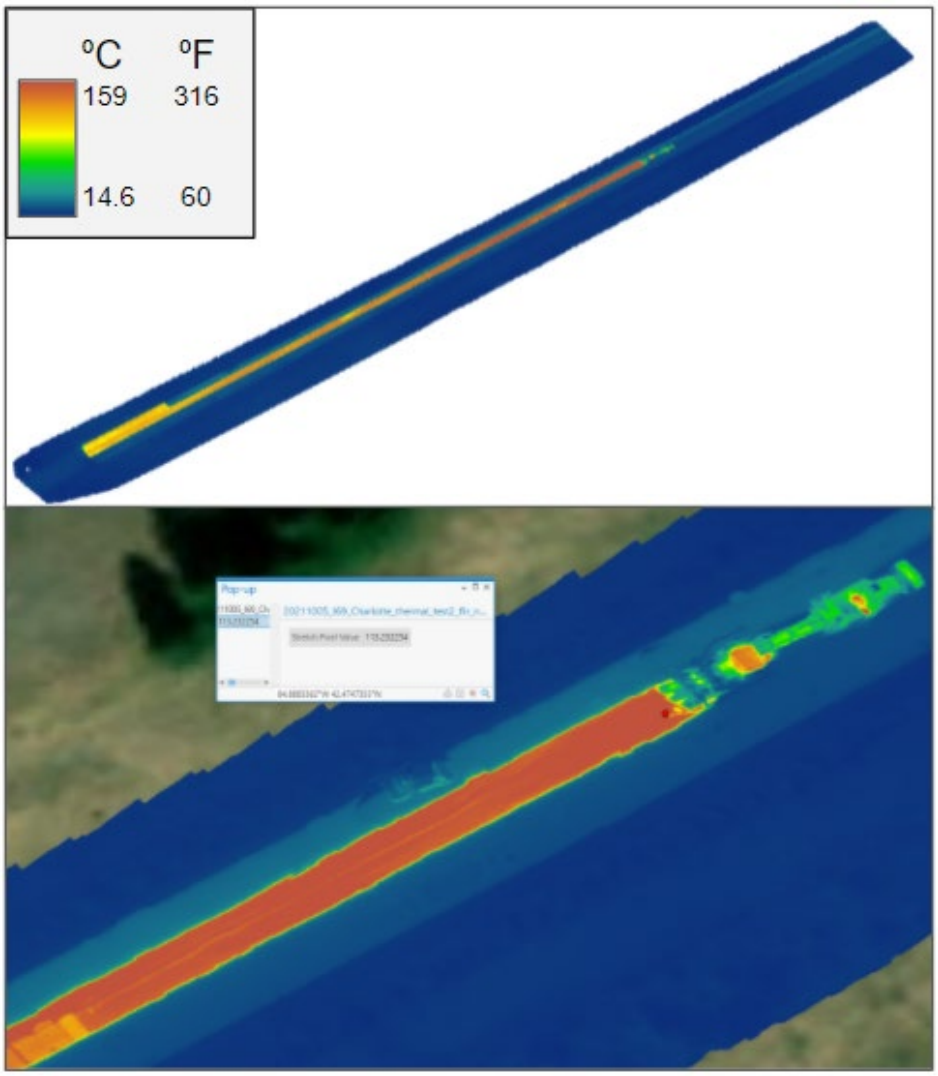

Figure 6.7.3: Example thermal orthoimage created in Pix4D, by stitching together R-JPEGs produced using ThermoConverter, produced from raw DJI RGB images, captured in one mapping flight of the DJI Mavic 2 Enterprise Advanced during asphalt laying on I-69 near Charlotte, MI, on October 5th, 2021.

6.8 TADDA and Spallgorithm Results (Quantitative Delamination and Spall Data)

Spall ID (FID)	Area (in²)	Area (ft²)	Area (cm²)	Area (m²)	Volume (in³)	Volume (cm³)	Max Depth (m)	Max Depth (ft)
0	28.31	0.20	182.64	0.018	2.89	47.38	0.005	0.016
1	76.98	0.54	496.64	0.050	23.04	377.54	0.016	0.052
2	302.55	2.10	1951.95	0.195	107.83	1766.99	0.012	0.039
3	83.42	0.58	538.18	0.054	21.65	354.82	0.021	0.069

Table 6.8.1: Laplaisance Creek/ I-75 Exit Ramp spallgorithm spall results.

Delam. ID (ObjectID)	Shape_Length (m)	Shape_Length (ft)	Shape_Area (m²)	Shape_Area (ft²)
1	0.501	1.645	0.011	0.120
2	3.202	10.506	0.286	3.081
3	0.779	2.557	0.032	0.349
4	2.136	7.008	0.076	0.813
5	1.605	5.266	0.170	1.826
6	1.290	4.232	0.078	0.839
7	2.685	8.809	0.211	2.276
8	0.821	2.695	0.027	0.289
9	0.454	1.488	0.012	0.129
10	2.031	6.662	0.175	1.883
11	0.665	2.181	0.019	0.206
12	0.501	1.642	0.011	0.118
13	0.697	2.288	0.027	0.290
14	0.821	2.695	0.027	0.289
15	0.414	1.358	0.010	0.111
16	0.697	2.288	0.027	0.290
17	1.516	4.975	0.111	1.190
18	1.364	4.476	0.112	1.200

Delam. ID (ObjectID)	Shape_Length (m)	Shape_Length (ft)	Shape_Area (m²)	Shape_Area (ft²)
19	0.575	1.886	0.019	0.209
20	1.664	5.458	0.077	0.824
21	0.414	1.358	0.010	0.111
22	0.792	2.598	0.035	0.374
23	0.592	1.941	0.022	0.238
24	1.042	3.417	0.043	0.459
25	0.519	1.703	0.012	0.131
26	0.651	2.136	0.019	0.209
27	0.537	1.761	0.017	0.184
28	0.743	2.438	0.032	0.340
29	1.025	3.362	0.069	0.742
30	0.835	2.740	0.037	0.396
31	0.862	2.828	0.039	0.421
32	1.694	5.559	0.081	0.869
33	0.708	2.324	0.017	0.183
34	0.722	2.370	0.031	0.333
35	0.810	2.657	0.038	0.407
36	0.434	1.424	0.011	0.121
37	0.717	2.352	0.027	0.290
38	0.618	2.027	0.024	0.254
39	1.569	5.148	0.097	1.049
40	0.883	2.897	0.039	0.414
41	1.149	3.770	0.080	0.858
42	0.739	2.426	0.029	0.311
43	1.149	3.769	0.062	0.665
44	0.501	1.644	0.010	0.112
45	1.386	4.548	0.120	1.287
46	0.894	2.932	0.044	0.476
47	1.287	4.223	0.067	0.725

Table 6.8.2: Laplaisance Creek/ I-75 Exit Ramp delamination TADDA results.

Delam. ID (ObjectID)	Shape_Length (m)	Shape_Length (ft)	Shape_Area (m²)	Shape_Area (ft²)
48	1.288	4.227	0.066	0.705
49	0.708	2.324	0.029	0.317
50	1.222	4.009	0.058	0.629
51	1.249	4.097	0.043	0.468
52	1.682	5.517	0.123	1.329

Table 6.8.3: M-99/I-96 bridge spallgorithm spall results.

Spall ID (FID)	Area (in²)	Area (ft²)	Area (cm²)	Area (m²)	Volume (in³)	Volume (cm³)	Max Depth (m)	Max Depth (ft)
0	12.56	0.087	81.05	0.008	1.86	30.53	0.006	0.020
1	11.87	0.082	76.55	0.008	1.75	28.76	0.006	0.020
2	28.27	0.196	182.37	0.018	5.46	89.47	0.008	0.026
3	392.33	2.725	2531.16	0.253	102.49	1679.48	0.012	0.039

Table 6.8.4: M-99/I-96 bridge delamination TADDA results.

Delamination ID (ObjectID)	Shape_Length (m)	Shape_Length (ft)	Shape_Area (m²)	Shape_Area (ft²)
0	2.242	7.357	0.202	2.179
1	2.624	8.608	0.370	3.980
2	4.036	13.241	0.491	5.282
3	1.809	5.935	0.127	1.362
4	2.758	9.048	0.124	1.334
5	9.857	32.339	1.185	12.757
6	0.809	2.655	0.029	0.311
7	1.407	4.617	0.045	0.479
8	4.310	14.141	0.353	3.799
9	1.044	3.426	0.066	0.706
10	1.420	4.659	0.094	1.016
11	1.040	3.412	0.037	0.397
12	0.510	1.673	0.015	0.157

Delamination ID (ObjectID)	Shape_Length (m)	Shape_Length (ft)	Shape_Area (m²)	Shape_Area (ft²)
13	1.128	3.700	0.056	0.603
14	0.876	2.874	0.029	0.311
15	2.126	6.974	0.176	1.898
16	0.693	2.275	0.025	0.271
17	0.534	1.751	0.011	0.123
18	1.632	5.353	0.069	0.742
19	5.595	18.355	0.551	5.926
20	2.331	7.646	0.116	1.243
21	5.667	18.593	0.430	4.626
22	6.288	20.631	0.447	4.813
23	0.893	2.930	0.053	0.566
24	0.461	1.514	0.013	0.136
25	12.070	39.601	1.570	16.900
26	1.728	5.668	0.138	1.488
27	22.356	73.347	1.968	21.187
28	4.587	15.049	0.604	6.504
29	2.945	9.661	0.165	1.777
30	0.516	1.693	0.012	0.129
31	1.260	4.133	0.040	0.430
32	3.530	11.582	0.282	3.033
33	0.576	1.889	0.017	0.181
34	0.483	1.586	0.014	0.151
35	2.040	6.693	0.083	0.889
36	4.343	14.249	0.192	2.071
37	1.164	3.817	0.038	0.405
38	2.810	9.218	0.190	2.041
39	1.063	3.488	0.046	0.493
40	1.770	5.809	0.165	1.772
41	0.975	3.199	0.060	0.643

Table 6.8.5: Uncle Henry Rd. bridge spallgorithm spall results.

Spall ID (FID)	Area (in²)	Area (ft²)	Area (cm²)	Area (m²)	Volume (in³)	Volume (cm³)	Max Depth (m)	Max Depth (ft)
0	37.84	0.263	244.14	0.024	4.19	68.65	0.005	0.016
1	157.11	1.091	1013.59	0.101	48.26	790.83	0.016	0.052
2	69.05	0.48	445.46	0.045	15.38	252.1	0.012	0.039
3	153.28	1.064	988.93	0.099	59.58	976.41	0.021	0.069
4	19.55	0.136	126.19	0.013	2.15	35.3	0.005	0.016
5	17.91	0.124	115.56	0.012	1.94	31.83	0.005	0.016

Table 6.8.6: Uncle Henry Rd. bridge delamination TADDA results.

Delamination ID (ObjectID)	Shape_Length (m)	Shape_Length (ft)	Shape_Area (m²)	Shape_Area (ft²)
16	1.085	3.561	0.072	0.779
19	1.247	4.091	0.075	0.810
21	0.245	0.805	0.003	0.031
23	1.554	5.098	0.132	1.417
30	1.149	3.770	0.093	1.000
32	0.394	1.292	0.009	0.093
40	0.699	2.292	0.030	0.322
43	1.625	5.333	0.146	1.577
49	0.124	0.406	0.001	0.008
52	0.408	1.339	0.008	0.083
55	0.833	2.732	0.037	0.396
60	1.832	6.009	0.125	1.348
61	0.802	2.630	0.036	0.385
63	2.992	9.818	0.583	6.272
64	0.867	2.844	0.030	0.318
65	4.032	13.229	0.490	5.278

Delamination ID (ObjectID)	Shape_Length (m)	Shape_Length (ft)	Shape_Area (m²)	Shape_Area (ft²)
66	5.229	17.155	0.705	7.589
68	11.826	38.798	1.946	20.951
70	0.233	0.764	0.003	0.027
73	0.124	0.406	0.001	0.008

Table 6.8.7: Beyer Rd. bridge delamination TADDA results.

Delamination ID (ObjectID)	Shape_Length (m)	Shape_Length (ft)	Shape_Area (m²)	Shape_Area (ft²)
67	0.469	1.540	0.013	0.142
68	1.052	3.451	0.052	0.555
71	0.710	2.329	0.025	0.268
77	0.562	1.845	0.018	0.194
85	1.242	4.076	0.072	0.777
89	0.568	1.863	0.014	0.151
90	0.851	2.792	0.040	0.426
96	8.522	27.960	1.086	11.688
110	1.605	5.265	0.093	0.999
111	5.343	17.528	0.482	5.189
118	1.329	4.361	0.094	1.008
120	0.695	2.279	0.019	0.206
121	0.675	2.213	0.020	0.217
125	2.180	7.152	0.182	1.954
129	1.544	5.067	0.154	1.660
132	2.114	6.935	0.145	1.564
194	1.482	4.862	0.150	1.615
195	3.053	10.018	0.289	3.107
197	1.490	4.887	0.109	1.172

Table 6.8.8: Billwood Rd./ I-96 bridge delamination TADDA results.

Delamination ID (ObjectID)	Shape_Length (m)	Shape_Length (ft)	Shape_Area (m²)	Shape_Area (ft²)
0	1.109	3.638	0.053	0.567
1	1.066	3.499	0.030	0.328
2	2.528	8.295	0.153	1.650
3	1.085	3.560	0.016	0.173
4	0.665	2.183	0.011	0.117
5	2.352	7.715	0.102	1.101
6	9.281	30.450	0.289	3.106
7	1.780	5.841	0.037	0.397
8	1.479	4.852	0.031	0.338
9	3.052	10.013	0.100	1.074
10	2.079	6.821	0.057	0.618
11	1.413	4.635	0.037	0.397
12	2.568	8.427	0.050	0.535
13	3.281	10.763	0.118	1.272
14	1.928	6.324	0.052	0.565
15	0.694	2.277	0.016	0.174
16	0.913	2.995	0.021	0.226
17	1.564	5.132	0.050	0.541
18	2.166	7.105	0.054	0.576
19	0.778	2.552	0.016	0.177
20	0.660	2.166	0.024	0.261
21	0.876	2.874	0.016	0.175
22	0.657	2.154	0.016	0.175
23	0.574	1.885	0.010	0.111
24	1.015	3.331	0.025	0.274
25	0.673	2.209	0.012	0.129
26	2.095	6.874	0.059	0.632
27	0.910	2.987	0.019	0.204
28	0.658	2.158	0.013	0.144

Delamination ID (ObjectID)	Shape_Length (m)	Shape_Length (ft)	Shape_Area (m²)	Shape_Area (ft²)
29	1.537	5.044	0.046	0.492
30	0.563	1.846	0.011	0.115
31	0.999	3.278	0.016	0.176
32	4.693	15.398	0.176	1.890
33	3.411	11.191	0.106	1.137
34	0.580	1.903	0.011	0.120
35	0.840	2.758	0.013	0.142
36	0.908	2.979	0.019	0.208
37	2.695	8.843	0.109	1.169
38	1.716	5.629	0.072	0.774
39	0.898	2.946	0.045	0.488
40	0.989	3.245	0.036	0.393
41	0.426	1.398	0.011	0.117
42	0.878	2.881	0.023	0.247
43	0.578	1.896	0.012	0.126
44	0.675	2.216	0.012	0.129
45	0.532	1.745	0.012	0.131
46	1.249	4.097	0.038	0.404
47	0.802	2.631	0.028	0.302
48	1.446	4.744	0.037	0.398
49	1.211	3.972	0.040	0.427
50	0.671	2.200	0.011	0.122
51	1.229	4.032	0.064	0.685
52	0.493	1.616	0.012	0.131
53	0.596	1.955	0.012	0.133
54	4.741	15.555	0.184	1.979
55	0.960	3.149	0.033	0.360
56	0.967	3.173	0.033	0.359
57	1.050	3.446	0.027	0.286

Delamination ID (ObjectID)	Shape_Length (m)	Shape_Length (ft)	Shape_Area (m²)	Shape_Area (ft²)
58	2.670	8.760	0.103	1.104
59	0.815	2.674	0.023	0.250
60	1.198	3.931	0.041	0.444
61	0.577	1.892	0.011	0.121
62	0.701	2.300	0.020	0.217
63	2.187	7.176	0.095	1.022
64	1.297	4.255	0.041	0.445
65	0.441	1.445	0.012	0.130
66	0.904	2.966	0.024	0.256
67	0.951	3.121	0.024	0.253
68	0.903	2.964	0.024	0.259
69	0.864	2.835	0.027	0.287
70	0.738	2.421	0.014	0.150
71	2.199	7.214	0.068	0.731
72	0.590	1.936	0.015	0.167
73	0.627	2.058	0.010	0.108
74	0.998	3.274	0.020	0.216
75	0.415	1.360	0.010	0.109
76	0.486	1.596	0.014	0.148
77	0.528	1.732	0.011	0.122
78	0.958	3.144	0.029	0.315
79	2.090	6.858	0.066	0.711
80	0.502	1.648	0.013	0.136
81	3.593	11.788	0.114	1.225
82	5.202	17.065	0.175	1.880
83	3.526	11.567	0.122	1.316
84	2.530	8.299	0.108	1.163
85	0.511	1.678	0.014	0.151
86	0.462	1.515	0.012	0.125

Delamination ID (ObjectID)	Shape_Length (m)	Shape_Length (ft)	Shape_Area (m²)	Shape_Area (ft²)
87	2.071	6.794	0.133	1.433
88	0.694	2.277	0.016	0.168
89	1.102	3.616	0.045	0.483
90	3.347	10.982	0.184	1.977
91	2.142	7.028	0.088	0.951
92	1.041	3.414	0.026	0.279
93	1.035	3.395	0.041	0.437
94	0.930	3.050	0.037	0.394
95	1.192	3.910	0.045	0.489
96	2.855	9.367	0.121	1.306
97	7.693	25.239	0.277	2.983
98	1.128	3.700	0.030	0.319
99	1.789	5.868	0.068	0.727
100	0.630	2.067	0.012	0.133
101	1.323	4.342	0.027	0.293
102	4.381	14.373	0.123	1.324
103	2.104	6.904	0.096	1.028
104	2.980	9.777	0.114	1.230
105	0.637	2.089	0.018	0.198
106	1.034	3.392	0.027	0.294
107	0.473	1.553	0.011	0.114
108	0.582	1.910	0.012	0.130
109	0.488	1.601	0.011	0.118
110	1.328	4.359	0.045	0.484
111	1.013	3.323	0.024	0.254
112	0.958	3.142	0.035	0.381